J. Hydrol. Hydromech., 71, 2023, 1, 1–10
https://doi.org/10.2478/johh-2023-0001

sciendo Journal of Hydrology and Hydromechanics Institute of Hydrology SAS

Effect of gravel content on soil water retention characteristics and thermal capacity of sandy and silty soils

Steffen Beck-Broichsitter[1*], Zarghaam Haider Rizvi[2,3], Rainer Horn[1], Frank Wuttke[3]

[1] Institute for Plant Nutrition and Soil Science, Kiel University, 24118 Kiel, Germany.
[2] Department of Civil Environmental Engineering, University of Waterloo, Waterloo, Ontario, Canada.
[3] Geomechanics & Geotechnics, Kiel University, Kiel, 24118, Germany.
[*] Corresponding author. E-mail: s.beck-broichsitter@soils.uni-kiel.de

Abstract: The presence of gravel in soils modifies the porosity, pore connectivity and pore size distribution in the soil matrix as well as the soil matrix-gravel interfaces. The aim of the present study is to investigate the effect of relative volume of gravel in samples with gravel mass fractions of 5,10, 20 wt% and varying bulk densities (1.3, 1.45, 1.55, 1.60, 1.65 g cm^{-3}) on (i) total porosity, field capacity, plant available water holding capacity, (ii) pore size distribution and (iii) thermal capacity of repacked sandy and silty soils. The focus of the study was to determine if laboratory measured soil water retention curves considering (i), (ii), and (iii) can be predicted by a gravel-based weighting factor, R_v, considering comprehensive significance tests. The sand-gravel mixtures show a decrease in the volume fractions of macropores and wide cores pores with an increase in the gravel contents, while the silt-gravel mixtures show an opposite trend. The root mean square errors (RMSE) between measured and fitted volumetric water contents, θ, between 0.006 and 0.0352 and between 0.002 and 0.004 for R_v-weighted volumetric water contents indicate that the van Genuchten-based Peters-Durner-Iden (PDI) model is appropriate for fitting. The soil water retention curves with mass gravel contents of up to 10 wt% for silt and 20 wt% for sand can be well predicted by weighting factors (relative volume of rock fragments) in the range between 0.045 and 0.058 for silt, and between 0.112 and 0.119 for sand. The results also indicate a decrease in the R_v-weighted saturated, c_{vsat}, and dry, c_{vdry}, thermal capacity with an increase in the gravel contents for both soils. Further investigations are needed to examine if and whether measured sand- and silt-gravel mixtures with mass gravel contents below 10 % or rather 20 % can be predicted with a weighting factor.

Keywords: Pore size distribution; Soil water retention curve; Thermal capacity; PDI model.

1 INTRODUCTION

Natural and anthropogenic soils are formed or modified by erosion of bedrock, decomposition of organic matter or human activity (Howard et al., 2017). Terrestrial and semiterrestrial soils as well as hydromorphic and sub-enhydrous soils except peat soils are normally characterised by a mixture of fine soil matrix and a coarse soil fraction (Bronick and Lal, 2005; Lu et al., 2021; Naseri et al., 2019; Rizvi et al., 2022). There is a wide range of stony and gravelly soils consisting of weathered calcareous or other material such as rendzinas, rankers or regosols and its horizon-specific gravel content as well as the spatial distribution varies from region to region (Beck-Broichsitter et al., 2022; Corti et al., 2002). The coarse soil fraction with an effective diameter > 2 mm and < 63 mm can be classified as slack (angular form) and gravel (round form) as a loose aggregation of rock fragments following the German Soil Science classification (Ad-Hoc AG Boden, 2005).

The presence of gravel modifies the porosity, pore connectivity, pore size distribution, PSD, in the soil matrix as well as the soil matrix-gravel interfaces (Beck-Broichsitter et al., 2022; Chief et al., 2008; Lu et al., 2021), based on the way they were weathered (Naseri et al., 2019). Its connectivity depends on the layering and the size of stones and fragments, and even stones can have some porosity (Miller et al., 2014; Naseri et al., 2019). In fact, gravel limits the effective surface of soil particles and may lower the water, nutrients and organic carbon storage capacity, its accessibility (Rytter, 2012; USDA/NRCS, 2005) as well as its thermal capacity, c_v (Abu-Hamdeh, 2003; Arkhangelskaya, 2020; Arkhangelskaya and Lukyashchenko, 2018). The c_v values in turn are of major importance for a wide range of engineering and scientific applications such as geothermal cooling and heating systems or high-voltage underground cable (Ahmad et al., 2021; Rerak and Ocłon, 2017; Rizvi et al., 2020; Rizvi et al., 2022). The c_v value strongly depend on soil texture, dry bulk density, ρ_b, porosity, Φ, particle size, water content, and mineralogy, with more than 60 % of soils made up of silicate minerals (Bertermann et al., 2018; Dong et al., 2015; Rizvi et al., 2020).

For further investigations of soil water retention and thermal characteristics, it is worth to consider and determine the relative soil volume that is occupied by the coarse soil fraction and its skeleton networks (Poeplau et al., 2017). However, the role of gravel in soils is diverging because of poor experimental observations (Naseri et al., 2019), but it is difficult to measure and calculate the volume of coarse soil fraction due to the complexity and amorphous structures in the porous medium (Maroof et al., 2022).

The idea of the present study is to investigate the effect of different volume fractions of gravel and varying bulk densities on soil water retention and thermal characteristics of repacked sandy and silty soils. The aim of the study is to identify the effect of gravel contents on (i) soil water retention, (ii) pore size distribution, and (iii) thermal capacity considering a relative volume of rock fragments, R_v. As a working hypothesis, a decrease in the plant available water holding capacity and saturated thermal capacity with an increase in the gravel content was expected.

2 MATERIALS AND METHODS

2.1 General soil characteristics

The sandy soil material is derived from a C horizon of a Podzol in Büttgebüll (54º65'N, 8º90'E) in Northern Germany, and the silty soil material is derived from an A horizon of a Stagnic Luvisol in Harste (51º59'N, 9º85'E) in Central Germany (Table 1). The sandy and silty soil material was repacked in 100 cm^3 soil cores (height: 4 cm, diameter: 5.5 cm) with five specified bulk densities 1.3 g cm^{-3}, 1.45 g cm^{-3}, 1.55 g cm^{-3}, 1.60 g cm^{-3}, and 1.65 g cm^{-3} and in combination with four different gravel contents of 0 %, 5 %, 10 %, and 20 % (Fig. 1). Gravel contents (mixture of crushed basalt and granite) between 5 % and 10 % are classified as low, while 20% are classified as moderate (Ad-Hoc AG Boden, 2005). The investigated soil-gravel mixtures are presented in Table 1.

To ensure uniform bulk densities, the soil material was carefully packed by means of a load frame through a stamp (diameter: 5.5 cm) with a static load of 50 kN (Instron, Norwood, MA, USA).

The sand, silt, and clay contents (wt%) were analysed by wet sieving (> 63 µm) and pipette method (≤ 63 µm); organic carbon, OC (wt%), by coulometric carbon dioxide method; saturated hydraulic conductivity, Ks (cm d^{-1}), by falling-head method (Hartge and Horn, 2016); bulk density, ρ_b (g cm^{-3}), by drying intact soil cores of 100 cm^3 at 105 °C for 24 hours (Blake and Hartge, 1986). The Ks values and ρ_b parameters are further classified by Ad-Hoc AG Boden (2005).

Table 1. Particle size distribution (wt%) of silt and sand samples with different mixtures of basalt and granite (R_m, wt% gravel) including gravel (2 – < 4 mm), sand (2 mm – ≥ 0.063 mm), silt (< 0.063 mm – ≥ 0.002 mm), clay (< 0.002 mm), organic carbon, OC (wt%), and bulk density, ρ_b (g cm^{-3}). Mean values and from three replicates each (five replicates for ρ_t).

Soil	Mixture	Sand (wt%)	Silt (wt%)	Clay (wt%)	Gravel (wt%)	OC (wt%)	ρ_b (g cm^{-3})
Silt	1.3_0 %	11	68	21	–	≤ 2	1.3
Silt	R_m_1.3_5 %	11	68	21	5	≤ 2	1.3
Silt	R_m_1.3_10 %	11	68	21	10	≤ 2	1.3
Silt	1.45_0 %	11	68	21	–	≤ 2	1.45
Silt	R_m_1.45_5 %	11	68	21	5	≤ 2	1.45
Silt	R_m_1.45_ 10%	11	68	21	10	≤ 2	1.45
Silt	1.55_0 %	3	80	17	–	≤ 1.4	1.55
Silt	R_m_1.55_5 %	3	80	17	5	≤ 1.4	1.55
Silt	R_m_1.55_10 %	3	80	17	10	≤ 1.4	1.55
Silt	1.65_0 %	3	80	17	–	≤ 1.4	1.65
Silt	R_m_1.65_5 %	3	80	17	5	≤ 1.4	1.65
Silt	R_m_1.65_10 %	3	80	17	10	≤ 1.4	1.65
Sand	1.6_0 %	85	13	2	–	≤ 1	1.6
Sand	R_m_1.6_5 %	85	13	2	5	≤ 1	1.6
Sand	R_m_1.6_10 %	85	13	2	10	≤ 1	1.6
Sand	R_m_1.6_20 %	85	13	2	20	≤ 1	1.6
Sand	1.7_0 %	85	13	2	–	≤ 1	1.7
Sand	R_m_1.7_5 %	85	13	2	5	≤ 1	1.7
Sand	R_m_1.7_10 %	85	13	2	10	≤ 1	1.7
Sand	R_m_1.7_20 %	85	13	2	20	≤ 1	1.7

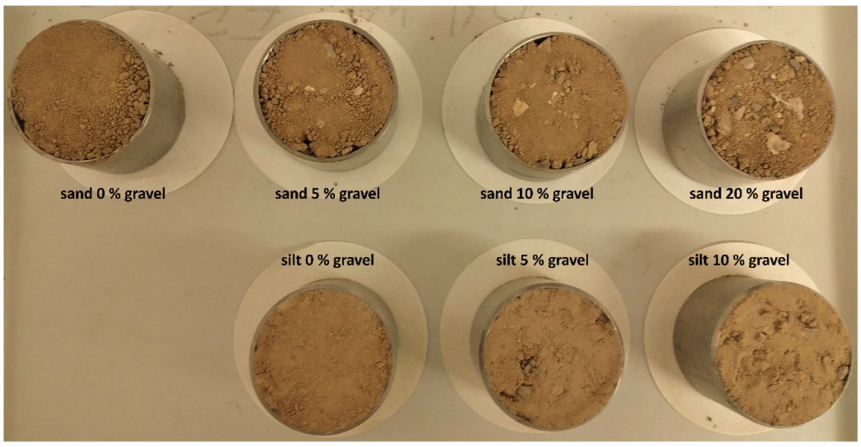

Fig. 1. Exemplary oven-dried soil cores with sand and silt material and different mass gravel contents of 0 wt%, 5 wt%, 10 wt%, and 20 wt%, respectively.

2.2 Soil physical properties

The mass gravel contents (dry mass of gravel per total dry mass) were R_m = 5 wt%, 10 wt%, and 20 wt% and the mass of the gravel, m_g (g) and the soil without gravel, m_s (g), were determined separately with oven-dried samples by previous sieving (2 mm mesh size) as mentioned by Naseri et al. (2019). The volume of gravel, V_g (cm^3), as mixture of basalt and granite (ρ_g: 2.853 g cm^3) and the volume of soil particles for quartz-dominated sand (ρ_g: 2.65 g cm^3) and silt (ρ_g: 2.8 g cm^3) were used to determine the volume of the soil, V_s (cm^3).

The volume of the gravel content was determined as follows (Bouwer and Rice, 1984; Naseri et al., 2019; Novak et al., 2011):

$$R_v = R_m \frac{\rho_b}{\rho_g} \quad (1)$$

The soil water retention curves, SWRC, of both datasets were obtained from intact soil cores of 100 cm^3 with 5–7 replicates per soil depth, respectively. Nearly saturated samples were dehydrated with suction plate for applied pressure heads, h, of –60, –150, –300, and –500 hPa, with a pressure chamber at –15000 hPa, and by drying at 105 °C for 24 h.

The residual water content, θ_r (cm^3 cm^{-3}), acts as fitting parameter of the commonly used van Genuchten SWRC model (MvG model) at which the slope of the SWRC becomes zero towards the dry end of the SWRC. This assumption is partially incorrect, because at the very dry end of the SWRC (pF 6.8), the water content eventually becomes zero (Haghverdi et al., 2020). Thus, the Peters-Durner-Iden (PDI) soil water retention curve model was proposed which reaches zero water content at oven dryness through a linear water content reduction in the dry range of the SWRC (Peters, 2013, 2014).

The so-called PDI model was used for analysing the soil water retention and hydraulic conductivity characteristics of the sandy and silty soils with varying gravel contents. Further information are listed in the HYPROP-FIT software manual (Pertassek et al., 2015).

The general form of the MvG-based PDI model consists of a capillary retention term, θ^{cap}, and an adsorptive retention term, θ^{ad}, following Peters (2013, 2014):

$$\theta(h) = \theta^{cap}(h) + \theta^{ad}(h) = (\theta_s - \theta_r)S^{cap} + \theta_r S^{ad} \quad (2)$$

where S^{cap} and S^{ad} are the capillary and the adsorption saturation functions and θ_r is the maximum water content for the water adsorption (Haghverdi et al., 2020). S^{cap} is substituted by the scaled version to ensure that θ reaches 0 cm^3 cm^{-3} at $h = h_0$ (Peters, 2013, 2014):

$$\theta(h) = (\theta_s - \theta_r)\frac{\Gamma(h) - \Gamma_0}{1 - \Gamma_0} + \theta_r S^{ad} \quad (3)$$

where $\Gamma(h)$ is the basic saturation function and Γ_0 is the basic function at $h = h_0$ (Haghverdi et al., 2020). The constrained unimodal expression for the model of van Genuchten (1980) is:

$$\Gamma(h) = \left[\frac{1}{1 + (\alpha h)^n}\right]^{1-1/n} \quad (4)$$

where θ_s is saturated and θ_r is residual water content (cm^3 cm^{-3}), α (cm^{-1}), n (–) and m (–), with m = 1 – 1/n, are empirical parameters.

The water adsorption saturation function is calculated as follows (Iden and Durner, 2014):

$$S^{ad}(x) = 1 + \frac{1}{x_a - x_0}\left\{x - x_a + b\ln\left[1 - \exp\left(\frac{x_a - x}{b}\right)\right]\right\} \quad (5)$$

with

$$b = 0.1 + \frac{0.2}{n^2}\left\{1 - \exp\left[-\left(\frac{\theta_r}{\theta_s - \theta_r}\right)^2\right]\right\} \quad (6)$$

where x_a and x_0 are the log h values equal to the suction at air-entry, ha (hPa), and the adsorptive retention, h_0 (hPa), and b is the shape parameter.

The SWRC of each soil-gravel mixture was used to describe the characteristic pore size distribution (PSD) considering macropores (MaP: h1 ≥ –10 hPa), wide coarse pores (wCP: –10 > h2 ≥ –60 hPa), narrow coarse pores (nCP: –60 > h3 ≥ –300 hPa), medium pores (MP: –300 > h4 ≥ –15000 hPa), and fine pores (FP: h5 < –15000 hPa). Based on the SWRC and the PSD, the characteristic retention properties can be derived as follows: total porosity (TP, $1–\rho_t\,\rho_g^{-1}$, Vol.%), air capacity (AC = proportion of wide coarse pores, Vol.%), plant available water capacity (AWC, proportion of narrow coarse and medium pores, Vol.%) and permanent wilting point (PWP, proportion of fine pores, Vol.%).

The SWRC was weighted by the R_v factor to receive an effective water retention curve, θ_e (cm^3 cm^{-3}), and hydraulic conductivity, K_e (cm d^{-1}), following Naseri et al. (2019):

$$\theta_e(h) = (1 - R_v)\theta_{soil}(h) \quad (7)$$

The SWR functions were fitted in a first step and the derived van Genuchten parameter like α, n, m, and Ks were then used in a second step for predicting the K(Se) functions.

The volumetric thermal capacity, c_v (J $m^{-3}K^{-1}$), was estimated using the de Vries model (1963) modified by Arkhangelskaya, 2009, 2020) and extended by the weighting factor, R_v, to consider the gravel content and its specific heat capacity:

$$c_v = \left(c_{mh} + \left(\frac{OM}{100}\right) + \left[(1 - R_v)c_{m\,min}\left(1 - \frac{OM}{100}\right) + R_v c_{m\,g}\left(1 - \frac{OM}{100}\right)\right]\right)\rho_b + c_{mw}\rho_w\theta \quad (8)$$

where c_{ms} (J $m^{-3}K^{-1}$) is specific thermal capacity of dry soil ($c_{m\,min}$ = average for sand, silt, and clay: 0.7525 J/m³*K; $c_{m\,g}$ = gravel: 0.815 J/m³*K), c_{mh} (J $m^{-3}K^{-1}$) is specific thermal capacity of soil organic matter (OM: 1.9 J/m³*K, OM = 1.97*OC), respectively.

2.3 Statistical analyses

The root mean square error, RMSE, is used to measure the error of the van Genuchten-based PDI model in predicting quantitative data (Pertassek et al., 2011):

$$RMSE = \sqrt{\frac{1}{n}\sum_{i=1}^{n}(K(Se)_{fit} - K(Se)_{obs})^2} \quad (9)$$

where $K(se)_{fit}$ are fitted and $K(se)_{obs}$ measured values.

The statistical software R (R Development Core Team, 2014) was used to evaluate the data. The data were normally distributed and heteroscedastic based on the results of Shapiro-Wilk-Test and graphical residue analysis. The statistical model was used for evaluating 1) volume fractions of MaP, wCP, nCP, MP, and FP in Table 2, and 2) TP, AC, AWC, and PWP in Table 3 including

the texture (sand, silt), gravel content (5, 10, and 20 wt%), bulk density (1.3, 1.45, 1.55, 1.6, 1.65, and 1.7 g cm^{-3}), and their interaction terms (two-fold and three-fold). An analysis of variance (ANOVA) was conducted with $p<0.05$ followed by Tukey`s HSD test (*p≤0.05, **p≤0.01, ***p≤0.001, ****p≤0.0001) according to Hasler and Horton (2008). The correlation coefficient (r^2) was used as an index for the goodness of fit.

3 RESULTS AND DISCUSSION

The results of the following chapter follow the description of the soil-gravel mixtures in Table 1. The results are focussed on the R_V-weighted SWRC's considering the PSD and the retention properties as well as the thermal capacity compared to the measured SWRC's.

3.1 R_v-weighted SWRC's vs. measured SWRC's

In the first step, the R_v values or rather the volume of the gravel content was calculated with Eq. 1. based on the weight and volume of the soil material in the intact soil cores of 100 cm^3 and mass of the added gravel (5 wt%, 10 wt%, 20 wt%), respectively. In the second step, the measured and fitted SWRC'S with 0 wt% gravel (prefix m_) and its corresponding PSD's and retention properties including m_1.3_0 %, m_1.45_0 %, m_1.55_0 %, m_1.65_0 %, m_1.6_0 %, m_1.7_0 % were corrected by the volume of the gravel content (prefix R_v_), respectively, using the R_v values in Table 2.

In Table 3, the Ks values of the sand-gravel mixtures (1.6_0% to R_v_1.6_20 %; 1.7_0 % to R_v_1.7_20 %) are larger than 300 cm d^{-1} and can be classified as extremely high (Ad-Hoc AG Boden, 2005). On the other hand, the Ks values of the silt-gravel mixtures between 3.0 and 8.9 cm d^{-1} are classified as low (Ad-Hoc Ag Boden, 2005). Thus, the hydraulic conductivity in silt- and sand-gravel mixtures depends on the gravel content (Lu et al., 2021; Miller et al., 2014).

For explanation, She et al. (2006) have shown that 100 % gravel soils stepwise filled with sand (+5 wt%, +20 wt%, +50 wt%) are characterised by a decrease in Ks values, because the sand fills the gap between the stones. Conversely, gravel may form a contact skeleton and therefore a preferential flow domain (Beck-Broichsitter et al., 2022; Lu et al., 2021) while stepwise added to a sandy or silty soil. Thus, the Ks values increase as also shown by Shakoor and Cook (1990), and Chapuis (2004).

Especially the results of Shakoor and Cook (1990) indicate an increase in the Ks values from increase of 0.01 cm d^{-1} up to 8640 cm d^{-1} though stepwise increase of the gravel content of a silty clay from 0 % to 70 % with a grain diameter of 2 to 4.75 mm.

Furthermore, the Ks values of gravelly sand usually range between 220 and 4620 cm d^{-1} and for gravelly silt between 0.43 and 43.2 cm d^{-1} as proposed by USDA/NRCS (2007) and underline the measured results in Table 3.

The sandy soils in Table 3 and Table 4 indicate a significant decrease in the volume fractions of macropores and wide coarse pores and therefore in the total porosity and air capacity with an increase in the gravel contents. Moreover, the volume fractions of narrow coarse pores, medium pores, and fine pores and therefore the available water capacity and permanent wilting point remain equal or tend to decrease with an increase in gravel contents. The reason for this is that gravel has a negligible (zero) retention capacity (Hlavacikova et al., 2015). For the silt-gravel mixtures in Table 3 and Table 4, the increase in the volume fractions of macropores and wide coarse pores can be derived by the so-called lacunar pores that are located at the interface between gravel fragments and fine fraction of silty and clayey soils (Fies et al., 2002; Sauer and Logsdon, 2002). These relatively stable macropores can be developed by drying-induced shrinkage (Beck-Broichsitter et al., 2018, 2020) and between the space of gravel and fine fraction if it is not fully filled with fine fraction (Fies et al., 2002; Miller et al., 2014). On the other hand, the pore space developed by coarse fraction are occupied by the fine fraction. Thus, the only open pores exist within the fine fraction, and the coarse fraction behaves as pore-free inclusions within a fine matrix effectively reducing the total porosity (Miller et al., 2014) as shown in Table 4.

In Table 5 and Table 6, the measured and fitted SWRC's of the sand- and silt-gravel mixtures considering Eq. 4–6 as well as the R_v-weighted and fitted SWRC's of the sand- and silt-gravel mixtures considering Eq. 7 and its empirical and statistical van Genuchten-based PDI model parameter (Peters, 2013,2014) are compared with each other. The RMSE values in Table 6 are used to quantify the error of the fitted data compared to the measured volumetric water contents, θ. The RMSE values for measured vs. fitted volumetric water contents of the SWRC's vary between 0.006 and 0.0352 cm^3 cm^{-3} and the RMSE values for measured vs. fitted R_v-weighted volumetric water contents of the SWRC's vary between 0.002 and 0.004 cm^3 cm^{-3}. Thus, there is a good agreement between the fitted data provided by the MvG-based PDI model and the measured data.

Table 2. Dry mass of the soil without gravel, m_s (g), dry mass of the gravel, m_g (g), volumetric stone content, R_v (–). Mean values from 5 replicates of measured SWRC'S (prefix m_) with 0 % gravel and R_m-weighted mixtures (prefix R_m_) with 5 wt%, 10 wt%, and 20 wt% of gravel.

Mixture	m_s g	m_g g	R_v –	Mixture	m_s g	m_g g	R_v –
m_1.3_0 %	130.5	–	–	R_m_1.65_5 %	165.91	8.29	0.029
R_m_1.3_5 %	131.1	6.55	0.022	R_m_1.65_10 %	166.45	16.65	0.058
R_m_1.3_10 %	131.2	13.12	0.045	m_1.6_0 %	159.38	–	–
m_1.45_0 %	145.3	–	–	R_m_1.6_5 %	159.27	7.96	0.028
R_m_1.45_5 %	145.65	7.28	0.025	R_m_1.6_10 %	159.21	15.92	0.056
R_m_1.45_ 10 %	145.79	14.58	0.051	R_m_1.6_20 %	161.11	32.22	0.112
m_1.55_0 %	156.64	–	–	m_1.7_0 %	168.48	–	–
R_m_1.55_5 %	156.02	7.81	0.027	R_m_1.7_5 %	168.61	8.43	0.029
R_m_1.55_10 %	156.53	15.65	0.054	R_m_1.7_10 %	168.03	16.81	0.059
m_1.65_0 %	165.21	–	–	R_m_1.7_20 %	167.74	33.54	0.119

Table 3. Saturated hydraulic conductivity, Ks (cm d^{-1}), and volume fractions of pore classes for macropores (MaP) with d > 0.3 mm, wide coarse pores (wCP) with 0.3 ≤ d > 0.05 mm, narrow coarse pores (nCP) with 0.05 ≤ d > 0.01 mm, medium pores (MP) with 0.01 ≤ d > 0.0002 mm, and fine pores (FP) with d ≤ 0.0002 mm (USDA/NRCS. 2005). Mean values from 5 replicates each. Statistical significance in the R_v-weighted (prefix R_v_) subgroups compared to the measured subgroup (prefix m_) without gravel (0 wt%), respectively, is indicated by p-values with a significance level ≤ 0.05, with *p≤0.05, **p≤0.01, ***p≤0.001, ****p≤0.0001.

Mixture	MaP	wCP	nCP	MP	FP	Ks
	$cm^3\ cm^{-3}$	$cm^3\ cm^{-3}$	$cm^3\ cm^{-3}$	$cm^3\ cm^{-3}$	$cm^3\ cm^{-3}$	$cm\ d^{-1}$
m_1.3_0 %	0.0043	0.0323	0.0831	0.2149	0.259	8.6±1.3
R_v_1.3_5 %	0.0052	0.0353*	0.0759	0.1984	0.2605	8.8±1.2
R_v_1.3_10 %	0.0059	0.0406	0.0809	0.1932	0.2414*	8.9±1.1
m_1.45_0 %	0.0016	0.0132	0.056	0.2199	0.2902	3.1±1.1
R_v_1.45_5 %	0.0021	0.0174	0.0654*	0.2152	0.2695	3.1±1.2
R_v_1.45_ 10%	0.0022	0.0185	0.0656**	0.2088	0.2665	4.2±1.1
m_1.55_0 %	0.0055	0.0377	0.0712	0.1746	0.2318	5.6±1.3
R_v_1.55_5 %	0.0048	0.0358	0.0728	0.1767	0.2294	7.0±1.2
R_v_1.55_10 %	0.006	0.0388	0.0652	0.1613	0.224	7.4±1.2
m_1.65_0 %	0.0012	0.0099	0.0496	0.2188	0.2818	3.0±1.1
R_v_1.65_5 %	0.0017	0.0142	0.0567	0.2018	0.2701	3.3±1.2
R_v_1.65_10 %	0.0025	0.0211**	0.0631	0.1859	0.2506	3.9±1.3
m_1.6_0 %	0.3137	0.0782	0.0156	0.0141	0.0177	1743±61
R_v_1.6_5 %	0.3086	0.0685**	0.0131	0.0134	0.018	1782±59
R_v_1.6_10 %	0.3035	0.0743	0.0136	0.0094	0.0107	1810±78
R_v_1.6_20 %	0.2714***	0.0656****	0.0123	0.0099	0.0121	1868±62
m_1.7_0 %	0.3256	0.0772	0.0166	0.0194	0.0267	1824±47
R_v_1.7_5 %	0.3194	0.0829	0.0165	0.0136	0.0161	1905±92
R_v_1.7_10 %	0.3073	0.07	0.0127	0.0107	0.0135	1814±76
R_v_1.7_20 %	0.2827***	0.0568****	0.01	0.0107	0.0146	1776±96

Table 4. Total porosity, TP ($cm^3\ cm^{-3}$), Air capacity, AC ($cm^3\ cm^{-3}$), plant available water capacity, AWC ($cm^3\ cm^{-3}$), and permanent wilting point, PWP ($cm^3\ cm^{-3}$). Mean values from 5 replicates each. Statistical significance in the R_v-weighted (prefix R_v_) subgroups compared to the measured subgroup (prefix m_) without gravel (0 wt%), respectively, is indicated by p-values with a significance level ≤ 0.05, with *p≤0.05, **p≤0.01, ***p≤0.001, ****p≤0.0001.

Mixture	TP	AC	AWC	PWP
	$cm^3\ cm^{-3}$	$cm^3\ cm^{-3}$	$cm^3\ cm^{-3}$	$cm^3\ cm^{-3}$
m_1.3_0 %	0.593	0.0366	0.298	0.259
R_v_1.3_5 %	0.573	0.0405	0.2743	0.2605
R_v_1.3_10 %	0.558	0.0465	0.2741	0.2414*
m_1.45_0 %	0.589	0.0148	0.2759	0.2902
R_v_1.45_5 %	0.578	0.0195	0.2806	0.2695
R_v_1.45_ 10%	0.565	0.0207	0.2744	0.2665
m_1.55_0 %	0.525	0.0432	0.2458	0.2318
R_v_1.55_5 %	0.525	0.0406	0.2495	0.2294
R_v_1.55_10 %	0.498	0.0448	0.2265	0.2241
m_1.65_0 %	0.601	0.0111	0.2684	0.2818
R_v_1.65_5 %	0.572	0.0159	0.2585	0.2701
R_v_1.65_10 %	0.527	0.0235**	0.2490	0.2506
m_1.6_0 %	0.438	0.3919	0.0297	0.0177
R_v_1.6_5 %	0.421	0.3771	0.0265	0.018
R_v_1.6_10 %	0.411	0.3778	0.023	0.0107
R_v_1.6_20 %	0.371	0.337***	0.0222	0.0121
m_1.7_0 %	0.464	0.4028	0.036	0.0267
R_v_1.7_5 %	0.448	0.4023	0.0301	0.0161
R_v_1.7_10 %	0.414	0.3773	0.0234	0.0135
R_v_1.7_20 %	0.374**	0.3395****	0.0207	0.0146

In Fig. 2 and Fig. 3, the SWRC's fitted with the van Genuchten-based PDI model (Peters, 2013, 2014) changed near saturation with increasing gravel content due to the additional formation of coarse voids at the soil matrix-gravel interfaces (Naseri et al., 2019). In Fig. 3, the measured and R_v-weighted SWRC's show almost congruence and because of the very low RMSE values and therefore the high correlation between fitted as well as measured and R_V-weighted SWRC's, only the fitted SWRC's are shown in Fig. 2 and Fig. 3.

Table 5. Mean values from 5 replicates of measured (prefix m_), R_v-weighted (prefix R_v_) and its fitted mean hydraulic parameter, respectively, by using the van Genuchten-based PDI model (Peters, 2013, 2014) model based on the HYPROP software (Pertassek et al., 2015). θ_s is saturated and θ_r is residual water content ($cm^3\ cm^{-3}$), α (cm^{-1}), n (–) and m (–), with m = 1 – 1/n, are empirical parameters.

Mixture	θ_r	θ_s	n	α	Mixture	θ_r	θ_s	n	α
	$cm^3\ cm^{-3}$		–	cm^{-1}		$cm^3\ cm^{-3}$		–	cm^{-1}
m_1.3_0 %	0.594	0.400	1.188	0.017	m_1.3_0 %	0.594	0.400	1.188	0.017
m_1.3_5 %	0.575	0.400	1.122	0.025	R_v_1.3_5 %	0.581	0.398	1.194	0.018
m_1.3_10 %	0.562	0.400	1.155	0.029	R_v_1.3_10 %	0.567	0.390	1.195	0.018
m_1.45_0 %	0.581	0.400	1.135	0.008	m_1.45_0 %	0.581	0.400	1.135	0.008
m_1.45_5 %	0.570	0.400	1.178	0.010	R_v_1.45_5 %	0.566	0.400	1.139	0.008
m_1.45_10%	0.562	0.400	1.165	0.011	R_v_1.45_10%	0.551	0.392	1.142	0.008
m_1.55_0 %	0.521	0.400	1.155	0.029	m_1.55_0 %	0.521	0.400	1.155	0.029
m_1.55_5 %	0.520	0.400	1.189	0.025	R_v_1.55_5 %	0.520	0.400	1.184	0.025
m_1.55_10 %	0.495	0.400	1.124	0.035	R_v_1.55_10 %	0.495	0.400	1.119	0.035
m_1.65_0 %	0.561	0.400	1.178	0.006	m_1.65_0 %	0.561	0.400	1.178	0.006
m_1.65_5 %	0.545	0.400	1.139	0.009	R_v_1.65_5 %	0.545	0.400	1.134	0.009
m_1.65_10 %	0.523	0.400	1.147	0.015	R_v_1.65_10 %	0.529	0.387	1.118	0.062
m_1.6_0 %	0.483	0.044	2.015	0.500	m_1.6_0 %	0.483	0.044	2.015	0.500
m_1.6_5 %	0.463	0.045	2.092	0.500	R_v_1.6_5 %	0.465	0.045	2.090	0.497
m_1.6_10 %	0.454	0.026	2.013	0.500	R_v_1.6_10 %	0.457	0.027	2.010	0.498
m_1.6_20 %	0.409	0.030	2.028	0.500	R_v_1.6_20 %	0.411	0.030	2.025	0.498
m_1.7_0 %	0.509	0.066	2.065	0.500	m_1.7_0 %	0.509	0.066	2.065	0.500
m_1.7_5 %	0.494	0.040	1.986	0.500	R_v_1.7_5 %	0.497	0.040	1.982	0.498
m_1.7_10 %	0.456	0.034	2.065	0.500	R_v_1.7_10 %	0.459	0.034	2.062	0.497
m_1.7_20 %	0.411	0.036	2.153	0.500	R_v_1.7_20 %	0.414	0.037	2.153	0.496

Table 6. Root mean square error (RMSE) for mean deviation between the fitted and measured θ (prefix m_) and R_v-weighted θ (prefix R_v_) by using the van Genuchten-based PDI model (Peters, 2013,2014) model based on the HYPROP software (Pertassek et al., 2015).

Mixture	RMSE θ	Mixture	RMSE θ	Mixture	RMSE θ	Mixture	RMSE θ
	$cm^3\ cm^{-3}$		$cm^3\ cm^{-3}$		$cm^3\ cm^{-3}$		$cm^3\ cm^{-3}$
m_1.3_0 %	0.032	m_1.65_5 %	0.028	m_1.3_0 %	0.032	R_v_1.65_5 %	0.002
m_1.3_5 %	0.023	m_1.65_10 %	0.027	R_v_1.3_5 %	0.002	R_v_1.65_10 %	0.002
m_1.3_10 %	0.023	m_1.6_0 %	0.004	R_v_1.3_10 %	0.002	m_1.6_0 %	0.004
m_1.45_0 %	0.018	m_1.6_5 %	0.007	m_1.45_0 %	0.018	R_v_1.6_5 %	0.004
m_1.45_5 %	0.018	m_1.6_10 %	0.002	R_v_1.45_5 %	0.002	R_v_1.6_10 %	0.004
m_1.45_10%	0.014	m_1.6_20 %	0.008	R_v_1.45_10%	0.002	R_v_1.6_20 %	0.004
m_1.55_0 %	0.034	m_1.7_0 %	0.010	m_1.55_0 %	0.035	m_1.7_0 %	0.011
m_1.55_5 %	0.035	m_1.7_5 %	0.006	R_v_1.55_5 %	0.002	R_v_1.7_5 %	0.004
m_1.55_10 %	0.027	m_1.7_10 %	0.007	R_v_1.55_10 %	0.002	R_v_1.7_10 %	0.004
m_1.65_0 %	0.035	m_1.7_20 %	0.004	m_1.65_0 %	0.035	R_v_1.7_20 %	0.004

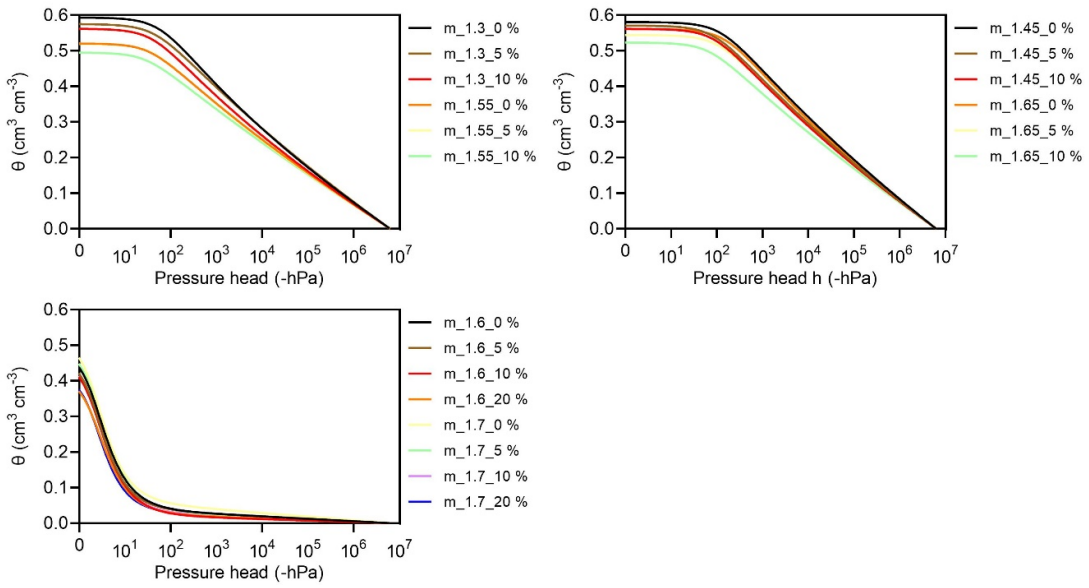

Fig. 2. Fitted soil water retention curves from based on the measured SWRC's (prefix m_). Fitting procedure with HYPROP-Fit software with constrained ($m = 1 - n^{-1}$) van Genuchten-based PDI model (Peters, 2013, 2014). The dry point is reached at pF 6.8 ($-10^{6.8}$ hPa).

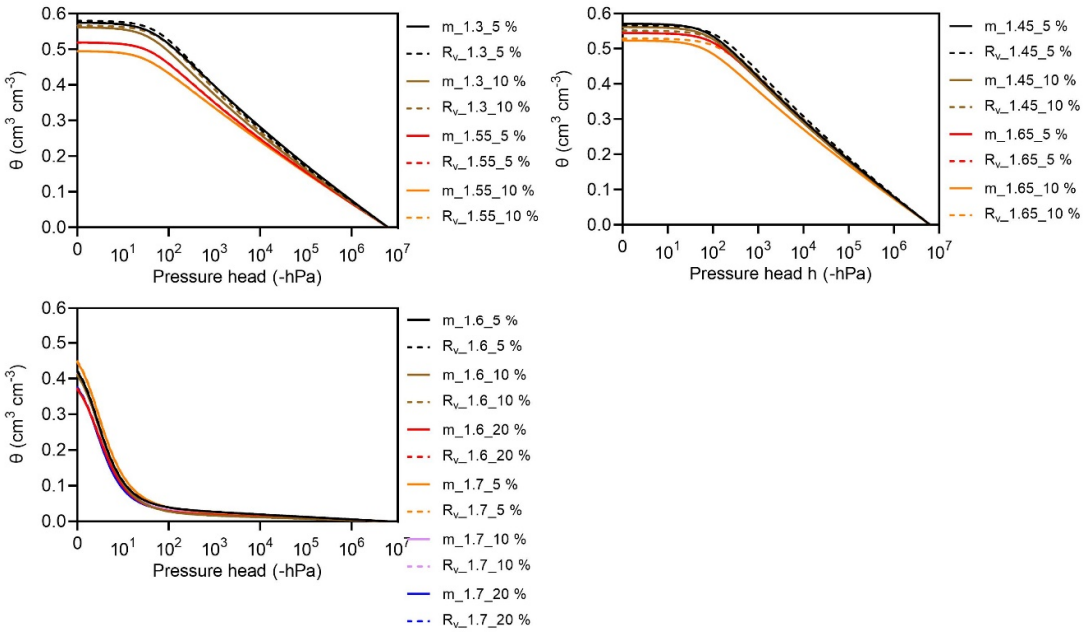

Fig. 3. Comparison of fitted soil water retention curves from based on the measured SWRC's (prefix m_) and R_v-weighted SWRC's (prefix R_v_). Fitting procedure with HYPROP-Fit software with constrained ($m = 1 - n^{-1}$) van Genuchten-based PDI model (Peters, 2013,2014). The dry point is reached at pF 6.8 ($-10^{6.8}$ hPa).

Table 7. Volume fractions of pore classes for macropores (MaP) with d > 0.3 mm, wide coarse pores (wCP) with 0.3 ≤ d > 0.05 mm, narrow coarse pores (nCP) with 0.05 ≤ d > 0.01 mm, medium pores (MP) with 0.01 ≤ d > 0.0002 mm, and fine pores (FP) with d ≤ 0.0002 mm (USDA/NRCS. 2005). Mean values from 5 replicates each. Statistical significance between the measured (prefix m_) and R_v-weighted (prefix R_v_) subgroup, respectively, is indicated by p-values with a significance level ≤ 0.05, with *p≤0.05, **p≤0.01, ***p≤0.001, ****p≤0.0001.

Mixture	MaP $cm^3\ cm^{-3}$	wCP $cm^3\ cm^{-3}$	nCP $cm^3\ cm^{-3}$	MP $cm^3\ cm^{-3}$	FP $cm^3\ cm^{-3}$
m_1.3_5 %	0.0052	0.0353	0.0759	0.1984	0.2605
R_v_1.3_5 %	0.0042	0.0310	0.0813	0.2101	0.2530
m_1.3_10 %	0.0059	0.0406	0.0809	0.1932	0.2414
R_v_1.3_10 %	0.0041	0.0308**	0.0791	0.2052	0.2472
m_1.45_5 %	0.0021	0.0174	0.0654	0.2152	0.2695
R_v_1.45_5 %	0.0015	0.0128	0.0540***	0.2144	0.2829
m_1.45_10 %	0.0022	0.0185	0.0656	0.2088	0.2665
R_v_1.45_10 %	0.0015	0.0125	0.053****	0.2086	0.2753
m_1.55_5 %	0.0048	0.0358	0.0728	0.1767	0.2294
R_v_1.55_5 %	0.0053	0.0366	0.0692	0.1698	0.2255
m_1.55_10 %	0.006	0.0388	0.0652	0.1613	0.224
R_v_1.55_10 %	0.0052	0.0356	0.0673	0.1651	0.2192
m_1.65_5 %	0.0017	0.0142	0.0567	0.2018	0.2701
R_v_1.65_5 %	0.0011	0.0096	0.0481*	0.2124	0.2736
m_1.65_10 %	0.0025	0.0211	0.0631	0.1859	0.2506
R_v_1.65_10 %	0.0013	0.0110**	0.0467**	0.2047****	0.2669**
m_1.6_5 %	0.3086	0.0685	0.0131	0.0134	0.0180
R_v_1.6_5 %	0.3049	0.0760	0.0151	0.0137	0.0172
m_1.6_10 %	0.3035	0.0743	0.0136	0.0094	0.0107
R_v_1.6_10 %	0.2961	0.0738	0.0147	0.0133	0.0167
m_1.6_20 %	0.2714	0.0656	0.0123	0.0099	0.0121
R_v_1.6_20 %	0.2785	0.0694	0.0138	0.0125	0.0157
m_1.7_5 %	0.3194	0.0829	0.0165	0.0136	0.0161
R_v_1.7_5 %	0.3161	0.0749	0.0161	0.0188	0.0259
m_1.7_10 %	0.3073	0.07	0.0127	0.0107	0.0135
R_v_1.7_10 %	0.3063	0.0726	0.0156	0.0182	0.0251
m_1.7_20 %	0.2827	0.0568***	0.01	0.0107	0.0146
R_v_1.7_20 %	0.2868	0.0680	0.0146	0.0170	0.0235

Table 8. Total porosity, TP, Air capacity, AC, plant available water capacity, AWC, and permanent wilting point, PWP. Mean values from 5 replicates each. Statistical significance between the measured (prefix m_) and R_v-weighted (prefix R_v_) subgroup, respectively, is indicated by p-values with a significance level ≤ 0.05, with *p≤0.05, **p≤0.01, ***p≤0.001, ****p≤0.0001.

Mixture	TP	AC	AWC	PWP
	$cm^3\ cm^{-3}$	$cm^3\ cm^{-3}$	$cm^3\ cm^{-3}$	$cm^3\ cm^{-3}$
m_1.3_5 %	0.573	0.0405	0.2743	0.2605
R_v_1.3_5 %	0.579	0.0360	0.2914	0.2533
m_1.3_10 %	0.558	0.0465	0.2741	0.2414
R_v_1.3_10 %	0.567	0.0349	0.2846	0.2473
m_1.45_5 %	0.578	0.0195	0.2806	0.2695
R_v_1.45_5 %	0.566	0.0144	0.2690	0.2829
m_1.45_10 %	0.565	0.0207	0.2744	0.2665
R_v_1.45_10 %	0.552	0.0140	0.2618	0.2754
m_1.55_5 %	0.525	0.0406	0.2495	0.2294
R_v_1.55_5 %	0.506	0.0420	0.2391	0.2255
m_1.55_10 %	0.498	0.0448	0.2265	0.2241
R_v_1.55_10 %	0.493	0.0408	0.2325	0.2193
m_1.65_5 %	0.567	0.0159	0.2585	0.2701
R_v_1.65_5 %	0.545	0.0108	0.2606	0.2736
m_1.65_10 %	0.527	0.0235	0.2490	0.2506
R_v_1.65_10 %	0.529	0.0123**	0.2507	0.2669**
m_1.6_5 %	0.421	0.3771	0.0265	0.018
R_v_1.6_5 %	0.427	0.3809	0.0288	0.0172
m_1.6_10 %	0.411	0.3778	0.023	0.0107
R_v_1.6_10 %	0.414	0.3699	0.0280	0.0167
m_1.6_20 %	0.371	0.3371	0.0222	0.0121
R_v_1.6_20 %	0.391	0.3480	0.0264	0.0157
m_1.7_5 %	0.4480	0.4023	0.0301	0.0161
R_v_1.7_5 %	0.4520	0.3911	0.0349	0.0259
m_1.7_10 %	0.4140	0.3773	0.0234	0.0135
R_v_1.7_10 %	0.4380	0.3790	0.0338	0.0251
m_1.7_20 %	0.3740	0.3395	0.0207	0.0146
R_v_1.7_20 %	0.4101	0.3548	0.0317	0.0235

In Table 7 and Table 8, small, but significant differences in the volume fractions of wide coarse pores, narrow coarse pores, medium pores, and fine pores were found for gravel contents of 10 wt% for silt-gravel mixture soils and 20 wt% for sand-gravel mixture. Thus, the R_v-weighted SWRC's can underestimate the plant available water capacity with increasing gravel content. For analysing for example, the effect of high-voltage underground cables on soils (Rizvi et al., 2020), the R_v-weighted would enable calculations on the so-called "safer side". However, R_v-based predictability of soils with gravel contents below 10 % and 20 % need further analyses.

3.2 Soil thermal capacity

The c_v values of soils are influenced by gravel contents, soil organic matter contents, and soil structure. The results in Fig. 4 and Table 9 show a decrease in the c_{vsat} and c_{vdry} values with increasing gravel contents for sand- and silt-gravel mixtures. The silt-gravel mixtures show comparatively higher c_v values for the same bulk density, texture, and SOM content than the sand-gravel mixtures (Abu-Hamdeh, 2003). However, the water contents need to be considered, because a decrease i*n* water content with increasing gravel content negatively affects the c_v values. The sand- and silt-gravel mixtures show an increase in the c_v values with increasing ρ_b values ($1.3 < 1.45 < 1.55 < 1.65$; $1.6 < 1.7$ g cm^{-3}) for same texture and SOM content, respectively. Thus, θ and ρ_b are also important and affect the thermal capacity of soils (Abu-Hamdeh, 2003; Arkhangelskaya, 2020).

Table 9. Saturated and dry thermal capacity, $c_{v,sat}$ and c_{vdry} predicted by Eq. 8 and corrected by the mass gravel content (prefix m_) in Table 2. Mean values from 5 replicates each. The dry point is reached at pF 6.8 ($-10^{6.8}$ hPa).

Mixture	c_{vsat}	c_{vdry}
	MJ m^{-3} K^{-1}	MJ m^{-3} K^{-1}
m_1.3_0 %	3.694	1.222
m_1.3_5 %	3.641	1.225
m_1.3_10 %	3.586	1.227
m_1.45_0 %	3.582	1.165
m_1.45_5 %	3.523	1.167
m_1.45_ 10%	3.462	1.169
m_1.55_0 %	3.411	1.243
m_1.55_5 %	3.354	1.246
m_1.55_10 %	3.298	1.248
m_1.65_0 %	3.636	1.302
m_1.65_5 %	3.572	1.305
m_1.65_10 %	3.507	1.308
m_1.6_0 %	3.256	1.241
m_1.6_5 %	3.202	1.243
m_1.6_10 %	3.148	1.246
m_1.6_20 %	3.042	1.252
m_1.7_0 %	3.444	1.318
m_1.7_5 %	3.385	1.321
m_1.7_10 %	3.325	1.325
m_1.7_20 %	3.203	1.331

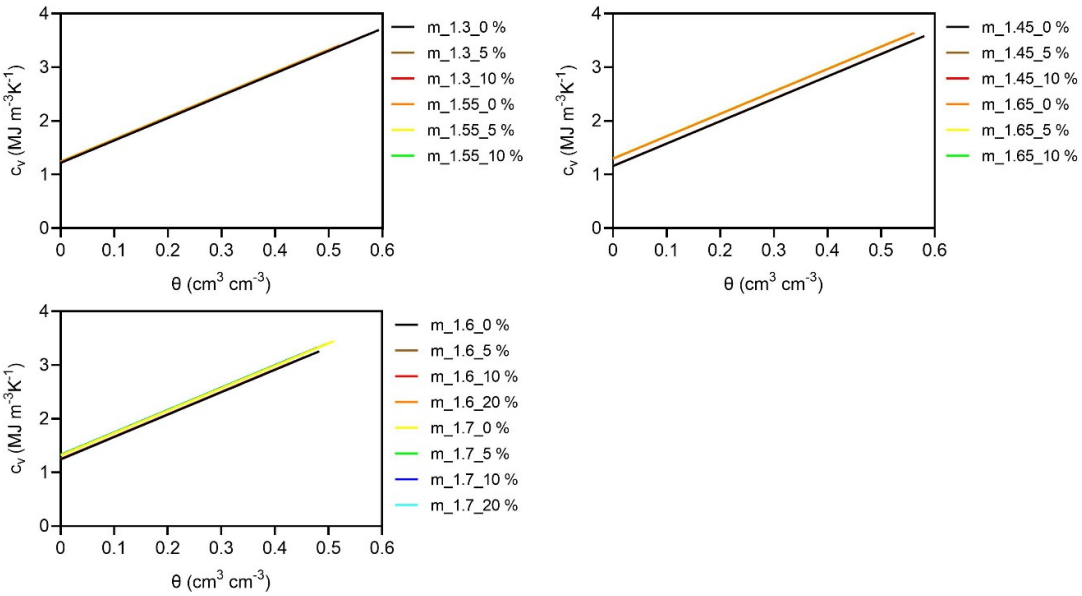

Fig. 4. Thermal capacity, c_v, predicted by Eq. 8 and corrected by the mass gravel content (prefix m_) in Table 2. Mean values from 5 replicates each. The dry point is reached at pF 6.8 ($-10^{6.8}$ hPa).

4 CONCLUSION

The results indicate a decrease in the volume fractions of macropores and wide coarse pores in the sand-gravel mixtures, while the silt-gravel mixtures show an opposite trend. The analysis of variance for the measured and volumetric gravel content weighted pore size distribution and soil water retention characteristics showed no significant differences. Thus, measured soil water retention curves with mass gravel contents of up to 10 wt% for silt and 20 wt% for sand can be well predicted by weighting factors (relative volume of rock fragments) in the range between 0.045 and 0.058 for silt, and between 0.112 and 0.119 for sand. Furthermore, very low root mean square errors show that the van Genuchten based PDI model is suitable for fitting measured soil water retention curves of soils with different gravel contents.

The sand- and silt-gravel mixtures show an increase in the thermal capacity with an increase in the dry bulk density for the same texture and soil organic matter content, respectively. Moreover, the volumetric water content and the dry bulk density significantly affect the thermal capacity of soils.

Further investigations are needed to examine if and whether measured sand- and silt-gravel mixtures with mass gravel contents below 10 % or rather 20 % can be predicted with a weighting factor. In addition to the capacity parameter, further investigations will take the hydraulic and thermal intensity parameter (i. e., unsaturated hydraulic conductivity, thermal conductivity) into account.

REFERENCES

Abu-Hamdeh, N.H., 2003. Thermal properties of soils as affected by density and water content. Biosyst. Eng., 86, 1, 97–102. DOI: 10.1016/S1537-5110(03)00112-0

Ad-Hoc AG Boden, 2005. Bodenkundliche Kartieranleitung (KA5). 5th Ed. Bundesanstalt für Geowissenschaften und Rohstoffe, E. Schweitzerbart'sche Verlagsbuchhandlung, Stuttgart.

Ahmad, S., Rizvi, Z.H., Arp, J.C.C., Wuttke, F., Tirth, V., Islam, S., 2021. Evolution of temperature field around underground power cable for static and cyclic heating. Energies, 14, 8191. https://doi.org/10.3390/en14238191

Arkhangelskaya, T., Lukyashchenko, K., 2018. Estimating soil thermal diffusivity at different water contents from easily available data on soil texture, bulk density, and organic carbon content. Biosyst. Eng., 168, 83–95. DOI: 10.1016/j.biosystemseng.2017.06.011

Arkhangelskaya, T., 2020. Parameters of the thermal diffusivity vs. water content function for mineral soils of different textural classes. Eurasian Soil Sci., 53, 39–49. DOI: 10.1134/S1064229320010032

Beck-Broichsitter, S., Gerke, H.H., Horn, R., 2018. Shrinkage characteristics of boulder marl as sustainable mineral liner material for landfill capping systems. Sustainability, 10, 11, 4025. DOI: 10.3390/su10114025

Beck-Broichsitter, S., Gerke, H.H., Leue, M., von Jeetze, P.J., Horn, R., 2020b. Anisotropy of unsaturated soil hydraulic properties of eroded Luvisol after conversion to hayfield comparing alfalfa and grass plots. Soil Till. Res., 198, 104553. DOI: 10.1016/j.still.2019.104553

Beck-Broichsitter, S., Dusek, J., Vogel, T., Horn, R., 2022. Anisotropy of soil water diffusivity of hillslope soil under spruce forest derived by x-ray CT and lab experiments. Environ. Earth Sci., 81, 457.

Bertermann, D., Mueller, J., Freitag, S., Schwarz, H., 2018. Comparison between measured and calculated thermal conductivities within different grain size classes and their related depth ranges. Soil Syst., 2, 3, 50. DOI: 10.3390/soilsystems2030050

Blake, G.R., Hartge, K.H., 1986. Bulk density. In: Klute, A. (Ed.): Methods of Soil Analysis: Part 1 Physical and Mineralogical Methods. 2nd ed. ASA and SSSA, Madison, WI, USA, pp. 363–375.

Bouwer, H., Rice, R.C. 1984. Hydraulic properties of stony vadose zones. Ground Water, 22, 6, 696–705. DOI: 10.1111/j.1745-6584.1984.tb01438.x

Bronick, C.J., Lal, R., 2005. Soil structure and management: a

review. Geoderma, 124, 3–22. DOI: 10.1016/j.geoderma.2004.03.005

Chapuis, R.P., 2004. Predicting the saturated hydraulic conductivity of sand and gravel using effective diameter and void ratio. Can. Geotech. J., 2004, 41, 787–795. DOI: 10.1139/t04-022

Chief, K., Ferre, T.P.A., Hinnell, A.C., 2008. The effects of anisotropy on in situ air permeability measurements. Vadose Zone J., 7, 941–947. DOI: 10.2136/vzj2007.0164

Corti, G., Ugolini, F.C., Agnelli, A., Certini, G., Cuniglio, R., Berna, F., Fernandez, M.J., 2002. The soil skeleton, a forgotten pool of carbon and nitrogen in soil. Eur. J. Soil Sci., 53, 283–298. DOI: 10.1046/j.1365- 2389.2002.00442.x

de Vries, D.A., 1963. Thermal properties of soils. In: van Wijk, W.R. (Ed.): Physics of Plant Environment. John Wiley and Sons, Inc., New York.

Dong, Y., McCartney, J.S., Lu, N., 2015. Critical review of thermal conductivity models for unsaturated soils. Geotech. Geol. Eng., 33, 207–221. DOI: 10.1007/s10706-015-9843-2

Fies, J. C., Louvigny, D.E., Chanzy, A., 2002. The role of stones in soil water retention. Eur. J. Soil Sci., 53, 1, 95–104. DOI: 10.1046/j.1365-2389.2002.00431.x

Haghverdi, A., Najarchi, M., Öztürk, H.S., Durner, W., 2020. Studying unimodal, bimodal, PDI and bimodal-PDI variants of multiple soil water retention models: I. Direct model fit using the extended evaporation and dewpoint methods. Water, 12, 3, 900. https://doi.org/10.3390/w12030900

Hartge, K.H., Horn, R., 2016. Essential Soil Physics: An Introduction to Soil Processes, Structure, and Mechanics. Schweizerbart Science Publishers, Stuttgart, Germany, 392 p.

Hasler, M., Horton, L.A., 2008. Multiple contrast tests in the presence of heteroscedasticity. Biometrical J., 50, 793–800. DOI: 10.1002/bimj.200710466

Hlavacikova, H., Novak, V., Holko, L., 2015. On the role of rock fragments and initial soil water content in the potential subsurface runoff formation. J. Hydrol. Hydromech., 63, 1, 71–81. DOI: 10.1515/johh-2015-0002

Howard, J., 2017. The Nature and Significance of Anthropogenic Soils. In: Anthropogenic Soils. Progress in Soil Science. Springer, Cham. DOI: 10.1007/978-3-319-54331-4_1

Iden, S., Durner, W., 2014. Comment on "Simple consistent models for water retention and hydraulic conductivity in the complete moisture range" by A. Peters. Water Resour. Res., 50, 7530–7534. DOI: 10.1002/2014WR015937

Lu, Y., Liu, S., Zjang, Y., Wang, L., Li, Z., 2021. Hydraulic conductivity of gravelly soils with various coarse particle contents subjected to freeze–thaw cycles. J. Hydrol., 598, 126302. DOI: 10.1016/j.jhydrol.2021.126302

Maroof, M.A., Eidgahee, D.R., Mahboubi, A., 2022. Particle Morphology Effect on the Soil Pore Structure. In: Feng, G. (Ed.): Proceedings of the 8th International Conference on Civil Engineering. ICCE 2021. Lecture Notes in Civil Engineering, vol 213. Springer, Singapore. DOI: 10.1007/978-981-19-1260-3_1

Miller, R. B., Heeren, D.M., Fox, G.A., Halihan, T., Storm, D.E., Mittelstet, A.R., 2014. The hydraulic conductivity structure of gravel-dominated vadose zones within alluvial floodplains. J. Hydrol., 513, 229–240. DOI: 10.1016/j.jhydrol.2014.03.046

Naseri, M., Iden, S.C., Richter, N., Durner, W., 2019. Influence of stone content on soil hydraulic properties: experimental investigation and test of existing model concepts. Vadose Zone J., 18, 1, 1–10. DOI: 10.2136/vzj2018.08.0163

Novak, V., Knava, K., Simunek, J., 2011. Determining the influence of stones on hydraulic conductivity of saturated soils using numerical method. Geoderma, 161, 177–181. DOI: 10.1016/j.geoderma.2010.12.016

Pertassek, T., Peters, A., Durner, W., 2015. HYPROP-FIT software user's manual, V.3.0. UMS GmbH, Munich, Germany.

Peters, A., 2013. Simple consistent models for water retention and hydraulic conductivity in the complete moisture range. Water Resour. Res., 49, 6765–6780. DOI: 10.1002/wrcr.20548

Peters, A., 2014. Reply to comment by S. Iden and W. Durner on "Simple consistent models for water retention and hydraulic conductivity in the complete moisture range". Water Resour. Res., 50, 7535–7539. DOI: 10.1002/2014WR016107.

Poeplau, C., Vos, C., Don, A., 2017. Soil organic carbon stocks are systematically overestimated by misuse of the parameters bulk density and rock fragment content. Soil, 3, 61–66. DOI: 10.5194/soil-3-61-2017

R Development Core Team, 2014. R: A language and environment for statistical computing. R Foundation for Statistical Computing, Vienna, Austria.

Rerak, M., Ocłon, P., 2017. Thermal analysis of underground power cable system. J. Therm. Sci., 26, 5, 465–471. DOI: 10.1007/s11630-017-0963-2

Rytter, R.-M., 2012. Stone and gravel contents of arable soils influence estimates of C and N stocks. Catena, 95, 153–159. DOI: 10.1016/j.catena.2012.02.015

Rizvi, Z.H., Zaidi, H.H., Akhtar, S.J., Sattari, A., Wuttke, F., 2020. Soft and hard computation methods for estimation of the effective thermal conductivity of sands. Heat Mass Transf., 56, 6, 1947–1959. DOI: 10.1007/s00231-020-02833-w

Rizvi, Z.H., Akhtar, S.J., Husain, S.M.B., Khan, M., Haider, H., Naqvi, S., Tirth, V., Wuttke, F., 2022. Neural network approaches for computation of soil thermal conductivity. Mathematics, 10, 3957. https://doi.org/10.3390/math10213957

Sauer, T.J., Logsdon, S.D., 2002. Hydraulic and physical properties of stony soils in a small watershed. Soil. Sci. Soc. Am. J., 66, 1947–1956. DOI: 10.2136/sssaj2002.1947

Shakoor, A., Cook, B.D., 1990. The effect of stone content, size, and shape on engineering properties of a compacted silty clay. Bull. Assoc. Eng. Geol., 27, 2, 245–253. DOI: 10.2113/GSEEGEOSCI.XXVII.2.245

She, K., Horn, D., Canning, P., 2006. Porosity and hydraulic conductivity of mixed sand-gravel sediment. In: Proc. 41st Defra Flood and Coastal Management Conference, 4 - 6 July 2006, York, UK.

USDA/NRCS. 2005. United States Department of Agriculture, Natural Resources Conservation Service, Soil Survey Manual. 1993, updated 2005. online source: http://soils.usda.gov/technical/manual/.

USDA/NRCS, 2007. United States Department of Agriculture, Natural Resources Conservation Service. Saturated hydraulic conductivity in relation to soil texture. online source: https://www.nrcs.usda.gov/wps/portal/nrcs/detail/soils/survey/office/ssr10/tr/?cid=nrcs144p2_074846

van Genuchten, M.T., 1980. A closed-form equation for predicting the hydraulic conductivity of unsaturated soils. Soil Sci. Soc. Am. J., 44, 892–898. DOI: 10.2136/sssaj1980.03615995004400050002x

Received 30 August 2022
Accepted 3 January 2023

J. Hydrol. Hydromech., 71, 2023, 1, 11–21
https://doi.org/10.2478/johh-2022-0042

sciendo Journal of Hydrology and Hydromechanics Institute of Hydrology SAS

Effects of pore size and pore connectivity on trapped gas saturation

Caroline H. Dias[1*], Felipe M. Eler[1], Carlos Cordeiro[1], Mateus G. Ramirez[1], José A. Soares[2], Denise Nunes[1], Maira C.O. Lima[1], Paulo Couto[1]

[1] Department of Civil Engineering, COPPE, Federal University of Rio de Janeiro, RJ, Brazil.
[2] Department of Mining Engineering, Federal University of Campina Grande, Paraíba, PB, Brazil.
[*] Corresponding author. E-mail: caroldias@petroleo.ufrj.br

Abstract: Trapped or residual air (or gas) is known to affect the multiphase hydraulic properties of both soils and rocks. Trapped air is known to impact many vadose zone hydrologic applications such as infiltration and flow in the capillary fringe, but is also a major issue affecting recoverable oil reserves. Although many studies have focused on the relationship between porosity and trapped gas saturation (S_{gt}) in sandstones, far fewer studies have been carried out for carbonate rocks. This work aims to analyze the influence of porous media properties on trapped gas saturation in carbonate rocks. For this we used thirteen Indiana Limestone and Silurian dolomite rock samples from the USA, and several coquinas from the Morro do Chaves formation in Brazil. Pore size distributions were obtained for all samples using Nuclear Magnetic Resonance (NMR), and Mercury Injection Capillary Pressure (MICP) data from three of the samples to determine their pore throat size distributions. Additionally, 3D microtomography (microCT) images were used to quantify macropore profiles and pore connectivities. Results indicate a lower capacity of gas trapping in carbonate rocks in which micro- and mesopores predominate. Results also indicate that in carbonate rocks, pore size exerts a greater influence on the ability of gas trapping compared to pore connectivity, so that rocks with a predominance of macropores have greater capacity for gas trapping, even when the macropores are well interconnected. These findings show that pore characteristics very much affect the processes governing gas trapping in carbonate rocks, and indirectly the multiphase hydraulic properties and recoverable oil reserves of carbonate rock reservoirs.

Keywords: Trapped gas; Carbonate rocks; Pore size distribution; Coordination number.

INTRODUCTION

Air or gas trapping in porous media occurs during displacement of an initially present non-wetting phase by an infiltrating wetting phase (Mohammadian et al., 2015; Raeini et al., 2015; Tanino and Blunt, 2012). Trapped air can significantly affect multiphase flow phenomena in vadose zone hydrologic applications such as infiltration and flow processes in the capillary fringe (e.g., Faybishenko, 1995; Fayer and Hillel, 1986; Gonçalves et al., 2019; and references therein). Gas trapping plays an important role also in hydrocarbon recovery and carbon capture and storage (CCS) processes (Fatemi and Sohrabi, 2013; Wang et al., 2016). Regarding hydrocarbon recovery efficiency, capillary trapping of gas reduces residual oil saturation (Afzali et al., 2018; Element et al., 2003). In case of CCS, the main objective is to maximize capillary trapping to increase CO_2 storage (e.g., Ruspini et al., 2017). These various studies show that air or gas trapping is a function of many parameters, including the prevailing wetting rate, wettability, and especially grain texture and pore structure.

Understanding and quantifying the effects of trapped gas in oil reservoirs is a challenge, particularly for carbonate rocks which have an unusually complex multiscale heterogeneous pore structure causing unique fluid retention and flow properties (Godoy et al., 2019; Sun et al., 2017). Carbonate hydrocarbon reservoirs, including the Brazilian Pre-Salt, are the subject of several scientific investigations due to their geological complexity and economic value (Herlinger et al., 2017; Lima et al., 2022).

One of the main uncertainties in estimating recoverable reserves of oil fields is the large variation in observed values of trapped gas saturation (S_{gt}). Various experimental and simulation studies have been conducted to assess how selected porous media properties affect the degree of gas trapping (e.g., Bona et al., 2014; Jerauld, 1997). Pore structure and pore connectivity play especially a key role in the gas trapping process. Gas trapping is favored when wide pores are connected to narrow throats, with a well-connected pore system disfavoring gas trapping (Krevor et al., 2015). Fatemi and Sohrabi (2013) verified the influence of wettability on gas trapping. They observed that wettability to water leads to more gas trapping, probably due to increased snap-off in such systems. Suzanne et al. (2003), Tanino and Blunt (2013), and Kazemi et al. (2020), among others, found that trapped gas saturation (S_{gt}) tended to increase with initial gas saturation (S_{gi}). Various studies have looked at the specific relationships between porosity ($\emptyset$) and trapped gas saturation (S_{gt}), including factors causing values to deviate from established correlations. Most of these studies involved sandstone rocks. For example, Hamon et al. (2001) performed 300 S_{gt} measurements on samples taken from three different sandstone gas reservoirs to analyze their variation and trend with petrophysical properties. S_{gt} values ranged from 5% to 85%, with the plot of S_{gt} values versus porosity showing two trends. For porosity values below 14%, Fontainebleau samples showed an increase in S_{gt} as the porosity decreased, while S_{gt} values decreased for two sandstones. For samples with porosities above 14%, S_{gt} values were on average 25–35% for the three analyzed reservoirs. In these samples, clay presence was detected, showing that the amount of clay controls the S_{gt}. The authors concluded that increasing the clay content decreased gas trapping. Suzanne and Billiote (2004) studied the influence of microporosity on S_{gt} in sandstones samples. They found that microporosity did not retain gas due to the proportion between pore bodies and pore throat

sizes and the gas diffusion mechanism. Ni et al. (2019) correlated several trapping coefficients (notably the linear and nonlinear Land trapping coefficients) with a range of petrophysical parameters (porosity, permeability, heterogeneity degree) estimated using computer tomography (CT) images. They found that the trapping capacity of sandstones decreased with porosity and increased with the degree of heterogeneity of the samples, but that the pore size distribution had little or no impact on the degree of CO_2 trapping. Kazemi (2020) evaluated the effects of different parameters, including porosity, on S_{gt} in unconsolidated sandstones samples. They also observed that increasing the porosity led to a decrease in S_{gt}, consistent with other studies. No favorable scenario was found for the snap-off trapping processes in regions of high porosity. Compared to sandstones, relatively few gas trapping studies have focused on carbonate rocks. Tanino and Blunt (2012) evaluated the effects of pore structure on capillary trapping in both sandstone and carbonate samples. They found that capillary trapping increased mostly with increasing pore body-to-throat aspect ratios and tended to decrease with higher pore coordination numbers. They also correlated trapped saturation with the microporosity fraction of the pore volume but could not find a consistent relationship between these two parameters. The microporosity part of their samples had a pore aspect ratio and connectivity similar as those of the macroporosity region. In another study, Khisamov et al. (2020) proposed a method for estimating the saturation of trapped gas based on quantitative characteristics of the pore space structure and wettability. They found that the ratio between pore bodies and pore throats controlled the trapping capacity of their carbonate samples. They also showed that carbonate rocks with large pores, especially when water-wet, had higher trapped gas saturations. Our preliminary research showed a decreasing trend of S_{gt} values with increasing porosity, similarly as several earlier studies (e.g., Kazemi, 2020; Ruspini, 2017). However, we noted a significant variation in the S_{gt} values for samples with similar porosity. This indicated that, in addition to porosity, other factors must have affected S_{gt}. Motivated by these initial results, we investigated the influence of specific properties on S_{gt} of carbonate rocks samples. Nuclear magnetic resonance (NMR), capillary pressure by mercury injection (MICP) and 3D microtomography images (microCT) were used to obtain a better understanding of the complete pore space, including microporosity and pore connectivity.

MATERIALS AND METHODS

In total, 46 carbonate rock samples were used for the S_{gt} analyses. The samples had porosities between 6% and 29.6%, and permeability between 1.70 mD and 1440 mD. Of these samples, 13 were used to analyze the pore size distribution using NMR. The 13 samples were selected based on part of a S_{gt} versus porosity plot which showed the greatest variability in the measured gas saturation values. Fig. 1 shows a graph of S_{gt} versus porosity for all carbonate samples. At a porosity of about 15%, the values of S_{gt} varied from 18.4% to 64.3%. The 13 samples at or near this porosity value we selected for analysis of the pore size distribution; they are highlighted in Fig. 1 with different colors and grouped in terms of Indiana limestones (IL), coquinas (MC) from the Morro do Chaves formation in Brazil (Silveira et al., 2022), and silurian dolomites (SD).

Table 1 provides a list of the carbonate samples that were used, along with standard petrophysical properties (porosity and permeability) of the samples and measured trapped gas values. Below we provide details about the various measurements.

Trapped gas saturation tests

Procedures for estimating S_{gt} followed closely the approach described by Aissaoui (1983). Samples (5.0 cm long and 3.8 cm in diameter) were kept first for 24 hours in a controlled humidity oven at (60 °C and a relative humidity of 40%) to ensure completely dry plugs with air saturations at near 100%. Coreflood tests were subsequently performed to determine air-water S_{gt} values by imbibing water under laboratory conditions. We used a confining pressure of 1,000 psi (6.89 MPa) and ambient fluid pressures, with the temperature being 21 ºC.

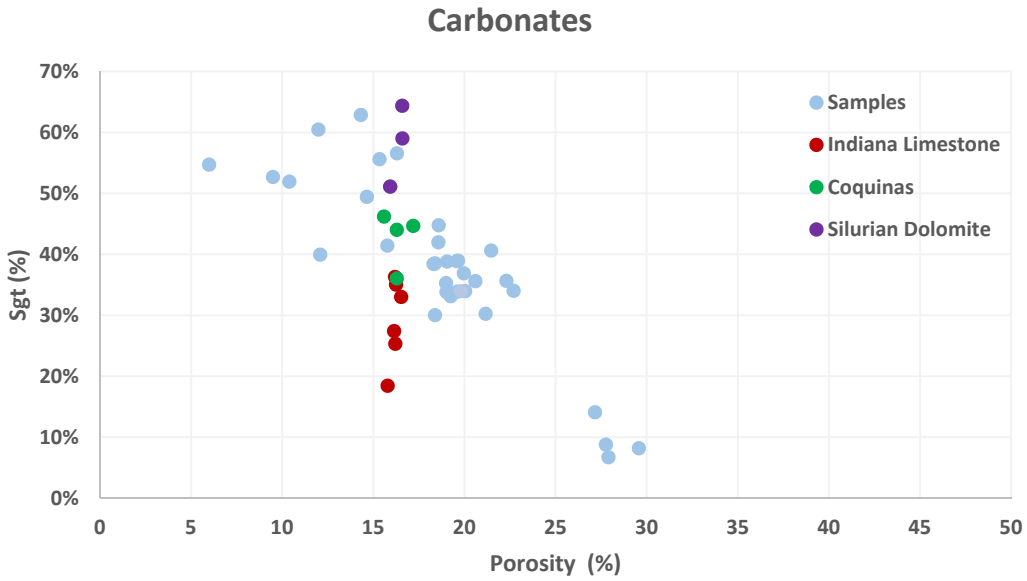

Fig. 1. Trapped gas saturation (S_{gt}) versus porosity for all carbonate samples. The samples selected for the pore size distribution analysis are highlighted according to their geological formation: Indiana Limestones (red circles), Coquinas (green circles), and Silurian Dolomites (purple circles).

Table 1. Measured porosities ($Ø$), permeabilities (k) and trapped gas saturations (S_{gt}) 13 carbonate rock samples.

Samples	$Ø$ (%)	k (mD)	S_{gt} (%)
IL_09_01	16.3	10.9	35.0
IL_09_02	16.5	18.7	33.0
IL_09_03	16.1	10.5	27.4
IL_09_04	16.2	14.0	25.3
IL_09_05	15.8	7.4	18.4
IL_09_06	16.2	15.5	36.3
MC15P1_B	16.3	10.6	36.0
MC15P2	15.6	13.9	46.2
MC20P1	16.3	208.6	44.0
MC20P2	17.2	296.4	44.6
SD_35_03	16.6	1338.9	64.3
SD_35_04	16.6	1326.5	59.0
SD_35_05	15.9	117.3	51.0

The experimental apparatus comprised a positive displacement pump, a confinement cell, pressure differential measurement transducers, graduated glassware, and an image capture system (Fig. 2).

After inserting the sample into the core holder, the confining pressure was raised to 1,000 psi (6.89 MPa, the same confining pressure used to measure the routine core properties). A positive displacement pump was used to inject distilled water into the system at a flow rate of 1 cm³/min. The distilled water was carefully deaired to ensure that no gas was injected into the sample and during the imbibition. The gas initially contained in the dry samples was displaced and collected at the equipment outlet during a period of 24 hours. This information was recorded, along with the time and temperature at which production occurred, to yield estimates of S_{gt}.

Nuclear magnetic resonance (NMR)

Nuclear Magnetic Resonance (NMR) is a technique that stands out in the investigation of the physical and chemical properties of materials in the oil and gas industry (Trevizan, et al., 2014). The transverse relaxation time T_2 is obtained through controlled radiofrequency pulses applied to previously saturated rock samples. From T_2 it is possible to obtain various information about the porous system, such as porosity, pore distribution, and permeability estimation, among others (Alyafei, 2015).

Before the tests, the samples were submitted to vacuum for 8 h, and subsequently saturated with 30,000 ppm of a KCl solution at a constant pressure of 1.500 psi (10.34 MPa) to minimize possible reactions of clay material in the samples.

To estimate the percentage of pores capable of retaining fluids by capillarity, the NMR analyzes were performed with the samples at complete saturation and after centrifugation, thereby providing estimates of irreducible saturation (S_{wi}) for determination of the T_2 cut-off value. The T_2 cut-off value is an essential parameter in NMR measurements since its value differentiates pores occupied by free fluid from pores occupied by fluid trapped by capillarity. This approach assumes that free fluids occupy large pores while irreducible fluid preferentially occupies the smaller pores (Lai et al., 2018).

The equipment used to acquire the NMR data was a low-field Oxford spectrometer (model Geospec+ 12/53 3D Imager). Following the methodology of Meiboom and Gill (1958), the CPMG sequence widely used in petrophysics was applied, leading to estimates of the porosity and pore size distribution. The approach assumes that decay (relaxation) during magnetization is proportional to the volume/surface ratio of a single pore/throat, which makes it possible to obtain the pore size (r) using

$$r = V/S = \rho_2 T_2 \quad (1)$$

where V/S is the volume to surface ratio (μm), ρ_2 is the surface relaxivity (a rock specific scalar constant) (μm/ms), and T_2 is the transverse relaxation time.

Mercury intrusion capillary pressure (MICP)

Mercury intrusion capillary pressure (MICP) tests, in turn, are widely used to assess the complexity and heterogeneity of the pore throat structure (Li et al., 2016; Washburn, 1921). Through this test, the capillary pressure curve per pore volume is obtained, which can be transformed into a size distribution of the pore throat radii. For the MICP measurements we placed the rock samples is in a closed container under vacuum, and then filled the container with mercury. Initially, pressure is used to fill the largest pores, and as the pressure is increased, the mercury can enter the smaller pores, thereby allowing all pores at the end of the experiments to be filled with the non-wetting fluid (Washburn, 1921). The pore throat radii are then calculated from the pressure data using

$$P_c = \frac{2\sigma|\cos\theta|}{R_t} \quad (2)$$

where P_c is the capillary pressure (MPa), R_t is the throat radius (μm), σ is the surface tension (mN/m) and θ is the contact angle (◦). Since MICP is a destructive technique, three subsampled plugs (SD_35_03, MC20P2, and IL_09_05) were selected to obtain the pore throat size distribution curves.

Integration of NMR and MICP results provides estimates of the surface relaxivity (ρ_2), which is needed to calibrate the relaxation time curve T_2 to produce the pore size distribution (Fleury and Romero-Sarmiento, 2016). Approximating the pore network

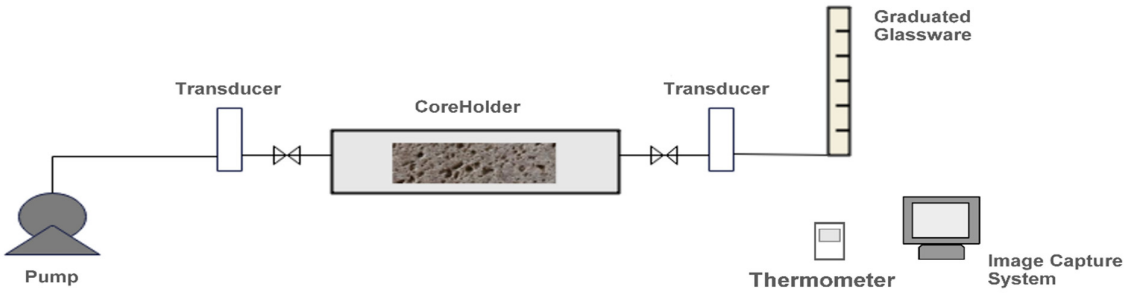

Fig. 2. Experimental setup used for the trapped gas (S_{gt}) measurements.

as a bundle of cylindrical capillary tubes of radius r, the pore structure can be correlated with T_2 by means of ρ_2 according to:

$$\left(\frac{S}{V}\right)_{cylinder} = \frac{2\pi rl}{\pi r^2 l} = \frac{2}{r} \rightarrow r_{spherical} = 3\rho_2 T_2 \quad (3)$$

where l is the length of the capillary, and 3 a shape parameter for pores considered to be spherical (Ge et al., 2021; Lima et al., 2020). If the pores are considered cylindrical, the shape parameter becomes 2.

X-ray microtomography (microCT)

Investigations of pore structures at scales ranging from micrometers to a few millimeters are possible using microCT scanners that provide non-destructive 3D images of the internal structure of materials (Lima et al., 2022). Image acquisitions were performed using CoreTOM equipment (Tescan/XRE) with a 25 µm voxel size, while the images were reconstructed using the Acquila reconstruction software (Tescan/XRE). Image processing was carried out using Avizo 9.5 (Thermo Fisher Scientific). Image segmentation into pores and the mineral matrix (Fig. 3) was performed using the threshold tool (Otsuki et al., 2006). Threshold values were determined by comparing the pixel size with the NMR curve, with T_2 values first being converted to pore radii using Eq. (3) (Lima et al., 2020). After this, the pore structure was analyzed by transforming the pore space into a skeleton showing individual pores and throats in the pore network (Wildenschild and Sheppard, 2013). The skeleton was subsequently used in the PoreFlow software (Raoof et al., 2013) to obtain a more complete quantitative understanding of the entire pore system.

RESULTS AND DISCUSSION

Pore size distribution analysis using T_2 distribution graphs

Porosity values obtained using NMR showed good agreement with the routine core measurements, and hence were considered to be of good quality. According to Souza (2012), the porosity values obtained by these two techniques are not expected to be the same, but they should have errors less than approximately about 2%.

The pore size distributions were analyzed using T_2 relaxation time distributions since the T_2 values are proportional to pore size, with its amplitude being directly related to the incremental porosity of the sample (Shao et al., 2017). Silva et al. (2015) partitioned the pores of carbonate rocks into five different families: micropores (T_2 values up to 1 ms), a transition from micropores to mesopores (1 to 10 ms), mesopores (10 to 100 ms), a transition from mesopores to macropores (100 to 1000 ms) and macropores (T_2 values above 1000 ms). We used these transition regions to facilitate a well-defined classification of pore sizes for the carbonate rocks because of their complex heterogeneous nature.

Figure 4 presents the pore size distributions of the six Indiana limestone samples. Notice that the curves for the six samples have very similar shapes, with the distribution of pore sizes and average relaxation times being essentially the same regardless of the selected sample. The plots themselves show bimodal distributions with T_2values varying between 0.1 ms and about 9000 ms. The bimodality T_2 distributions suggest that the samples are composed of both micro/mesopores (on average 31% of the pore volume) and macropores (about 69%). The bimodality also indicates the presence of a discontinuous range of pore sizes reflecting considerable heterogeneity of the samples.

Figure 5 shows the distributions of T_2 times of the four coquina samples. Samples MC15P1_B and MC15P2 exhibited bimodal curves reflecting the internal pore heterogeneity present in these samples. The curves for samples MC20P1 and MC20P2, on the other hand, are very much unimodal, thus highlighting the far more homogeneous pore size distributions of these two samples. There is a predominance of macropores (about 77% of the pores are in the macropores range), for microprosity and mesoporosity this value is 23% on average for all samples. It is also observed that the contribution of smaller pores concerning total porosity is not significant.

Figure 6 shows the pore size distributions for the three silurian dolomite samples analyzed. As observed for the Indiana limestone samples, the curves for the three silurian dolomite samples show similarity between them, showing that, regardless of the selected sample, it will represent well the other two samples analyzed. T_2 values range from 0.1 ms to 9000 ms in a unimodal distribution. The high occurrence of pore size above 100 ms (average of 79%) suggests that the sample is formed mainly by macropores.

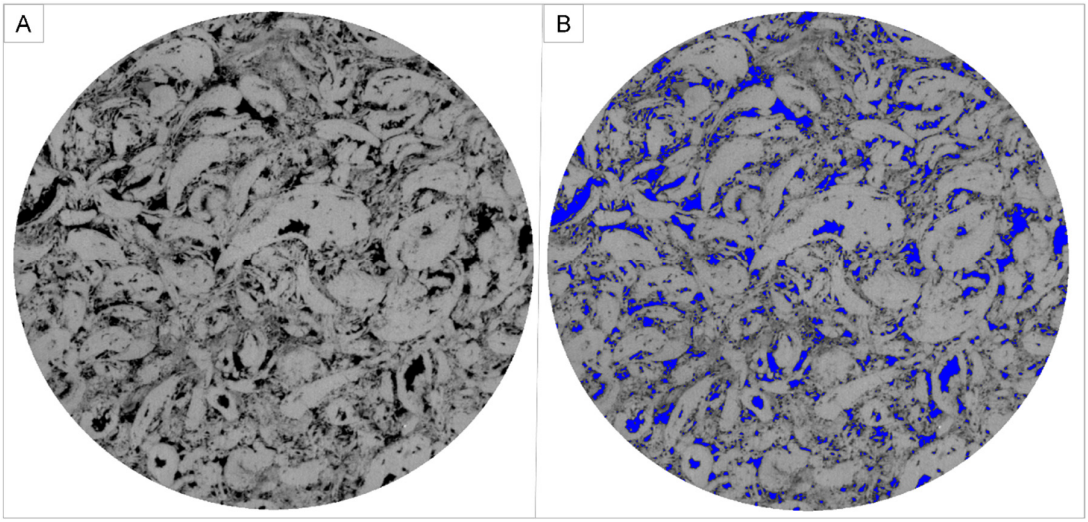

Fig. 3. MicroCT slices of sample MC20P2 with a voxel size of 25: (A) Grayscale image with pores in black and the rock matrix in gray; (B) Grayscale image with the segmented pores in blue.

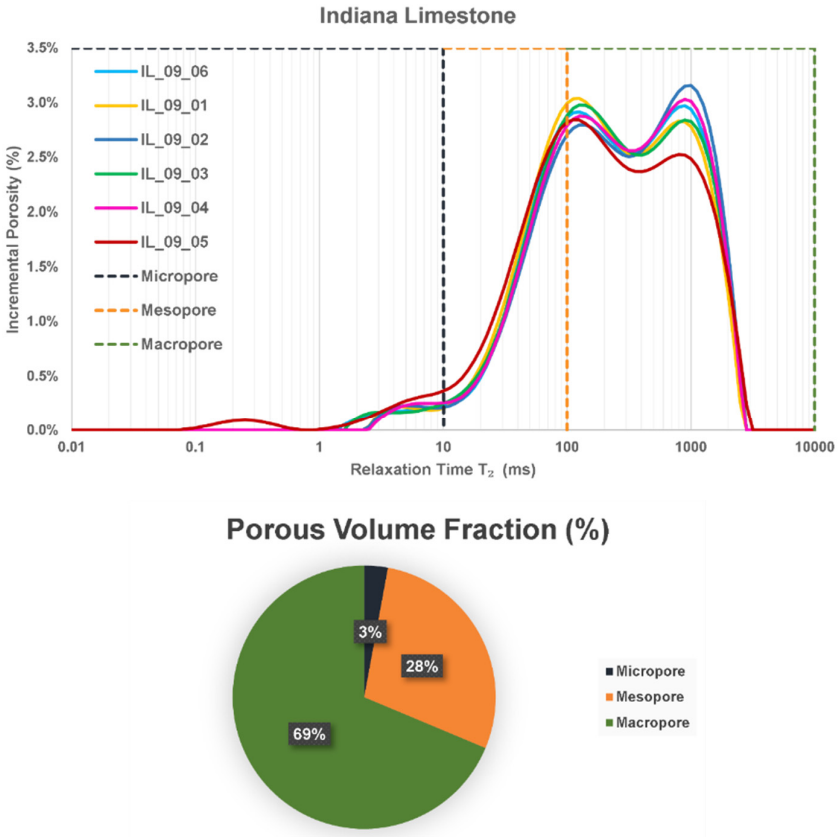

Fig. 4. Distribution of T_2 times for Indiana limestone samples (top) and volumetric fractions of the pore space partitioning (micropore, mesopore and macropore).

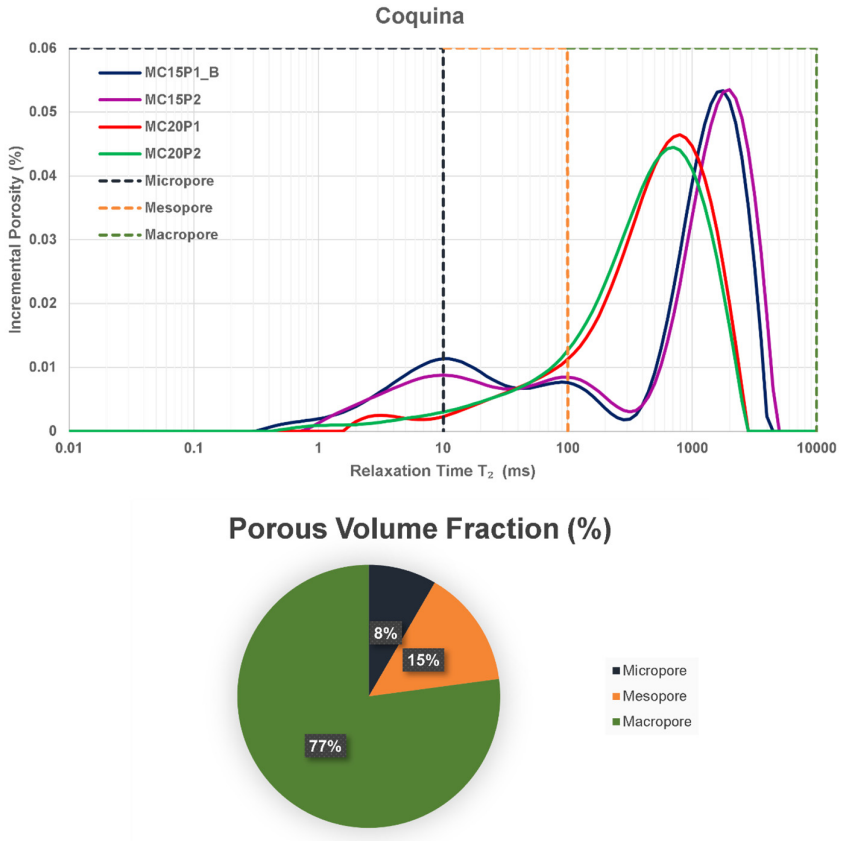

Fig. 5. Distribution of T_2 times for coquina samples and volumetric fractions of pore space partitioning (micropore, mesopore and macropore).

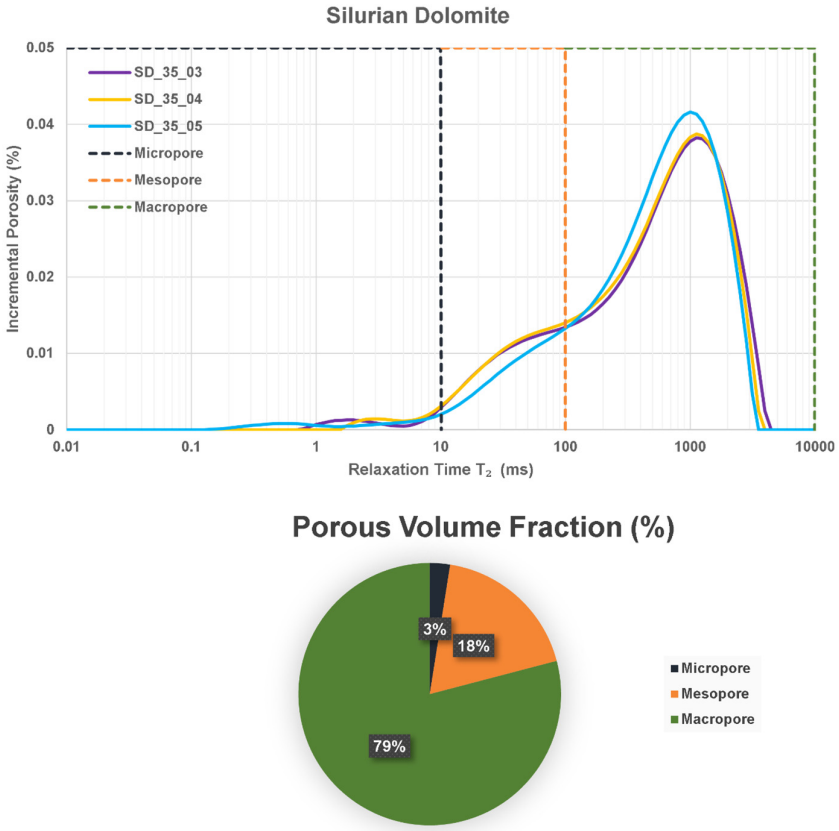

Fig. 6. Distribution of T_2 times for silurian dolomite samples and volumetric fractions of pore space partitioning (micropore, mesopore, and macropore).

Kazemi et al. (2020) previously listed S_{gt} values for limestones having porosity values of 15% (similar porosities as our samples as shown in Fig. 1). Their S_{gt} values ranged from 40% to about 60%, consistent with our silurian dolomite and coquina results, except for coquina sample MC15P1_B. When analyzing the T_2 time distributions of the Indiana limestone samples, in comparison with the other samples, we noted that this group had the highest percentage of microporosity. According to Suzanne and Billiote (2004), among others, high levels of microporosity diminishes gas trapping due to the low proportion of pore body and pore throats. This is also consistent with MC15P1_B coquina sample having an S_{gt} value of 36%, not too much different from those of the Indiana limestones. The proportion of micro- and meso-porosity porosity for this sample was 31%, while the average of the coquina samples was only 23% (the same as for the Indiana limestone samples). Micro/mesoporosities greater than 30% hence seemed to have negative influence on gas trapping.

A useful complementary analysis to NMR is the characterization of the distribution of pore openings (e.g., their radii) using MICP. With this approach, the entire pore system represented by pore bodies (corresponding to the largest voids) and pore throats (connections between pore bodies) can be evaluated (Yuan and Rezaee, 2019). Figure 7 shows the pore throat size distributions, obtained via MICP tests, for the analyzed samples, as well as the volumetric fraction of pores partitioned into micro-, meso- and macroporosity. As noted earlier reported, only three samples were submitted to MICP tests based on the choice of S_{gt} values (high, medium, and low value), i.e., samples SD_35_03 (silurian dolomite), MC20P2 (coquina), and IL_09_05 (Indiana limestone). The throat size partitioning scheme described by Gyllensten et al. (2008) was used to differentiate between different regions of the pore system: micropores from 0 to 0.5 µm, mesopores from 0.5 to 5 µm, and macropores above 5 µm.

The pore throat size distribution graph for the Indiana limestone sample in Fig. 7 shows a high percentage of throats in the micro/mesopore scale, about 60%, indicating that this sample is mostly composed of pores connected to small throats. The other two samples had similar profiles, indicating that the coquina and silurian dolomite samples contain mostly pores connected to large throats, with the volumetric fractions in the macroporosity scale being 88% and 77%, respectively.

The combined use of NMR and MICP results enables a conversion of the relaxation time distributions into pore radii distributions by superimposing the NMR curve over the MICP curve, and equating the peaks of the curves. Once it is verified that the distributions are well correlated, the surface relaxivity ρ_2 in Eq. (1) can be adjusted until the distributions present the same maximum as seen in Fig. 8 (Lima, et al., 2020). This correlation of the results makes it possible to partition the pores (e.g., Gyllensten et al., 2008).

Correlations of the NMR and MICP curves for samples SD_35_03 (silurian dolomite), MC20P2 (coquina) and IL_09_05 (Indiana limestone) are presented in Fig. 8. The Silurian Dolomite sample shows a reasonable correlation between the two curves, with the sample containing mostly macropores (about 77% of the pores), connected to large throats. The percentage of micropores and mesopores is only 23%, indicating that microporosity does not significant contribute to total porosity. The Coquina sample similarly shows a good close overlapping of the NMR and MICP curves. The sample is formed mainly by macropores (about 69% of the pores) connected to large throats, while the percentage of micro- and mesopores being 31%.

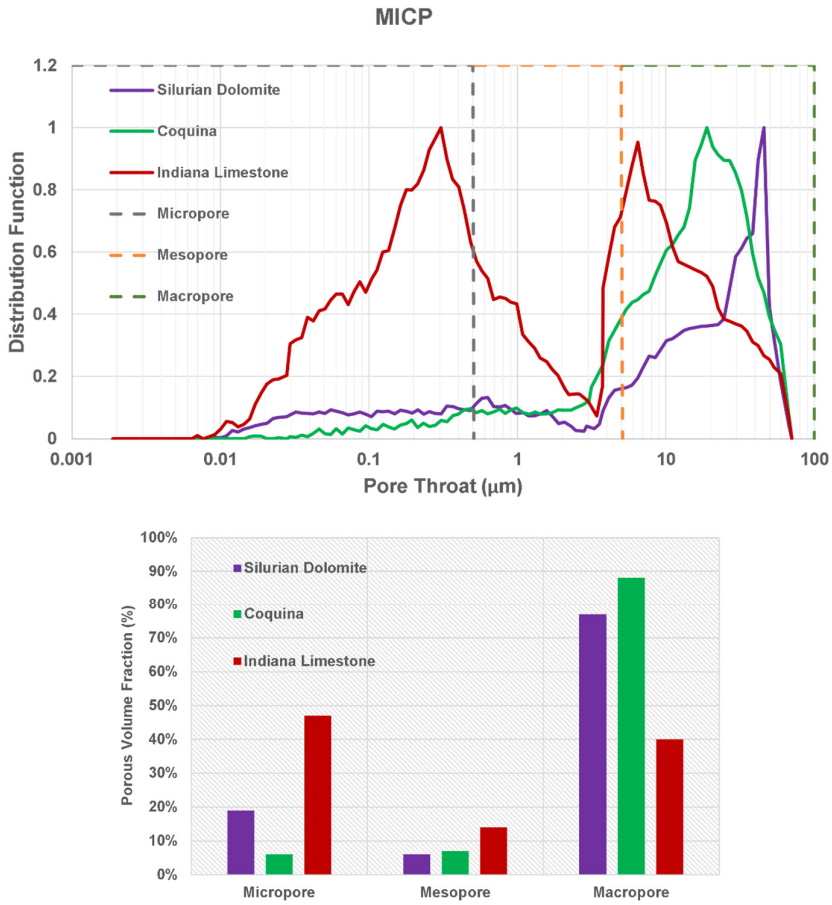

Fig. 7. Pore throat size distributions of the silurian dolomite, coquina, and Indiana limestone samples and volumetric fractions of the pore space partitions (micropore, mesopore and macropore) for each group of samples.

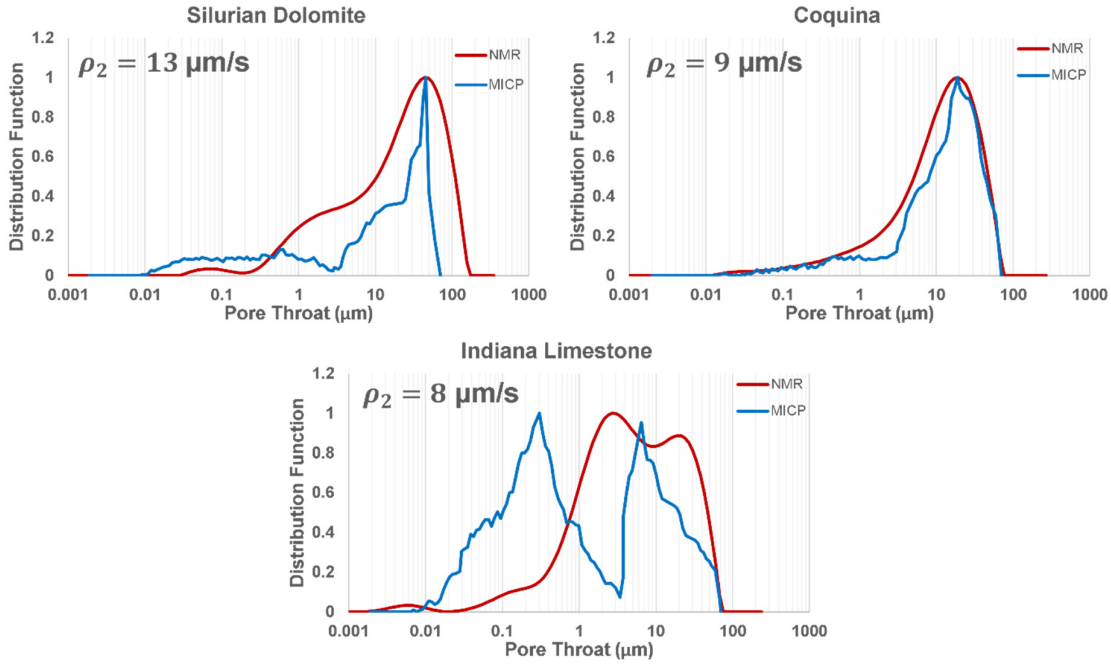

Fig. 8. Correlation between the NMR and MICP results for silurian dolomite sample SD_35_03, coquina sample MC20P2 and Indiana limestone sample IL_09_05.

By comparison, Indiana limestone sample IL_09_05 shows a relatively poor correlation in Fig. 8 between the NMR and MICP curves. Still, both curves indicate a bimodal pore distribution, with pore throats in mostly the micropore and mesopore regions. The MICP analysis indicates that about 54% of the pore throats are in the micropore and mesopores regions (following the scheme of Gyllenstein et al., 2008). With this analysis, we corroborate the view that Indiana limestone sample (IL_09_05) is formed mainly by small pores connected to small throats, unlike the two other samples. Fig. 8 also presents important information about the relaxivity ρ_2. The values used here (8, 9 and 13 μm/s) are typical of carbonate rocks.

The results obtained using NMR and MICP showed that the Indiana limestone samples have a high percentage of micropores and mesopores in their structure and that these pores are connected to throats also at the micropore and mesopores scale. Thus, we conclude that the microporosity and mesoporosity in these samples are the main cause of the low S_{gt} values, conforming that gas trapping decreases substantially with an increase in relatively small pores. According to Jerauld (1997), gas trapping in micropores is not effective and will occur only at relatively high initial or maximum gas saturations. Changes in the saturation of trapped gas with increasing maximum gas saturation decreases with increasing maximum gas saturation, eventually approaching zero, thus indicating little entrapment in microporosity.

The silurian dolomite and coquina samples did not show significant proportions of micropores in their structures in terms of changing the trapping capacity of these samples. To further investigate this, we investigated the pore structure of these samples using microCT, in addition to obtaining estimates of the pore size distribution (via NMR) and the pore throat size distribution (via MICP). The skeletons generated for each sample made it possible to extract information about the pore connectivity (Godoy et al., 2019; Sahimi et al., 2012). The coordination number (or pore connectivity) represents the number of pore bodies that are connected with adjacent pores. Fig. 9 presents a comparison of coordination number versus frequency of the silurian dolomite SD_35_03 and coquina MC20P2 samples. The silurian dolomite sample showed better connectivity than the coquina sample. The coquina sample, in turn, had a higher frequency of pores connected (up to 7 throats). These results are opposite to those observed by Jerauld (1997), likely because the silurian dolomite sample with its better connectivity than the coquina sample, generated greater gas trapping.

For better characterization of the connectivity, a pore frequency graph by connection number was generated for different pore radii (Fig. 10). For pores with smaller radii we observed that coquina presents a higher frequency for all coordination numbers. Once the pore radius increases, the frequency became higher for the silurian dolomite sample regardless of coordination number. Making a parallel with the S_{gt} values, we observed that profile of samples that trapped more gas are the samples that have pores with larger radii and better connectiveness. According to Blunt et al. (2013), the water films increase in the throats and along the pore walls as the water pressure increases during imbibition of water-wettable rocks. This increase occurs until the non-wetting fluid (gas in our case) loses contact with the surface of the solid. In this situation, all engulfed throats can become filled by wetting fluid while the the non-wetting phase is retained in the pore bodies, leading to a considerable amount of trapping in those pores since they contain most of the void volume in a rock (Fleury and Romero-Samiento, 2016; Krevor et al., 2015). Even with the silurian dolomite samples having pores better connected than the coquina samples (which would make gas trapping difficult), the frequency of larger pores in its structure was decisive to favor more gas trapping as compared to the coquina samples.

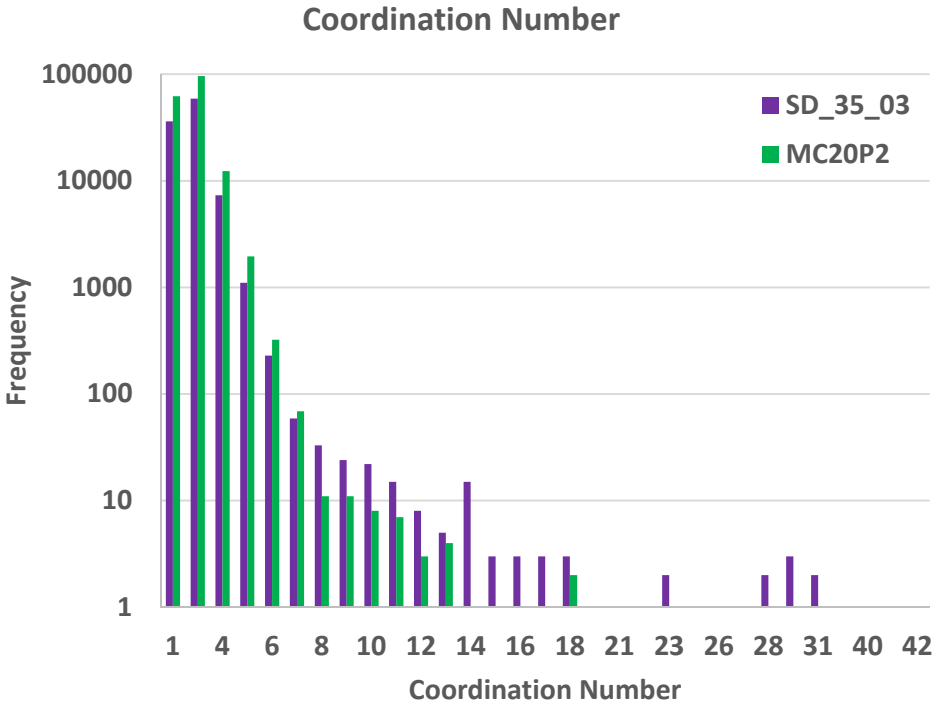

Fig. 9. Comparison of coordination numbers by frequency of silurian dolomite samples SD_35_03 (in purple) and of coquina sample MC20P2) (in green).

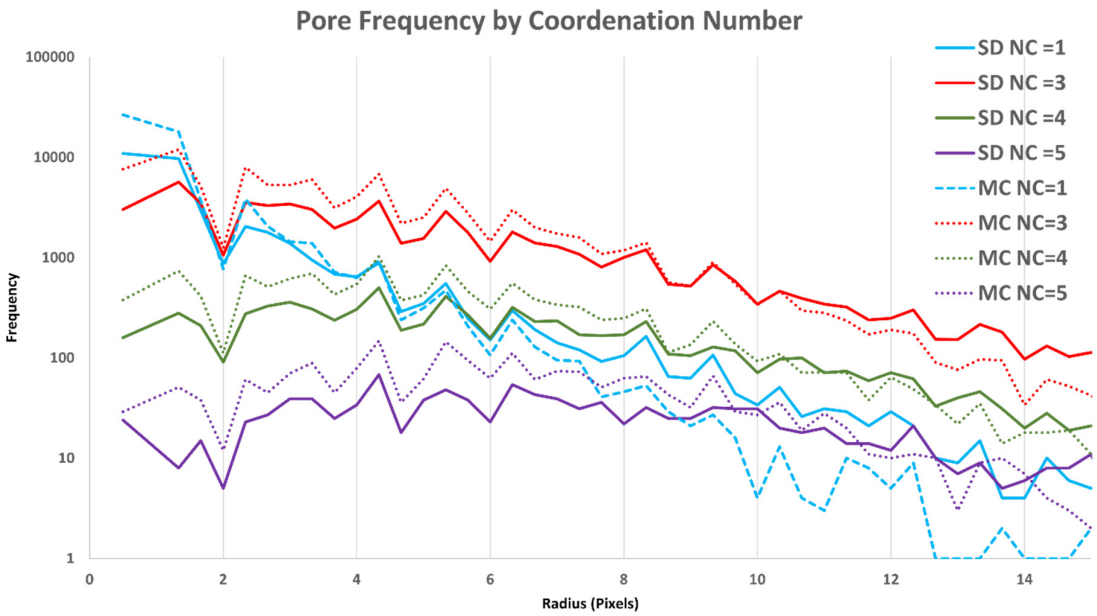

Fig. 10. Pore frequency by coordination number for different pore sizes for the silurian dolomite (SD) and coquina (MC) samples.

CONCLUSIONS

Our research focused on the effects of pore structure, pore size distribution and pore connectivity on observed values of S_{gt} in carbonate rock samples having very similar porosity values. NMR and MICP studies were performed on silurian dolomite, coquina, and Indiana limestone samples. Integration of the NMR and MICP methods enabled the estimates of the surface relaxation necessary to transform relaxation times into the pore size distribution, which in turn enabled the partitioning of pores into micro-, meso-, and macropores. MicroCT images were further used to obtain skeletons that provided the necessary input data (points, segments, and nodes) to generate 3D pore spaces and their connections.

The analysis of the pore bodies and pore throats through NMR and MICP could explain some of the observed variations in measured S_{gt} values. For the Indiana limestone samples a considerable volume of pores existed within the micropore and mesopore ranges. Since microporosity interferes with effective gas trapping, this caused lower S_{gt} values of these samples compared to the coquina and Indiana limestone plugs with less micropores and mesopores in their pore structure.

The 3D characterization of the pore space using microCT images provided an attractive means of explaining the high S_{gt} values obtained for the silurian dolomite and coquina samples. We observed that even with a well-connected pore network, the frequency of pores with larger radii was decisive for greater trapping of the silurian dolomite sample compared to the coquina sample, thus showing that pore radii exert a greater influence on gas trapping than pore connectivity.

Acknowledgements. This research was carried out in association with ongoing R&D projects registered as ANP 19027-2, "Desenvolvimento de infraestrutura para pesquisa e desenvolvimento em recuperação avançada de óleo – EOR no Brasil" (UFRJ/Shell Brasil/ ANP) setting-up a advanced EOR Lab facility for R&D in Brasil, and ANP 20163-2, "Análise experimental da recuperação de petróleo para as rochas carbonáticas do pré-sal brasileiro através da injeção alternada de CO_2 e água", sponsored by Shell Brasil under the ANP R&D levy as "Compromisso de Investimentos com Pesquisa e Desenvolvimento". This study was financed in part by the Coordenação de Aperfeiçoamento de Pessoal de Nível Superior- Brasil (CAPES) - Finance Code 001 and carried out with the support of CNPq (National Council of Scientific and Technological Development, Brazil). We also thank the research teams of LRAP/COPPE/UFRJ.

REFERENCES

Afzali, S., Rezaei, N., Zendehboudi, S., 2018. A comprehensive review on enhanced oil recovery by water alternating gas (WAG) injection. Fuel, 227, 218–246. https://doi.org/10.1016/j.fuel.2018.04.015

Aissaoui, A., 1983. Etude théorique et expérimentale de l'hystérésis des pressions capillaires et des perméabilités relatives en vue du stockage souterrain de gaz. Ecole des Mines de Paris, Paris.

Alyafei, N., 2015. Capillary trapping and oil recovery in altered-wettability carbonate rock. PhD thesis. Dept. of Earth Science and Engineering, Imperial College London.

Blunt, M., Bijeljic, B., Dong, H., Gharbi, O., Iglauer, S., Mostaghimi, P., Pentland, C., 2013. Pore-scale imaging and modelling. Adv. Water Resour., 51, 197–216. DOI: https://doi.org/10.1016/j.advwatres.2012.03.003

Bona, N., Garofoli, L., Radaelli, F., 2014. Trapped gas saturation measurements: New perpectives. SPE Annual Technical Conference and Exhibition, Amsterdam, The Netherlands, SPE- 170765-MS. https://doi.org/10.2118/170765-MS

Element, D., Master, J., Sargent, N., Jayasekera, A., Goodyear, S., 2003. Assesment of three-phase relative permeability models using laboratory hysteresis data. SPE Int. Improved Oil Recovery Conf. in Asia Pacific, Kuala Lumpur, Malaysia, SPE-84903-MS. https://doi.org/10.2118/84903-MS

Fatemi, S.M., Sohrabi, M., 2013. Experimental and theoretical investigation of oil and gas trapping under two- and three-phase flow including water alternating gas (WAG) injection. SPE Annual Techn. Conf. and Exhibition, New Orleans, Louisiana, USA, SPE-166193-MS. https://doi.org/10.2118/166193-MS

Faybishenko, B.A., 1995. Hydraulic behavior of quasi-saturated soils in the presence of entrapped air: Laboratory experiments. Water Resour. Res., 31, 2421–2435. https://doi.org/10.1029/95WR01654

Fayer, M.J., Hillel, D., 1986. Air encapsulation: II. Profile water storage and shallow water table fluctuations. Soil Sci. Soc. Am. J., 50, 572–577. https://doi.org/10.2136/sssaj1986.03615995005000030006x

Fleury, M., Romero-Sarmiento, M.. 2016. Characterization of shales using T1–T2 NMR maps. J. Petrol. Sci. Eng., 137, 55–62. https://doi.org/10.1016/j.petrol.2015.11.006

Ge, X., Myers, M.T., Liu, J., Fan, Y., Zaid, M.A., Zhao, J., Hathon, L., 2021. Determining the transverse surfave relaxivity of reservoir rocks: A critical review and perspective. Marine and Pet. Geol., 126. https://doi.org/10.1016/j.marpetgeo.2021.104934

Godoy, W., Pontedeiro, E.M., Hoerlle, F., Raoof, A., van Genuchten, M.Th., Santiago, J., Couto, P., 2019. Computational and experimental pore-scale studies of a carbonate rock sample. J. Hydrol. Hydromech., 67, 4, 372–383. http://dx.doi.org/10.2478/johh-2019-0009

Gonçalves, R.D., Teramoto, E.H., Engelbrecht, B.Z, Soto, M.A., Chang, H.K van Genuchten, M.Th., 2019. Quasi-saturated layer: Implications for estimating recharge and groundwater modeling. Groundwater, 58, 3, 432–440. https://doi.org/10.1111/gwat.12916

Gyllensten, A., Al-Hammadi, M. I., Abousrafa, E., Boyd, A., Ramamoorthy, R., Neumann, S., Neville, T.J., 2008. A new workflow for comprehensive petrophysical characterization of carbonate reservoirs drilled with water-base muds. Abu Dhabi Int. Petrol. Exhibition and Conf., Abu Dhabi, UAE, SPE-118380-MS. https://doi.org/10.2118/118380-MS

Hamon, G., Suzanne, K., Billiote, J., Trocme, V., 2001. Field-wide variations of trapped gas saturation in heterogeneous sandstone. SPE Annual Techn. Conf. and Exhibition, New Orleans, Louisiana, SPE-71524-MS. https://doi.org/10.2118/71524-MS

Herlinger, R.J., Zambonatto, E.E., de Ros, L.F., 2017. Infuence of diagenesis on the quality of lower Cretaceous Pre-Salt Lacustrine carbonate reservoirs from Northern Campos Basin, offshore Brazil. J. Sedim. Res., 87, 12, 1285–1313. https://doi.org/10.2110/jsr.2017.70

Jerauld, G.R., 1997. Prudhoe Bay gas/oil relative permeability. SPE Res. Eng., 12, SPE-35718-PA, 66–73. https://doi.org/10.2118/35718-PA

Kazemi, F., Azin, R., Osfouri, S., 2020. Evaluation of phase trapping models in gas-condensate systems in an unconsolidated sand pack. J. Petrol. Sci. Eng., 195, 107848. https://doi.org/10.1016/j.petrol.2020.107848

Khisamov, R.S., Bazarevskaya, V.G., Burkhanova, I.O., Kuzmin, V.A., Bolshakov, M.N., Marutyan, O.O.. 2020. Influence of the pore space structure and wettability on residual gas saturation. Georesour., 22, 2, 2–7. DOI:10.18599/grs.2020.2.2-7

Krevor, S., Blunt, M.J., Benson, S.M., Pentland, C.H., Reynolds, C., Al-Menhali, A., Niu, B., 2015. Capillary trapping for geologic carbon dioxide storage – From pore scale physics to field scale implications. Int. J. Greenh. Gas Control, 40, 221–237. https://doi.org/10.1016/j.ijggc.2015.04.006

Lai, J., Wang, G., Wang, Z., Chen, J., Pang, X., Wang, S., Fan, X., 2018. A review on pore structure characterization in tight sandstones. Earth Sci. Rev., 117, 436–457. https://doi.org/10.1016/j.earscirev.2017.12.003

Li, W., Lu, S., Xue, H., Zhang, P., Hu, Y., 2016. Microscopic pore structure in shale reservoir in the argillaceous dolomite from the Jianghan Basin. Fuel, 181, 1041–1049. https://doi.org/10.1016/j.fuel.2016.04.140

Lima, M.C., Pontedeiro, E.M., Ramirez, M.G., Favoreto, J., Santos, H.N., van Genuchten, M.Th., Raoof, A., 2022. Impacts of mineralogy on petrophysical properties. Transp. Porous Media, 145, 103–125. https://doi.org/10.1007/s11242-022-01829-w

Lima, M.C., Pontedeiro, E.M., Ramirez, M., Boyd, A., van Genuchten, M.Th., Borghi, L., Raoof, A., 2020. Petrophysical correlations for the permeability of coquinas (carbonate rocks). Transp. Porous Media, 135, 287–308. https://doi.org/10.1007/s11242-020-01474-1

Meiboom, S., Gill, D., 1958. Modified spin-echo method for measuring nuclear relaxation times. Rev. Sci. Instrum., 29, 688. https://doi.org/10.1063/1.1716296

Mohammadian, S., Geistlinger, H., Vogel, H.-J., 2015. Quantification of gas-phase trapping within the capillary fringe using computed microtomography. Vadose Zone J., 14, 1–9. https://doi.org/10.2136/vzj2014.06.0063

Ni, H., Boon, M., Garing, C., Benson, S.M., 2019. Prediction CO2 resudual trapping ability based on experimental petrophysical properties for different sandstone types. Int. J. Greenh. Gas Control, 86, 158–176. https://doi.org/10.1016/j.ijggc.2019.04.024

Otsuki, B., Takemoto, M., Fujibayashi, S., Neo, M., Kokubo, T., Nakamura, T., 2006. Pore throat size and connectivity determine bone and tissue ingrowth into porous implants: Three-dimensional micro-CT based structural analyses of porous bioactive titanium implants. Biomaterials, 27, 892–900. DOI: 10.1016/j.biomaterials.2006.08.013

Raeini, A.Q., Bijeljic, B., Blunt, M.J., 2015. Modelling capillary trapping using finite volume simulation of two-phase flow directly on micro-CT images. Adv. Water Resour., 83, 102–110. https://doi.org/10.1016/j.advwatres.2015.05.008

Raoof, A., Nick, H.M., Hassanizadeh, S.M., Spiers, C.J., 2013. Poreflow: A complex pore-network model for simulation of reactive transport in variably saturated porous media. Comp. Geosci., 61, 160–174. https://doi.org/10.1016/j.cageo.2013.08.005

Ruspini, L.C., Farokhpoor, R., Oren, P.E., 2017. Pore-scale modeling of capillary trapping in water-wet porous media: A new cooperative pore-body filling model. Adv. Water Resour., 108, 1–14. https://doi.org/10.1016/j.advwatres.2017.07.008

Sahimi, M., 2012. Flow and Transport in Porous Media and Fractured Rock: From Classical Methods to Modern Approaches. Wiley, Germany. DOI: 10.1002/9783527636693

Shao, X., Pang, X., Li, L., Zheng, D., 2017. Fractal analysis of pore network in tight gas sandstones using NMR method: A case study from the Ordos Basin, China. Energy Fuels, 31, 10, 10358–10368. https://doi.org/10.1021/acs.energyfuels.7b01007

Silva, P.N., Gonçalvez, E.C., Rios, E.H., Muhammad, A., Moss, A., Pritchard, T., Azeredo, R.B., 2015. Automatic classification of carbonate rocks permeability from ^{1}H NMR relaxation data. Expert Systems Appl., 9, 9, 4299–4309. https://doi.org/10.1016/j.eswa.2015.01.034

Silveira, T.M., Hoerlle, F., Rocha, A.S., Lima, M.C., Ramirez, M.G., Pontedeiro, E.M., van Genuchten, M.Th., Couto, P., 2022. Effects of carbonated water injection on the pore system of a carbonate rock (coquina). J. Hydrol. Hydromech., 70, 2, 257–268. DOI: https://doi.org/10.2478/johh-2022-0001

Souza, A.A., 2012. Estudo de Propriedades Petrofísicas de Rochas Sedimentares por Ressonância Magnética. PhD thesis, Materials Science and Engineering, São Paulo University, 207p.

Sun, H., Vega, S., Tao, G., 2017. Analysis of heterogeneity and permeability anisotropy in carbonate rock samples using digital rock physics. J. Petr. Sci. Eng., 156, 419–429.

https://doi.org/10.1016/j.petrol.2017.06.002

Suzanne, K., Billiote, J., 2004. Influence de la microporosité sur le piégeage du gaz dans un milieu poreaux naturel. Comptes Rendus Geosci., 336, 12, 1071–1078. https://doi.org/10.1016/j.crte.2004.04.010

Suzanne, K., Hamon, G., Billiotte, J., Trocme, V., 2003. Experimental relationships between residual gas saturation and initial gas saturation in heterogeneous sandstone reservoirs. SPE Annual Techn. Conf. and Exhibition, Denver, Colorado, SPE-84038-MS. https://doi.org/10.2118/84038-MS

Tanino, Y., Blunt, M., 2013. Laboratory investigation of capillary trapping under mixed-wet conditions. Water Resour. Res., 49, 7, 4311–4319. https://doi.org/10.1002/wrcr.20344

Tanino, Y., Blunt, M., 2012. Capillary trapping in sandstone and carbonates: Dependence on pore structure. Water Resour. Res., 48, 8525. DOI: 10.1029/2011WR011712

Trevizan, W., Netto, P., Coutinho, B., Machado, V.F., Rios, E.H., Chen, S., Romero, P., 2014. Method for predicting permeability of complex carbonate reservoirs using NMR logging measurements. Petrophys., 55, 03, SPWLA-2014-v55n3a4, 240–252.

Washburn, E.W., 1921. Note on a method of determining the distribution of pore sizes in a porous material. Proc. Nat. Acad. Sci. USA, 7, 115–116. DOI: 10.1073/pnas.7.4.115

Wang, S., Tokunaga, T.K., Wan, J., Dong, W., Kim, Y,, 2016. Capillary pressure-saturation relations in quartz and carbonate sands: Limitations for correlating capillary and wettability influences on air, oil, and supercritical CO_2 trapping. Water Resour. Res., 52, 6671–6690. DOI: 10.1002/2016WR018816

Wildenschild, D., Sheppard, A.P., 2013. X-Ray imaging and analysis techniques for quantifying pore-scale structure and processes in subsurface porous medium systems. Adv. Water Resour., 51, 217–246. https://doi.org/10.1016/j.advwatres.2012.07.018

Yuan, Y., Rezaee, R., 2019. Comparative porosity and pore structure assessment in shales: Measurement techniques, infuencing factors and implications for reservoir characterization. Energies, 12, 2094. https://doi.org/10.3390/en12112094

Received 22 October 2022
Accepted 30 December 2022

J. Hydrol. Hydromech., 71, 2023, 1, 22–34
https://doi.org/10.2478/johh-2022-0039

sciendo Journal of Hydrology and Hydromechanics Institute of Hydrology SAS

Evaluation of a general model for multimodal unsaturated soil hydraulic properties

Katsutoshi Seki[1*], Nobuo Toride[2], Martinus Th. van Genuchten[3,4]

[1] Natural Science Laboratory, Toyo University, 5-28-20 Hakusan, Bunkyo-ku, Tokyo 112-8606, Japan.
[2] Graduate school of Bioresources, Mie University, 1577 Kurimamachiya-cho Tsu, Mie 514-8507 Japan.
[3] Department of Earth Sciences, Utrecht University, Princetonlaan 8a, 3584 CS Utrecht, Netherlands.
[4] Department of Nuclear Engineering, POLI & COPPE, Federal University of Rio de Janeiro, UFRJ, Rua Horácio Macedo, Bloco G, Cidade Universitária, Rio de Janeiro, RJ 21941-450, Brazil.
[*] Corresponding author. E-mail: seki_k@toyo.jp

Abstract: Many soils and other porous media exhibit dual- or multi-porosity type features. In a previous study (Seki et al., 2022) we presented multimodal water retention and closed-form hydraulic conductivity equations for such media. The objective of this study is to show that the proposed equations are practically useful. Specifically, dual-BC (Brooks and Corey)-CH (common head) (DBC), dual-VG (van Genuchten)-CH (DVC), and KO (Kosugi)$_1$BC$_2$-CH (KBC) models were evaluated for a broad range of soil types. The three models showed good agreement with measured water retention and hydraulic conductivity data over a wide range of pressure heads. Results were obtained by first optimizing water retention parameters and then optimizing the saturated hydraulic conductivity (K_s) and two parameters (p, q) or (p, r) in the general hydraulic conductivity equation. Although conventionally the tortuosity factor p is optimized and (q, r) fixed, sensitivity analyses showed that optimization of two parameters ($p + r$, qr) is required for the multimodal models. For 20 soils from the UNSODA database, the average R^2 for log (hydraulic conductivity) was highest (0.985) for the KBC model with $r = 1$ and optimization of (K_s, p, q). This result was almost equivalent (0.973) to the DVC model with $q = 1$ and optimization of (K_s, p, r); both were higher than R^2 for the widely used Peters model (0.956) when optimizing (K_s, p, a, ω). The proposed equations are useful for practical applications while mathematically being simple and consistent.

Keywords: Water retention; Unsaturated hydraulic conductivity; General hydraulic conductivity model; Multimodal hydraulic models.

INTRODUCTION

Knowledge of the water retention (WRF) and hydraulic conductivity (HCF) functions is important for simulating water retention and flow in unsaturated soils and other porous media. Frequently used analytical expressions for these functions were proposed by Brooks and Corey (1964), van Genuchten (1980) and Kosugi (1996), further referred to as the BC, VG and KO models respectively. The models were obtained by combining expressions for the water retention function with statistical pore-size distribution models that consider soils to be made up of a bundle of capillary tubes (Burdine, 1953; Mualem, 1976).

Formally, the above models are restricted to capillary flow within a bundle of capillary tubes. As the water content of a soil decreases, the retention of water changes from capillarity to fluid adsorption, with the mechanism of water flow changing from capillary movement to film and corner flow. For this reason, several used Mualem's model only at relatively high water contents (the capillary water range) and modeled the hydraulic conductivity at low water content (i.e., the adsorption water range) independently (e.g., Peters, 2013), or avoided the use of capillary bundle models altogether to independently describe the WRF and HCF over the whole moisture range (e.g., Luo et al., 2022).

Another approach for expressing the HCF over a wide range of pressure heads is to make the Burdine or Mualem expressions more flexible by increasing the number of adjustable parameters. Hoffmann-Riem et al. (1999) proposed for this purpose a general HCF with three adjustable parameters p, q, r as

$$K_r(h) = \frac{K(h)}{K_s} = S(h)^p \left[\frac{\int_0^{S(h)} h(S)^{-q} dS}{\int_0^1 h(S)^{-q} dS} \right]^r \quad (1)$$

where h is the pressure head (assumed in this study to be positive for unsaturated conditions), K_r is the relative hydraulic conductivity, K the unsaturated hydraulic conductivity, K_s the saturated hydraulic conductivity, and S effective saturation defined by

$$S = \frac{\theta - \theta_r}{\theta_s - \theta_r} \quad (2)$$

where θ is the volumetric water content, and θ_r and θ_s are the residual and saturated water contents, respectively. In particular, $p = 2$, $q = 2$, and $r = 1$ for Burdine's model, and $p = 0.5$, $q = 1$, and $r = 2$ for Mualem's model.

Although the Burdine and Mualem models consider only one parameter (i.e., the tortuosity factor p) to be variable, and q and r to be constants, Hoffmann-Riem et al. (1999) showed that optimizing p and r for the VG model would improve estimations of the HCF. They suggested that neither the general formulation nor the simpler Burdine and Mualem variants should be interpreted as being physically based. Kosugi (1999) showed that optimizing two parameters (i.e., p and q) improved estimations of the HCF using his KO model, especially when the range of pressure head was wide.

To make the WRF more flexible for multi-porosity media, Durner (1994) proposed a linear superposition of VG equations (the multi-VG retention model). Priesack and Durner (2006) subsequently provided a closed-form hydraulic conductivity equation for the multi-VG model by using the general HCF. The

multimodal model proved to be far more flexible in describing the hydraulic properties of both near-saturated soils and dry soils. Mualem's model ($q = 1$, $r = 2$) with a free parameter p has since been used for multimodal WRFs in many studies (Dimitrov et al., 2014; Lipovetsky et al., 2020; Schelle et al., 2010; Watanabe and Osada, 2016).

In our previous study (Seki et al., 2022) we derived closed-form general HCF equations for the multimodal model in terms of a linear superposition of any combinations of the BC, VG, and KO models. We also showed that the asymptotic slope of log h – log K curve at low water contents (i.e., slope of the sub-curve expressing film flow) for Mualem's model cannot be smaller than $qr = 2$, which contradicts the result by Peters (2013) that the slope is approximately 1.5 for many soils. We hence suggested that the value of q or r may need to be modified from Mualem's parameter to enhance better descriptions of $K(h)$ at relatively low water contents. Based on this result and recommendations by Hoffmann-Riem et al. (1999) and Kosugi (1999) to consider two parameters of the general HCF as free variables, the hypothesis of this study is that the general HCF with two free HCF parameters (p, q) or (p, r) is able to express the HCF over a wide range of pressure heads.

In this study we apply the general HCF equations of the multimodal models proposed by Seki et al. (2022) to previously published water retention and hydraulic conductivity data of soils with various textures over a wide range of pressure heads. Our focus is especially on the benefit of optimizing q or r in addition to p in Eq. (1).

METHODOLOGY

Model description

The water retention function (WRF) of multimodal soils may be defined as

$$S(h) = \sum_{i=1}^{k} w_i S_i(h) \tag{3}$$

where k is the number of subsystems, and w_i are weighing factors with $0 < w_i < 1$ and $\Sigma w_i = 1$. The sub-retention functions $S_i(h)$ used in this study are summarized in Table 1. The closed-form hydraulic conductivity equations derived from $S_i(h)$ in Table 1 with the general HCF equation (Eq. 1) are provided by Seki et al. (2022). Note that the parameter q in the HCF is common with the WRF in the VG subfunction (Table 1). For the multimodal models we assume $\theta_r = 0$, which allows Eq. (2) to be written as

$$\theta(h) = \theta_s S(h) \tag{4}$$

In this paper, we focus on multimodal models with $k = 2$, where $S_1(h)$ is expected to express capillary water and $S_2(h)$ adsorbed water. Eqs. (3) and (4) can then be summarized as

$$\theta(h) = \theta_s[wS_1(h) + (1 - w)\, S_2(h)] \tag{5}$$

by denoting w_1 as w. Out of 9 possible combinations of the sub-retention functions (i.e., BC, VG, and KO), this paper focuses on three models: a dual-BC (DB) model with BC type $S_1(h)$ and $S_2(h)$ equations, a dual-VG (DV) model with VG type $S_1(h)$ and $S_2(h)$ equations (this model is equivalent to the one proposed by Durner (1994)), and a KO_1BC_2 (KB) model with KO type $S_1(h)$ and BC type $S_2(h)$ equations.

We additionally use the CH (common head) assumption of Seki et al. (2022) in which h_{b_i} for the BC model, α_i^{-1} for the VG model, and h_{m_i} for the KO model have the same value (i.e., $H = h_{b_i} = \alpha_i^{-1} = h_{m_i}$). The CH assumption is very useful for soils showing a single inflection point in the water retention data (i.e., still having a unimodal pore-size distribution) but is ineffective for soils which have a clear bimodality of soil pore sizes (such as Andisols). Since the verification dataset used in this study does not include such soils, we use for this scenario the CH assumption. To summarize, this paper verifies dual-BC-CH (DBC), dual-VG-CH (DVC) and KO_1BC_2-CH (KBC) models as summarized in Table 2.

Table 1. Sub-retention functions for the Brooks-Corey (BC), van Genuchten (VG) and Kosugi (KO) models.

Type	Equation	Parameters
BC	$S_i(h) = \begin{cases} \left(\frac{h}{h_{b_i}}\right)^{-\lambda_i} & (h > h_{b_i}) \\ 1 & (h \le h_{b_i}) \end{cases}$	h_{b_i}, λ_i
VG	$S_i(h) = [1 + (\alpha_i h)^{n_i}]^{-m_i}$, $m_i = 1–q/n_i$	α_i, n_i, q
KO	$S_i(h) = Q\left[\frac{\ln(h/h_{m_i})}{\sigma_i}\right]$, $Q(x) = \frac{1}{2}\left[\mathrm{erfc}\left(\frac{x}{\sqrt{2}}\right)\right]$	h_{m_i}, σ_i

Table 2. Parameters in the selected water retention (WRF) and hydraulic conductivity (HCF) functions. Fixed parameters are shown within bracket, with $h_b = 2$ cm and $h_0 = 6.3 \times 10^6$ cm; other fixed values are shown in the table.

Model name	Abbreviation	WRF parameters	HCF parameters
van Genuchten	VG	θ_s, θ_r, H, n, ($q = 1$)	K_s, p, ($r = 2$)
Modified VG	MVG	θ_s, θ_r, H, n, (h_b, $q = 1$)	K_s, p, ($r = 1$)
dual-BC-CH	DBC	θ_s, w, H, λ_1, λ_2	K_s, p, q, ($r = 1$)
dual-VG-CH	DVC	θ_s, w, H, n_1, n_2, ($q = 1$)	K_s, p, r
Modified DVC	MDVC	θ_s, w, H, n_1, n_2, (h_b, $q = 1$)	K_s, p, r
KO_1BC_2-CH	KBC	θ_s, w, H, σ_1, λ_2	K_s, p, q, ($r = 1$)
Modified KBC	MKBC	θ_s, w, H, n_1, n_2, (h_b)	K_s, p, q, ($r = 1$)
Peters	PE	θ_s, w, H, σ, (h_0)	K_s, p, a, ω
Modified PE	MPE	θ_s, w, H, σ, (h_b, h_0)	K_s, p, a, ω

We also compared the VG (van Genuchten, 1980) and PE (Peters, 2013) models. The WRF of Peters (2013) is given by Eq. (5), in which $S_1(h)$ is a KO type subfunction as shown in Table 1 with $h_m = H$, while $S_2(h)$ is given by

$$S_2(h) = \begin{cases} \dfrac{L(h_0) - L(h)}{L(h_0) - L(H)} & (h > H) \\ 1 & (h \le H) \end{cases} \tag{6}$$

where $L(h) = \log(1 + h/H)$. Note that h_0 is the pressure head where θ first becomes zero. The HCF of the PE model is expressed as

$$K_r(h) = (1 - \omega) K_1(h) + \omega K_2(h) \tag{7}$$

where $K_1(h)$ is Mualem's equation (Eq. (1) with $q = 1$, $r = 2$) for $S_1(h)$, while $K_2(h)$ is a BC type function given by

$$K_2(h) = \begin{cases} \left(\dfrac{h}{H}\right)^a & (h > H) \\ 1 & (h \le H) \end{cases} \tag{8}$$

where K_s and p in Eq. (1), ω in Eq. (7) and a in Eq. (8) are HCF parameters of the PE model. When $n < 1.1$ in the VG or DVC models, or $\sigma > 2$ in the KBC or PE models, we used a modified formulation which introduces a hypothetical air-entry head near saturation ($h_b = 2$ cm) as proposed by Vogel et al. (2000) and was adapted to the multimodal model by Seki et al. (2022) to suppress extreme changes in the HCF curve near saturation. These modified models are denoted as MVG, MDVG, MKBC and MPE in Table 2.

Reason for optimizing 2 HCF variables

Although the original Burdine and Mualem models assume fixed values of the parameters p, q, r in the general hydraulic conductivity function given by Eq. (1), it is possible to optimize the tortuosity factor, p, in both models. This section discusses why it may be advantageous to optimize two of the three parameters, notably (p, q) or (p, r) simultaneously for the dual-porosity models shown in Table 2.

As shown by Seki et al. (2022), the slope a_i of a log h – log K plot of a multi-BC model in which i-th subcurve is predominant can be approximated by

$$a_i = (p + r)\lambda_i + qr \tag{9}$$

with a_i having a positive value. By defining $\alpha = p + r$ and $\beta = qr$, the relationship between λ_i and a_i is given by a linear function $a_i = \alpha\lambda_i + \beta$, which indicates that a pair of parameters (α, β) determines the shape of the HCF curve. For a single BC model, we only have one equation for the relationship between a_1 and λ_1, which implies that when q and r are fixed, p can be optimized to fix the values of a_1 and λ_1. For the dual-BC model, on the other hand, one has two equations for the (a_i, λ_i) relationship, which shows that two free parameters of (p, q, r) are needed to solve the simultaneous equations. For the dual-modal function it is hence reasonable to optimize two parameters of (p, q, r) simultaneously.

However, making all three parameters (p, q, r) freely adjustable is not reasonable, even for multi-models with $k = 3$ (the tri-model), because, as noted above, α and β are the only free parameters such that we have only two degrees of freedom. When using the tri-model it is hence also reasonable to optimize only two of the parameters p, q, and r. Seki et al. (2022) showed that for any multimodal model, the fitted water retention parameters will produce very similar hydraulic conductivity curves as long as the same (p, q, r) parameter set is used. Therefore, the discussion of this section with multi-BC model can be generalized to any combinations of sub-retention functions, as will be verified with actual soil data later.

Parameter optimization

The WRF and HCF for the models in Table 2 were tested using selected $\theta(h)$ and $K(h)$ data sets from Mualem (1976) and the UNSODA unsaturated soil hydraulic database (Nemes et al., 1999). The WRF parameters in Table 2 were determined using a least-squares optimization method in which the mean squared error (MSE) between the estimated and measured θ values was minimized. The HCF parameters were optimized subsequently by minimizing the MSE errors between estimated and measured log(K) values. For the HCF optimization we kept the WRF derived parameters constant and only adjusted the remaining HCF parameters. For the PE model we followed Peters (2013) and fixed h_0 at 6.3×10^6 cm. Although Peters (2013) assumed $a = -1.5$ to be a constant, in this study a was also optimized to assess the flexibility of the model for multimodal data sets.

Except for K_s, Eq. (1) has 3 HCF parameters: p, q, and r. For the multimodal models we fixed one of these three parameters and optimized the remaining two parameters as explained in the last section. For the DBC and KBC models, we used $r = 1$ and optimized p and q. We selected $r = 1$ since Kosugi (1999) showed that $r = 1$ is ideal for a single KO model (Fig. 4 in his paper), in which case the HCF expression of multimodal model can be simplified to a sum of sub-functions (Seki et al., 2022). The same method was not used for the DVC model since q is a DVC water retention parameter and cannot be used as an optimized parameter for the hydraulic conductivity once the WRF parameters are known. Since $q = 1$ is widely used for the VG model, we also used this value for the DVC model and optimized p and r. For the VG model we used Mualem's hydraulic conductivity model ($q = 1$, $r = 2$) and optimized p. For the PE model, p, a, ω were optimized as explained earlier. The optimized and fixed parameters are summarized in Table 2.

The HCF parameters were optimized in two steps. At first, multiple initial conditions, notably (1, 2, 4, 6) for p and (0.5, 1, 2) for q or r (12 combinations in total) were used and the parameters optimized with a relatively loose convergence criterion to facilitate rapid calculations. The fitted parameter set with the least MSE was used next as initial condition for a second optimization step using much stricter convergence criteria to obtain more accurate parameter values. The software used for the WRF and HCF parameter optimizations is published as a Python library named unsatfit. On the website of unsatfit (i.e., https://sekika.github.io/unsatfit/), sample codes are provided for determining the WRF and HCF parameters by using the same optimization strategy as used here and also for drawing similar figures as published in this paper. A relatively simple web interface (SWRC Fit) for optimizing water retention parameters of the multimodal models is also available (Seki, 2007).

RESULTS AND DISCUSSION

Below are results obtained with the various models. We first present results obtained for Gilat loam since this soil was also used by Peters (2013) as an example of hydraulic properties covering a wide range of pressure heads. A detailed sensitivity analysis of the parameter optimization of Gilat loam is presented next. We subsequently show applications of the models to many other soils.

Gilat loam

Figure 1 shows fitted water retention and hydraulic conductivity curves of Gilat loam (Mualem, 1976), which was analyzed also (as soil 4) by Peters (2013). Fixed values of $\theta_s = 0.44$ and $K_s = 1.37 \times 10^{-4}$ cm/s were used consistent with the optimization procedure adopted by Peters (2013). The DBC, DVC, KBC and PE models all fitted the WRF and HCF data over the whole range of pressure heads, including the adsorption moisture range, nearly perfectly. This result confirms that the general HCF is effective for a wide range of pressure heads.

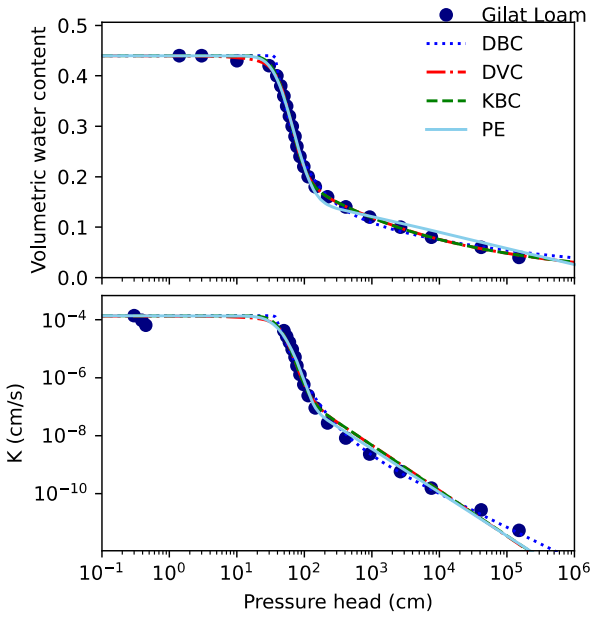

Fig. 1. Water retention and hydraulic conductivity curves for Gilat loam fitted with the DBC, DVC, KBC and PE models.

Sensitivity analysis

Fig. 2 shows a contour plot of RMSE (the root mean squared error) of the estimated $\log_{10}(K)$ for the KBC ($r = 1$) optimization of Gilat loam, along with the optimized values of (p, q). It is clear that the original Burdine parameter set (p, q) = (2, 2) did not give the lowest RMSE, while optimizing p with a fixed $q = 2$ also did not give the lowest RMSE.

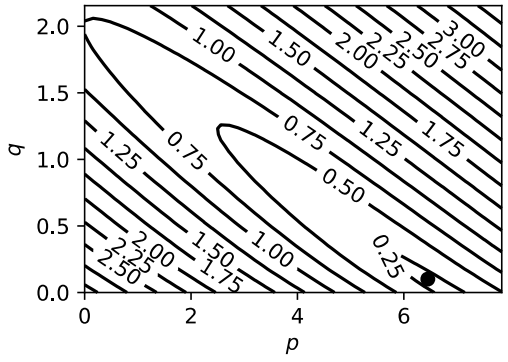

Fig. 2. Contour lines of RMSE of $\log_{10}(K)$ using various p and q values, and the optimized parameter (closed circle) obtained with the KBC model ($r = 1$) for Gilat loam.

Using Burdine's setting of (q, r) = (2, 1), the HCF curve did not match the entire range of pressure head, as shown in Fig. 3a1; the curve in the low pressure head range ($h < 100$ cm) matched the data well when $p = 4$, but the calculated curve at higher pressure heads ($h > 100$ cm) did not match the data. However, the measured and calculated curves matched over the whole range of pressure heads when (p, q, r) = (6.4, 0.1, 1) (Fig. 3a3). For the DVC optimization ($q = 1$), similar curves can be drawn as shown in Fig. 3b. For Mualem's setting of (q, r) = (1, 2) (Fig. 3b1), the HCF curve did not match the observed data over the whole range of pressure heads, while the curve matched the data for all pressure heads when (p, q, r) = (7.3, 1, 0.1) (Fig. 3b3). As noted earlier from Eq. (9) that the ($p + r$, qr) pair is a critical parameter set, Fig. 3b was drawn so that the ($p + r$, qr) values corresponded to those for Fig. 3a. As a result, similar curves were drawn for each corresponding KBC and DVC optimization, especially for the second (a2 and b2) and the third (a3 and b3) plots.

Fig. 3 demonstrates that the slope of the log h – log K curve in the low and high pressure head ranges can be controlled with two parameters p and q and a constant $r = 1$ (Fig. 3a), or alternatively with p and r and a constant $q = 1$ (Fig. 3b), as emphasized in the Methodology section. For Gilat loam, the dual-BC-CH fitting resulted in $\lambda_1 = 1.15$ and $\lambda_2 = 0.14$, and (p, q, r) = (6.4, 0.1, 1), and hence a_1=8.6 and a_2=1.14 when using Eq. (9). That equation hence indicates that points (λ_i, a_i) are on the straight line $a = (p + r)\lambda + qr$ in a λ-a plane, as shown in Fig. 4 for Gilat loam. The optimized values (λ_1, a_1) = (1.15, 8.6) and (λ_2, a_2) = (0.14, 1.14) are both on the red straight line $a = (p + r)\lambda + qr$ with the optimized (p, q, r) = (6.4, 0.1, 1). In other words, for a soil with WRF parameters (λ_1, λ_2) and corresponding slopes of the log h – log K curve (a_1, a_2), the parameters (p, q, r) are optimized to values corresponding to the red line in this Fig. 4. If we use

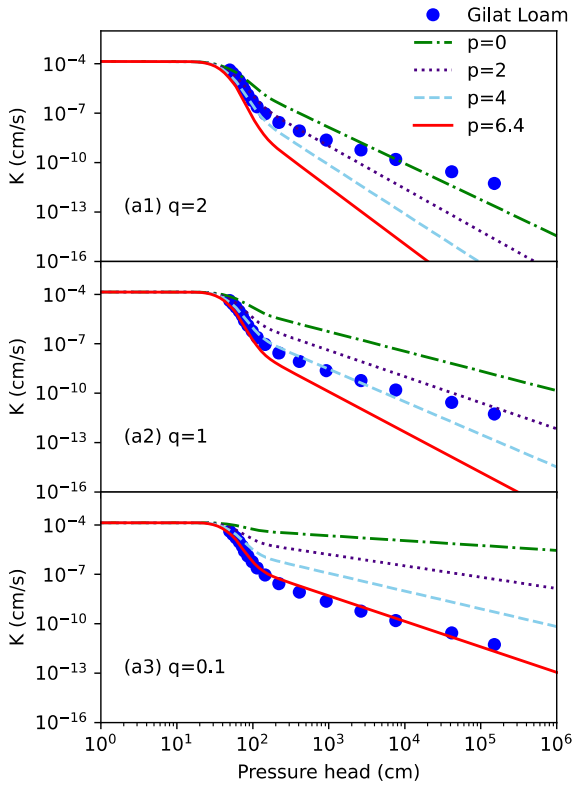

Fig. 3a. Hydraulic conductivity curves for Gilat loam as obtained with the KBC model using a fixed $r = 1$ and changing p, for (a1) $q = 2$ (a2) $q = 1$ (a3) $q = 0.1$.

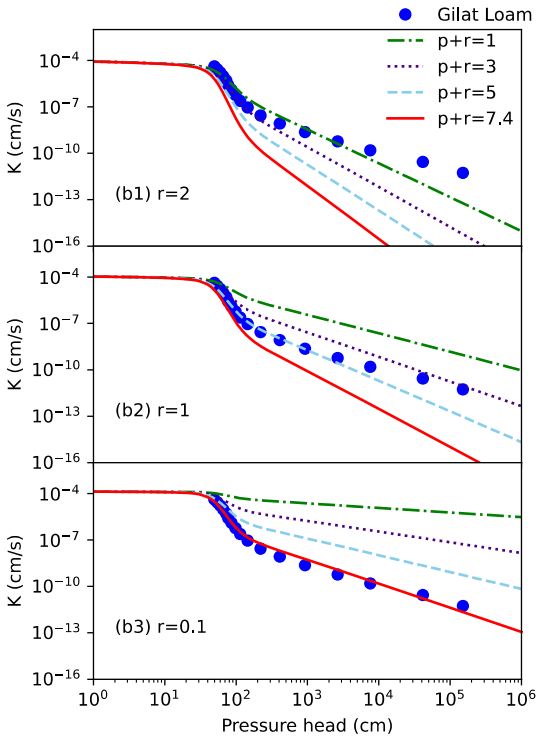

Fig. 3b. Hydraulic conductivity curves of Gilat loam as obtained with the DVC model using a fixed $q = 1$ and changing p, for (b1) $r = 2$ (b2) $r = 1$ (b3) $r = 0.1$.

Burdine's parameters of $q = 2$ and $r = 1$ or Mualem's parameters of $q = 1$ and $r = 2$, the line is expressed as $a = (p + r)\lambda + 2$ and fixed to the (0, 2) point, and hence cannot lie on (λ_1, a_1) and (λ_2, a_2) simultaneously. For this condition we can only optimize to the capillary point (λ_1, a_1), where the blue dotted line ($a = 5.7\lambda+2$) is obtained. This corresponds to $p = 4.7$, $q = 2$, $r = 1$ or $p = 3.7$, $q = 1$, $r = 2$, which causes the slope of the HCF curve to be steeper than the measured values in the high pressure head range as demonstrated in Figs. 3a1 and 3b1.

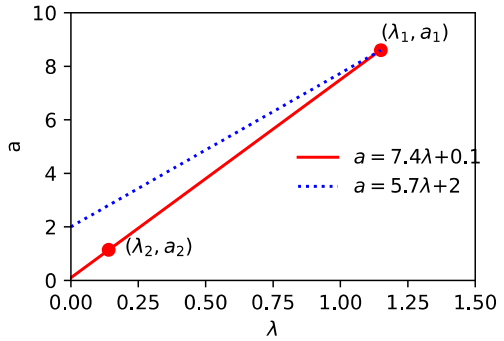

Fig. 4. Illustration that the (λ_i, a_i) points are on the same line $a = (p + r)\lambda + qr$ (red straight line) in a λ-a plane for Gilat loam. The blue-dotted line connects (0, 2) and (λ_1, a_1), which expresses the condition that the product qr equals 2 for the Mualem ($q = 1$, $r = 2$) or Burdine ($q = 2$, $r = 1$) models.

As discussed earlier, Eq. (9) suggests that different parameter sets for (p, q, r), but with the same ($p + r$, qr), all will produce similar HCF curves for all multimodal models. This is verified in Fig. 5. As we obtained (p, q, r) = (6.4, 0.1, 1) for the optimized (p, q) with fixed r for the KBC model, different parameter sets with the same ($p + r$, qr) = (7.4, 0.1) were chosen. We found that all curves were almost identical, which justifies that only two parameters need to be selected for the optimizations. Since the ($p + r$, qr) pair has two degrees of freedom, optimizing three parameters (p, q, r) simultaneously will cause overparameterization.

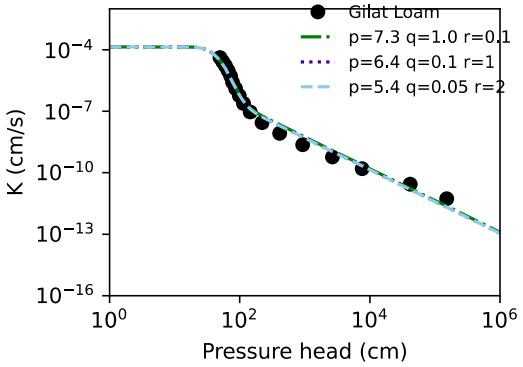

Fig. 5. Hydraulic conductivity curves of Gilat loam as obtained with the KBC model using different fixed values of (p, q, r), where ($p + r$, qr) = (7.4, 0.1).

Other soils

Fig. 6 shows fitted curves for 20 soils taken from the UNSODA database: 2 clays, 1 clay loam, 3 loams, 2 loamy sands, 6 sands, 1 silty clay, and 5 silty loams. The optimized parameters are listed in the Appendix.

For the examined datasets, all of the multimodal models represented the overall shape of WRF and HCF very well. For clay soils C2360 and C2362 and loam soil L4592 (Fig. 6a), the VG and MVG model fitted the WRF and HCF data well over a wide range of pressure heads, which shows that in this case there is no need to use multimodal models. For CL3033 in Fig. 6a, L4780 in Fig. 6b, S3182 in Fig. 6c, S4661, SiL3370 in Fig. 6d and SiL4673 in Fig. 6e, the VG and MVG models did not express the change in the slope well between the low (< 100 cm) and high pressure heads, while also underestimating the hydraulic conductivity at high pressure heads. The multimodal models (DBC, DVC, MDVC, KBC, MKBC) and the PE and MPE models on the other hand closely matched the water retention and hydraulic conductivity data within the measurement range. The DBC formulation furthermore was suitable for soils with a distinct air-entry head, such as L4770 in Fig. 6b, but for soils without a distinct air-entry head (such as the silty clay (SiC) and silty loam (SiL) soils in Figs. 6d and 6e), the DVC and KBC performed better than DBC.

Table 3 summarizes the coefficients of determination (R^2) for the fitted curves of Fig. 6. The average R^2 for θ was highest (0.992) for the (modified) DVC model, while R^2 for log K was highest (0.985) for the (modified) KBC. DBC had the highest R^2 for log K for 5 soils, even though the average value was not very high (0.938). R^2 for log K was higher for the (modified) KBC compared to the (modified) PE for 13 soils, and higher for the (modified) DVC relative to the (modified) PE model for 11 soils. Although the DVC and KBC models had fewer parameters than PE (Table 2), they can be used as an alternative to the PE model with similar or better fitting performance for many soils.

Our results confirm that the water retention and hydraulic conductivity properties can be expressed with a multimodal model in the same way as the PE model, by expressing capillary water retention with the first subfunction and adsorptive water with the second subfunction, while the hydraulic conductivity characteristics can be described using two parameters such as (p, q) or (p, r).

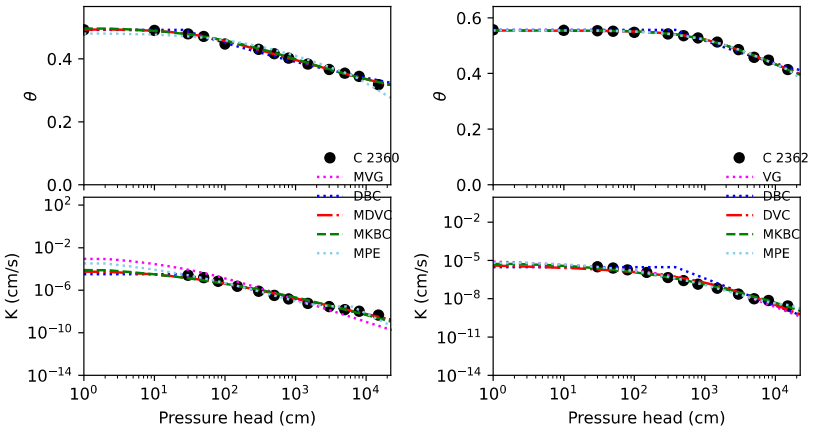

Fig. 6a. Measured water retention and hydraulic conductivity data and fitted curves for soil samples identified with the abbreviated name of soil texture and the UNSODA ID. Data for $h = 0$ are shown at $h = 1$ cm.

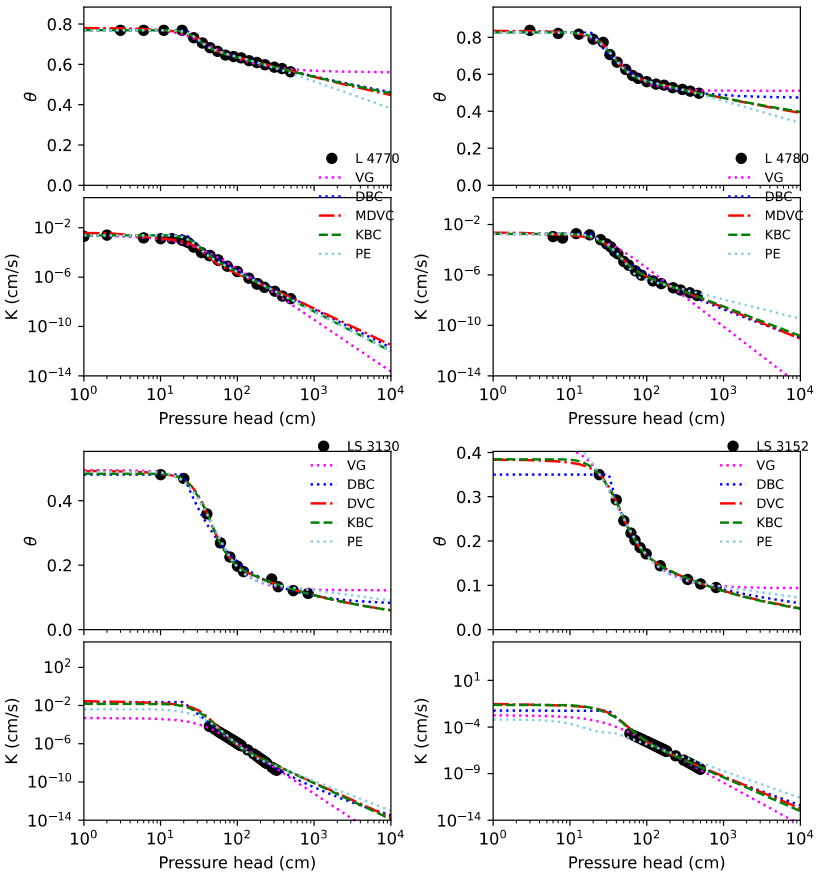

Fig. 6b. Measured water retention and hydraulic conductivity data and fitted curves for soil samples identified with the abbreviated name of soil texture and the UNSODA ID. Data for $h = 0$ are shown at $h = 1$ cm.

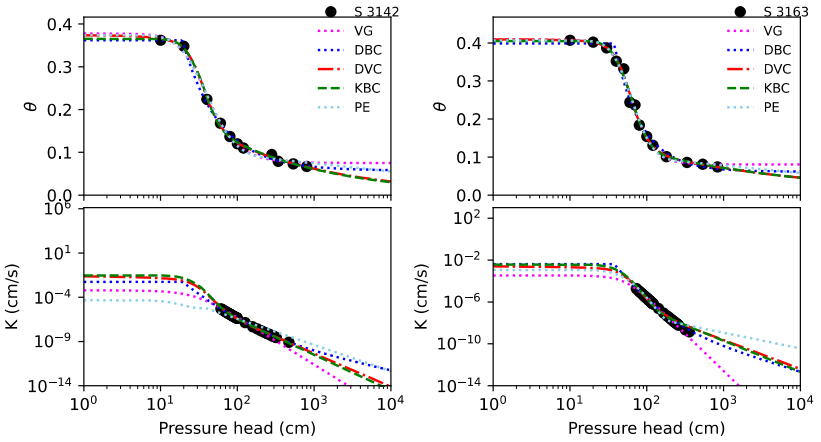

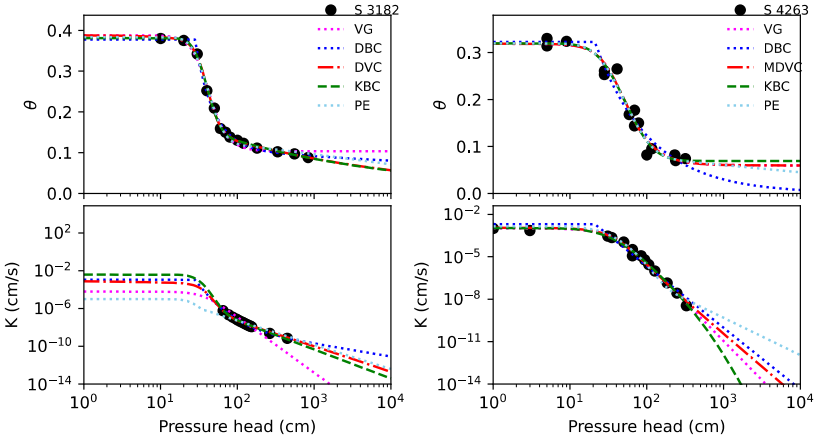

Fig. 6c. Measured water retention and hydraulic conductivity data and fitted curves for soil samples identified with the abbreviated name of soil texture and the UNSODA ID. Data for $h = 0$ are shown at $h = 1$ cm.

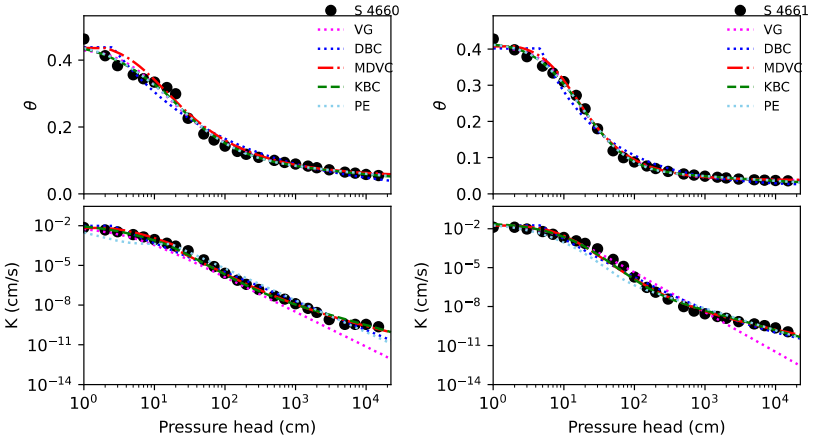

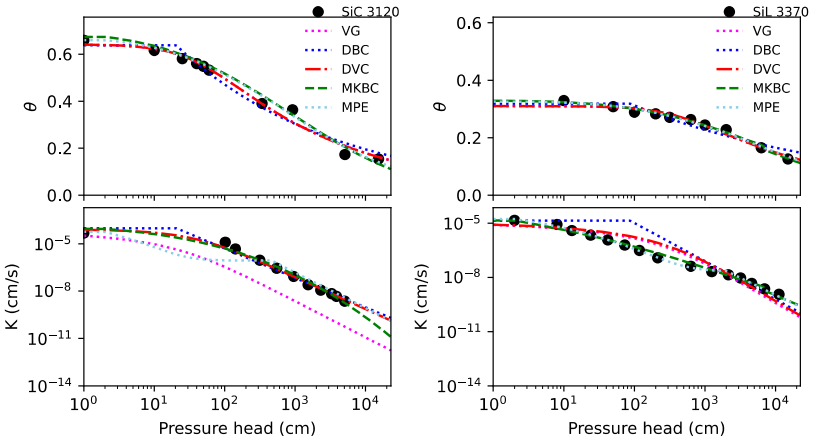

Fig. 6d. Measured water retention and hydraulic conductivity data and fitted curves for soil samples identified with the abbreviated name of soil texture and the UNSODA ID. Data for $h = 0$ are shown at $h = 1$ cm.

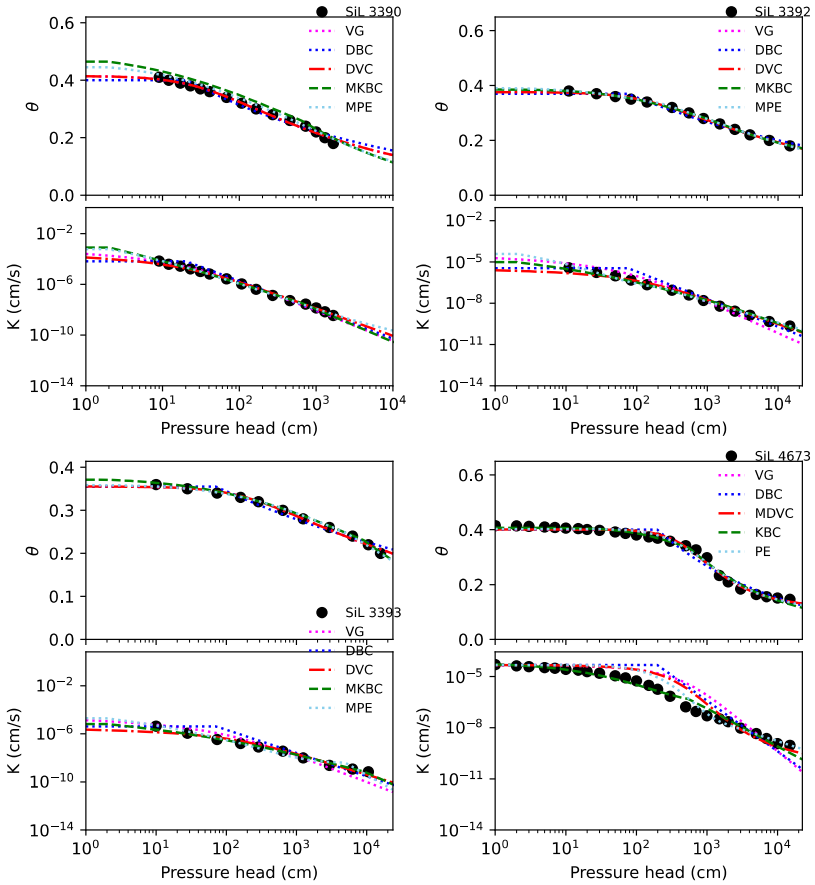

Fig. 6e. Measured water retention and hydraulic conductivity data and fitted curves for soil samples identified with the abbreviated name of soil texture and the UNSODA ID. Data for $h = 0$ are shown at $h = 1$ cm.

Table 3. Coefficient of determination (R^2) of θ and log K for the models fitted in this study. The best fit (largest R^2) values for a particular soil sample are shown in bold. Total best-fit numbers are shown in the bottom row. Soil samples are identified with their abbreviated soil texture name and the UNSODA ID.

Sample	VG, MVG		DBC		DVC, MDVC		KBC, MKBC		PE, MPE	
	θ	log K	θ	log K	θ	log K	θ	log K	θ	log K
C2360	**0.9958**	0.8330	0.9887	**0.9931**	0.9958	0.9823	0.9936	0.9710	0.9607	0.9845
C2362	**0.9968**	0.9650	0.9727	0.8087	0.9968	0.9689	0.9967	0.9897	0.9965	**0.9968**
CL3033	0.9968	-2.030	0.9918	0.9416	0.9968	0.9536	**0.9983**	**0.9639**	0.9976	0.8168
L4592	**0.9999**	0.6115	0.9988	0.9783	0.9997	**0.9831**	0.9988	0.9783	0.9955	0.9767
L4770	0.9868	0.9867	**0.9989**	0.9771	0.9954	0.9899	0.9984	0.9893	0.9964	**0.9902**
L4780	0.9943	0.9042	0.9907	0.9852	**0.9978**	**0.9949**	0.9970	0.9945	0.9968	0.9917
LS3130	0.9955	0.9964	0.9900	**0.9935**	0.9986	0.9554	**0.9986**	0.9564	0.9956	0.9711
LS3152	0.9971	**0.9961**	**0.9998**	0.9817	0.9991	0.9748	0.9992	0.9789	0.9967	0.9041
S3142	0.9946	0.9620	0.9973	**0.9998**	**0.9981**	0.9966	0.9980	0.9968	0.9936	0.8869
S3163	0.9942	0.9863	0.9875	**0.9958**	**0.9948**	0.9813	0.9942	0.9765	0.9938	0.9700
S3182	0.9928	0.4823	0.9972	**0.9969**	**0.9979**	0.9889	0.9977	0.9912	0.9953	0.9033
S4263	0.9683	0.9925	0.9539	0.9656	0.9683	0.9889	**0.9703**	**0.9927**	0.9699	0.9776
S4660	0.9890	0.9191	0.9747	0.9877	0.9813	**0.9959**	**0.9936**	0.9956	0.9926	0.9760
S4661	0.9966	0.9322	0.9842	0.9858	0.9949	0.9943	**0.9981**	**0.9944**	0.9979	0.9728
SiC3120	0.9842	-0.078	0.9703	0.9806	0.9842	**0.9869**	0.9842	0.9833	**0.9883**	0.8924
SiL3370	0.9695	0.9029	0.9163	0.6737	0.9695	0.8927	**0.9882**	0.9917	0.9871	**0.9970**
SiL3390	**0.9920**	0.9923	0.9799	0.9716	0.9920	0.9949	0.9167	0.9977	0.9738	**0.9981**
SiL3392	0.9978	0.9145	0.9817	0.9196	0.9978	0.9852	**0.9993**	0.9928	0.9989	**0.9937**
SiL3393	0.9925	0.8679	0.9732	0.8229	0.9925	0.9650	0.9947	**0.9878**	**0.9955**	0.9746
SiL4673	0.9885	0.8143	0.9715	0.8059	0.9885	0.8948	**0.9914**	**0.9812**	0.9887	0.9443
Average	0.9911	0.6976	0.9810	0.9383	**0.9920**	0.9734	0.9903	**0.9852**	0.9905	0.9559
Total best	4	1	2	5	4	4	8	5	2	5

CONCLUSIONS

Multimodal water retention (WRF) and hydraulic conductivity (HCF) equations proposed by Seki et al. (2022) were shown to be effective with different types of soils. Our study confirms that the selected models are very flexible in terms of fitting observed WRF and HCF curves of various soils, especially when optimizing two parameters in the general conductivity equation, notably (p, q) or (p, r), in addition to K_s. Among the verified models, the KO_1BC_2-CH (KBC) model with $r = 1$ and the optimized (p, q) parameters performed best, with the dual-VG-CH (DVC) model with $q = 1$ also performing well and being compatible with the original Durner (1994) multimodal formulation. The latter model showed a good fitting performance when (p, r) were optimized simultaneously. We conclude that the proposed model formulations should be very useful for practical applications, while mathematically being relatively simple and consistent.

REFERENCES

Brooks, R.H., Corey, A.T., 1964. Hydraulic properties of porous media. Hydrology Papers 3. Colorado State University, Fort Collins, CO, USA.

Burdine, N.T., 1953. Relative permeability calculations from pore-size distribution data. Petroleum Transactions of the American Institute of Mining and Metallurgical Engineers, 198, 71–77.

Dimitrov, M., Vanderborght, J., Kostov, K.G., Jadoon, K.Z., Weihermüller, L., Jackson, T.J., Bindlish, R., Pachepsky, Y., Schwank, M., Vereecken, H., 2014. Soil hydraulic parameters and surface soil moisture of a tilled bare soil plot inversely derived from L-band brightness temperatures. Vadose Zone Journal, 13, 1, 1–18.

Durner, W., 1994. Hydraulic conductivity estimation for soils with heterogeneous pore structure. Water Resources Research, 30, 2, 211–223.

Hoffmann-Riem, H., van Genuchten, M. Th., Flühler, H., 1999. A general model of the hydraulic conductivity of unsaturated soils. In: van Genuchten et al. (Eds.): Proceedings of the international workshop Characterization and measurement of the hydraulic properties of unsaturated porous media. Riverside, CA. 22-24 Oct. 1997. University of California, Riverside.

Kosugi, K., 1996. Lognormal distribution model for unsaturated soil hydraulic properties. Water Resources Research, 32, 2697–2703.

Kosugi, K., 1999. General model for unsaturated hydraulic conductivity for soils with lognormal pore-size distribution. Soil Science Society of America Journal, 63, 270–277.

Lipovetsky, T., Zhuang, L., Teixeira, W.G., Boyd, A., Pontedeiro, E.M., Moriconi, L., Alves, J.L.D., Couto, P., van Genuchten, M.Th., 2020. HYPROP measurements of the unsaturated hydraulic properties of a carbonate rock sample. Journal of Hydrology, 591, 125706.

Luo, Z., Kong, J., Yao, L., Luo, Y., 2022. Assessment and application of an alternative formula to describe the hydraulic conductivity over the full moisture range. Hydrological Processes, 36, 7, e14639.

Mualem, Y., 1976. A new model for predicting the hydraulic conductivity of unsaturated porous media. Water Resources Research, 12, 513–522.

Nemes, A., Schaap, M. G., Leij, F. J., 1999. The UNSODA unsaturated soil hydraulic database Version 2.0. US Salinity Laboratory, Riverside, CA, USA.

Peters, A., 2013. Simple consistent models for water retention and hydraulic conductivity in the complete moisture range. Water Resources Research, 49, 10, 6765–6780.

Priesack, E., Durner, W., 2006. Closed-form expression for the multi-modal unsaturated conductivity function. Vadose Zone Journal, 5, 1, 121–124.

Schelle, H., Iden, S.C., Peters, A., Durner, W., 2010. Analysis of the agreement of soil hydraulic properties obtained from multistep-outflow and evaporation methods. Vadose Zone Journal, 9, 4, 1080–1091.

Seki, K., 2007. SWRC fit – a nonlinear fitting program with a water retention curve for soils having unimodal and bimodal pore structure. Hydrology and Earth System Sciences Discussion, 4, 407–437.

Seki, K., Toride, N., van Genuchten, M.Th., 2022. Closed-form hydraulic conductivity equations for multimodal unsaturated soil hydraulic properties. Vadose Zone Journal, 21, 1, e20168.

van Genuchten, M. Th., 1980. A closed-form equation for predicting the hydraulic conductivity of unsaturated soils. Soil Science Society of America Journal, 44, 892–898.

Vogel, T., van Genuchten, M.Th., Cislerova, M., 2000. Effect of the shape of the soil hydraulic functions near saturation on variably-saturated flow predictions, Advances in Water Resources, 24, 2, 133–144.

Watanabe, K., Osada, Y., 2016. Comparison of hydraulic conductivity in frozen saturated and unfrozen unsaturated soils. Vadose Zone Journal, 15, 5, 1–7.

ABBREVIATIONS

BC	Brooks and Corey
C	Clay
CH	Common head
CL	Clay loam
DB	dual-BC
DBC	dual-BC-CH
DV	dual-VG
DVC	dual-VG-CH
HCF	Hydraulic conductivity function
KB	KO_1BC_2
KBC	KO_1BC_2-CH
KO	Kosugi
L	Loam
LS	Loamy sand
MDVC	Modified dual-VG-CH
MKBC	Modified KO_1BC_2-CH
MPE	Modified Peters
MSE	Mean squared error
MVG	Modified van Genuchten
PE	Peters
RMSE	Root mean squared error
S	Sand
SiC	Silty clay
SiL	Silty loam
UNSODA	Unsaturated soil hydraulic database
VG	van Genuchten
WRF	Water retention function

Received 7 August 2022
Accepted 6 December 2022

APPENDIX. Optimized parameters of the examples shown in Fig. 6.

Clay soil C 2360

Model	θ_s	θ_r	w	H (cm)	N_1[a)]	N_2[a)]	K_s (cm/s)	p	qr or a	ω
MVG	0.493	0.000		47.9	1.07		8.99.E-4	–0.18	2[b)]	
MKBC	0.496	0[b)]	0.438	139.8	2.95	0.000	7.93.E–5	6.00	1.00	
DBC	0.492	0[b)]	0.788	25.3	0.079	0.011	3.19.E–5	6.00	1.00	
MDVC	0.493	0[b)]	0.772	47.9	1.07	1.07	5.53.E–5	6.00	1.00	
MPE	0.480	0[b)]	0.555	6379.8	3.00		3.22.E–4	5.79	–3.25	1.22.E–5

Clay soil C 2362

Model	θ_s	θ_r	w	H (cm)	N_1[a)]	N_2[a)]	K_s (cm/s)	p	qr or a	ω
VG	0.554	0.000		1215.8	1.11		2.69.E–5	0.00	2 [b)]	
MKBC	0.554	0[b)]	0.397	8000.0	2.00	0.0148	5.38.E–6	0.42	1.52	
DBC	0.557	0[b)]	0.747	383.1	0.093	0.026	3.08.E–6	8.74	1.40	
DVC	0.554	0[b)]	0.773	1215.8	1.11	1.11	9.13.E–6	5.36	1.41	
MPE	0.555	0[b)]	0.510	14999.8	2.30		6.57.E–6	1.00	–1.50	3.76.E–4

Clay loam soil CL 3033

Model	θ_s	θ_r	w	H (cm)	N_1[a)]	N_2[a)]	K_s (cm/s)	p	qr or a	ω
VG	0.569	0.272		41.6	1.77		1.88.E–3	–0.70	2 [b)]	
KBC	0.569	0[b)]	0.313	49.9	1.01	0.0944	2.29.E–5	1.00	0.50	
DBC	0.571	0[b)]	0.719	17.4	0.29	0.000	2.07.E–5	1.00	0.50	
MDVC	0.568	0[b)]	0.384	43.2	2.02	1.06	2.63.E–5	2.02	0.50	
PE	0.570	0[b)]	0.350	53.5	0.959		5.69.E–5	9.57	–1.47	2.77.E–1

Loam soil L 4592

Model	θ_s	θ_r	w	H (cm)	N_1[a)]	N_2[a)]	K_s (cm/s)	p	qr or a	ω
VG	0.444	0.092		46.4	1.18		2.39.E–4	–0.01	2 [b)]	
MKBC	0.408	0[b)]	0.000	56.2	2.50	0.111	4.83.E–7	0.93	1.13	
DBC	0.408	0[b)]	0.500	56.2	0.111	0.111	4.83.E–7	0.93	1.13	
MDVC	0.444	0[b)]	0.794	46.4	1.18	1.00	2.55.E–6	2.01	1.00	
PE	0.421	0[b)]	0.140	88.9	0.865		2.17.E–6	6.15	–1.46	1.38.E–1

Loam soil L 4770

Model	θ_s	θ_r	w	H (cm)	N_1[a)]	N_2[a)]	K_s (cm/s)	p	qr or a	ω
VG	0.778	0.561		32.8	1.98		2.41.E–3	0.25	2 [b)]	
KBC	0.770	0[b)]	0.100	29.0	0.322	0.0713	2.41.E–3	9.32	2.47	
DBC	0.769	0[b)]	0.090	21.9	2.22	0.0679	2.41.E–3	9.25	2.42	
MDVC	0.780	0[b)]	0.098	33.9	5.42	1.08	3.69.E–3	3.93	2.46	
PE	0.770	0[b)]	0.111	29.9	0.310		2.41.E–3	8.64	–3.22	5.33.E–2

Loam soil L 4780

Model	θ_s	θ_r	w	H (cm)	N_1[a)]	N_2[a)]	K_s (cm/s)	p	qr or a	ω
VG	0.834	0.511		32.6	2.75		1.78.E–3	–0.47	2[b)]	
KBC	0.827	0[b)]	0.264	32.9	0.462	0.0749	1.78.E–3	9.43	1.55	
DBC	0.825	0[b)]	0.428	19.0	0.789	0.000	1.78.E–3	10.00	1.36	
MDVC	0.835	0[b)]	0.256	33.3	4.27	1.08	2.22.E–3	4.00	2.00	
PE	0.826	0[b)]	0.276	33.8	0.446		1.78.E–3	1.00	–1.52	1.11.E–3

Loamy sand soil LS 3130

Model	θ_s	θ_r	w	H (cm)	N_1[a)]	N_2[a)]	K_s (cm/s)	p	qr or a	ω
VG	0.495	0.122		38.8	2.64		4.88.E–4	0.01	2[b)]	
KBC	0.484	0[b)]	0.509	40.5	0.494	0.250	1.50.E–2	6.01	2.01	
DBC	0.481	0[b)]	0.840	19.8	0.680	0.000	2.24.E–2	8.14	1.39	
DVC	0.493	0[b)]	0.515	40.3	3.85	1.25	4.19.E–2	5.42	1.84	
PE	0.490	0[b)]	0.684	48.1	0.656		4.08.E–3	2.35	–3.11	3.91.E–4

Loamy sand soil LS 3152

Model	θ_s	θ_r	w	H (cm)	N_1[a)]	N_2[a)]	K_s (cm/s)	p	qr or a	ω
VG	0.418	0.094		32.5	2.28		1.81.E–3	–0.02	2[b)]	
KBC	0.385	0[b)]	0.469	39.0	0.557	0.264	2.35.E–2	5.66	1.87	
DBC	0.350	0[b)]	0.534	32.1	1.46	0.176	5.77.E–3	5.75	1.80	
DVC	0.384	0[b)]	0.476	41.0	3.62	1.26	4.23.E–2	5.58	1.60	
PE	0.450	0[b)]	0.722	38.8	0.914		6.36.E–4	9.10	–2.88	3.46.E–2

Sand soil S 3142

Model	θ_s	θ_r	w	H (cm)	N_1[a)]	N_2[a)]	K_s (cm/s)	p	qr or a	ω
VG	0.378	0.075		32.2	2.70		6.13.E–4	–0.03	2[b)]	
KBC	0.365	0[b)]	0.537	33.8	0.430	0.303	2.98.E–2	5.86	1.94	
DBC	0.362	0[b)]	0.841	19.2	0.900	0.000	5.41.E–3	6.03	1.03	
DVC	0.374	0[b)]	0.556	33.8	4.09	1.29	3.56.E–2	2.90	2.28	
PE	0.374	0[b)]	0.742	40.1	0.658		4.60.E–5	8.87	–2.96	1.19.E–1

Sand soil S 3163

Model	θ_s	θ_r	w	H (cm)	N_1[a)]	N_2[a)]	K_s (cm/s)	p	qr or a	ω
VG	0.409	0.081		57.0	3.58		3.47.E–4	–0.02	2[b)]	
KBC	0.405	0[b)]	0.695	60.7	0.446	0.195	3.78.E–3	4.00	2.00	
DBC	0.399	0[b)]	0.845	37.5	1.23	0.000	4.20.E–3	6.01	1.01	
DVC	0.409	0[b)]	0.697	57.0	4.12	1.19	3.41.E–3	2.03	2.01	
PE	0.407	0[b)]	0.761	63.7	0.487		1.14.E–3	1.00	–1.50	6.43.E–5

Sand soil S 3182

Model	θ_s	θ_r	w	H (cm)	N_1[a)]	N_2[a)]	K_s (cm/s)	p	qr or a	ω
VG	0.388	0.103		38.5	4.01		6.27.E–5	–0.70	2[b)]	
KBC	0.381	0[b)]	0.601	39.5	0.327	0.181	3.87.E–3	5.79	1.84	
DBC	0.377	0[b)]	0.707	28.0	1.85	0.0546	1.10.E–3	5.95	0.98	
DVC	0.388	0[b)]	0.602	38.7	5.35	1.18	1.22.E–3	2.00	2.00	
PE	0.383	0[b)]	0.677	41.5	0.388		1.01.E–5	8.29	–2.57	4.97.E–2

Sand soil S 4263

Model	θ_s	θ_r	w	H (cm)	N_1[a)]	N_2[a)]	K_s (cm/s)	p	qr or a	ω
VG	0.319	0.060		42.6	2.78		1.04.E–3	–0.01	2[b)]	
KBC	0.320	0[b)]	0.784	52.5	0.674	0.000	1.09.E–3	1.29	1.91	
DBC	0.323	0[b)]	0.500	21.1	0.618	0.618	2.02.E–3	4.89	0.73	
MDVC	0.319	0[b)]	0.813	42.6	2.78	1.00	1.13.E–3	1.13	1.67	
PE	0.320	0[b)]	0.760	51.1	0.664		1.44.E–3	0.30	–2.64	8.60.E–4

Sand soil S 4660

Model	θ_s	θ_r	w	H (cm)	N_1[a)]	N_2[a)]	K_s (cm/s)	p	qr or a	ω
VG	0.436	0.049		6.8	1.49		1.45.E–2	–0.70	2[b)]	
KBC	0.450	0[b)]	0.656	14.2	1.67	0.148	1.45.E–2	4.68	0.64	
DBC	0.438	0[b)]	0.500	2.5	0.266	0.266	9.64.E–3	5.86	0.36	
MDVC	0.436	0[b)]	0.888	6.8	1.49	1.00	6.88.E–3	5.20	0.61	
PE	0.451	0[b)]	0.749	17.1	1.68		1.44.E–2	9.02	–2.41	2.86.E–2

Sand soil S 4661

Model	θ_s	θ_r	w	H (cm)	N_1[a)]	N_2[a)]	K_s (cm/s)	p	qr or a	ω
VG	0.408	0.037		9.9	1.82		2.64.E–2	–0.70	2[b)]	
KBC	0.416	0[b)]	0.798	16.6	1.21	0.132	2.64.E–2	3.14	0.97	
DBC	0.402	0[b)]	0.950	4.6	0.484	0.00	1.79.E–2	5.53	0.10	
MDVC	0.408	0[b)]	0.909	9.9	1.82	1.00	1.75.E–2	4.56	0.60	
PE	0.415	0[b)]	0.837	17.6	1.23		2.39.E–2	0.97	–1.68	2.70.E–4

Silty clay soil SiC 3120

Model	θ_s	θ_r	w	H (cm)	N_1[a)]	N_2[a)]	K_s (cm/s)	p	qr or a	ω
VG	0.641	0.000		42.1	1.23		9.75.E–5	–0.70	2[b)]	
MKBC	0.673	0[b)]	1.000	857.2	3.30	205	8.83.E–5	6.00	0.50	
DBC	0.638	0[b)]	0.500	20.4	0.191	0.191	9.75.E–5	1.51	1.38	
DVC	0.641	0[b)]	0.787	42.1	1.23	1.23	9.72.E–5	6.76	0.38	
MPE	0.660	0[b)]	0.816	459	2.78		5.67.E–5	9.95	–2.25	5.44.E–4

Silty loam soil SiL 3370

Model	θ_s	θ_r	w	H (cm)	N_1[a)]	N_2[a)]	K_s (cm/s)	p	qr or a	ω
VG	0.310	0.000		453	1.24		1.37.E–5	–0.70	2[b)]	
MKBC	0.328	0[b)]	0.961	6745.3	3.19	19200	1.41.E–5	0.71	1.34	
DBC	0.319	0[b)]	0.500	86.9	0.138	0.138	1.37.E–5	3.73	1.46	
DVC	0.310	0[b)]	0.780	453.0	1.24	1.24	1.37.E–5	0.30	1.82	
MPE	0.326	0[b)]	0.667	2000.0	2.53		1.71.E–5	1.51	–1.88	4.25.E–4

Silty loam soil SiL 3390

Model	θ_s	θ_r	w	H (cm)	N_1[a)]	N_2[a)]	K_s (cm/s)	p	qr or a	ω
VG	0.415	0.000		33.9	1.19		1.02.E–3	–0.02	2[b)]	
MKBC	0.464	0[b)]	0.957	657.4	3.83	1.19	8.02.E–4	2.13	1.73	
DBC	0.400	0[b)]	0.500	20.5	0.153	0.153	6.52.E–5	0.56	2.03	
DVC	0.415	0[b)]	0.786	33.9	1.19	1.19	4.28.E–4	0.85	1.68	
MPE	0.445	0[b)]	0.783	340.3	3.00		6.02.E–4	1.00	–1.50	5.43.E–7

Silty loam soil SiL 3392

Model	θ_s	θ_r	w	H (cm)	N_1[a)]	N_2[a)]	K_s (cm/s)	p	qr or a	ω
VG	0.376	0.000		148.2	1.16		6.24.E–5	0.00	2[b)]	
MKBC	0.385	0[b)]	0.558	992.0	2.44	0.0449	9.52.E–6	0.31	1.40	
DBC	0.370	0[b)]	0.487	75.1	0.122	0.128	3.53.E–6	4.39	1.33	
DVC	0.376	0[b)]	0.800	148.2	1.16	1.16	4.50.E–6	4.07	1.00	
MPE	0.390	0[b)]	0.298	225.6	2.31		3.85.E–5	1.00	–1.50	4.68.E–4

Silty loam soil SiL 3393

Model	θ_s	θ_r	w	H (cm)	N_1[a)]	N_2[a)]	K_s (cm/s)	p	qr or a	ω
VG	0.355	0.000		188.4	1.12		6.42.E–5	0.00	2[b)]	
MKBC	0.371	0[b)]	0.771	9021.0	3.88	0.259	6.61.E–6	6.00	1.00	
DBC	0.355	0[b)]	0.502	71.5	0.091	0.091	4.22.E–6	0.70	1.78	
DVC	0.355	0[b)]	0.772	188.4	1.12	1.12	5.09.E–6	4.82	1.07	
MPE	0.358	0[b)]	0.617	4905.0	3.00		1.96.E–5	0.72	–3.41	2.35.E–5

Silty loam soil SiL 4673

Model	θ_s	θ_r	w	H (cm)	N_1[a)]	N_2[a)]	K_s (cm/s)	p	qr or a	ω
VG	0.401	0.113		575.1	1.75		4.76.E–5	–0.04	2[b)]	
KBC	0.407	0[b)]	0.354	547.3	1.56	0.224	5.65.E–5	0.45	1.72	
DBC	0.400	0[b)]	0.500	198.0	0.248	0.248	4.76.E–5	3.88	1.76	
MDVC	0.401	0[b)]	0.719	575.1	1.75	1.00	4.76.E–5	7.83	2.50	
PE	0.403	0[b)]	0.546	858.1	1.16		4.76.E–5	7.44	–1.34	9.17.E–4

Note: (a) $N_i = n$, λ_i, n_i or σ_i (b) Fixed parameter

J. Hydrol. Hydromech., 71, 2023, 1, 35–48
https://doi.org/10.2478/johh-2022-0040

sciendo Journal of Hydrology and Hydromechanics Institute of Hydrology SAS

Discharge coefficient, effective head and limit head in the Kindsvater-Shen formula for small discharges measured by thin-plate weirs with a triangular notch

Šimon Pospíšilík*, Zbyněk Zachoval

Brno University of Technology, Faculty of Civil Engineering, Institute of Water Structures, Veveří 331/95, Brno, 602 00, Czech Republic.
* Corresponding author. E-mail: pospisilik.s@fce.vutbr.cz

Abstract: The paper deals with the determination of the discharge coefficient, effective head and newly the limit head in the Kindsvater-Shen formula for the determination of a relatively small discharge of clear water using a thin-plate weir with a triangular notch. The determination of the discharge coefficient, effective head and limit head is based on extensive experimental research and is verified by previous measurements by other authors. The experimental research was characterised by a large range of notch angles (from 5.25° to 91.17°), weir heights (from 0.00 m to 0.20 m), and water temperatures (from 15 °C to 45 °C), as well as a focus on relatively small heads (from 0.02 m to 0.18 m), which is where the strengths of the Kindsvater-Shen formula stand out. The experimental research supplemented existing knowledge about the overflow occurring with small heads and small weir notch angles. The newly determined dependencies in the Kindsvater-Shen formula extended its applicability to weirs with small notch angles and newly enabled the determination of the limit head, which restricts its applicability in the determination of small discharges.

Keywords: Triangular notch (V-notch); Thin-plate weir; Kindsvater-Shen formula; Discharge coefficient; Effective head; Limit head.

INTRODUCTION

Thin-plate weirs (TPWs) used for the determination of water discharge are generally defined by the length of the weir crest in the direction of flow, ranging from 1 mm to 2 mm (ISO 1438, 2017). A triangular notch (also referred as V-notch) is a notch in the wall of a weir which widens in the upwards direction from the bottom of the approach channel. The widening of the notch is usually symmetrical with respect to the longitudinal plane of symmetry of the approach channel. The weir wall is a planar and hydraulically smooth surface with a rectangular upstream weir crest edge. The basic geometric characteristics of a weir located vertically and perpendicularly to the side walls and bottom of an approach channel with a rectangular cross-section comprise the notch angle, the weir height and the distance of the vertical weir axis from the side walls. The overflow is affected by water properties such as viscosity and surface tension. Their values depend mainly on the water temperature and dissolved substances. The overflow is also affected by impurities that adhere to the weir. An important condition for applicability is the requirement for a developed velocity profile in the approach channel.

CURRENT STATE OF KNOWLEDGE

The measurement of water discharge using a TPW with a triangular notch was first proposed by Thomson (1858) for a notch angle of 90°. Subsequently, Thomson (1861) also published the results of follow-up experiments with notch angles of 90° and 126.87°. Barr (1910) undertook the verification and extension of Thomson's (1858, 1861) experiments using other variants of approach channel width and weir height with notch angles of 90° and 54°. Following on from Barr (1910), Strickland (1910) derived a relation for determining the discharge coefficient through experiments. A method of automated water discharge measurement via a TPW with a triangular notch, which involved using a float with an automatic level recorder, was designed by Yarnall (1912). Cozzens (1915) investigated the use and calibration of a TPW with a triangular notch in situ. The effect of water temperature on the coefficient of discharge was investigated by Cozzens (1915) and Switzer (1915). Based on measurements taken, Switzer (1915) evaluated the effect of temperature on the coefficient of discharge as being negligible (up to 2 %) compared to other effects. King (1916) presented a new relationship for calculating the water discharge based on a comparison of his own experimental data with Thomson´s (1858, 1861) and Barr´s (1910) data. Cone (1916) investigated TPWs with rectangular, trapezoidal and triangular notches. Cone subsequently (1917) presented a practical guide for application of TPWs. Barrett (1924) extended the application range to include small heads (> 0.029 m). Mawson (1927) investigated the application of dimensional analysis in Barr´s experimental research (1910). The accuracy of discharge measurement was investigated by Yarnall (1927). O'Brien (1927) presented a mathematical proof that a TPW with a 90° triangular notch offers the highest accuracy compared to other notch angles. Schoder and Turner (1929) investigated the influence of the geometric characteristics of a weir crest on the overflow. Thornton (1929) compared the accuracy of Barr´s (1910) and Yarnall´s (1927) experiments. The effect of viscosity and surface tension on the overflow was investigated by Greve (1930; 1932; 1945) and Lenz (1942). Barrett (1931) and Allerton (1932) investigated the introduction of energy head in the calculation of water discharge. Based on Yarnall´s (1927) research, Smith (1934; 1935) investigated the effect of water temperature. Wirak (1934) published the results of experimental measurements performed on TPWs with a triangular notch. Numachi et al. (1937) investigated the means of attachment of a TPW edge with a triangular notch. Hertzler (1938) investigated the use of TPWs

with a 120° triangular notch in practical applications. Extensive research focusing on the effect of the approach channel width and the weir height for notch angle 90° was conducted by Numachi et al. (1940a; 1940b), Numachi and Hutizawa (1941a; 1941b; 1942a; 1942b). Viparelli (1947) determined the rules for the installation and use of triangular-notch TPWs to measure water discharge. Numachi and Saito (1948; 1951) and also Milburn and Burney (1988) investigated the minimum length of the approach channel and the use of boxes for the placement of TPWs. The measurement of oil discharge overflowing a TPW with a triangular notch was carried out by Itaya and Takenaka (1955). Based on the results of his own experiments and experiments performed by Grossi (1961), Schlag (1962) derived a new relationship for discharge. Shen (1981) summarized the findings of previous experiments on triangular-notch TPWs and he recommended to express the combined effects of surface tension and viscosity of water by defining the effective head and the effective discharge coefficient. Eli (1986) described two methods for the determination of discharge based on measurements of the height and width of the water surface in a notch profile. The collection of water samples using a TPW with a triangular notch was described by Cuttle and Mason (1988). Procedures concerning the selection, installation and use of TPWs to measure discharge were published by Bos (1989). Ghodsian (2004) obtained a new relationship for the calculation of coefficient of discharge. Martínez et al. (2005), Piratheepan et al. (2007) and Ali et al. (2015) investigated composite TPWs with a triangular notch. Ji (2007) and Ramamurthy et al. (2013) experimentally investigated TPWs with several triangular notches. A comparison of TPWs with rectangular, trapezoidal and triangular notches, supplemented with measurement error determination, was performed by Martikno et al. (2013). Chanson and Wang (2012; 2013) investigated the calibration of TPWs with a triangular notch under unsteady flow. Bautista-Capetillo et al. (2013) investigated the use of slow-motion photography to determine the discharge coefficient. Caroline and Afshar (2014) published the effect of the bed slope of the approach channel on the overflow. A comparison of flow through TPWs with rectangular and triangular notches was carried out by Adeyemi et al. (2017). Reddy and Reddy (2017) presented the results of research concerning the effect of water density (clear and muddy) on the discharge coefficient. Hattab et al. (2019) investigated the use of gauging TPWs with a triangular notch in confined conditions (2019). Vatankhah and Khamisabadi (2019) investigated the shape of the triangular notch and notches with curved extensions. Experiments with a 2.67° notch angle were carried out by Pospíšilík (2020). Vicena (2020) determined the minimum overflow height depending on the triangular notch angle of a TPW. Pospíšilík (2021) investigated the identification and quantification of uncertainties in determining the coefficient of discharge. Pospíšilík (2022) analysed the extent to which overflow through TPWs with a triangular notch has been explored.

The above overview demonstrates that research in the field of TPWs with a triangular notch has been taking place intensively for a great many years, and that it is far from complete. Basic research associated with TPWs with a triangular notch has a direct impact on their applicability in practice. Triangular notch TPW are widely used for the determination of discharge, and this led to their inclusion in the ISO 1438 (2017) standard.

THEORY

The equations for determining the discharge Q overflowing a TPW with a triangular notch can be divided according to the method of derivation into analytically derived, semi-empirical and empirical. For analytical derivation the energy conservation equation or the momentum equation (submerged weirs) are used, for semi-empirical method dimensional analysis is used in addition to the above. According to the method of calculation, the equations can be divided into implicitly or explicitly expressed. As far as practical use is concerned, explicitly expressed relations where the discharge is calculated directly on the basis of measured quantities are more commonly employed.

The measured quantities at a free overflow are the notch angle α, the approach channel width B, the level of the approach channel bottom Z_b, the level of the weir crest Z_P, and the water surface level Z_h at an agreed distance upstream from the weir ($2h_{max}$ to $4h_{max}$, where h_{max} is the maximum head (ISO 1438, 2017)). From the values of the levels, the weir height is calculated $P = Z_P - Z_b$, as well as the head $h = Z_h - Z_P$.

Worldwide, the most widely used equation for the determination of water discharge using a TPW with a triangular notch is currently the Kindsvater-Shen (Shen, 1981)

$$Q_C = C_d \cdot \frac{8}{15} \cdot \tan\frac{\alpha}{2} \cdot (2 \cdot g)^{1/2} \cdot h_e^{5/2}, \tag{1}$$

which is explicitly expressed semi-empirical equation based on the energy conservation equation and the experimental measurements, where C_d is the discharge coefficient, g is acceleration due to gravity (9.80665 m·s^{-2}) and h_e is the effective head. Effective head

$$h_e = h + k_h \tag{2}$$

expresses, using the height

$$k_h = f_1\{\alpha\} \tag{3}$$

the combined effect of the viscosity and surface tension of clear water. It is assumed that the effect of the change in water temperature T in the range of 5 °C to 30 °C (Bos, 1989) (causing the change in density, viscosity and surface tension of water) is negligible. The applicability of the calculation method for precise flow discharge measurement is limited by Shen (1981) to a minimum head of h_s = 0.06 m, a minimum notch angle of 20° and a maximum notch angle of 100°, at which, according to Shen (1981), instabilities of the nappe begin to appear, or there is a lack of measured data. Due to the inconsistencies in the measured data, the calculation method is also limited to a minimum weir height of 0.09 m.

Based on the evaluation of data from the measurements of the above-mentioned authors as well as our own data it was found that the lower limit h and α of the applicability of the Kindsvater-Shen method of calculation is not so much due to the instability of the nappe, but primarily to the change in the dependence of C_d on h. For this reason, the calculation method newly incorporates limit head h_l, which defines the lower limit of the application area of the modified calculation method. Thus, for values $h \geq h_l$, where

$$h_l = f_2\{\alpha\}, \tag{4}$$

it is possible to use the Kindsvater-Shen calculation method, otherwise not.

The coefficient C_d is a function of only three variables when function (3) is valid (Shen, 1981) and when the limiting condition $h \geq h_l$ stated above is fulfilled

$$C_d = f_3\left\{\frac{h}{P}, \frac{P}{B}, \alpha\right\}. \tag{5}$$

Assuming a sufficiently large value of B (or small P/B ratio), independence from P (or h/P) can be expected, which in the new defined range $h \geq h_l$ leads to the simplification of the functional dependence (5) on

$$C_d = f_4\{\alpha\}. \quad (6)$$

It is possible to determine the functional dependencies (3), (4) and (5) (or (6)) on the basis of experimental measurements. Although a considerable number of measurements have been made, there is still a lack of data in the region of small values of h and α (Pospíšilík, 2022; Shen, 1981), so extensive experimental research has been carried out in Brno University of Technology (BUT).

EXPERIMENT

A short rectangular flume (box) with a length 1.23 m, width B = 0.50 m and height 0.43 m (Fig. 1) was used. The flume was made of waterproof plywood with a smooth finish. At the end of the flume, there was a frame structure to which the investigated TPWs with a triangular notch (angles α = 5.25°; 10.18°; 15.19°; 20.23°; 25.21°; 30.53°; 60.67° and 91.17°) were inserted. The value α was determined by the two-cylinder method (ISO 1438, 2017; Pospíšilík, 2020). The frame structure prevented the deflection of the weir plate, allowed the centring of the weir in the flume and enabled vertical changes to be made to the position of the weir plate. By vertically changing the position of the weir plate, the selected value P was set at five height levels (Table 1). The TPWs were made from 1 mm thick stainless-steel sheeting, the notch edges were right-angled. In the flume, at a distance of 0.82 m from the weir, a flow straightener was placed to ensure the uniform distribution of longitudinal velocities along the cross-section profile of the flume (Fig. 2, white plates). The flow straightener consisted of two pairs of perforated plates with circular holes of 38 mm diameters spaced 20 mm apart. The distance between each pair of plates was 0.20 m. The paired arrangement of the plates enabled the size of the openings in the regulating element to be changed via the vertical displacement of one plate of the respective pair. In order to limit the formation of waves on the water surface, a floating plate made of expanded polystyrene with a width 0.49 m, length 0.25 m and thickness 0.015 m was placed downstream of the regulating element. The mentioned elements ensured the even distribution of longitudinal velocities in the cross-section profile with the measurement of the water surface level, which was confirmed by measuring the field of longitudinal velocities (Pospíšilík et al., 2022). The flume was connected to a hydraulic system with water recirculation. The water was supplied by a hose to the damping part of the flume and flow freely over the TPW into a storage tank. The discharge was provided by two pumps; it was possible to define the frequency of revolutions of the pump to set the desired value of Q. To quantify the effect of a change in water temperature T, which causes a change in viscosity and surface tension, a pair of 2 × 1000 W heaters was placed in the storage tank.

The value of Q was determined using the volume method ($Q \leq 0.00003$ m^3·s^{-1}, expanded combined uncertainty up to 0.52 %, graduated cylinders of class A), the mass method ($Q \leq 0.00050$ m^3·s^{-1}, expanded combined uncertainty up to 0.42 %, calibrated scales), and also calibrated electromagnetic flowmeters (expanded combined uncertainty 2 %) with the diameters DN10 (0.000016 m^3·s^{-1} ≤ Q ≤ 0.00050 m^3·s^{-1}) and DN32 (0.00033 m^3·s^{-1} ≤ Q ≤ 0.0034 m^3·s^{-1}). The time for determining the discharge was at least 180 s. Measurement of the Z_b, the upper surfaces of the inserted cylinders and the Z_h was carried out using a digital point gauge with a resolution of 0.01 mm placed on a cross beam in the longitudinal plane of symmetry of the flume. The Z_h for the determination of h was measured at a distance of 0.38 m upstream from the weir plate ($2h_{max}$). The B was measured using a calibrated metal tape gauge with a resolution of 1 mm. The T was measured with a digital thermometer with a resolution of 0.1 °C.

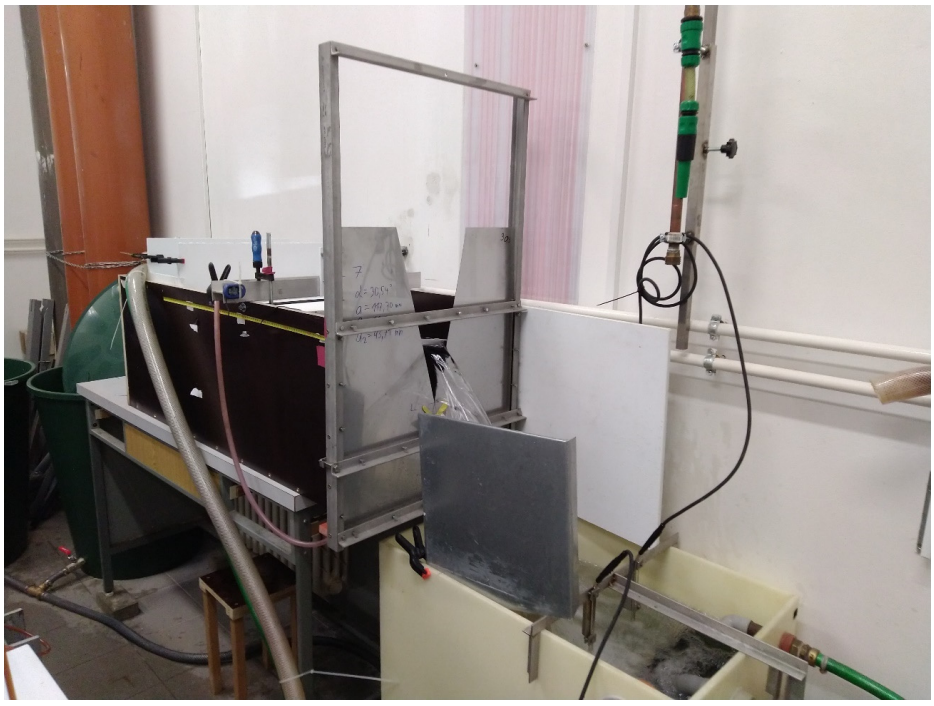

Fig. 1. Experimental equipment.

Table 1. Ranges of the measured quantities.

α [°]	P [mm]	h [mm]	T [°C]	$Q \times 10^{-3}$ [m^3·s^{-1}]
05.25	0.53; 49.51; 100.65; 100.71; 150.65; 198.85	51.07–181.31	15.1–19.5	0.0425–1.0089
	1.98; 50.81; 99.18; 100.65; 150.05; 198.75	29.32–180.46	38.4–42.5	0.0090–1.0128
10.18	0.86; 50.38; 98.60; 99.97; 151.06; 200.34	44.46–180.68	16.0–18.3	0.0589–1.8917
	0.68; 50.05; 98.60; 99.15; 151.94; 199.30	30.13–180.79	38.8–43.4	0.0209–1.9011
15.19	0.10; 50.51; 98.61; 100.54; 149.38; 200.33	48.59–181.12	16.0–18.5	0.1087–2.7722
	1.78; 50.85; 98.61; 100.30; 148.79; 196.96	30.45–181.38	39.0–45.0	0.0327–2.7722
20.23	0.46; 50.16; 98.61, 100.26; 150.86; 201.12	46.84–180.76	15.8–19.2	0.1320–3.6116
	1.76; 50.00; 98.61; 98.70; 150.00; 197.70	29.81–180.52	39.1–45.3	0.0408–3.6461
25.21	0.89; 50.60; 96.58; 101.46; 150.49; 200.87	45.39–167.53	14.7–19.5	0.1517–3.6588
	0.52; 51.16; 96.58; 100.44; 149.22; 199.62	29.31–166.67	39.0–44.1	0.4888–3.6950
30.53	0.57; 50.90; 98.83; 99.85; 149.35; 200.60	45.66–155.27	16.2–19.7	0.1857–3.6627
	0.85; 51.17; 98.83; 101.42; 151.47; 200.58	19.81–154.56	36.2–42.3	0.0233–3.6661
60.67	0.23; 49.58; 97.59; 99.75; 150.10; 199.93	40.41–115.48	14.5–19.5	0.2677–3.6577
	1.32; 51.10; 97.59; 101.97; 152.32; 201.36	20.24–114.72	39.0–43.4	0.0472–3.6816
91.17	0.46; 50.23; 99.43; 102.70; 149.80; 199.82	39.33–93.26	15.9–18.1	0.4188–3.6522
	0.31; 50.34; 100.87; 102.70; 150.65; 199.07	20.19–93.47	39.1–44.0	0.0744–3.6994

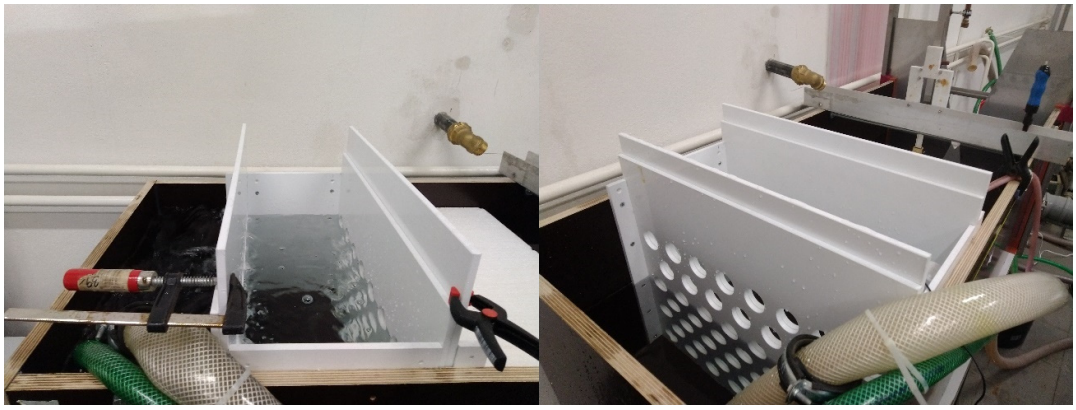

Fig. 2. Flow straightener.

The measurement of all the above quantities was always carried out under a steady state of flow. The range of Z_h measurements was limited by the maximum head $h_{max} = 0.18$ m and the head when the nappe adheres to the downstream face of weir plate (which depends on the α value). To verify the effect of the T on the Q, measurements were made in two ranges of T values. The first range was from 15 °C to 20 °C, while the second was from 36 °C to 45 °C. The range of the measured data is shown in Table 1. A detailed description of the experimental equipment, gauges and measurements was published by Pospíšilík (2020). Uncertainties affecting C_d were identified and quantified (Pospíšilík, 2021) according to the Guide to the Expression of Uncertainty in Measurement (JCGM 100, 2008).

DATA PROCESSING METHOD AND ITS EVALUATION

The data processing method consisted in finding such values of C_d, k_h and h_l that C_d is constant for a relevant α in the range $h_l \le h \le h_{max}$. This was achieved in such a way that from $h = 0.015$ m the h was divided into intervals per $\Delta h = 0.010$ m (interval Δh_1 is from $h = 0.015$ m to $h = 0.025$ m, interval Δh_2 is from $h = 0.025$ m to $h = 0.035$ m, etc.). Separately for given α and for given interval the average value of the discharge coefficient $\bar{C}_d$ was calculated from all the measured values C_d in that interval (for given α in the interval Δh_1 are values $C_{d1,1}$, $C_{d1,2}$, etc. for which the average value $\bar{C}_{d1}$ was calculated; for interval Δh_2 are values $C_{d2,1}$, $C_{d2,2}$, etc. for which the average value $\bar{C}_{d2}$ was calculated; etc.). A linear function with zero direction was drawn through the values $\bar{C}_d$. The value h_l and simultaneously the value k_h were sought in order to achieve a constant $\bar{C}_d$ in the largest possible range of h (iterative process). The invariance of $\bar{C}_d$ on h was evaluated by an approximation line segment with a zero direction in the range $h_l \le h \le h_{max}$. The value h_l was determined by a deviation of ±1 % from the average of $\bar{C}_d$ values determined in the range $h_l \le h \le h_{max}$.

For a detailed illustration of the above-mentioned method and its evaluation, the dependencies of C_d, k_h and h_l on h are shown in the graphs. Fig. 3 shows the dependence of C_d on h for individual α. They are supplemented with values for $\bar{C}_d$, and the course of the linear approximation curve with a zero direction and a deviation of ±1 %. The values of the approximation curve correspond to the value C_d of approximation curve (7). The graphs in Fig. 3 are supplemented by the definition of value h_l determined by relation (9). A division in the dependence of C_d at h_l is evident. The dependence of C_d on h can be considered linear (invariant) for the area $h_l \le h \le h_{max}$. For the values $h < h_l$, the linear dependence does not apply, and the C_d values decrease.

6 types of regression functions were used for the determination of functional dependencies (3), (4) and (6). The appropriateness of the chosen regression function was assessed by comparing the values of the coefficients of determination R^2.

In order to demonstrate the invariance of k_h on h in the range $h_l \le h \le h_{max}$, the graphs in Fig. 4 show the dependence of k_h on h for individual values of α. They are supplemented with the course of the linear approximation curve with a zero direction

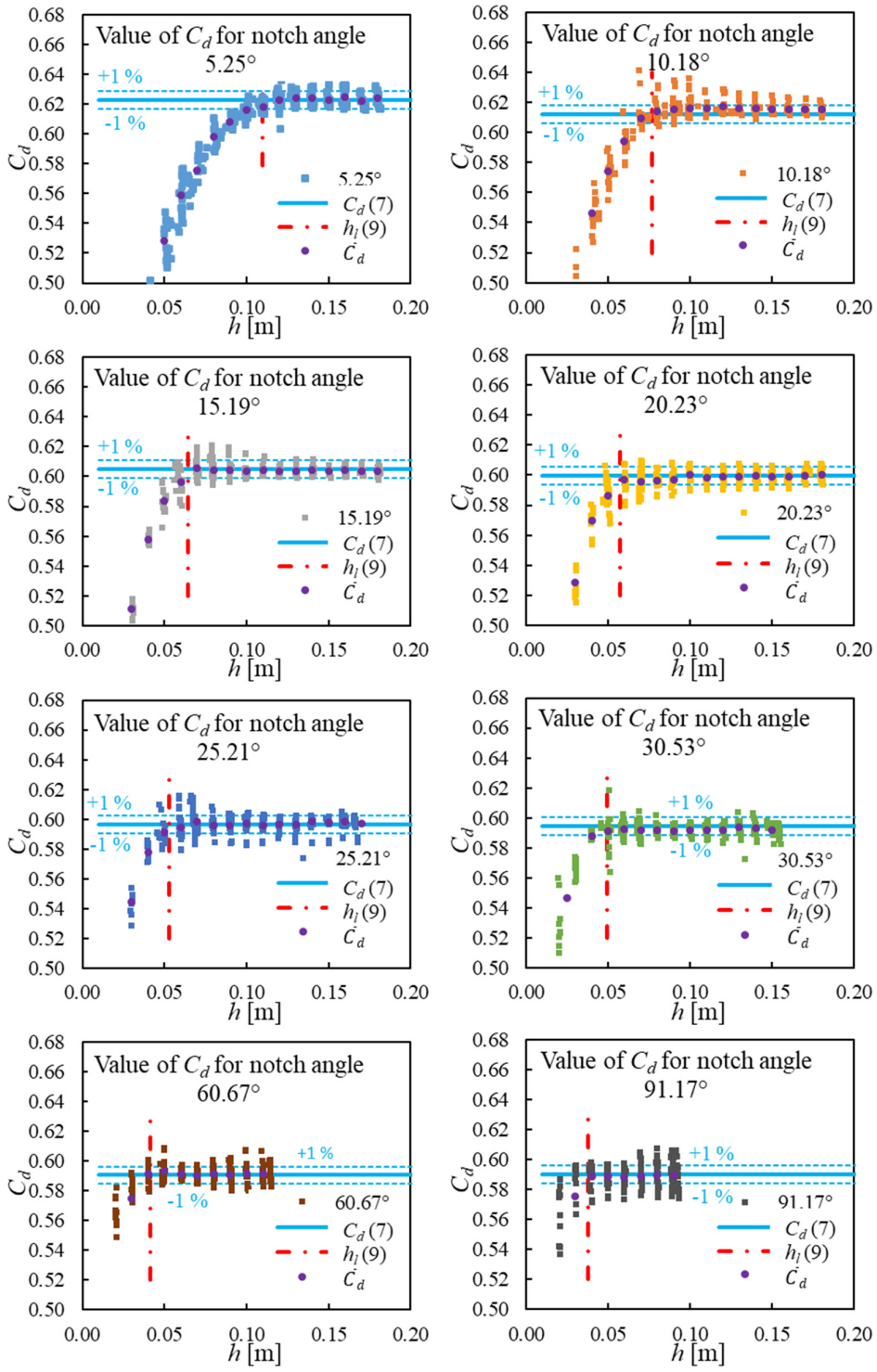

Fig. 3. Evaluation of the dependence of C_d on h for individual values of α; determination of h_l.

and a deviation of ±1 mm. The values of the linear approximation curve correspond to the value k_h of approximation curve (8). Also here, a division in the dependence of k_h is visible at the location of the h_l value. The dependence of k_h on h can be considered linear (invariant) for the area $h_l \le h \le h_{max}$. For values $h < h_l$, the linear dependence does not apply and the k_h values decrease. The values k_h in the range $h_l \le h \le h_{max}$ lie, with some exceptions, within the limits of a deviation of ±1 mm from the approximation curve. For a comprehensive verification of the correctness of the method used, a correlation matrix was created between C_d and the variables of function (5) in the range $h_l \le h \le h_{max}$. The correlation matrix shows a significant dependence only between C_d and α. The dependence of C_d on the ratios P/B and h/P is negligible.

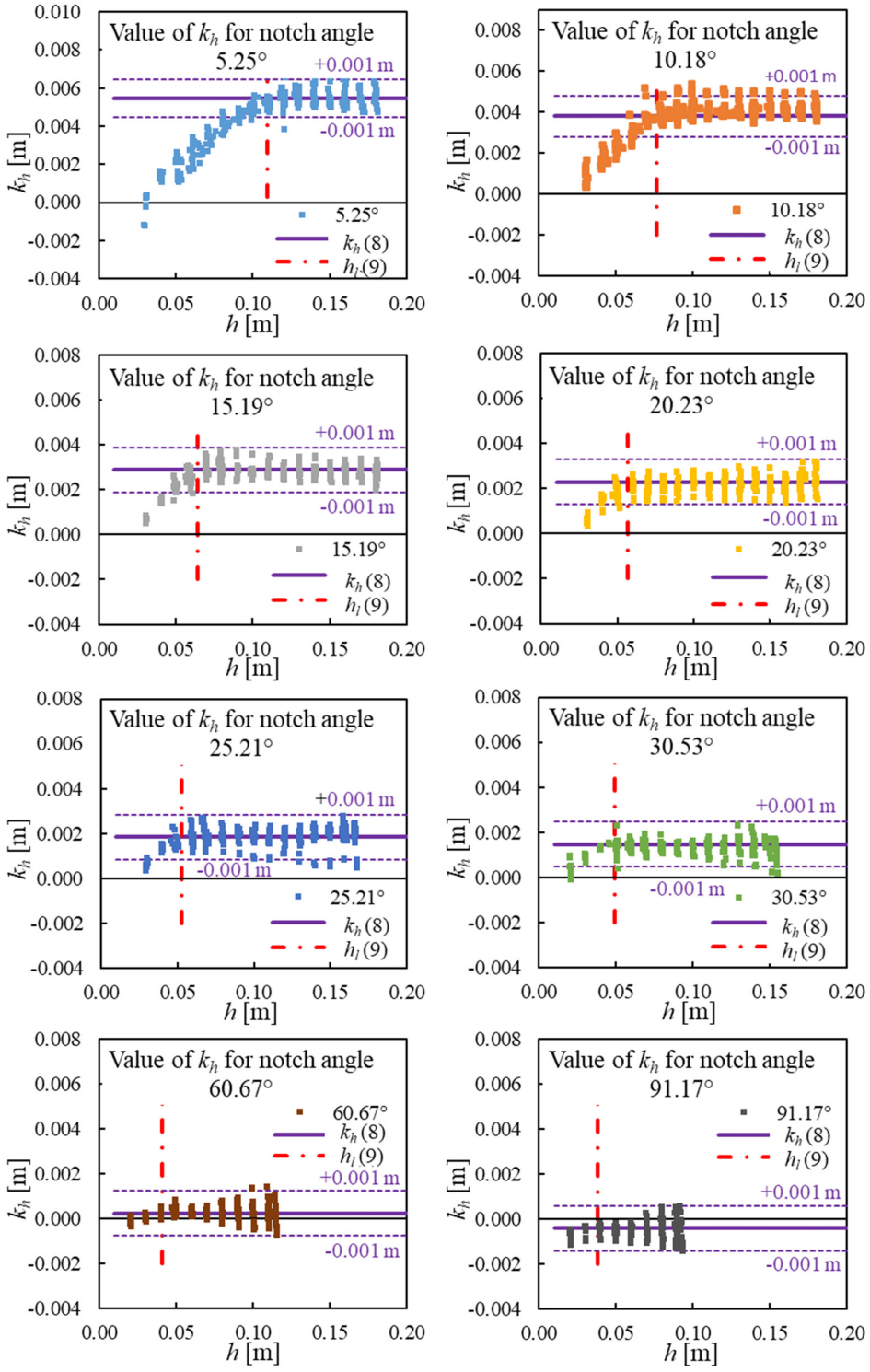

Fig. 4. Evaluation of the dependence of k_h on h.

RESULTS AND DISCUSSION

The main result is the quantification of functional dependencies (3), (4) and (6) by the above-mentioned method using the measured data in the range $h_l \leq h \leq h_{max}$. For $\alpha = 91.17°$, it is valid only for $P/B \leq 0.2$. The parameters in the equations were rounded to the minimum number of significant digits in such a way that the rounding has no effect on the calculated value with three significant digits.

The dependence of C_d on α (6) was described by an approximation curve

$$C_d = 0.05 \cdot \exp(-0.08 \cdot \alpha) + 0.59 \quad (7)$$

with $R^2 = 0.983$. The approximation curve, together with the values C_d determined from the measurements for the individual values α and k_h calculated according to Equation (8), is shown graphically in Fig. 5 and supplemented with a deviation of ±1 %.

For comparison, the dependence is supplemented with a Shen curve (1981). The area delimited by the ±1 % deviation of the approximation curve contains a significant part of the measured values C_d. Compared to the curve presented by Shen (1981), the approximation curve shows higher C_d values across the entire range of values and has a different shape of dependence.

The dependence of k_h on α (3) was described by an approximation curve

$$k_h = 0.0194 \cdot \alpha^{-0.186} - 0.0088 \quad (8)$$

with $R^2 = 0.997$. The dependence is shown together with the values determined from the measurements and a deviation of ±0.001 m in the graph in Fig. 6. The graph is supplemented by a curve presented by Shen (1981). The approximation curve describes the values k_h in the whole range of measured values α. Compared to the curve defined by Shen (1981), the approximation curve shows lower k_h values across the entire range of α.

The dependence of h_l on α (4) was described by an approximation curve

$$h_l = 0.3 \cdot \alpha^{-0.8} + 0.03 \quad (9)$$

with $R^2 = 0.945$. The approximation curve supplemented with the h_l values determined in the aforementioned way is shown in the graph in Fig. 7. Fig. 7 is supplemented with the boundary area of the measured data and the curve h_s stipulated by Shen (1981), who determined it mainly because of the instability of the nappe and the lack of measured data. It can be seen from the graph that the approximation curve of h_l aptly intersects the values determined by the above-mentioned method of evaluation. In the range of intersection of the values α determined by Shen (1981) and the measured values (10° to 90°), the approximation curve shows a different course of values h_l compared to the values h_s presented by Shen (1981). In the area of $h_l \leq h \leq h_{max}$, the instabilities of the nappe mentioned by Shen (1981) were not observed. The lower value of h_l in the area of 20° to 90° quite significantly expands the application area of the use of TPWs with a triangular notch for the determination of small values of Q. In the range of values α from 10° to 20°, on the other hand, the application range is reduced, and in the range of α from 5° to 10° it is newly determined.

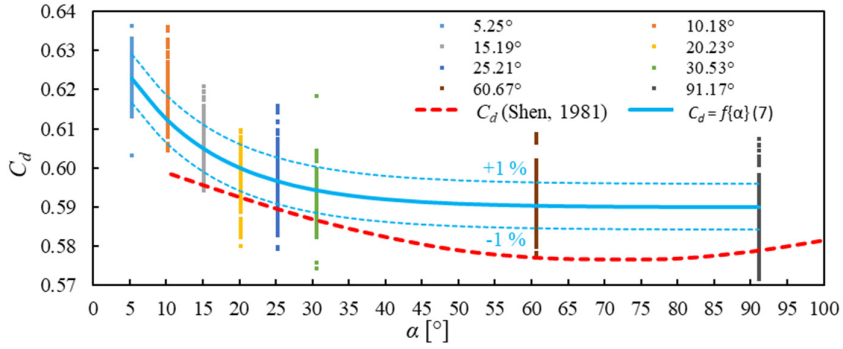

Fig. 5. Dependence of C_d on α.

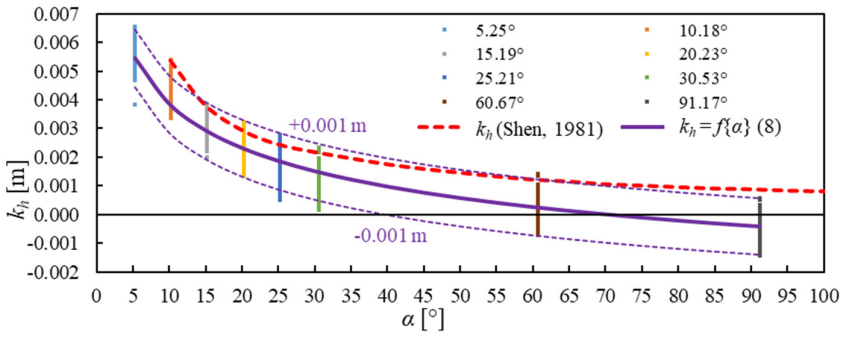

Fig. 6. Dependence of k_h on α.

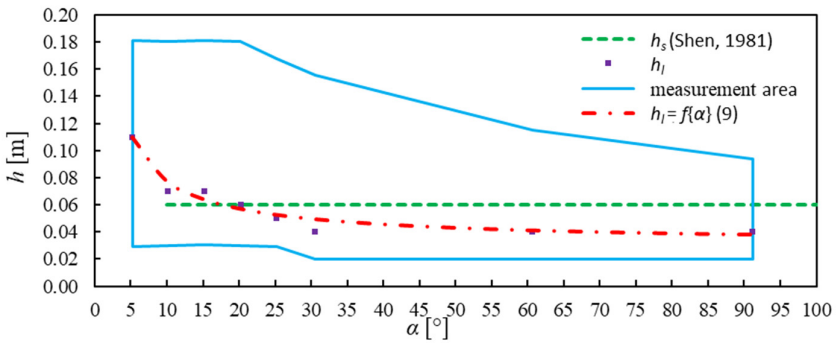

Fig. 7. Dependence of h on α.

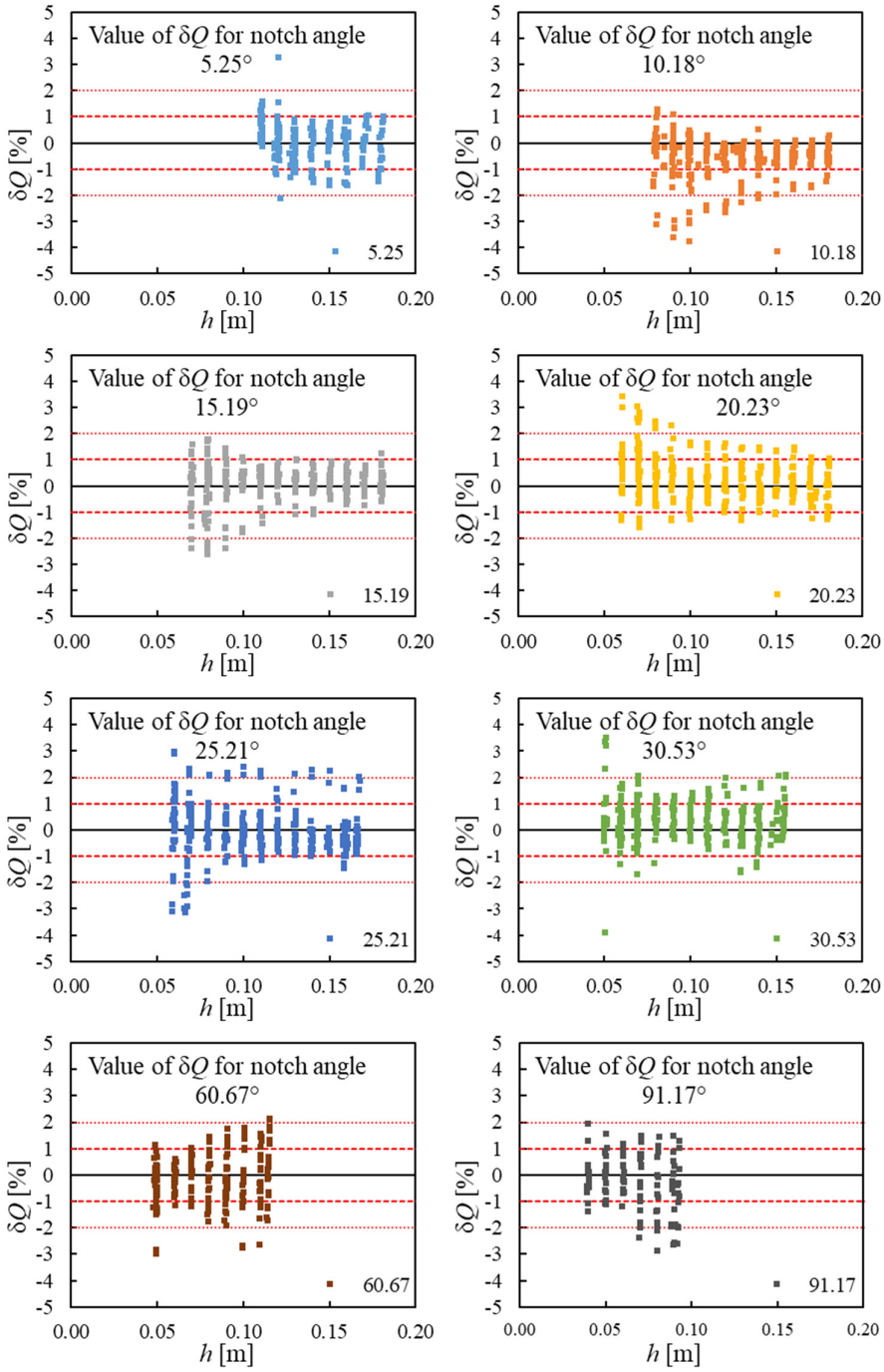

Fig. 8. Evaluation of the dependence of δQ on h for individual α.

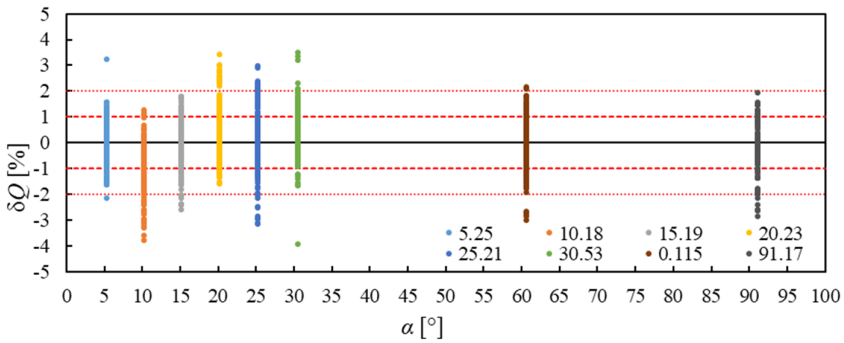

Fig. 9. Dependence of δQ on α.

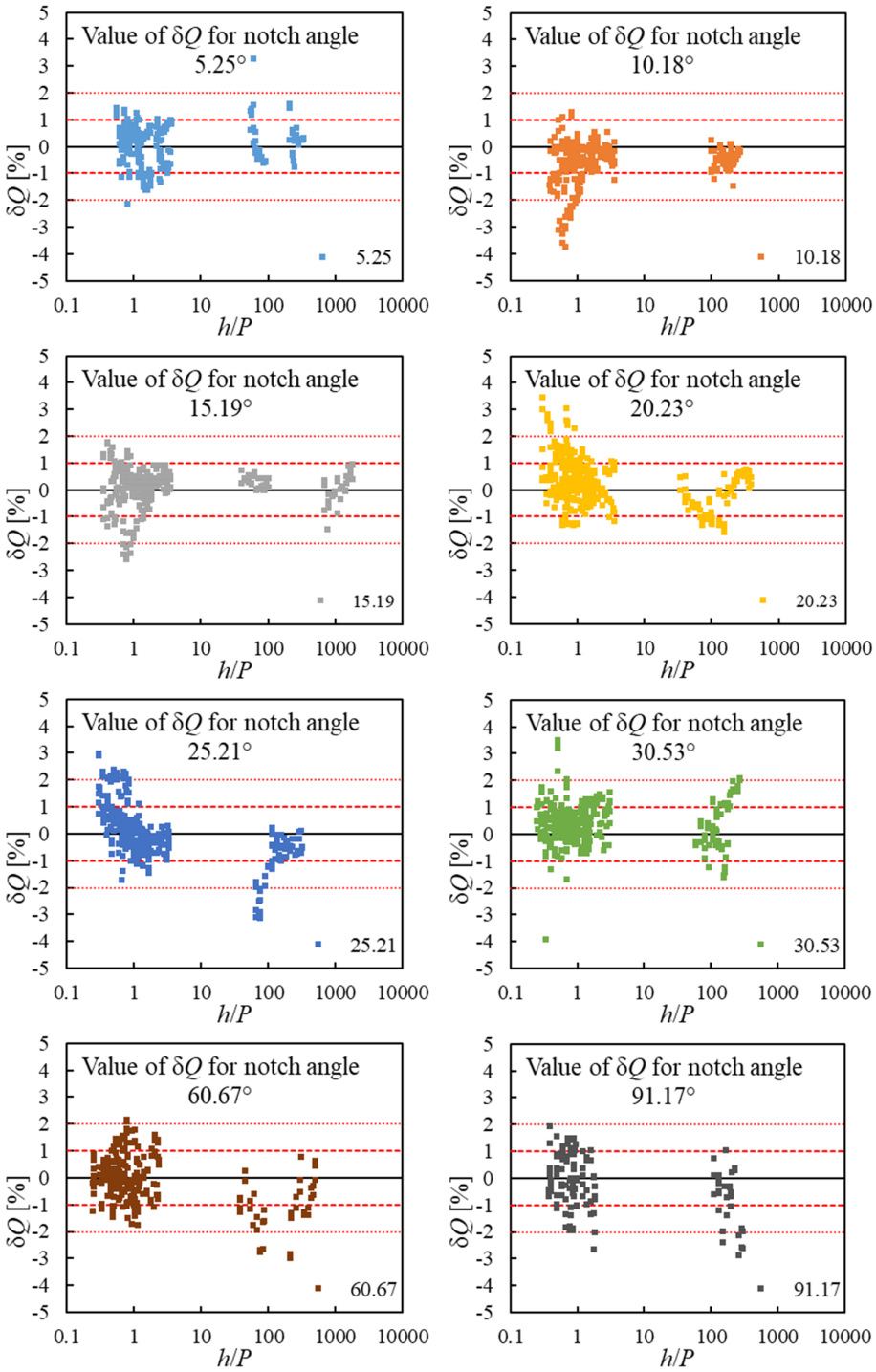

Fig. 10. Evaluation of the dependence of δQ on the ratio h/P.

Equations (7), (8) and (9) quantify the functional dependencies (3), (4) and (6). In this way, the values of Q can be calculated in the validity ranges of $5° \leq \alpha \leq 90°$, $0.00\ \text{m} \leq P \leq 0.20\ \text{m}$ and $h_l \leq h \leq h_{max}$ with h_{max} defined by the extent of the area depicted in the graph in Fig. 7. The validity of the equations for $\alpha = 91.17°$ is also limited by the ratio $P/B \leq 0.2$, which, to some extent, confirms the conclusions of Numachi and Hutizawa (1941a; 1941b). Application for $h > h_{max}$ (extrapolation) is not possible, because the overflow is affected by scale effect and missing measured data for majority of notch angles. The validity of the equations is further limited by the characteristics of the flume (box). The advantages of the aforementioned method for the determination of Q are, unlike in the case of other methods recommended by various authors, the large application range for determining small values of Q, the comprehensive option for calculation without the need to use graphs (ISO 1438, 2017), the relative simplicity of the dependencies (functional dependencies are expressed only by α), and the accuracy of the determination.

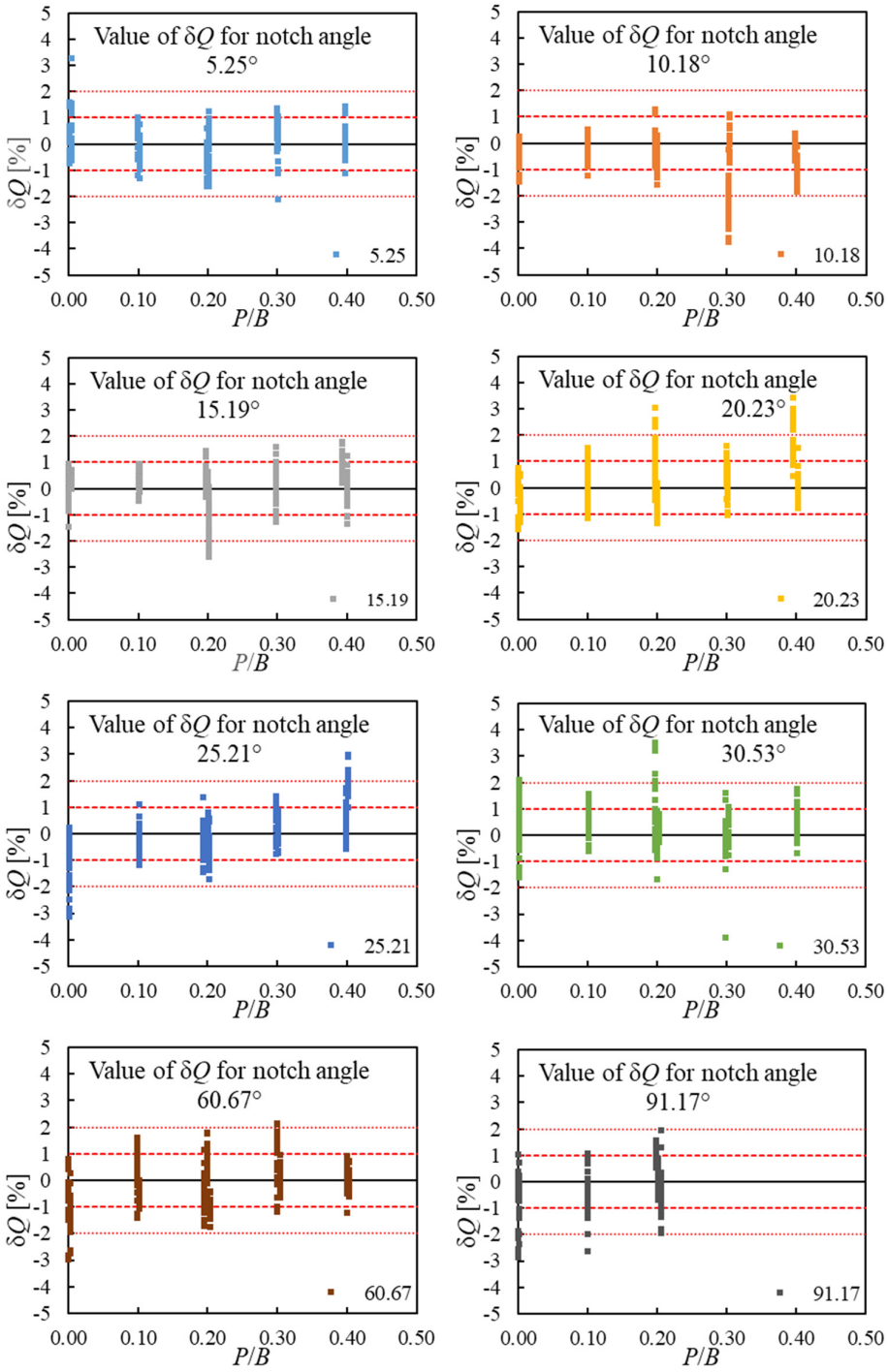

Fig. 11. Evaluation of the dependence of δQ on the P/B ratio.

A detailed analysis of the accuracy of the discharge determination using relationships (1), (2), (7), (8) and (9) can be performed by comparing the calculated discharge Q_C and the measured discharge Q using the relative error

$$\delta Q = \frac{Q_C - Q}{Q}. \tag{10}$$

Two functional dependencies are stated. The dependence of δQ on h for all values of α is shown in the graph in Fig. 8. The dependence of δQ on α is shown in the graph in Fig. 9. The distribution of δQ values in the interval ±1 % can be considered invariant with regard to h with some exceptions (Fig. 8). The vast majority of values for both dependencies lie within the interval ±1 %. The values outside the interval ±2 % are likely to originate from measurement inaccuracies.

A detailed evaluation of the validity of the simplification of functional dependence (5) on dependence (6) in the range $h_l \leq h \leq h_{max}$ and for $\alpha = 91.17°$ also in the range $P/B \leq 0.2$, i.e.

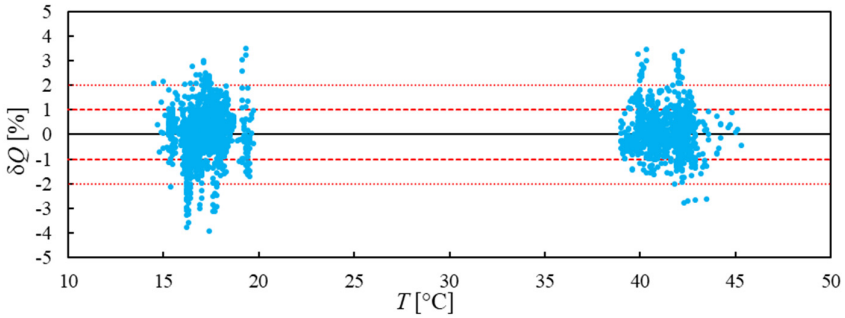

Fig. 12. Dependence of δQ on T.

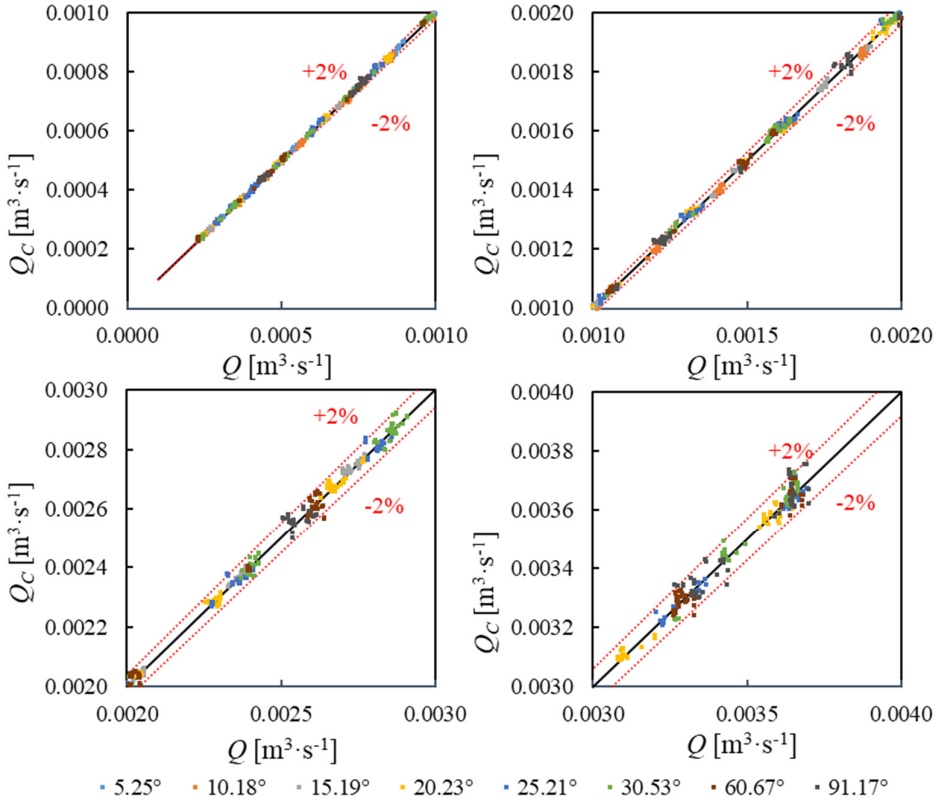

Fig. 13. Comparison of Q_C and Q.

the influence of ratios h/P and P/B on δQ, is shown graphically in Fig. 10 and Fig. 11 for individual values of α. No dependence is obvious from the distribution of values δQ on h/P or on P/B. The vast majority of δQ values lie within the interval ±1 %. The values outside the interval ±2 % are likely to originate from measurement inaccuracies. The graphs in Fig. 10 and Fig. 11 confirm the independence of δQ from the ratios h/P and P/B in the range $h_l \leq h \leq h_{max}$.

Confirmation of the validity of neglecting the effect of the water temperature change in the total range of 15 °C ≤ T ≤ 45 °C for $h_l \leq h \leq h_{max}$ for the above-mentioned evaluation method is shown graphically in Fig. 12. The graph shows the dependence of δQ on T and proves that the effect of the temperature change in the range $h_l \leq h \leq h_{max}$ is too minor to calculate within the framework of the uncertainties when determining Q.

A direct comparison of values Q_C and Q is shown in the graph in Fig. 13. The graph is supplemented with a line of agreement for their values. The Q_C values follow the line of agreement and confirm the suitability of the relations used over the entire range of the Q values measured. The histogram of δQ was performed which showed that 79.1 % of the values are within the ±1 % interval and 95.5 % of the values are within the ±2 % interval.

Verification of the accuracy of the calculation method is carried out by comparing the values Q_C and measured values of Q from selected authors in Fig. 14. The majority of the Q_C values lie near the line of agreement. With some exceptions, the Q_C values up to the $Q = 0.0017$ m^3·s^{-1} are very close to the line of agreement but above the mentioned value, some of them deviate. The deviation maintains the same trend. The effect of the deviation is probably caused by the different characteristics of the approach channel and the accuracies of the experimental measurements of the individual authors. Fig. 14 shows the relatively large deviation of Barrett´s (1924) values from the values of other authors. The deviation of Barrett's (1924) values may be caused for big values of discharges by the use of a short measurement time interval (10 s) and for small values of discharges by the clinging of water to the weir plate.

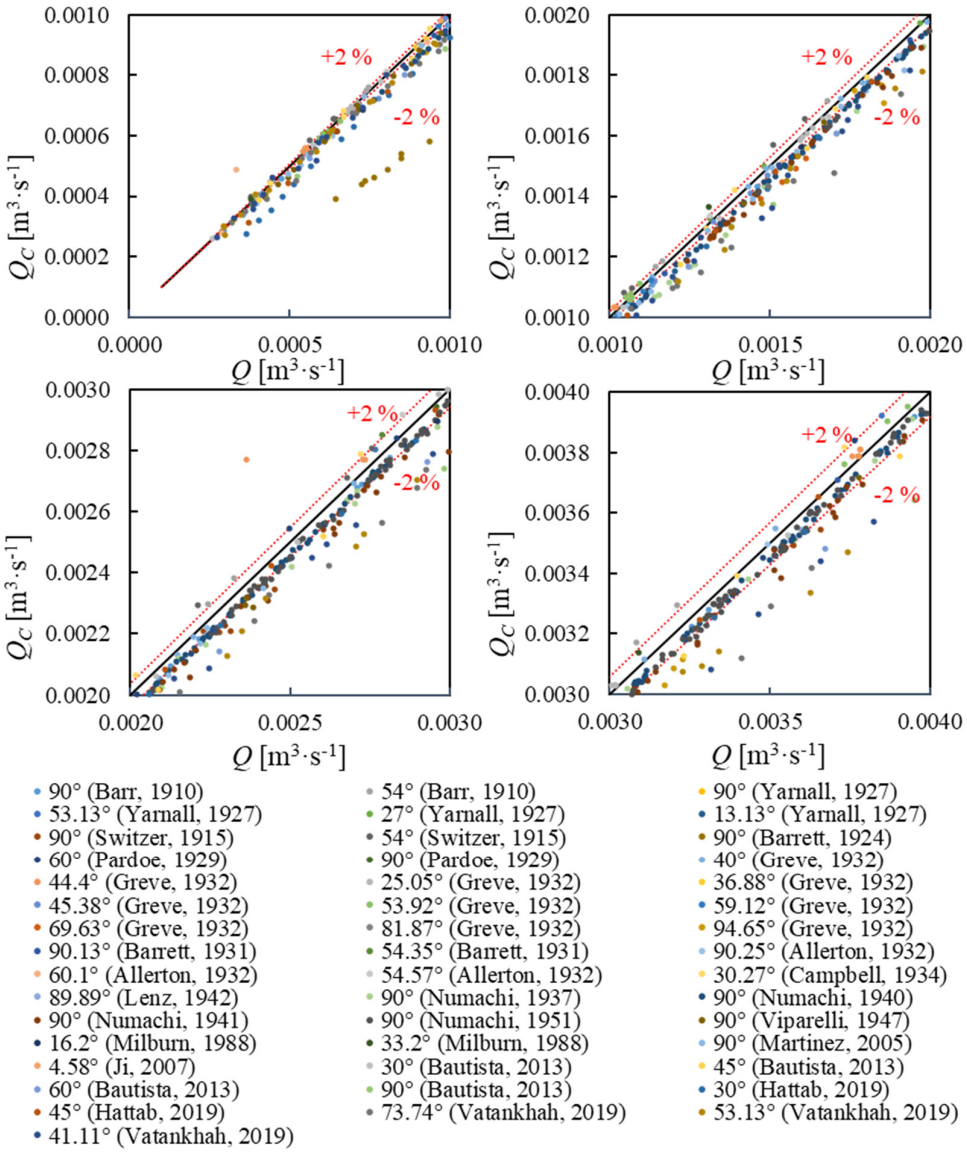

Fig. 14. Comparison of Q_C values and the Q values of other authors.

CONCLUSION

The application range of the calculation method according to Kindsvater-Shen (Shen, 1981) for the determination of Q using a TPW with a triangular notch is relatively limited for the determination of small values of Q, which is due, among other things, to the instability of the nappe and the amount of measured data. Due to a lack of measured data, extensive experimental research was carried out in which it was possible to take measurements in the range of $5.25° \leq \alpha \leq 91.17°$, $0.00\ \text{m} \leq P \leq 0.20\ \text{m}$, $0.020\ \text{m} \leq h \leq 0.18\ \text{m}$ and $15\ °\text{C} \leq T \leq 45\ °\text{C}$. The evaluation of the experimental measurements included the determination of their uncertainties. The results from the experimental measurements formed the basis for extending the applicability and modification of the Kindsvater-Shen method of calculation.

The Kindsvater-Shen method of calculation does not take into account h_l, which limits from below the area of applicability of the invariant dependence of C_d on h at the relevant α. Only the value h_s is given due to nappe instability and the limited amount of measured data. Due to the limitations of the applicability of the Kindsvater-Shen calculation method, h_l was newly incorporated, and its dependence on α was determined. The modified method of calculation of Q consisted in finding such values of C_d, k_h and h_l that C_d is invariant for the respective α in the range $h_l \leq h \leq h_{max}$. The modified method of calculation (compared to the original method) significantly expands the application area and defines it from below, mainly with regard to the determination of small values of Q.

The independence of the modified method of calculating Q from ratios h/P, P/B, and also from T in the entire range of values $h_l \leq h \leq h_{max}$ and the range of values α, P, B and T was proved. The exception was a TPW with $\alpha = 91.17°$, for which independence is valid only for $P/B \leq 0.2$, which to some extent confirms the conclusions of Numachi and Hutizawa (1941a; 1941b).

A detailed analysis of the accuracy of the determination of Q in relation to both h and α for $h_l \leq h \leq h_{max}$ was conducted. It was evaluated using δQ. The majority of the δQ values were within the ±1 % interval, and the vast majority of the δQ values were within ±2 %.

A results from frequency histogram of δQ was also presented. It confirmed the high accuracy of determination using the newly adapted calculation method. To verify the applicability of the adapted calculation method in the whole range of the measured values Q, calculated values Q_C were compared with experimentally measured. The correctness of the adjusted calculation method was thus confirmed across the entire range of measured values of Q.

Verification of the accuracy of the adjusted calculation method was performed by comparing the values of Q_C and the values of Q measured by all the authors mentioned above. The agreement in the area of determining small discharges is obvious.

Acknowledgements. The contribution was created with the support of project FAST-J-21-732 "Flow over thin-plate weirs with triangular notches with small heads".

REFERENCES

Adeyemi, O.I., Oreko, B.U., Abam, J., 2017. Experimental determination of the effect of notch shape on weir flow characteristics using constant head discharge apparatus. Asian J. Curr. Res., 2, 2, 55–64.

Ali, A.A.M, Ibrahim, M., Diwedar, A.I., 2015. The discharge coefficient for a compound sharp crested V-notch weir. Asian J. Eng. Technol., 3, 5, 494–501.

Allerton, R.W., 1932. Flow of water over triangular weirs. Thesis. Princeton University, Princeton.

Barr, J., 1910. Experiments upon the flow of water over triangular notches. Engineering, 89, 435–437, 470–473.

Barrett, F.B., 1931. The flow of water over triangular weirs. Thesis. Princeton University, Princeton.

Barrett, J.M., 1924. A study of the flow of water over triangular weirs and the determination of coefficients of discharge for small heads. Thesis. Utah Agricultural College, Logan.

Bautista-Capetillo, C., Robles, O., Júnez-Ferreira, H., Playán, E., 2013. Discharge coefficient analysis for triangular sharp-crested weirs using low-speed photographic technique. J. Irrig. Drain. Eng. - ASCE, 140, 3, 06013005.

Bos, M.G., 1989. Discharge measurement structures. 3. ILRI.

Caroline, L.L., Afshar, N.R., 2014. Effect of types of weir on discharge. J. Civ. Eng. Sci. Technol., 5, 2, 35–40. https://doi.org/10.33736/jcest.137.2014

Cone, V.M., 1916. Flow through weir notches with thin edges and full contractions. J. Agric. Res., 5, 23, 1051–1113.

Cone, V.M., 1917. Construction and use of farm weirs. Farmers' Bulletin, 813, 1–18.

Cozzens, H.A., 1915. Flow over V-notch weirs. Power, 42, 21, 714.

Cuttle, S.P., Mason, D.J., 1988. A flow-proportional water sampler for use in conjunction with a V-notch weir in small catchment studies. Agr. Water Manage., 13, 93–99. https://doi.org/10.1016/0378-3774(88)90135-7

Eli, R.N., 1986. V-notch weir calibration using new parameters. J. Hydraul. Eng. - ASCE, 112, 4, 321–325. https://doi.org/10.1061/(ASCE)0733-9429(1986)112:4(321)

Ghodsian, M., 2004. Stage discharge relationships for triangular weir. Int. J. Civ. Eng., 2, 1, 1–7.

Greve, F.W., 1930. Calibration of 16 triangular weirs at Prude. Eng. News-Rec., 105, 5, 166–167.

Greve, F.W., 1932. Flow of water through circular, parabolic, and triangular vertical notch-weirs. Eng. Bulletin Purdue University, 40, 2–84.

Greve, F.W., 1945. Flow of liquids through vertical circular orifices and triangular weirs. Eng. Bull. Purdue University, 29, 3, 1–68.

Grossi, P., 1961. Su uno stramazzo triangolare in parete sottile, libero, con angolo al vertice molto piccolo (On a thin-plated, free triangular weir with a very small vertex angle). L'Acqua, 4, 99–100. (In Italian.)

Hattab, M.H., Mijic, A.M., Vernon, D., 2019. Optimised triangular weir design for assessing the full-scale performance of green infrastructure. Water, 4, 11, 773–790. https://doi.org/10.3390/w11040773

Hertzler, R.A., 1938. Determination of a formula for the 120-deg V-notch weir. Civil. Eng., 8, 11, 756–757.

Chanson, H., Wang, H., 2012. Unsteady discharge calibration of a large V-notch weir: REPORT No. CH88/12. 1. The University of Queensland, Brisbane, 282355720.

Chanson, H., Wang, H., 2013. Unsteady discharge calibration of a large V-notch weir. Flow Meas. Instrum., 29, 19–24. https://doi.org/10.1016/j.flowmeasinst.2012.10.010

ISO 1438, 2017. Hydrometry – Open channel flow measurement using thin-plate weirs. 3. ISO, Geneva.

Itaya, S., Takenaka, T., 1955. Measurement of oil flow by means of 60° sharp-edged triangular weir. Trans. Jpn. Soc. Mech. Eng., 21, 101, 94–96. (In Japanese.) https://doi.org/10.1299/kikai1938.21.94

JCGM 100, 2008. Evaluation of measurement data — Guide to the expression of uncertainty in measurement. 1. BIPM.

Ji, K., 2007. Discharge characteristics of V-shaped multi-slit weirs. Thesis. Concordia University, Montreal.

King, H.W., 1916. Flow of water over right-angled V-notch weir. The Michigan Technic, 29, 3, 189–195.

Lenz, A.T., 1942. Viscosity and surface tension effects on V-notch weir coefficients. Trans. Am. Soc. Civ. Eng., 351–374.

Martikno, R., Humaedi, M., Ashat, A., Situmorang, J., Novianto, Hadi, J., 2013. Evaluation of weirs calculation to estimate well capacity: a numerical study. In: Proc. 13th Indonesia International GEOTHERMAL Convention & Exhibition 2013. Jakarta. 332060750

Martínez, J., Reca, J., Morillas, M.T., López, J.G., 2005. Design and calibration of a compound sharp-crested weir. J. Hydraul. Eng. - ASCE., 131, 2, 112–116. https://doi.org/10.1061/(ASCE)0733-9429(2005)131:2(112)

Mawson, H., 1927. Applications of the principles of dimensional and dynamical similarity to the flow of liquids through orifices, notches and weirs. Proc. Inst. Mech. Eng., 112, 537–547.

Milburn, P., Burney, J., 1988. V-notch weir boxes for measurement of subsurface drainage system discharges. Can. Agr. Eng., 30, 2, 209–212.

Numachi, F., Hutizawa, S., 1941a. On the overflow coefficient of a right-angled triangular weir) (2. Notice). J. Soc. Mech. Eng., 44, 286, 286. (In Japanese.) https://doi.org/10.1299/jsmemag.44.286_5_1

Numachi, F., Hutizawa, S., 1941b. On the overflow coefficient of a right-angled triangular weir (2. Notice). Trans. Jpn. Soc. Mech. Eng., 7, 27–3, 5–9. (In Japanese.) https://doi.org/10.1299/kikai1938.7.27-3_5

Numachi, F., Hutizawa, S., 1942a. On the overflow coefficient of a right-angled triangular weir (3. Notice). J. Soc. Mech. Eng., 45, 308, 725. (In Japanese.) https://doi.org/10.1299/jsmemag.45.308_725_2

Numachi, F., Hutizawa, S., 1942b. On the overflow coefficient of a right-angled triangular weir (3. Notice). Trans. Jpn. Soc. Mech. Eng., 8, 33–3, 37–40. (In Japanese.) https://doi.org/10.1299/kikai1938.8.33-3_37

Numachi, F., Kurokawa, T., Hutizawa, S., 1940a. On the overflow coefficient of a right-angled triangular weir. J. Soc. Mech. Eng.,

43, 275, 45. (In Japanese.) https://doi.org/10.1299/jsmemag.43.275_45_2
Numachi, F., Kurokawa, T., Hutizawa, S., 1940b. On the overflow coefficient of a right-angled triangular weir). Trans. Jpn. Soc. Mech. Eng., 6, 22–3, 10–14. (In Japanese.) https://doi.org/10.1299/kikai1938.6.22-3_10
Numachi, F., Kurokawa, T., Tota, E., 1937. Influence of the surface of the weir edge of a right-angled triangular weir, which projected discontinuously upstream due to the creation of an overlap, on the flow coefficient. Trans. Am. Soc. Mech. Eng., 3, 11, 174–176. (In Japanese.) https://doi.org/10.1299/kikai1935.3.11_174
Numachi, F., Saito, I., 1948. On allowable shortest length of channel for triangular notch. J. Soc. Mech. Eng., 51, 357, 229–230. (In Japanese.) https://doi.org/10.1299/jsmemag.51.357_229_2
Numachi, F., Saito, I., 1951. On allowable shortest length of channel for triangular notch. Trans. Jpn. Soc. Mech. Eng., 17, 56, 1–3. (In Japanese.) https://doi.org/10.1299/kikai1938.17.1
O'Brien, M.P., 1927. Least error in V-notch weir measurements when angle is 90 degrees. Eng. News-Rec., 98, 25, 1030.
Piratheepan, M., Winston, N.E.F., Pathirana, K.P.P., 2007. Discharge measurements in open channels using compound sharp-crested weirs. J. Inst. Eng., 40, 3, 31–38. https://doi.org/10.4038/engineer.v40i3.7144
Pospíšilík, Š., 2020. 2.67° triangular-notch thin-plate weir. In: Juniorstav 2020. ECON Publishing, Brno, pp. 598–603. (In Czech.). https://juniorstav.fce.vutbr.cz/download
Pospíšilík, Š., 2021. Identification and quantification of uncertainties in the measurement and evaluation of the discharge coefficient of triangular-notch thin-plate weir. In: Juniorstav 2021. ECON Publishing, Brno, pp. 512–517. (In Czech.). https://juniorstav.fce.vutbr.cz/download
Pospíšilík, Š., 2022. Analysis of the exploration range of triangular–notch thin–plate weirs. In: Juniorstav 2022. 1. ECON Publishing, Brno, pp. 468–474. (In Czech.). https://juniorstav.fce.vutbr.cz/download
Pospíšilík, Š., Zachoval, Z., Pařílková, J., 2022. Characteristics of velocity field in short flume in front of triangular-notch thin-plate weir. In: Proc. 34th Symposium on Anemometry. Institute of Hydrodynamics CAS, Prague, pp. 40–49. (In Czech.)
Ramamurthy, A.S., Kai, J., Han, S.S., 2013. V-shaped multislit weirs. J. Irrig. Drain. Eng. - ASCE, 139, 7, 582–585. https://doi.org/10.1061/(ASCE)IR.1943-4774.0000574
Reddy, M.S., Reddy, Y.R., 2017. Experimental investigation on the influence of density of fluid on efficiency of V-notch. Int. J. Adv. Sci. Res. Eng., 3, 9, 35–41. https://doi.org/10.7324/%20IJASRE.2017.32515
Schlag, A., 1962. Note on flow measurement for triangular weir. La Tribune de Cebedeau. Liege, 15, 218, 22–24. (In French.)
Schoder, E.W., Turner, K. B., 1929. Precise weir measurements. Trans. Am. Soc. Civ. Eng., 1929, 93, 999–1190.
Shen, J., 1981. Discharge characteristics of triangular-notch thin-plate weirs: Studies of flow of water over weirs and dams. Geological survey water-supply paper, 1617-B. U. S. Government Printing Office, Washington.
Smith, E.S., 1934. The V-notch: Weir for hot water. American Society of Mechanical Engineers, 56, 9, 787–789.
Smith, E.S., 1935. The V-notch weir for hot water. Trans. Am. Soc. Mech. Eng., 57, 249–250.
Strickland, T.P., 1910. Mr. James Barr's experiments upon the flow of water over triangular notches. Engineering, 90, 598.
Switzer, F.G., 1915. Test of the effect of temperature on weir coefficients. Engineering News, 73, 13, 636–637.
Thomson, J., 1858. On experiments on the measurement of water by triangular notches in weir boards. In: Proc. Twenty-eight Meeting of the British Association for the Advancement of Science. John Murray, Albemarle street, London, pp. 181–185.
Thomson, J., 1861. On experiments on the gauging of water by triangular notches. In: Proc. Thirty-first Meeting of the British Association for the Advancement of Science. John Murray, Albemarle street, London, pp. 151–158.
Thornton, B.M., 1929. Measurement of fluid flow with triangular notches. Power Engineer, 24, 313–315.
Vatankhah, A.R., Khamisabadi, M., 2019. Stage-discharge relationship for triangular and curved-edge triangular weirs. Flow. Meas. Instrum., 69, 1–10. https://doi.org/10.1016/j.flowmeasinst.2019.101609
Vicena, D., 2020. Minimum head of triangular-notch thin-plate weir. Thesis. BUT, Brno. (In Czech.)
Viparelli, M., 1947. On the Thompson weir. In: Estratto da Atti Fondazione Politecnica del Mezzogiorno, 3, pp. 1–24. (In Italian.)
Wirak, L.R., 1934. An investigation of the flow of water over triangular weirs of different angles. Thesis. Princeton University, Princeton.
Yarnall, D.R., 1912. The V-notch weir method of measurement. J. Am. Soc. Mech. Eng., 34, 2, 1479–1494.
Yarnall, D.R., 1927. Accuracy of the V-notch-weir method of measurement. Trans. Am. Soc. Mech. Eng., 48, 939–964.

NOMENCLATURE

DN	diameter nominal
TPW	thin-plate weir
B	approach channel width [m]
C_d	discharge coefficient
$\bar{C}_d$	average discharge coefficient
g	standard acceleration due to gravity [m/s^2]
h	head [m]
h_e	effective head [m]
h_l	limit head [m]
h_{max}	maximum head [m]
h_s	minimum head of stable nappe [m]
k_h	height representing the combined effects of viscosity and surface tension [m]
P	weir height [m]
Q	discharge, measured discharge [m^3/s]
Q_C	computed discharge [m^3/s]
R^2	coefficient of determination
T	temperature [°C]
Z_b	bottom level [m]
Z_h	water surface level upstream in front of the weir at distance from $2h_{max}$ to $4h_{max}$ [m]
Z_P	crest level [m]
α	notch angle [°]
δQ	relative error of discharge

Received 3 October 2022
Accepted 13 December 2022

J. Hydrol. Hydromech., 71, 2023, 1, 49–63
https://doi.org/10.2478/johh-2022-0027

sciendo Journal of Hydrology and Hydromechanics Institute of Hydrology SAS

Reconstruction of the 1974 flash flood in Sóller (Mallorca) using a hydraulic 1D/2D model

Carys Thomas[1*], Ioanna Stamataki[2], Joan Rosselló-Geli[3]

[1] Department of Architecture and Civil Engineering, University of Bath, Bath, North East Somerset, BA2 7AY, United Kingdom.
[2] School of Engineering, University of Greenwich, Chatham Maritime, Kent ME4 4TB, United Kingdom.
[3] Estudis d'Arts i Humanitats, Universitat Oberta de Catalunya, 08018 Barcelona, Spain.
[*] Corresponding author. Tel.: +44 7794945764. E-mail: carys.a.thomas@bath.edu

Abstract: Flash flood events are common in the Mediterranean basin, because of a combination of rugged coastal topography and climatological characteristics. The Balearic Islands are a flood-prone region with the research area, Sóller (Mallorca) being no exception. Between 1900 and 2000, Sóller experienced 48 flash floods with 17 categorised as catastrophic. In Sóller, the local surface water network comprises ephemeral streams. These are natural water networks that only carry water during periods of intense rainfall. Using the available evidence from the 1974 flash flood, this research used Flood Modeller to simulate the event. The research developed a one-dimensional (1D) and a one-dimensional two-dimensional (1D-2D) model that assisted in the understanding of the behaviour of the ephemeral stream during the flood. Analysis of hydraulic parameters such as water flow, depth and velocity provided an appreciation of the interaction between the channel and floodplain. Model development aims to forecast the impending impacts of climate change and urbanisation.

The results suggest that the characteristics of Sóller's catchment area naturally encourage flash flooding and hence can be deemed a flashy catchment. The model demonstrates that the interaction between the channel and floodplain relies heavily on surface roughness of both areas. The model proves that if flood intensity increases with climate change, the extent of flooding and consequently the damage will become more severe.

Keywords: Flash floods; Hydraulic model; Documentary sources; Historical flood reconstruction; Hydrograph; Mallorca.

1 INTRODUCTION

Understanding the effects and severity of past flood events has been of interest to engineers, geographers, and the local communities for many centuries. Learning from past flood events is a step into making more informed decisions regarding flood risk in the present and future.

Flash floods are one of the most hazardous natural disasters (Sene, 2013). Due to the local climate of the Mediterranean, the frequency of flash floods is higher than the rest of Europe (Gaume et al., 2009; Gaume et al., 2016; Llasat et al., 2016). Between 1940 and 2015, Gaume et al (2016) collected information regarding 172 flash flood events that occurred only in the Mediterranean. Flash floods are usually caused by intense rainfall and are characterised by their localised nature and high speed. Over the years, people have described them as "walls of water". They are particularly common in mountainous areas occurring on previously dried river beds. The main challenge of these events is that due to their quick nature they are rarely captured or measured on-site and thus their effect can be even more devastating (Alcoverro et al., 1999; Costa, 1987; Creutin and Borga, 2003; Gaume and Borga, 2008).

The use of a hydraulic flood model allows for a numerical and visual representation of flood events. Having the freedom to explore various scenarios and mitigation solutions adds depth to the understanding of flash floods and their impacts. Using imported data or data manually collected from the field, factors such as topography, catchment areas, land use, and infrastructure can be modelled accurately for each site, allowing for the simulation of past and future flood events. The imminent impact of climate change is growing evermore severe, with extreme weather and a rise in sea level playing a critical role in flood risk. An increase in the frequency and intensity of rainfall inevitably increases the risk and severity of flooding (Mahmood et al., 2016). This coupled with the existing cyclonic weather induced by Mallorca's location and topography has the potential to be disastrous (Nunez, 2019).

Incorporating historical flood events when estimating the risk for future flood events can help with the associated uncertainty as it reduces the risk for the required interpolation of these values (Stamataki and Kjeldsen, 2021). Furthermore, looking into these events in more depth and modelling them numerically, can provide a baseline for flood paths, areas of greatest danger and the severity of potential effects. Building from these events provides realistic representations of possible future flood events. Recognising how flooding will impact communities is vital to ensure a safer future. The use of flood modelling therefore provides a helpful approach to understanding flood management and flood defence solutions (Wheater, 2002).

There has been a lot of research into reconstructing the peak flow of historical flood events. Researchers over the years (Elleder, 2010; Elleder et al., 2013; Herget and Meurs, 2010; Herget et al. 2014) have primarily focused on reconstructing the magnitude of historical flood events rather than creating an accurate representation of the river system hydraulics including the effect of hydraulic structures (e.g. bridges). Even though many of the aforementioned researchers have used the slope area method for the reconstruction of peak flows, the technique results in some simplifications. The complex hydrodynamic

effects of the river flow's interaction with its floodplains and hydraulic structures is not represented. Consequently, this can result in additional uncertainty associated with the reconstruction of the peak flow.

For the majority of cases, historical flood data and accompanying meteorological data is limited. The evidence primarily used in flood reconstruction includes epigraphic evidence (flood water levels marks), photographs and witness documentary sources (Elleder, 2010; Herget et al., 2014; Stamataki and Kjeldsen, 2021). These sources in conjunction with hydraulic models play an important role in reconstructing floods and predicting future impacts. Stamataki and Kjeldsen (2021) reconstructed 16 historical flood events in the city of Bath using a 1D hydraulic model. They used recorded peak flow values to calibrate the model and assessed the peak flow of historical flood events using epigraphic evidence in the city (flood marks). Thus they extended the annual maximum series of peak flow back to 1866.

Identifying risks and reducing vulnerability is key in reducing flood impacts. Vulnerability combines demographic, financial and exposure factors; hence it is clear that the flood severity is dependent on both flood and catchment parameters. Identifying these risks is often done by identifying and using peak discharge values to determine flood depths and extents. This can be completed using stage-discharge curves and/or one/two-dimensional hydraulic flood models (Moel et al., 2009). Results of both approaches can be translated into flood hazard maps which identify areas of concern.

This paper investigates the development of a hydraulic model to estimate the flood extent and effects of the 1974 flash flood in Soller (Mallorca) using available documentary sources. Hydrological and cross-sectional data were collected from different sources and the numerical model was calibrated using eye-witness records and photographic evidence. We discuss how a one dimensional (1D) hydraulic model enabled us to reconstruct numerically the 1974 historical flood and what we learnt from the model. Then the model expanded to a 1D-2D coupled model utilising DEM topographical data and was used to investigate the events flood extents. To summarise, the importance of using numerical models and the effort required to incorporate them in modern flood risk assessments is discussed and the uncertainty associated with this methodology is described. Additionally, the impact of climate change on the floodplain extents is assessed for future mitigations.

2 RESEARCH AREA

The research area is located on the western coast of Mallorca (Figure 1), adjacent to the Tramuntana mountain range, the highest of the island. With a surface of 50 km^2, the valley of Sóller is enclosed by mountains over 1,000 m a.s.l., a rugged relief close to the coast. This results in two different areas; the plain being the lowest and closest to the sea, and the mountain lying on the slopes of the mountain range.

Geologically, the plain is settled over quaternary alluvial soils while the mountains lie over Keuper and Muncheskalk materials, mostly calcareous and conglomerate rocks.

The rainfall in the area is determined by the Mediterranean geographical location of Mallorca. Annual amounts increase from the coast, averaging 600 mm/year, to the mountain tops, where averages reach 1,000 mm/year. There is a large interannual irregularity and an alternance of dry and rainy periods is very common. In terms of the rainfall seasonality, autumn is the primary rainy season, followed by spring and winter. Summer is the driest season of the year, with July having the lowest record of rainfall, usually 0 mm.

The geological and climatological conditions of the area have led to a water surface network of ephemeral catchments, known locally as “torrents” (Figure 2). Such streams are characterised by large infiltration rates (due to the karstified bedrock) and long dry periods. Runoff usually depends on the occurrence of heavy precipitation episodes (HPEs), which are common and result in flash flood events.

The valley’s main catchment is the torrent Major, resulting from the combination of three tributaries: torrent de Fornalutx, torrent de Biniaraix and torrent de’s Coll. The three tributaries meet in the middle of the town of Sóller and run towards the sea, discharging in the port of Sóller Bay (Figure 3). The torrent Major is 10.6 km long with a surface area of 49.3 km^2. Upstream the slope is steep whilst the final three kilometres run through the plain, which is almost flat. The average slope is 0.11.

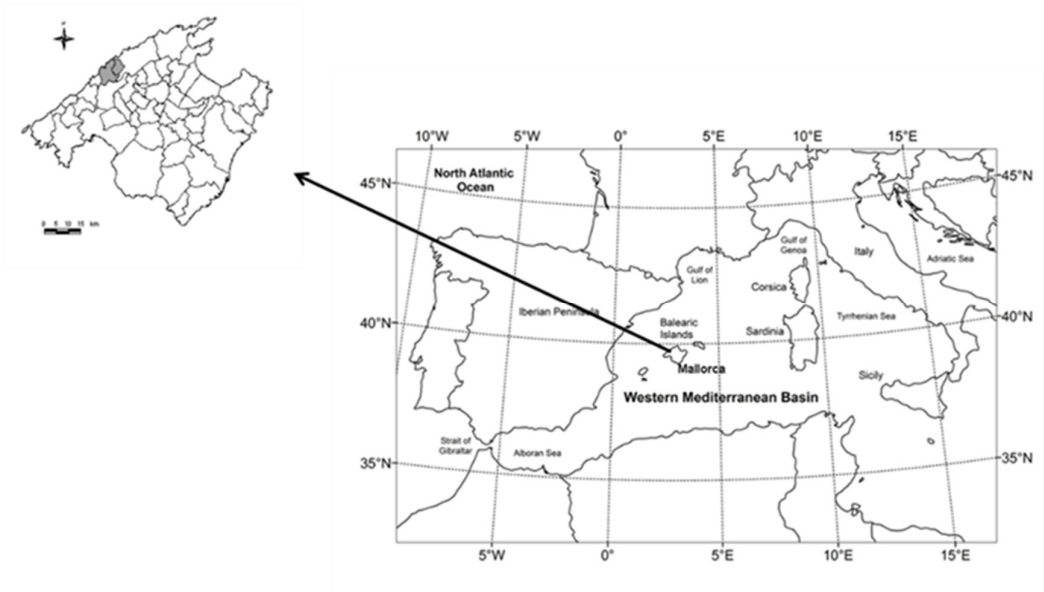

Fig. 1. Location of the research area in Mallorca and Mallorca within the Western Mediterranean (Rosselló-Geli and Cortés, 2021).

Fig. 2. Downstream section of Torrent Major and new Ca'n Repic bridge.

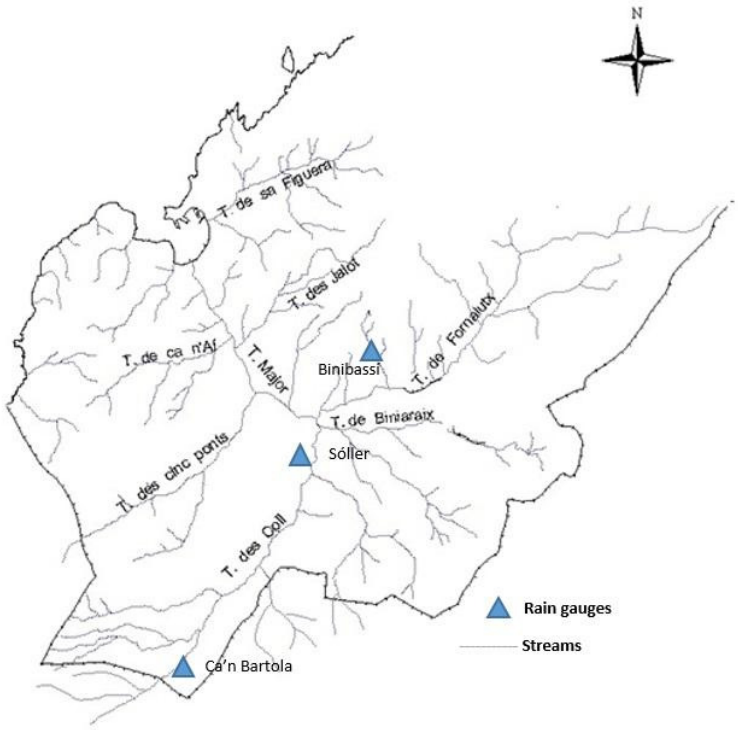

Fig. 3. Surface runoff system of the Sóller valley (modified from Rosselló-Geli, 2000).

The catchment has a low torrentiality coefficient (1.52), which indicates that it has a low ratio of the number of first-order stream to basin area (Romero-Díaz and López-Bermudez, 1987). Despite this, floods have affected the catchment since as early as the 17th century. According to a documentary source (Rullan, 1885), between 1640 and 1855, 13 floods affected the area, most often with catastrophic effects. Since 1900, 48 events have been identified (Rosselló-Geli and Cortés, 2021), with damages ranging from ordinary to catastrophic, following the classification by Barriendos and Llasat (2003); the latter being a flood that results in high infrastructure and economic costs and is of serious danger to the local population while the former is a flood that affects the closest area to the stream, causing minor damages in farming land and riverbed infrastructures.

3 STUDY EVENT

On March 30 1974, a significant area of the torrent Major catchment was severely flooded, primarily impacting the low-lands of the valley. The flood resulted from a sudden increase in surface water runoff which was related to heavy precipitation that commenced on March 29th across the island of Mallorca.

A low pressure region off the Algerian coast drove a flux of humid air towards the Balearic Islands, which upon collision with Mallorcian reliefs, resulted in intense precipitation (Figure 4).

Within the area of interest, precipitation commenced during the 29th with values of over 150 mm of rainfall recorded for the entire catchment. According to the Spanish National Meteorological Institute (INM), a maximum rainfall of 349.5 mm across 2 days was recorded in the area. Table 1 shows rainfall recordings for 3 different gauges within the area.

The high precipitation resulted in a sudden increase of the water levels within the catchment's ephemeral streams. The streams were overwhelmed causing flooding in the lowest area of the valley. Flooding of the "Torrent dels Cinc Ponts", located on the western side of the basin had a severe impact (Figure 3). Water levels breached the ephemeral stream walls and caused

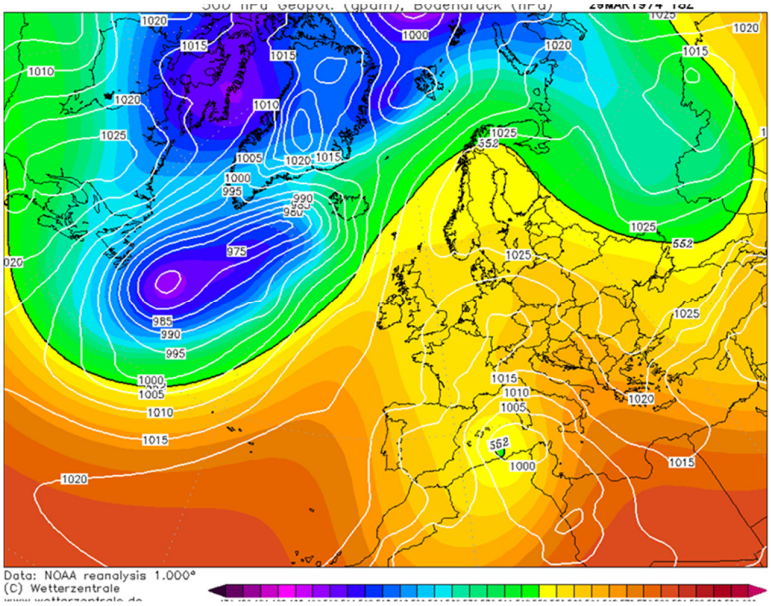

Fig. 4. Atmospheric situation March 29 1974 (Wetterzentrale, 2021).

Table 1. Rainfall distribution. Source: INM.

Code number and raingauge name	March 29th 1974	March 30th 1974	Total
B046 Binibassí	195 mm	154.5 mm	349.5 mm
B059 Ca'n Bartola	170 mm	46.5 mm	216.5 mm
B061 Sóller	165 mm	95 mm	260 mm


SÓLLER
SEMANARIO DE INFORMACIÓN LOCAL
INUNDACIONES EN LA HUERTA Y ES CAMP DE SA MAR
EL EXCMO. SR. D. ENRIQUE RAMOS, GOBERNADOR DE LA PROVINCIA, VISITO LA ZONA AFECTADA
Información en pags. centrales

Fig. 5. Screenshot of the cover of the Semanario Sóller showing the effects of the flood (BMS, 2021a).

flooding of the right hand side (looking downstream) of the "torrent Major". This had a considerable impact on the main road to the port of Sóller and the houses and orchards in proximity to the flooded area (Figure 5).

Sóller citizens accused neglected and inconsiderate infrastructure for causing the flood. These included a lack of maintenance of irrigation canals and ditches on the agricultural land and the inconsiderate construction of the main road leading from Sóller to the harbour which destroyed the historical water drainage system that encouraged rainwater to move into the ephemeral streams. From a meteorological perspective, the cause of the flash flood was the prolonged precipitation the week prior to the flood which resulted in complete saturation of the ground during the flood event.

The associated societal impacts were most severe and expressed, with reports reaching national newspapers. Domestic dwellings and agricultural land were flooded, two women had to be rescued from their home which was unreachable due to high water levels, and the connection between Sóller and its harbour was temporarily hindered due to both road and tram line damages, in addition to water and debris blockages. The flood damages were valued at approximately 45,000,0000 pesetas, equivalent to €4,000,000 today. These were primarily related to the valley's agricultural industry and the coastal tourism industry.

4 METHOD

To estimate flood extents both a one-dimensional (1D) and a one-dimensional two-dimensional (1D-2D) linked model were developed. A hydraulic model is a numerical representation of the movement of a fluid through a system and it allows the

understanding of the corresponding hydraulic behaviour (Stamataki and Kjeldsen, 2020). It numerically simulates the flow of water through a river and how the water interacts with the channel, the floodplain and surrounding infrastructure.

The 1D model was initially developed, followed by the construction of the 1D-2D linked model. Once both models were constructed and calibrated, the model was used to further understand the behaviour of ephemeral streams under different conditions and investigate the impact of climate change.

4.1 Model

The research used Flood Modeller; a computational programme that allows for the numerical representation of water flow through channels, across floodplains and via drainage systems, thus permitting for surface flow analysis in 1D and and 2D. The construction of a 1D-2D linked model is also possible, where the river channel is represented in 1D, whilst the floodplain and surrounding catchment is represented in 2D via the incorporation of a digital elevation model (DEM). This is a topographical model. The dynamic link between 1D and 2D models means that if water overspills the 1D channel, it becomes an input in the 2D model. 1D values that overspill to the 2D floodplain are numerically factored to ensure they are representative of the 2D domain (Jacobs, 2020). Flood Modeller was chosen as the primary research software as it allows the development of a realistic model despite limited input information.

The governing equations in Flood Modeller are the 1D Shallow Water equations, also known as the Saint-Venant equations (Eq. 1 and Eq. 2) (Jacobs, 2020). These are derived from depth-integrating the Navier-Stokes equations assuming that the length scale of our system is much greater than the vertical length and express the conservation of mass and momentum of a water body. The Manning's equation is also used in solving the normal depth boundary condition in addition to describing the interaction of flow with infrastructure.

$$Mass\ Conservation \rightarrow \frac{dQ}{dx} + \frac{dA}{dt} = 0 \quad (1)$$

$$Momentum\ Conservation \rightarrow \frac{dQ}{dt} + \frac{d}{dx}\left(\frac{Q^2}{A}\right) + gA(So - Sf) = 0 \quad (2)$$

where Q is the flow rate (m^3/s); x is the longitudinal channel distance (m); A is the cross sectional area (m^2); t is the time (s); g is acceleration due to gravity (m/s^2); So is the bed slope (m/m) and Sf is the friction slope (m/m).

4.2 Model construction

Building a historical hydraulic model is not an easy task and some fundamental input data are required in order to begin modelling. The data required for the 1D and the coupled 1D-2D models are described below.

4.2.1 1D model construction

For the base of the 1D model, the data was provided by the Climatology, Hydrology, Natural Hazards and Landscape Research Group at the University of Balearic Islands (UIB) and included:

- Data related to rainfall and peak flow of the 1974 flood and an image of the hydrograph from a flood event in Sóller in 1978 (Rosselló-Geli, 2000).
- Cross section geometry of the ephemeral stream along its length, with corresponding stream roughness values.
- Digital elevation model (DEM) data of local topography to a 2.5 m resolution (IDEIB, 2021).
- Location, dimensions, and cross sections of the bridge at the lower boundary of the model (AMS, 2021).

Figure 6 shows the simplified setup used when using a hydraulic model to represent a river. This includes defining an inflow hydrograph, river cross sections, bridges and a downstream boundary condition. These are all defined relative to the river's length. Each step is explained analytically below.

Inflow hydrograph: The first schematic (Figure 6) represents the inflow hydrograph. Flood hydrographs are graphs showing how a catchment responds to a rainfall event by plotting the flow rate over time for the duration of the flood. In hydraulic models it represents the model's upstream boundary condition - in this case at Barona Bridge - and it determines the propagation of the water flow along the system. The model's results are highly dependent on flood hydrographs as the intensity of the inflow dictates the characteristics of the flood. During the 1974 flash flood, no flood data were recorded as there were no flood gauges at the time. However, by the time of the 1978 flood event, the gauges were in operation, and the 1978 flood event was accurately recorded. Due to lack of data, the assumption was made that the shape of the hydrograph from 1978 was representative of that for the 1974 event. This relates to similarities in catchment's response time to different rainfall and flood events. Therefore, the rate of rise and fall of the flow corresponds to the 1978 flood events. The recorded peak discharge of the 1978 flood via gauges was 30.86 m^3/s and thus the calculated and scaled peak discharge of the 1974 flood was 114.22 m^3/s. A ratio between the two values was defined, and the 1978 hydrograph was scaled to represent the peak discharge of the 1974 flood (Figure 7). The rising limb of the hydrograph begins at 17 hours, the time taken between the initial precipitation on the catchment and the beginning of the initiating discharge.

River cross sections: The second and fourth schematics (Figure 6) refer to the stream's cross sections. These are required at different locations along the stream to define the river channel, as shown on Figure 8. The channel geometry and surface roughness (Manning's coefficient) are input parameters required in order to model the river. Longitudinal distances between each section are also defined. The model presented in this work, consisted of 8 cross-sections, labelled Cross section 1 (CS1) – Cross section 8 (CS8) where CS1 is furthest upstream whilst CS8 lies at the downstream boundary. Figure 8 is

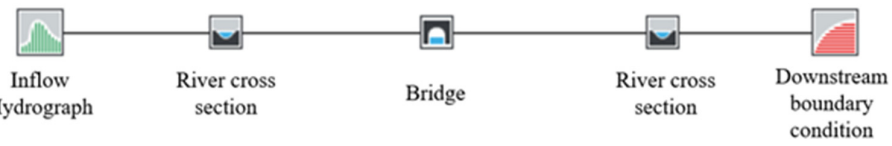

Fig. 6. Schematic showing a simplified setup with an inflow hydrograph, a river cross section, followed by a bridge, another river cross section and finally a downstream boundary condition.

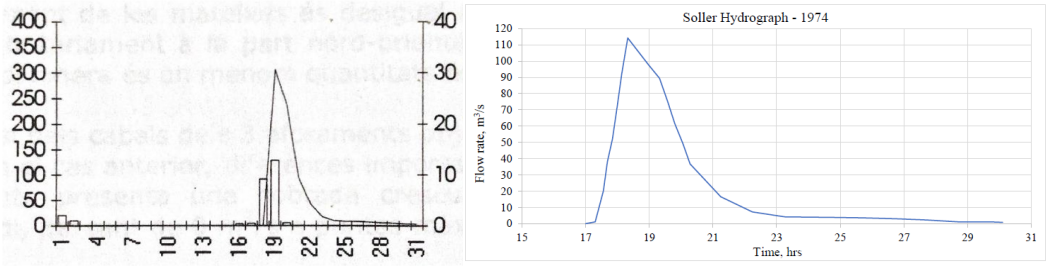

Fig. 7. Scanned hydrograph of the 1978 flood (left) from Rosselló-Geli (2000) and scaled hydrograph of the 1974 flash flood event (right).

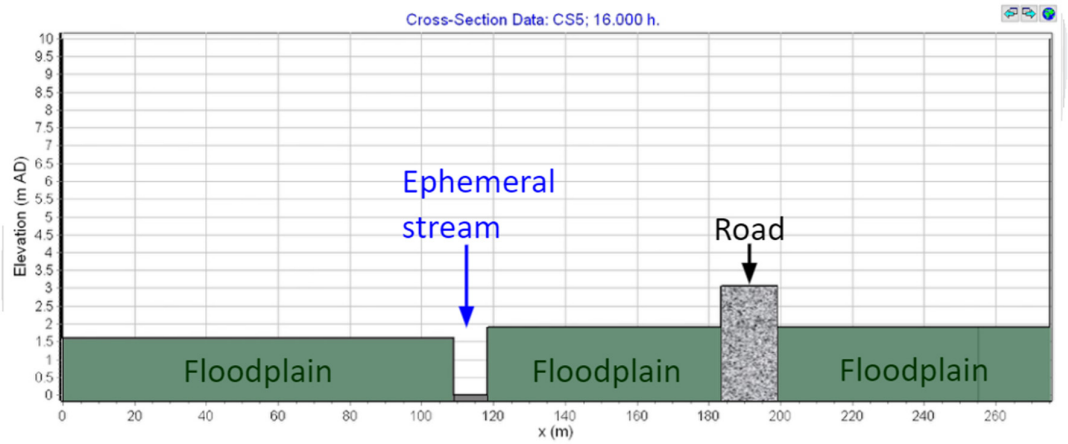

Fig. 8. Example of a river cross section definition in Flood modeller showing the different materials (floodplain, road) and the location of the ephemeral stream.

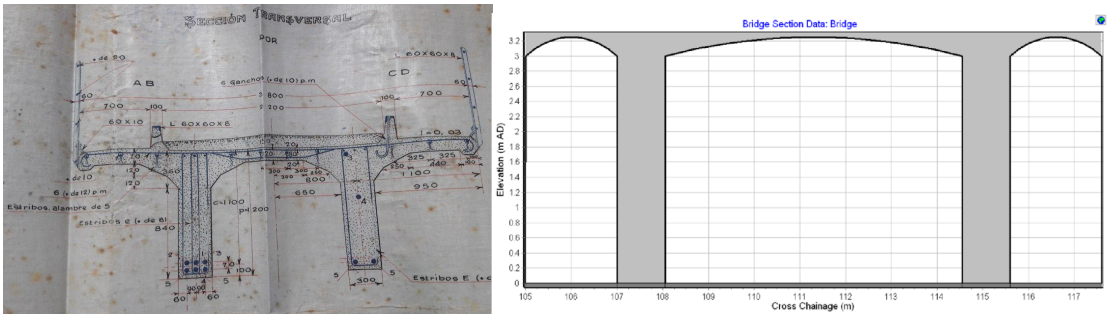

Fig. 9. Blueprint of Ca'n Repic bridge's dimensions (AMS, 2021) (left) and example of the numerical representation of Ca'n Repic bridge in Flood Modeller (right).

an example of CS5 where it shows the defined river cross section of the ephemeral stream, the elevated road and floodplains.

Bridge: The third schematic relates to the definition of hydraulic structures and in this case bridges within the modelled section of the river/stream. To define a bridge in Flood Modeller, firstly the bridge's dimensions need to be determined and the location of the bridge relative to the adjacent cross sections specified. Incorporating the bridge within the model was a vital step of the research as bridges often cause obstructions during flood events and have an impact on the flow of water. Cross sections CS6 – CS8 in the model therefore primarily relate to the Ca'n Repic bridge (Figure 9).

Downstream boundary condition: The last schematic in Figure 6 is the downstream boundary condition which provides the conditions at the end of the model. Here the slope of the stream's bed is defined and the flow is characterised in terms of depth and velocity. This primarily relates to the numerical calculations of the hydraulic model.

A plan view of the finished model and the location of the 8 different cross sections can be seen in Figure 10.

4.2.2 1D-2D linked model construction

Constructing the 1D-2D linked model follows the same schematic as described above for the 1D model, however the geometry of the river cross sections differs. The 1D-2D cross sections now only represent the river channel itself and hence are modelled as a simple rectangular shaped channel. The floodplain is incorporated via the provided 2D 2.5 m resolution DEM data (IDEIB, 2021), which clearly defines the river's course and the surrounding floodplain. The two-dimensionality of the DEM provides an accurate representation of the flood path which is dictated by the topographical characteristics.

Initially, the DEM data is imported and the river is outlined by a shape file. The cross section geometries, bridge location and boundary conditions are also incorporated within the 1D

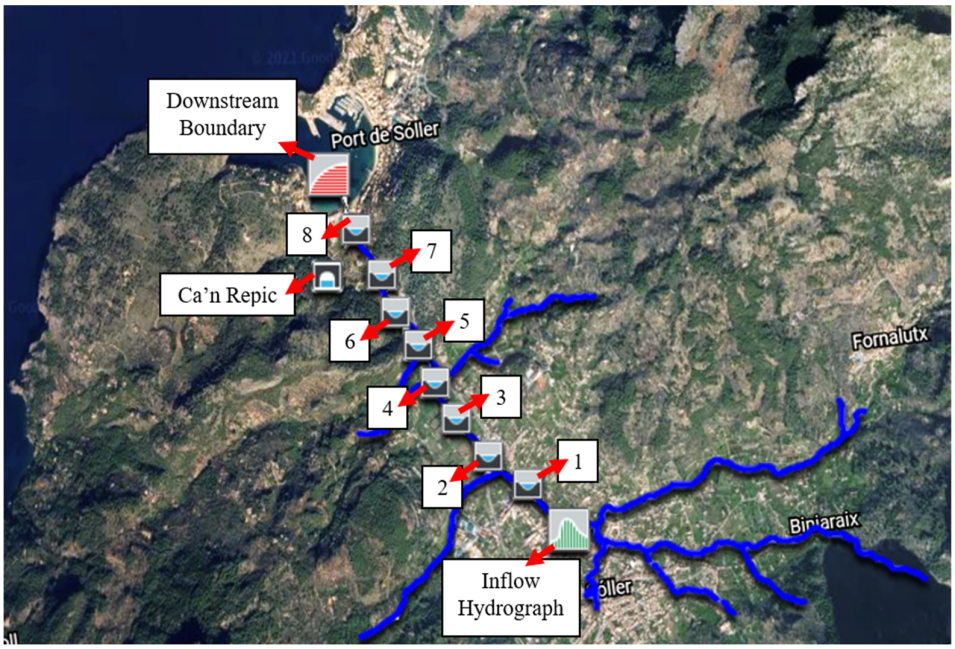

Fig. 10. Plan view of the stream showing the location of the different cross sections (CS1–CS8) (Google Earth, 2021).

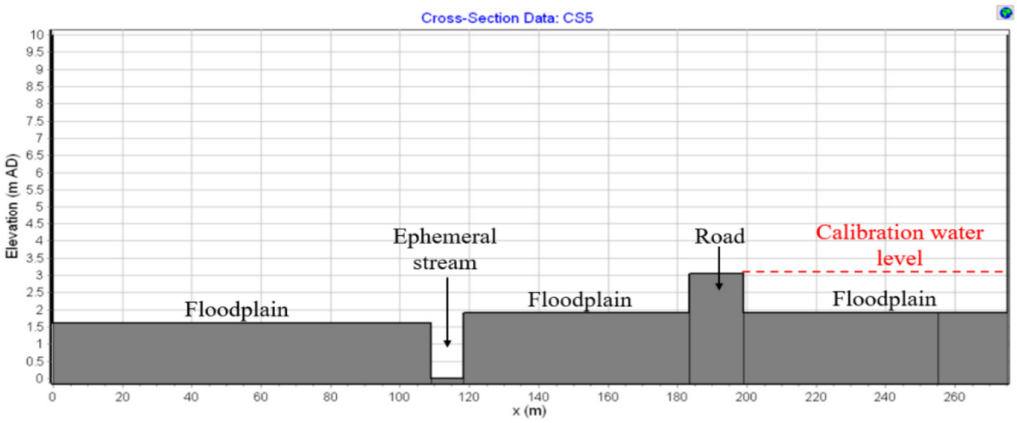

Fig. 11. Cross section 5 (CS5) with calibration point.

model. To concentrate the DEM data to the area of interest, an active flood area is assigned around the river channel. The connected 1D river data and 2D DEM are then linked within the model.

4.3 Model calibration

Once all information is inputted into the modelling system, the process of model calibration can begin. This is the process of adjusting the unknown factors in the model until the model can provide a good description of the river system. The purpose of calibrating a flood model is to ensure it is an accurate and valid representation of the stream and the system hydraulics during the flood event. For the 1974 flood event, a calibration point on agricultural land at cross section 5 (CS5) was selected. An eyewitness (the land owner) stated that the flood level reached 1.5 m within his field, a value that was also supported by photograph measurements from the flood (Figure 11).

With a fixed inflow hydrograph and stream geometry the changeable parameters were the stream's roughness. The river roughness was therefore adjusted within some acceptable uncertainty markets in order for the simulated model water levels to match (within 5%) the known calibration point (1.5 m water depth in the floodplain of CS5). An important factor for calibration was the saturation level of the ground prior to the flood. Due to the significant rainfall measurements recorded the week prior to the flood event, it was assumed that the floodplain was partially if not fully saturated. The floodplain saturation provides additional water volume to the catchment and therefore, to incorporate this into the model, a constant water depth of 0.1 m was assumed to reside on the floodplain.

To calibrate the 1D-2D model, the 1D calibrated simulation results are incorporated as an input file into the 2D simulation. The 2D analysis uses the resulting 1D hydraulic parameters to produce the 1D-2D linked results.

4.3.1 Testing

The calibrated model allowed for analysis of the flood extent of the 1974 event in addition to further research into the behaviour of ephemeral streams and the impact of climate change.

The testing schedule was as follows:

1D simulation of the 1974 flood event (the calibrated model)
1D-2D linked simulation of the 1974 flood event
1D-2D simulation of the impacts of climate change

With climate change growing ever more severe global temperatures and frequencies and magnitudes of extreme weather events are increasing, especially high precipitation events across the Mediterranean (Cos et al., 2022; Tuel and Eltahir, 2020). The rise in temperature increases the moisture content of the atmospheric air (Mahmood et al., 2016). For each degree of temperature rise, the air's water vapour capacity increases by approximately 7%. (Clark, 2011). Although it is recognised that the atmosphere's moisture content does not increase homogeneously, nor does an increase in water vapour capacity result directly in larger volumes of rain, in order to conduct a simplified exercise representing climate change, the input flow was increased by 7%.

5 RESULTS

The aim of this research project was to reconstruct the historical flood of 1974 in order to obtain a more accurate assessment of the effect of the flood, which would prove useful in understanding the contemporary flood risk of Sóller.

5.1 1D Model results

It is important to note that the 1D model reconstructed the river system as it was at the time of the flood using a variety of sources.

Figure 12 shows the flow rate (blue), velocity (green) and water depth (red) at cross section 5 (CS5 - calibration point). It is interesting to indulge into the details of what is happening at this specific cross section. From a fundamental perspective, conservation of mass states that matter cannot be created nor destroyed though it may be transformed from one form to another (e.g. by a chemical or nuclear process). Thus in response to the increasing flow (first hour of flash flood event), one of two things needs to happen to satisfy continuity, the conservation of matter: (i) either the velocity needs to increase if the cross sectional area remains unchanged and/or (ii) the cross-sectional area must increase in order to for the velocity to decrease but the flow to remain constant throughout the system. Looking at the graph in more detail, the water remains in the ephemeral stream channel until 18.5 hours, restricting the cross-sectional area, resulting in an initial steep rate of velocity increase. The increase in the velocity of the flood water is therefore the stream's initial response. The velocity reduces severely once the water breaches the stream's banks and extends to the floodplain and hence we see it accompanied by an increase in the water depth. After the flow rate reaches its peak flow, the maximum value, the water remains on the floodplain, with the water depth (red line) decreasing at a slow rate of approximately 0.14 m per hour. The velocity also continues to decrease. This represents the hydrograph's decreasing flow rate and the friction asserted on the flow from the floodplain and slope. The secondary peak in velocity apparent at 30.5 hours occurs due to the sudden restriction in the cross sectional area where the water begins to flow only through the stream channel once again.

The event's rapid onset and steep slope of the hydrograph's rising limb highlights the severity of the flash flood event. Figure 13 is a series of screenshots from the simulation of the event at CS5, the calibration point. The 14 screenshots are at approximately 1 hour intervals, from 17 to 31 hours, in which 17 hours is the beginning of the flood readings. Images 1–4 highlight the shear increase in flow and water depth, whilst images 5–14 demonstrate the slower rate of falling water depth. It is important to note the velocity increase discussed from 17 to 18.5 hours where the water remains in the stream channel (Screenshots 1 and 2) and the flow is restricted within the stream's cross sectional area. Looking at Screenshot 3, the water has breached the stream's banks and has now extended to the floodplain. This relates to the sudden drop in the velocity discussed earlier and the corresponding increase in the water depth. The described decreasing flow rate of the hydrograph accompanied by the slow decrease of water depth and velocity is apparent in Screenshots 4–13. Finally, the secondary peak in velocity at 30.5 hours is apparent in Screenshot 14 when all water returns back to the stream channel.

While running the model, another noteworthy factor was that the upstream floodplains of the model were submerged for a greatest length of time with a depth of 3.4 m. Moving downstream through the cross-sections, the submersion time and water depth reduced, with only a maximum depth of 1.96 m across CS6, CS7 and CS8.

The maximum velocity in the channel and on the floodplain occurs at CS8 with values of 1.21 m/s and 1.14 m/s respectively. The floodplain velocity is only sustained for a short period of time; however, its impact remains significant. The average velocity across the floodplain at all cross-sections during the average 4 hours submersion time is 1.06 m/s, which is 0.19 m/s above the average velocity throughout the entire flood event duration.

Finally, in order to assess the interaction between the bridge and ephemeral stream's flow, a comparison was made between CS6, situated directly upstream of the bridge and CS8, situated directly downstream of the bridge in terms of water depth (Figure 14 left) and velocity (Figure 14 right). By comparing the values at the two different locations (CS6 is upstream and shown in blue and CS8 is downstream and shown in red), it is evident that the bridge structure has a significant impact on the flood event.

A way to understand the effect a bridge has in a water stream is to calculate its afflux which is the rise in water level on the upstream side of the bridge (CS6) caused by the effective reduction of the channel's width. Looking at the left image, there is a 0.41 m surge in water level upstream of the bridge location. This suggests that the bridge is restricting the movement of water and causing the water depth to accumulate and increase on the upstream side and thus it can be identified as a significant obstacle in the flow during a flash flood event. This occurs between times of 19.5 and 23.2 hours, which correlates with the times that the water is on the floodplain, illustrated in Figure 13. While this blockage is obvious on the left figure by an increase in water depth, it also translates to a decrease in velocity of 0.61 m/s between CS6 to CS8 during that time. This sudden decrease in velocity can once more be explained using the continuity equation where, as the water depth increases, the cross sectional area is increasing and thus the velocity must decrease to satisfy continuity.

5.2 1D-2D linked model results

The results for the 1D-2D 1974 flood event and the climate change event models are described below. Figure 15 provides a reference for the results presented highlighting important cross section locations (CS1–CS8) and the location of the Ca'n Repic bridge.

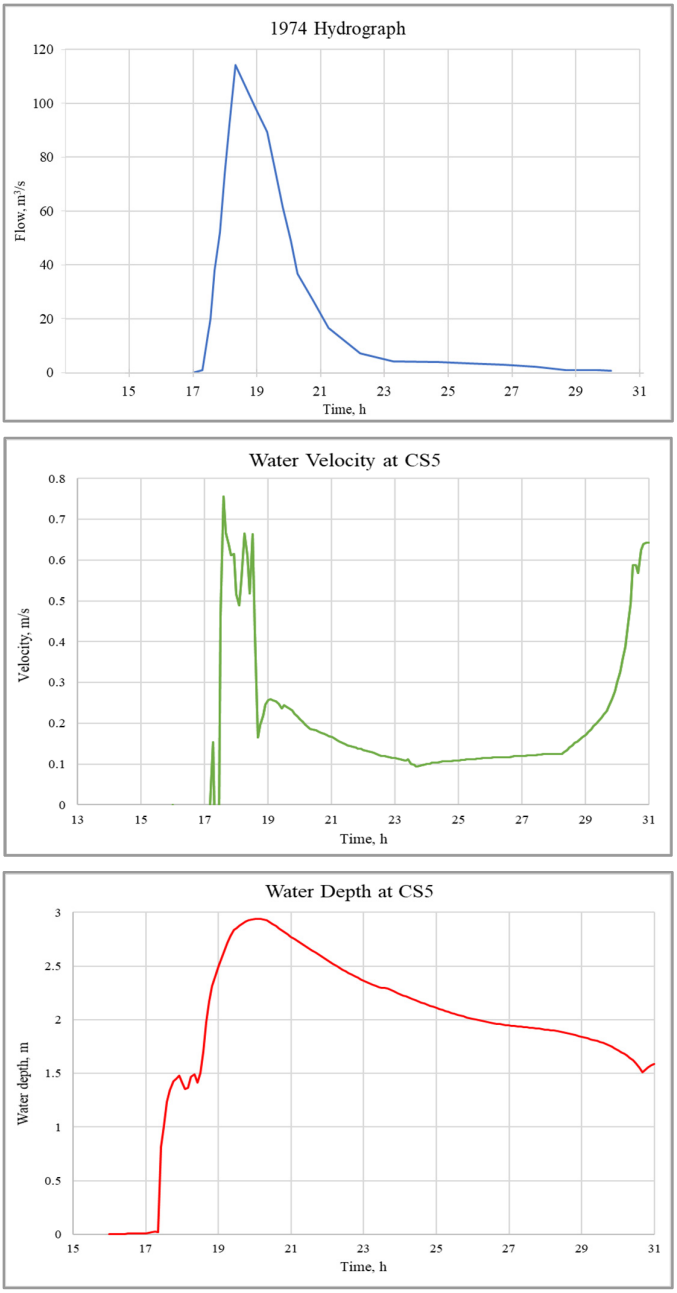

Fig. 12. Simulated flow rate (blue), velocity (green) and water depth (red) at cross section 5 (CS5 - calibration point) during the 1974 flash flood event.

5.2.1 The 1974 flood event

Following the successful modelling of the 1974 flash flood, the 1D (one-dimensional) model was coupled with a 2D (two-dimensional) model to simulate the hydrodynamic behaviour of the flood along the floodplains more accurately. Figure 16 shows a series of screenshots simulating the flood extents of the event on the floodplains. The 8 screenshots are at intervals of approximately 2 hours, from 17 to 31 hours and the different colours (see legend) represent different water depths along the floodplain ranging from 0.01–0.111 m with dark blue to 1.929–2.028 m in red.

The results produced by the 1D-2D model are consistent with the local topography and results from the 1D simulation of the flood. Figure 16 clearly shows the influence of the surrounding topography on the flood path. Low lying areas correspond to vast flood extents, whilst the section running between the two mountain ranges experiences less flooding as it is clearly constricted by the steep adjacent land. The worst flooding occurs between CS3 and CS5, with a maximum water depth of 2.5 m whilst in general the right hand side of the river banks experiences greater depths than the left hand side, due to the local topography. Further to this, looking more specifically at the bridge, the modelled water depths upstream of the bridge were greater than those downstream which implies that the bridge's blocking effect extends significantly upstream. The velocities were greater downstream of the bridge which successfully correlates with the restriction of depth caused by the

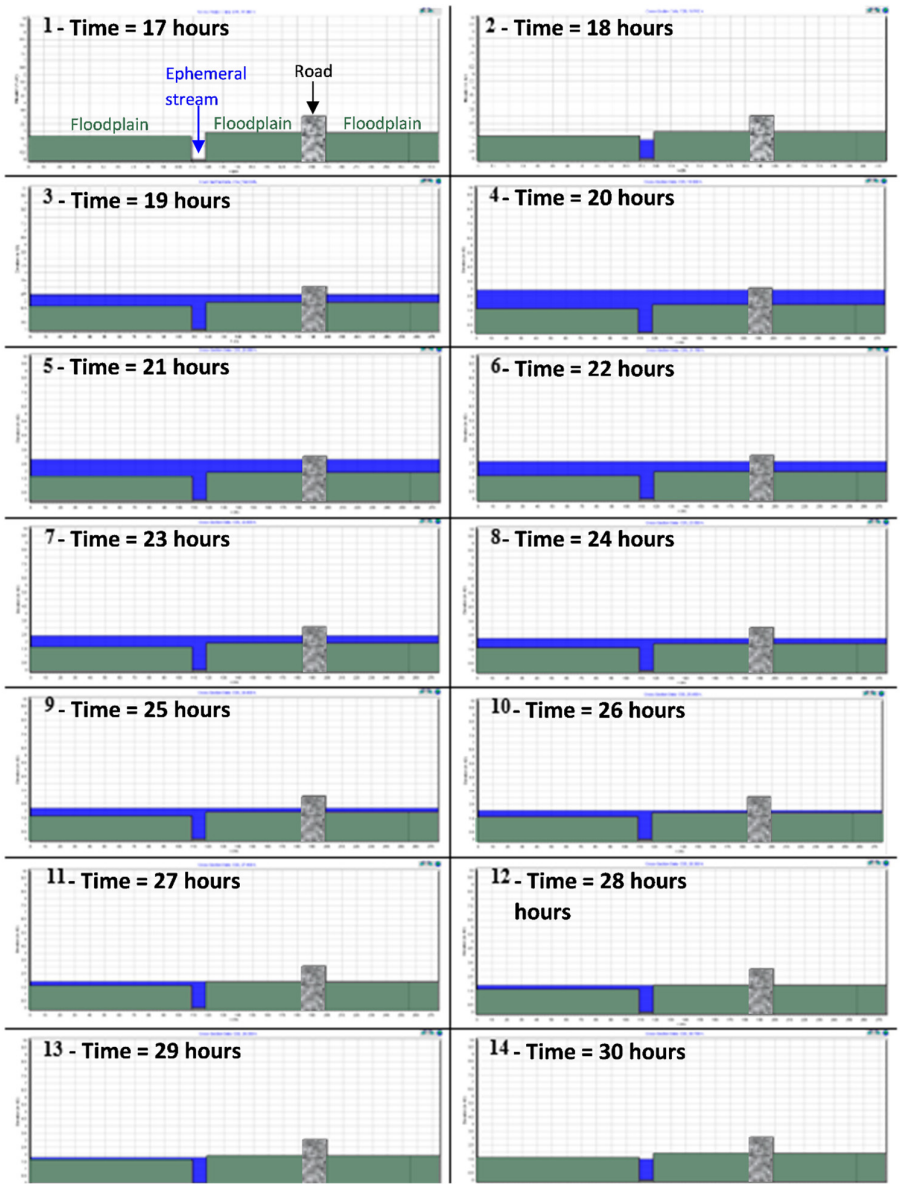

Fig. 13. 1D model simulation results at CS5 from 17 hours (beginning of flash flood event) to 30 hours.

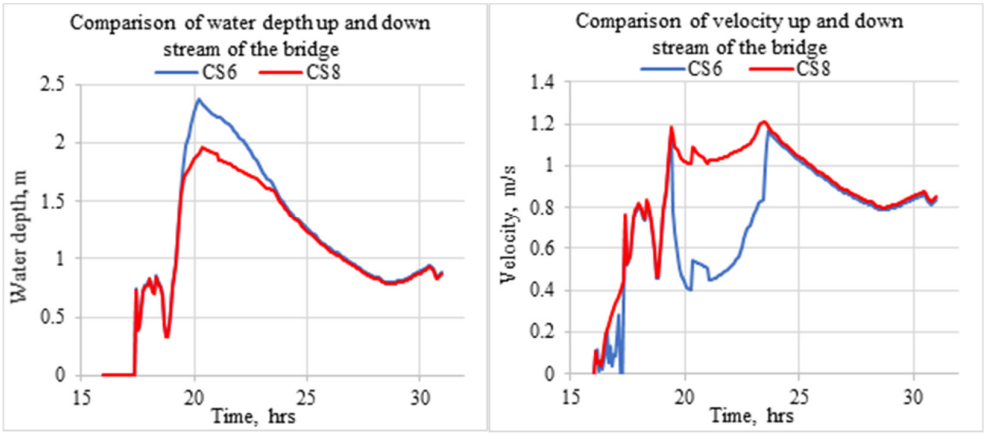

Fig. 14. Simulated water depth (left) and velocity (right) at cross sections CS6 (upstream of the bridge - shown in blue) and CS8 (downstream of the bridge -shown in red) during the 1974 flash flood event.

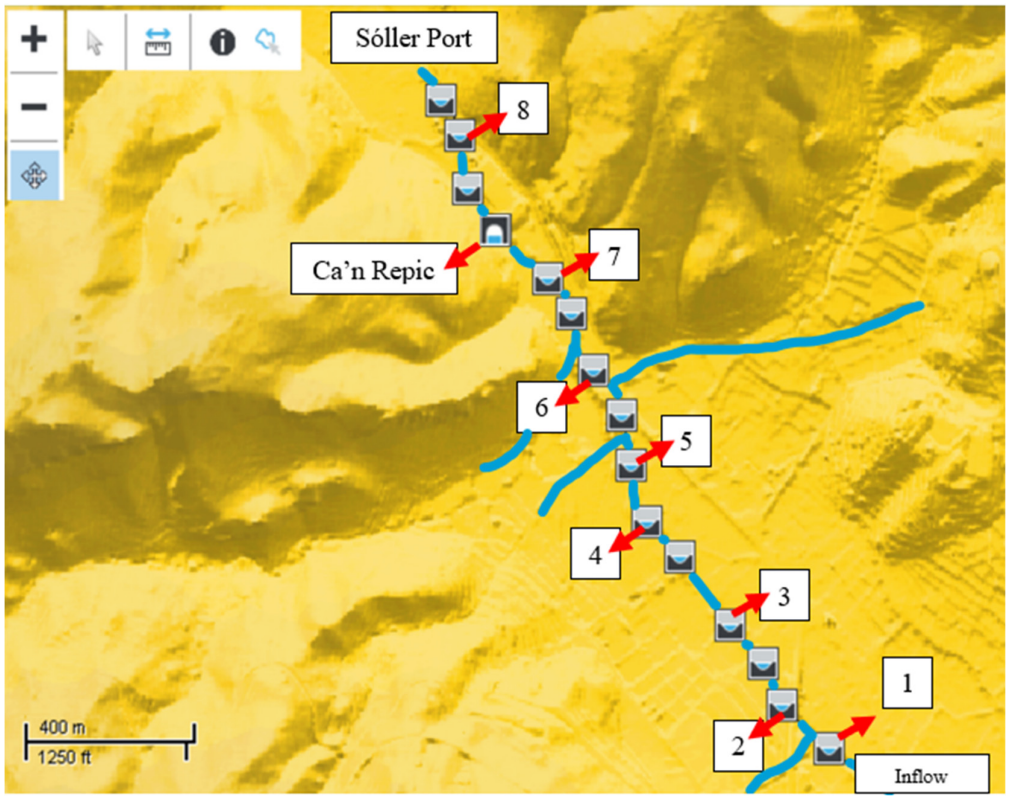

Fig. 15. Reference map for the 1D-2D linked model results.

bridge and satisfies continuity. Finally, it is interesting to compare figures 13 and 16 especially the initial hours of the event. They demonstrate the shear speed of the flood occurrence with both highlighting that the floodplain is inundated by 19 hours, only 1.5 hours after the start of the flood event.

5.2.2 Impact of climate change

As previously mentioned, increased precipitation and more extreme weather conditions accompany climate change. The hypothesis tested is that with Mallorca already experiencing cyclonic weather, and this being a prominent cause of flooding, the impact of climate change could be disastrous (Nunez, 2019). Recognising the magnitude of the expected increase will assist future predictions and consequently aid with future flood mitigation efforts.

Comparison of the 1D-2D model results for the 1974 flood and climate change tests illustrate the difference in flood extent (Figure 16). Figure 16 shows the flood extent data from 1974 in blue and compares them with the expected flood extents due to the 7% flow increase, shown in green. Figure 17 shows 8 screenshots at approximately 2 hours intervals, from 17 to 31 hours and the different colours (see legend) represent different water depths along the floodplain ranging from 0.01–0.23 m with light blue to 1.97–2.19 m in blue and 0.01–0.27 m in light green and 2.36–2.62 m in dark green.

This figure shows that climate change will only exaggerate the effects of the 1974 flood, thereby posing future risks to Sóller. Climate change combined with an expected increase in urbanisation will definitely result in an overall increase in floodplain velocities and water depths, which enhance the dynamic pressure and the impacts on the floodplain as well as the impact on the existing infrastructure. These are scenarios identified as being detrimental to Sóller due to its increased risk to the community's livelihood, its present and future economy and the infrastructure.

6 DISCUSSION

The hydraulic model has shown the significant impact the 1974 flood event had on Sóller. The flood extent, velocities and depth are all directly influenced by the flood hydrograph and the surrounding catchment. The initially steep catchment promotes rapid movement of water whilst the downstream low-lying and textured catchment reduces velocities and encourages pooling. The shape of the inflow hydrograph demonstrates the falshiness of the event; the peak discharge is reached only a mere hour into the beginning of the flooding records. This natural encouragement of flash flooding deems Soller's catchment as flashy, that is, *"a catchment area that, because of geographic, topographic, and geological factors, shows an almost immediate response to intense rainfall, resulting in a flash flood*" (Werner and Cranston, 2009). It can be concluded that the town's flood risk is permanent.

CS1–CS4 are most heavily populated in terms of infrastructure and population, with the density wilting from CS5 onwards. The proximity of residence to the stream deems this vicinity as high risk. Water levels reach the ground floor of homes and local businesses, consequently having devastating financial and wellbeing impacts. In addition, it is not compulsory to have flood insurance for a property within flood zones in Sóller hence flood damages place an enormous financial burden on property owners. With regards to the wider outlook, it is not compulsory for any property owner to disclose to potential

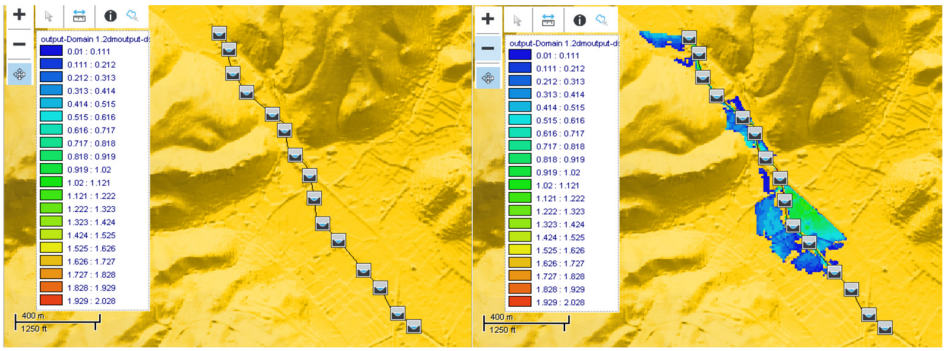

Time = 17 hours Time = 19 hours

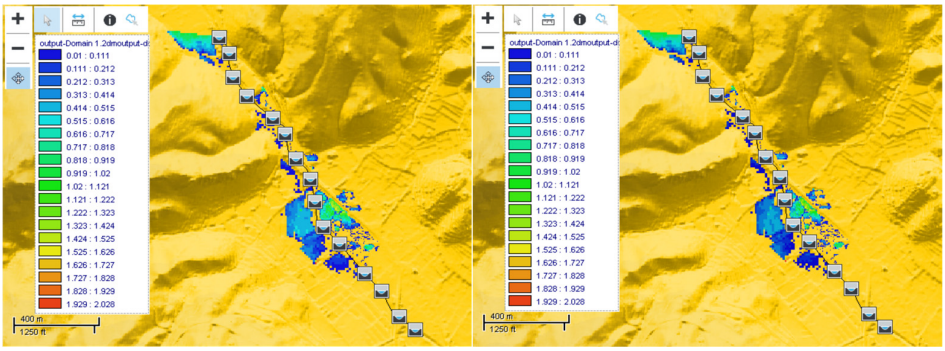

Time = 21 hours Time = 23 hours

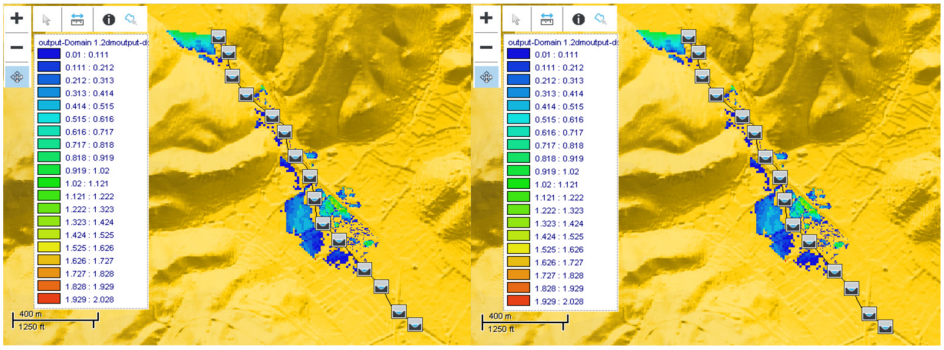

Time = 25 hours Time = 27 hours

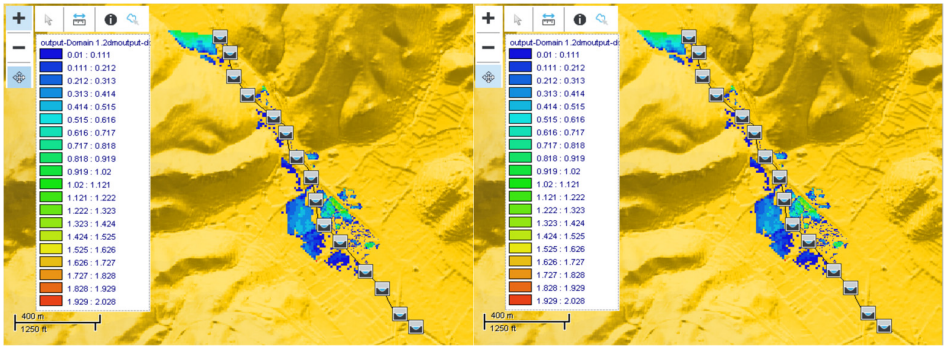

Time = 29 hours Time = 31 hours

Fig. 16. 1D-2D model simulation showing the flood extent during the 1974 flood. The different colours in the model represent water depths along the floodplains ranging from 0.01–0.111 m with dark blue to 1.929–2.028 m in red.

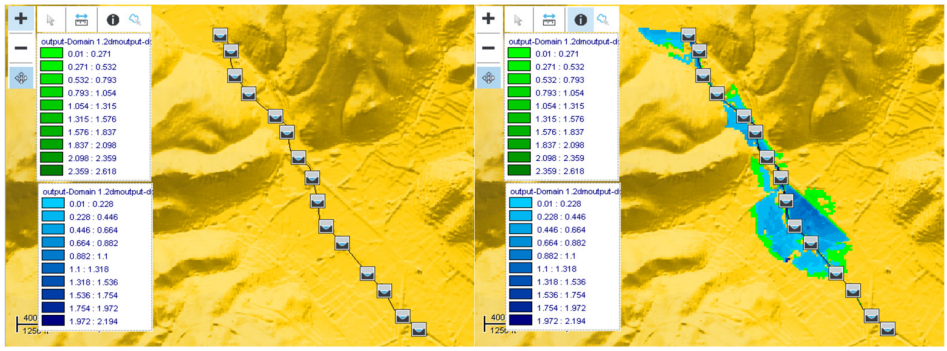

Time = 17 hours Time = 19 hours

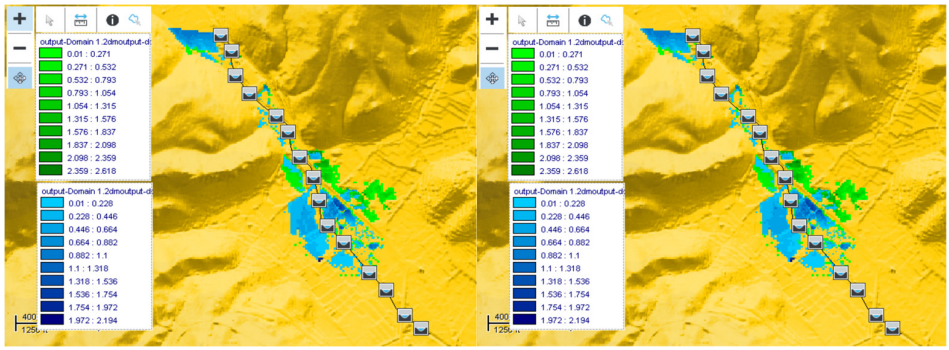

Time = 21 hours Time = 23 hours

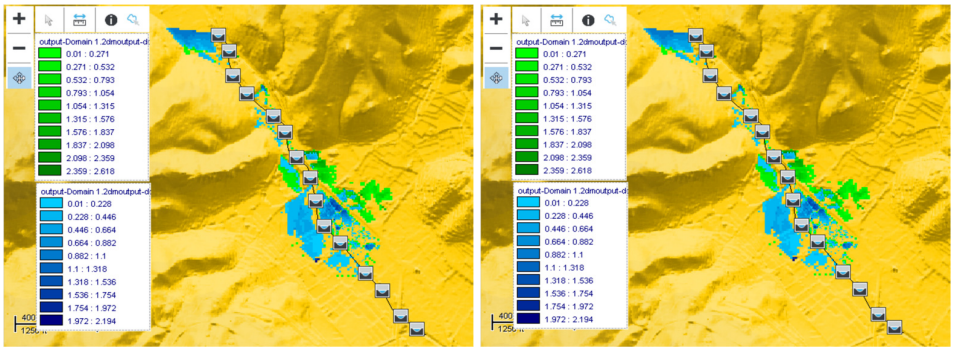

Time = 25 hours Time = 27 hours

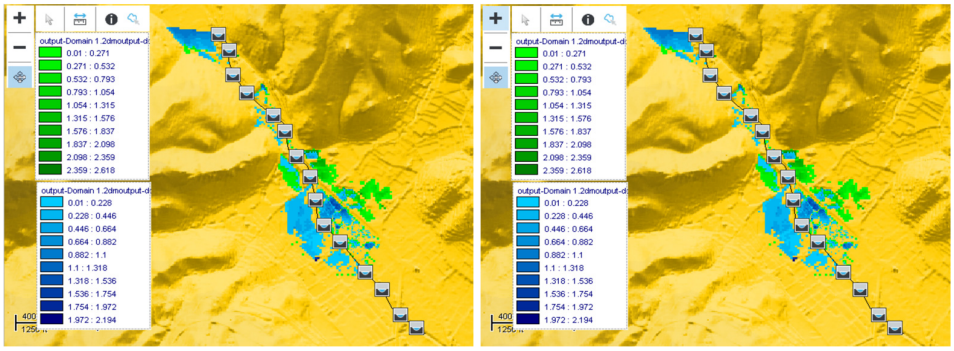

Time = 29 hours Time = 31 hours

Fig. 17. 1D-2D model simulation comparing the 1974 (blue) flood to the effect of climate change (green). The different colours represent different water depths along the floodplain ranging from 0.01–0.23 m with light blue to 1.98–2.19 m in blue and 0.01–0.27 m in light green and 2.36–2.62 m in dark green.

buyers that the property resides in a high-risk flood location which subsequently reduces community flood awareness and increases vulnerability (Rosselló-Geli, 2021).

The resulting significant period of submersion may result in ground saturation and an increase in the level of the groundwater table. Saturation disturbs and degrades the soil's nutrient levels which can consequently damage agricultural crops and biodiversity. Extensive submersion of crops will not only eliminate valuable community food resources, but impact the financial yield available on such products. An increase in the groundwater table will result in an increased risk of imminent future flooding due to current ground saturation. Pressure exerted onto low-lying infrastructural components could result in significant damage. To exacerbate the impacts, the flow magnitude and velocities witnessed will result in soil erosion which will reduce soil stability and hence increase Sóller's exposure to flooding.

The velocity reaches its peak within the channel for all cross-sections, with a maximum peak at CS8. A higher velocity transports more debris and sediment, attributing to blockages and increasing flood risk. The ephemeral stream contains no flow under normal conditions, therefore despite the low magnitude of the velocity, the sudden increase may exert unique pressures on the channel. The peak velocity on the floodplain also occurs at CS8. The velocity is only sustained for a short period, but it remains to have the capacity to cause damage due to the dynamic pressure of the water flow.

The hydrostatic pressure exerted by the water depth and flood submersion time will impact both the channel and the floodplain infrastructure. The maximum pressure occurs at CS1, at a value of 8.63 kilopascals (kPa). This represents only 21% of the minimum pressure required to crush limestone (Pabon, 2019). Despite the pressure weakness, pressure accumulation due to submersion time has the ability to disrupt the structural integrity of the channel and surrounding infrastructure. This coupled with bed and wall erosion and infrastructure scour will only worsen the effects.

Further to this, the main road to the coast is flooded for approximately 3 hours, thus temporarily causing traffic disruption and dangerous driving conditions. Additionally, it was reported locally that the flood structurally damaged the road thus, causing further disruptions and economic impacts (BMS, 2021b). The local tram line that also runs alongside the road was also flooded for over 3 hours.

Considering the time of the flood event, it is unlikely that any sufficient or sophisticated rescue and medical resources were available. Socially, this would have caused stress and worry within the community. These social impacts in conjunction with the previously mentioned economic effects would have had a great impact on the communities wellbeing and livelihoods. Further to this, the 3 consecutive catastrophic floods of 1972–1974 would have likely reduced the town and community resilience, hence the 1974 flood could have been more devastating than expected.

6.2 Model limitations

The primary limitation of the hydraulic model relates to the limited information available regarding the 1974 flash flood in Sóller. The available documentary sources of (eye-witness flood mark, approximate flood reach locations) increase the uncertainty associated with the results. Additionally, mirroring the 1978 flood hydrograph introduces some further uncertainties and more in depth research is required into the shape of the hydrograph for the area. To reduce uncertainties, comparing a model with accurately collected data to the same scenario but with less reliability will highlight anomalies and suggest improvements.

Furthermore, a limitation of the 1D Model relates to the one-dimensionality assigned to the floodplain. Its nature prompts the assumption that the inflow hydrograph is input across the entire cross-section, whereas in reality the water would only enter at the streams channel. Modelling in 1D also assumes a constant water level rise despite infrastructure blockages and due to the input, set flood reach boundaries. This restricts the simulation of a natural flood reach and path and therefore does not allow for an organic flood progression and representation. These limitations however, are overcome in the 1D-2D linked model. A progression of the research could examine the influence of the 1D limitations by comparing the 1D and 1D-2D model results.

Generally, research does not consider inevitable river blockages such as trees and debris, which will provide obstruction. Blockages are unpredictable and vary depending on the catchment and flood severity however they would likely intensify flood's impact. The model assumes that debris does not provide any further obstruction. However, this is not a realistic view and must be considered as an intensifying factor.

7 CONCLUSION

This research highlights the significant effects of flash flooding on Soller, Mallorca. It clearly demonstrates that both catchment and topographical characteristics play a significant role in flood parameters and thus impacts. The degree of interaction between the flood path and surrounding infrastructure determines the scope of impacts and the risk of damage. Due to the densely populated upstream catchment, this increases vulnerabilities.

The research shows the importance of hydraulic modelling in informing future flood risk within the area. Climate change will lead to an increase in the frequency and magnitude of extreme weather and thus will lead to more flash flood events. With regards to Soller, this will widen and deepen flood paths, hence potentially worsening flood effects. Flash flooding will continue to be of significant concern in Soller and therefore it is vital to increase awareness and encourage action to be taken.

Flooding is a multi-disciplinary hazard that interests geographers, engineers, social scientists and locals. It is important therefore, to pave new avenues for bringing all this knowledge together in a multi-disciplinary way as it is the only way to approach these events and understand them in a holistic way.

Acknowledgements. The authors are grateful to Jacobs for providing a Flood Modeller licence for educational purposes and allowing us to undertake this research. Additionally, we would like to show our gratitude to Antoni Quetglas, Sóller Municipal Archivist, for his help in accessing the newspaper's data and bridge blueprints.

REFERENCES

Alcoverro, J., Corominas, J., Gomez, M., 1999. The Barranco de Arás flood at 7 august 1996 (Biescas, Central Pyrenees, Spain). Engineering Geology, 51, 10, 237–255.

AMS, 2021. Projectes de construcció i reparació de ponts. Folder 4387. Arxiu Municipal de Sóller (AMS).

Barriendos, M., Llasat, M.C., 2003. The case of the Maldà anomaly in the Western Mediterranean basin (AD 1760-1800): an example of strong climatic variability. Climatic Change, 61, 191–216.

BMS, 2021a. Collecció Setmanari Sóller, nº 4542, April 4th 1974. Biblioteca Municipal de Sóller (BMS). Consulted on: 25 September 2021.

BMS, 2021b. Collecció Setmanari Sóller, nº 4544, April 20th 1974. Biblioteca Municipal de Sóller (BMS). Consulted on: 25 September 2021.

Clark, D., 2011. How will climate change affect rainfall? Available at: https://www.theguardian.com/environment/2011/dec/15/climate-change-rainfall. [Accessed on 18 April 2021]

Cos, J., Doblas-Reyes, F., Jury, M., Marcos, R., Bretonnière, P-A, Samsó, M., 2022. The Mediterranean climate change hotspot in the CMIP5 and CMIP6 projections. Earth System Dynamics, 13, 321–340.

Costa, J.E., 1987. Comparison of the largest rainfall-runoff floods in the United States with those of the People's Republic of China and the world. Journal of Hydrology, 96, 1–4, 101–115.

Creutin, J.D., Borga, M., 2003. Radar hydrology modifies the monitoring of flash floods. Hydrological Processes, 17, 1453–1456.

Elleder, L., 2010. Reconstruction of the 1784 flood hydrograph for the Vltava River in Prague, Czech Republic. Global and Planetary Change, 70, 117–124.

Elleder, L., Herget, J., Roggenkamp, T., Niessen, A., 2013. Historic floods in the city of Prague—A reconstruction of peak discharges for 1481-1825 based on documentary sources. Hydrology Research, 44, 202–214.

Gaume, E., Borga, M., 2008. Post-flood field investigations in upland catchments after major flash floods: proposal of a methodology and illustrations. J. Flood Risk Management, 1, 175–189.

Gaume, E. et al., 2009. A collation of data on European flash floods. Journal of Hydrology, 367, 70–78.

Gaume, E. et al. Sub-chapter 1.3.4. Mediterranean extreme floods and flash floods. In: The Mediterranean region under climate change: A scientific update [online]. Marseille: IRD Éditions, 2016 (generated 30 mars 2022). Available on the Internet: <http://books.openedition.org/irdeditions/23181>. ISBN: 9782709922203. DOI: https://doi.org/10.4000/books.irdeditions.23181

Google Earth., 2021. Plan view of Soller and model river cross sections. Google Earth[online]. Available at: https://earth.google.com/web/. [Accessed on: 18 November 2021].

Herget, J., Meurs, H., 2010. Reconstructing peak discharges for historic flood levels in the city of Cologne, Germany. Global and Planetary Change, 70, 108–116.

Herget, J., Roggenkamp, T., Krell, M., 2014. Estimation of peak discharges of historical floods. Hydrology and Earth System Sciences, 18, 4029–4037. DOI: 10.5194/hess-18-4029-2014

IDEIB, 2021. Digital Elevation Model of the Balearic Islands. Available from: http://ideib.caib.es/cataleg/srv/cat/catalog.search;jsessionid=18BCF32A72E2E70D3D78E0177870BC3A#/metadata/16A574B8-7099-4E04-8757-71BF0BEB1786 [Accessed 18 November 2021]

Jacobs., 2020. Flood Modeller (v4.6.7) [computer programme]. Available from: Flood Modeller | Industry leading flood modelling software [Accessed 16 February 2022].

Llasat, M.C. et al., 2016. Flash floods trends versus convective precipitation in a Mediterranean region. Journal of Hydrology. DOI: 10.1016/j.jhydrol.2016.05.040

Mahmood, S., Khan, A., Ullah, S., 2016. Assessment of 2010 flash flood causes and associated damages in Dir Valley, Khyber Pakhtunkhwa Pakistan. International Journal of Disaster Risk Reduction [Online], 16, 215–223. doi.org/10.1016/j.ijdrr.2016.02.009

Moel, H., van Alphen, J., Aerts, J.C.J.H., 2009. Flood maps in Europe - Methods, availability, and use. Natural Hazards and Earth System Science, 9, 2, 289–301. doi.org/10.5194/nhess-9-289-2009. [Accessed 08 March 2022]

Nunez, C., 2019. Floods Explained [online]. National Geographic. Available at: www.nationalgeographic.com/environment/natural-disasters/floods [Accessed 20 January 2021].

Pabon, C., 2019. How much force is needed to break a cubic metre of stone? Quora. Unpublished.

Romero-Díaz, M.A., López-Bermudez, F., 1987. Morfometría de redes fluviales: revisión crítica de los parámetros más utilizados y aplicación al Alto Guadalquivir. Papeles de Geografía (Física), 12, 47–62.

Rosselló-Geli, J., 2000. Cabals a la vall de Sóller: episodis d'escorrentia intensa. Master's Thesis. Universitat de les Illes Balears. Palma de Mallorca. 156 p.

Rosselló-Geli, J., 2021. Discussion of progress and summary of hydraulic model. Unpublished.

Rosselló-Geli, J., Cortés, M., 2021. La prensa local, fuente para el estudio de inundaciones: el semanario Sóller (Mallorca) de 1900 a 200. Ería, 2, 2, 207–222.

Rullan, J., 1885. Inundación de Sóller y Fornalutx. Imprenta Felipe Guasp, Palma de Mallorca.

Sene, K., 2013. Flash Floods Forecasting and Warning. 1st ed. Springer, New York.

Stamataki, I., Kjeldsen, T.R., 2021. Reconstructing the peak flow of historical flood events using a hydraulic model: The city of Bath, United Kingdom. Journal of Flood Risk Management, 14, 3, Article Number: e12719. DOI: doi.org/10.1111/jfr3.12719

Stamataki, I., Kjeldsen, T., 2020. Hydraulic modelling of Bath's historical floods pre-Bath Flood Defence Scheme: Part 1 [Online]. Hydric-Bath. Available from: Hydraulic modelling of Bath's historical floods pre-Bath Flood Defence Scheme: Part I - HYDRIC-BATH (weebly.com) [Accessed 30 March 2021]

Tuel, A., Eltahir, E.A.B., 2020. Why is the Mediterranean a climate change hotspot? Journal of Climate, 33, 14, 5829–5843. DOI: https://doi.org/10.1175/JCLI-D-19-0910.1

Werner, M., Cranston, M., 2009. Understanding the value of radar rainfall nowcasts in flood forecasting and warning in flashy catchments. Meteorological Applications, 16, 1, 41–55.

Wetterzentrale. Atmospheric situation March 29th 1974. Available at: http://wetterzentrale.de. [Accessed on: 15 November 2021]

Wheater, H.S., 2002. Progress in and prospects for fluvial flood modelling. Philosophical Transactions of the Royal Society of London Series A 360, 1409–1431.

Received 27 April 2022
Accepted 13 September 2022

J. Hydrol. Hydromech., 71, 2023, 1, 64–79
https://doi.org/10.2478/johh-2022-0026

sciendo Journal of Hydrology and Hydromechanics Institute of Hydrology SAS

A novel H-shape fishway with excellent hydraulic characteristics

Di Zhang[1], Chunming Liu[1], Xiaotao Shi[2*], Yakun Liu[1], Yingmin Qu[1]

[1] School of Hydraulic Engineering, Faculty of Infrastructure Engineering, Dalian University of Technology, Dalian, 116024, China.
[2] Hubei International Science and Technology Cooperation Base of Fish Passage, China Three Gorges University, Yichang, 443002, China.
[*] Corresponding author. Tel.: +86-0717-6394339. E-mail: fishlab@163.com

Abstract: Fishway design not only takes into account the swimming abilities of target fishes, but also considers the hydrodynamic characteristics within the fishway. In this study, the flow fields of one vertical-slot fishway (*i.e.* VSF), five T-shape fishways (*i.e.* TSF-1~TSF-5) and two H-shape fishways (i.e. HSF-1 and HSF-2) are numerically simulated by solving the three-dimensional Reynolds-averaged Navier-Stokes equations and the K-Omega-SST turbulence model. The numerical results clearly indicate that the hydrodynamic properties of HSF-2 are overall superior to the remaining seven cases, in terms of the time-averaged flow pattern, the time-averaged velocity magnitude, the depth-mean time-averaged velocity magnitude along the vertical-slot section, the volume percentages of the time-averaged velocity magnitude less than some critical values, and the distribution of the time-averaged turbulent kinetic energy. Therefore, HSF-2 is more friendly for fishes with relatively smaller sizes and weaker swimming capacities to transfer upstream. The novel HSF-2 is firstly proposed in this paper, and it is naturally designed during the process of improving the flow regime. Furthermore, the generalizability of the superiority of HSF-2 over VSF and the original T-shape fishway (*i.e.* TSF-1) has been exhibited with the aid of the numerical results of four operating conditions (*i.e.* Q = 400 L/s, 600 L/s, 800 L/s and 1000 L/s).

Keywords: Hydraulic characteristics; Vertical-slot fishway; H-shape fishway; T-shape fishway; Turbulent kinetic energy; K-Omega-SST turbulence model.

INTRODUCTION

The construction of transverse dams truncates the natural rivers, hinders the feeding and reproduction of migratory aquatic organisms, and consequently results in their reduction and even their extinction (Santos et al., 2012). In order to restore the connectivity and the biological diversity of the river, the construction of such objects is often accompanied by the building of some fish passage facilities, usually fishways (Rodríguez et al., 2006). The water depth, the velocity field, the turbulent kinetic energy and the energy dissipation rate are the key factors affecting the success of fish passage (Puertas et al., 2012). For the purpose of changing the hydrodynamic conditions and providing a more suitable environment for fish to swim upstream, the structural features of the fishway have been optimized by many scholars all over the world.

There are many fishway types, such as the Denil fishway, the pool-weir fishway, the vertical-slot fishway (VSF), the multi-slot fishway (MSF), the T-shape fishway (TSF), and so on (An et al., 2019; Bombač et al., 2017; Yagci, 2010). Denil fishway is a rectangular channel consisting of a series of equally spaced baffles at an angle of 45 degrees to the reverse flow, and those baffles can consume the energy and reduce the flow velocity in the pools. Rajaratnam and his coauthors (Katopodis et al., 1997; Rajaratnam et al., 1984) determined the relationship between the dimensionless flow and the relative flow depth in the standard or non-standard Denil fishway. Normally, the Denil fishway has a steep bed slope ranging from 15 to 25 percent, and is only suitable for fish larger than 300 mm.

The pool-weir fishway, which is composed of a series of weirs with or without orifices and notches, is designed for fishes with strong swimming ability (Yagci, 2010). The fishes use their burst swimming speed to swim over or jump over the weir (Rajaratnam et al., 1989). There are three main types of flow regimes in the pool-weir fishway, including the plunging flow, the transitional flow and the streaming flow (Ead et al., 2004).

In a vertical-slot fishway, different pools are separated by baffles and there is a vertical-slot between two adjacent pools. Fish can move from one pool to another through the vertical-slot (Fuentes-Pérez et al., 2014; Fuentes-Pérez et al., 2019). Rajaratnam et al. (1992) summarized the experimental results of 18 design schemes, and believed that the hydrodynamic environment was the most suitable for fish passage when the length-width ratio of the pool was equal to 10:8.

Most of the early fishways were designed for large economic species (*e.g.* salmon) (Katopodis and Williams, 2012), which tend to have a strong swimming ability. However, researchers found that smaller non-salmon species have difficulties passing through fishways with high velocity and turbulent kinetic energy (Quaresma et al., 2018). In order to reduce both the velocity magnitude and the turbulent kinetic energy within the pool, the T-shape fishway (Mao et al., 2012; Mao et al., 2019) was recently introduced providing a friendly hydrodynamic environment for fishes with relatively smaller sizes or with relatively weaker swimming and jumping capacities. The T-shape fishway (TSF), designed by Mao et al. (2012), consists of two symmetric lateral long baffles, one central T-shape pier, and two symmetric drop sills, as shown in Fig. 1. Due to the existence of the T-shape pier and the drop sill, TSF can consume the water energy adequately. Besides, being similar to VSF, the vertical-slot of TSF extends through the entire height of the pool, and therefore TSF can be suitable to fishes preferring to swim at different water depths. Mao et al. (2012, 2019) simplified the T-shape fishway by removing the two drop

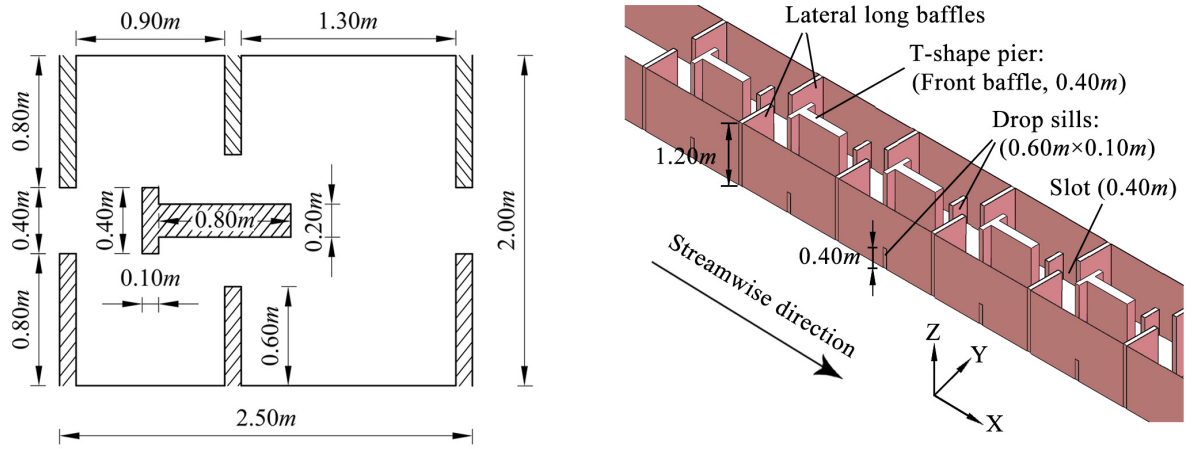

Fig. 1. The TSF designed by Mao et al. (2012). (a) plan view, and (b) 3D topology.

sills, and studied the influences of changing the pool length, the front-baffle length, and the distance between the front baffle and the vertical-slot.

This paper aims to firstly optimize the vertical-slot width of the T-shape fishway by making a comparison of four TSF cases (*i.e.* TSF-1, TSF-2, TSF-3 and TSF-4). Based on the optimum vertical-slot width, other three novel schemes (*i.e.* TSF-5, HSF-1 and HSF-2) are further designed and analysed. By comparing all the aforementioned eight fishways in terms of flow pattern, velocity field and turbulent kinetic energy, the optimal scheme (*i.e.* HSF-2) is recommended. Additionally, the generalizability of the superiority of HSF-2 over VSF and TSF-1 is demonstrated by the numerical results of four operating conditions.

MATERIALS AND METHODS

Numerical model

The numerical simulations are performed by using the Open Source Field Operation and Manipulation (OpenFOAM) C++ libraries. Model uses unsteady 3D continuity equation and Reynolds-Averaged Navier-Stokes (RANS) equation which can be described as (Zhang et al., 2021):

$$\frac{\partial \rho}{\partial t}+\frac{\partial\left(\rho \overline{u}_i\right)}{\partial x_i}=0 \tag{1}$$

$$\frac{\partial \overline{u}_i}{\partial t}+\frac{\partial}{\partial x_j}\left(\overline{u}_i \overline{u}_j+\overline{u_i' u_j'}\right)=-\frac{1}{\rho} \cdot \frac{\partial \overline{p}}{\partial x_i}+\nu \frac{\partial}{\partial x_j}\left(\frac{\partial \overline{u}_i}{\partial x_j}+\frac{\partial \overline{u}_j}{\partial x_i}\right) \tag{2}$$

where the subscripts i and j represent the i^{th} and j^{th} components of the Cartesian coordinate respectively, $\overline{u}$ and $\overline{p}$ indicate the time-averaged velocity and pressure fields respectively, t is the time, ρ is the density of the fluid, and ν is the kinematic viscosity of the fluid.

The interface between the water and the air is obtained by solving the advection equation of the volume of fraction (VOF), which can be written as (Zhang et al., 2014):

$$\frac{\partial \alpha_q}{\partial t}+\overline{u}_i \frac{\partial \alpha_q}{\partial x_i}=0 \tag{3}$$

where α_q is the volume fraction of the water. The improved unsteady K-Omega-SST turbulence model developed by Menter et al. (2003) is adopted here:

$$\frac{\partial k}{\partial t}+\frac{\partial\left(\overline{u}_i k\right)}{\partial x_i}=\tilde{P}_k-\beta^* k \omega+\frac{\partial}{\partial x_i}\left[\left(\nu+\sigma_k \nu_t\right) \frac{\partial k}{\partial x_i}\right] \tag{4}$$

$$\frac{\partial \omega}{\partial t}+\frac{\partial\left(\overline{u}_i \omega\right)}{\partial x_i}=\alpha \frac{\tilde{P}_k}{\nu_t}-\beta \omega^2+\frac{\partial}{\partial x_i}\left[\left(\nu+\sigma_\omega \nu_t\right) \frac{\partial \omega}{\partial x_i}\right]+ +2\left(1-F_1\right) \sigma_{\omega 2} \frac{1}{\omega} \frac{\partial k}{\partial x_i} \frac{\partial \omega}{\partial x_i} \tag{5}$$

$$\nu_t=\frac{\alpha_1 k}{max\left(\alpha_1 \omega, S F_2\right)} \tag{6}$$

where k is the turbulent kinetic energy, ω is the specific dissipation rate, ν_t represents the turbulent viscosity, S is the invariant measure of the strain rate, F_1 is the first blending function, F_2 is the second blending function, and $\tilde{P}_k$ denotes the limited value of the k production term.

Numerical scheme

The Pressure Implicit with Splitting of Operators (PISO) algorithm is utilized to deal with the pressure–velocity coupling problem on a collocated grid system in the context of finite volume method (FVM) (Zhang et al., 2014). The MUSCL scheme is employed to discretize the convection term, because various TVD/NVD schemes are able to provide good resolution in the steep gradient region without introducing spurious oscillations and at the same time have at least second-order accuracy in smooth regions (Zhang et al., 2015). The Gauss linear scheme is chosen to discretize the diffusion term and the pressure gradient term, and the second order Crank-Nicolson scheme is applied for the temporal discretization. The convergence criterion within one-time step is set as 10^{-9} for the VOF equation, but 10^{-7} for the continuity equation, the momentum equation, the k equation and the ω equation. The grid details of different cases are given out in Table 1, and will be discussed in a later section.

Table 1. The grid properties for all the cases.

Cases		Grid size ($\Delta x \times \Delta y$) (m)	Grid size (Δz) (m)	Grid number (10^6) Each pool	Grid number (10^6) Total cells
Coarse mesh (VSF)	Pool	0.060×0.060	0.030–0.034	0.121	1.227
	Slot	0.039×0.039			
Medium mesh (VSF)	Pool	0.050×0.050	0.026–0.030	0.226	2.077
	Slot	0.028×0.028			
Fine mesh (VSF)	Pool	0.040×0.040	0.020–0.026	0.411	3.518
	Slot	0.024×0.024			
TSF-1~TSF-5	Pool	0.044×0.044	0.026–0.030	0.337~0.372	3.411~3.820
	Slot	0.028×0.028			
HSF-1~HSF-2	Pool	0.044×0.044	0.026–0.030	0.328~0.330	3.436~3.447
	Slot	0.028×0.028			

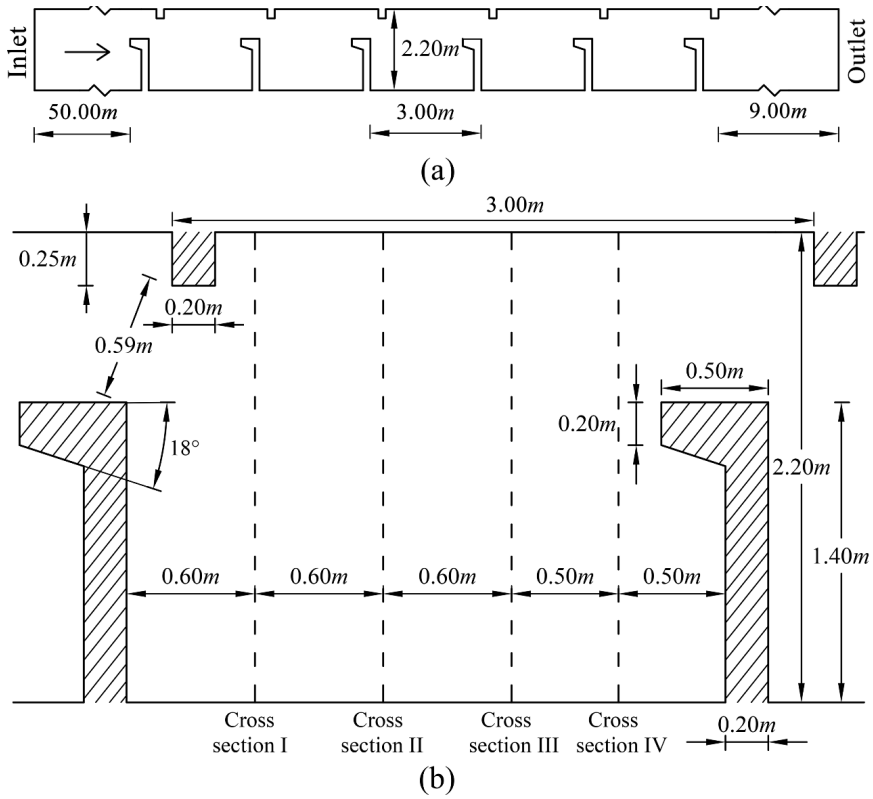

Fig. 2. The VSF studied by Bombač et al. (2014, 2015, 2017). (a) plan view, and (b) details of the pool.

Model validation

Test configuration

To validate the model, the vertical-slot fishway (VSF) studied by Bombač et al. (2014, 2015, 2017) was used as the validation test, and was simulated by simultaneously solving the aforementioned 3D continuity equation, the RANS equation, the VOF equation and the K-Omega-SST model. In addition to experimental results, Bombač et al. (2014, 2015) carried out the numerical study of their VSF as well, utilizing three different turbulent models (*i.e.* the constant eddy viscosity model, the Smagorinsky LES model and the *k*-*ε* model). The VSF considered in this paper was practically built at the Arto-Blanca hydropower plant, and extensive field measurements, physical model tests (1:4.4 scale) and numerical simulations of the flow field were carried out in the literature. Therefore, the VSF studied by Bombač et al. (2014, 2015, 2017) is selected as the validation case here. As shown in Fig. 2, the vertical-slot fishway is composed of five pools, each pool has a length of 3.0 m and a width of 2.2 m, the slot width is set as 0.59 m, and the thickness of the long/short baffles is equal to 0.2 m. The bed slope of the test VSF is S_0 = 1.67%, and the flow discharge is constant Q = 0.6 m^3/s. In order to ensure that the flow within the middle pool is not affected by the inlet and outlet boundary conditions, Bombač et al. (2014) claimed that a 6.0 m long inlet reach and a 9.0 m long outlet reach were necessary during their simulation. Although the outlet plane is also fixed at 9.0 m downstream of the last pool in the present study, considering that both the velocity data and the water depth are not available within the 6.0 m long inlet reach, the inlet plane of the fishway is actually further extended to the location 50 m upstream of the first pool, as illustrated by Fig. 2, which makes it possible to exert the uniform flow condition at the inlet plane.

Computational grids

In the present study, the computational domain is discretized by a non-uniform structured mesh, and three mesh levels are taken into account, namely Coarse mesh, Medium mesh and Fine mesh, which consist of 1.227 million, 2.077 million and 3.518 million cells, respectively, in order to perform the grid-independence verification and guarantee sufficient grid resolution. In view of larger velocity at the vertical-slot, a relatively smaller mesh size is adopted for this position, namely 0.039 m for Coarse mesh, 0.028 m for Medium mesh and 0.024 m for Fine mesh, respectively. When it comes to the vertical Z direction, the overall grid size is confined within the scope of 0.030 m–0.034 m (Coarse mesh), 0.026 m–0.030 m (Medium mesh) and 0.020 m–0.026 m (Fine mesh), respectively. The grid properties for all the cases are detailed in Table 1.

Boundary conditions

At the inlet plane, the uniform flow condition is imposed. Since the discharge is equal to Q = 0.6 m^3/s, the slope is S_0=1.67% and the Manning coefficient is selected as n = 0.01 in Bombač et al. (2014, 2015, 2017), employing the hydraulic uniform-flow equation $Q=A\frac{1}{n}R^{2/3}S_0^{1/2}$ leads to the uniform-flow water depth (*i.e.* $\overline{h}_{in}$) and the uniform-flow velocity (*i.e.* $\overline{u}_{in}$) of $\overline{h}_{in}$ = 0.102 m and $\overline{u}_{in}$ = 2.674 m/s, respectively. As stated by Bombač et al. (2014), the water depth at the outlet plane is fixed as $\overline{h}_{out}$ = 0.88 m.

At the outlet plane, the convective outflow condition is prescribed for the velocity field. In addition, the standard atmospheric pressure is specified on the top boundary, and the non-slip boundary condition is employed for the bottom plane and all the solid surfaces, which means that both the normal and tangential components of the velocity vector are set to zero.

Validation of the results

The depth-mean time-averaged streamwise and spanwise velocities along four cross-sections of the middle pool (*i.e.* Cross section I, II, III and IV depicted in Fig. 2) were presented and discussed in Bombač et al. (2014, 2015). Fig. 3 and Fig. 4

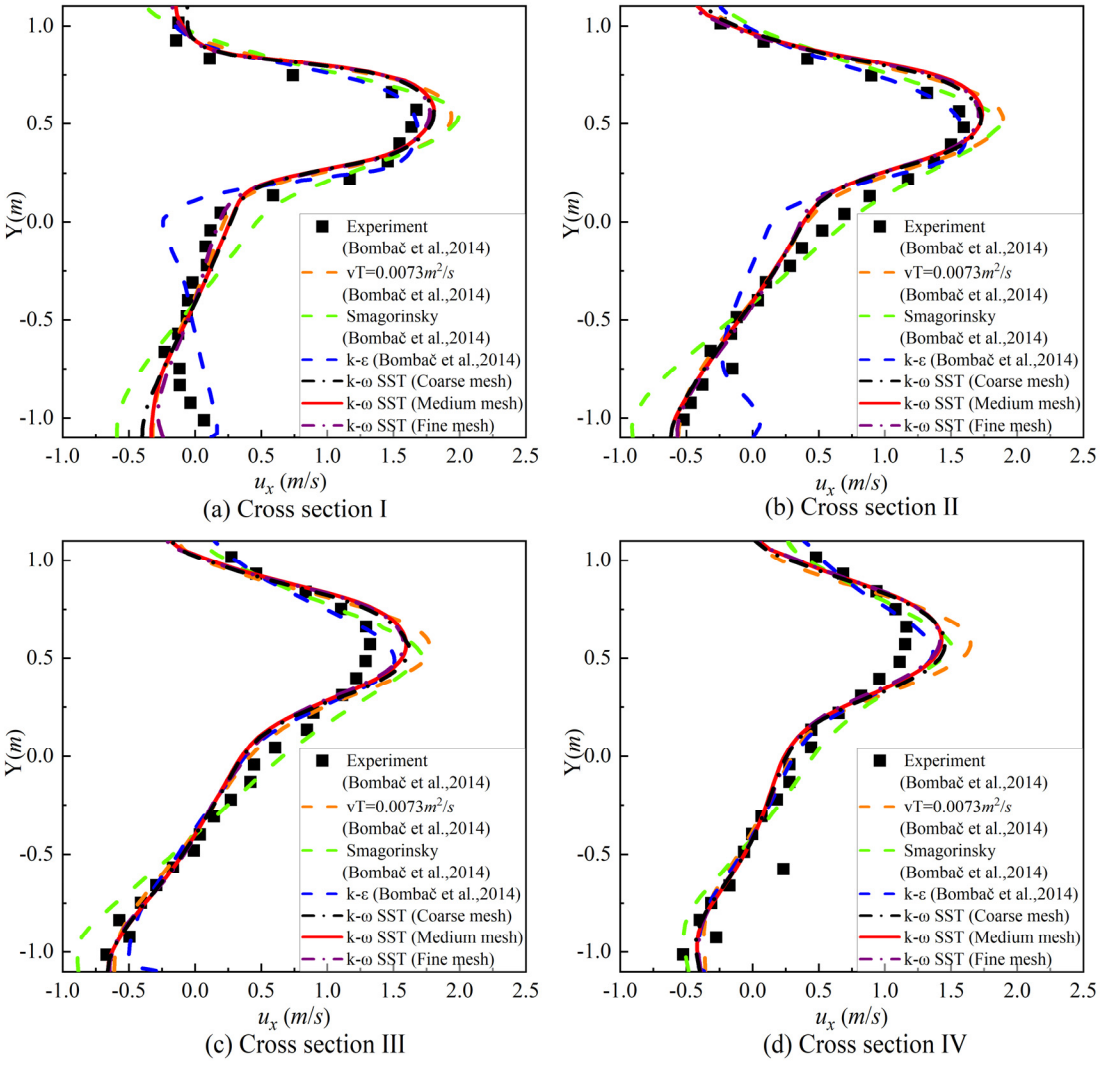

Fig. 3. Comparison of the depth-mean time-averaged streamwise velocity (*i.e.* u_x) for different turbulence models at four cross sections of the validation case VSF.

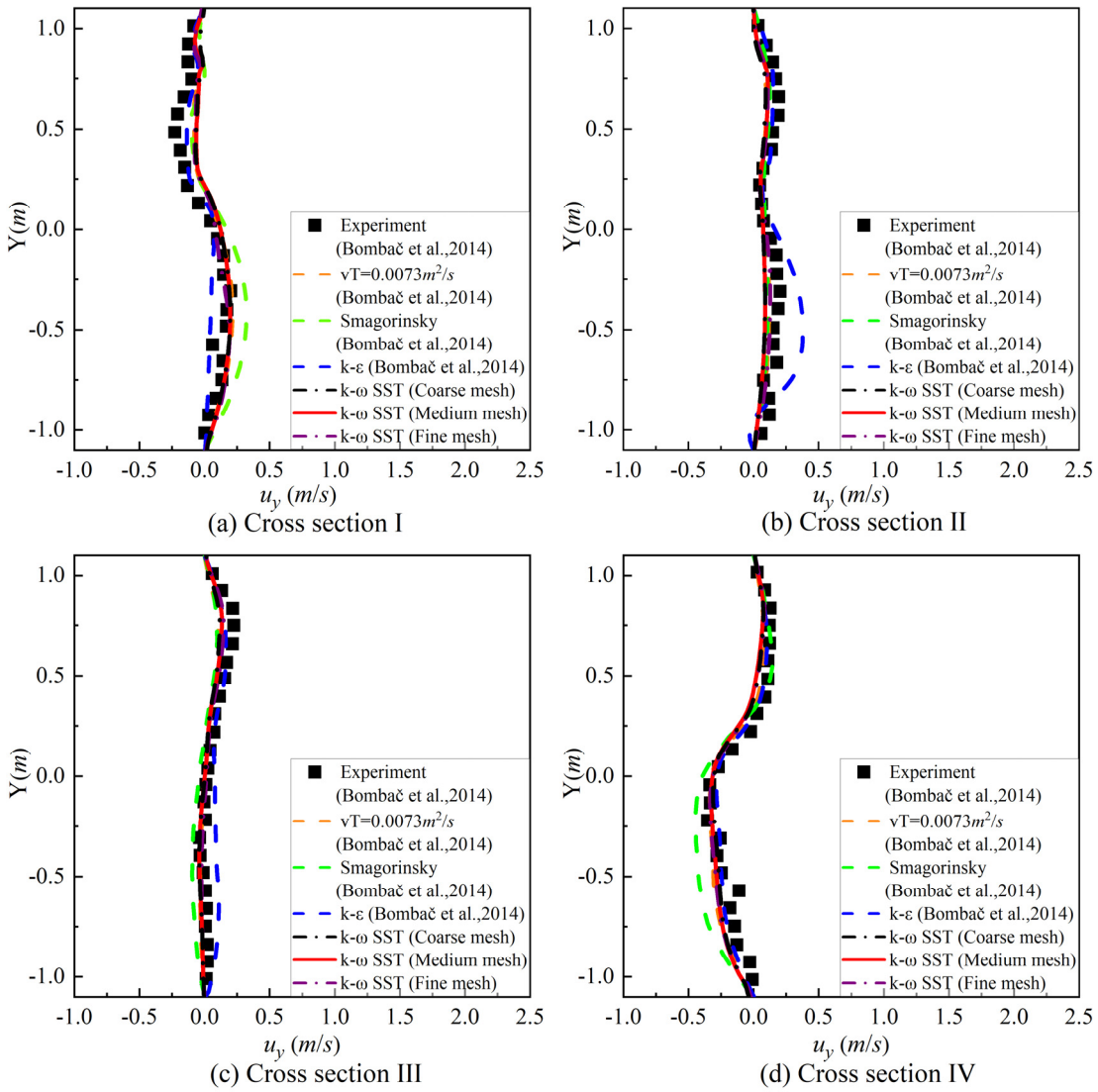

Fig. 4. Comparison of the depth-mean time-averaged spanwise velocity (*i.e.* u_y) for different turbulence models at four cross sections of the validation case VSF.

Table 2. The mean absolute error (MAE) between the experimental data of Bombač et al. (2014) and the numerical data for each cross-section, and the sum of MAE (u_x) and MAE (u_y) for all four representative cross-sections.

Error	Cross section	vT = 0.0073 m²/s	Smagorinsky	*k-ε*	*k-ω* SST
[a] MAE (u_x)	I	0.19	0.24	0.19	0.19
	II	0.15	0.17	0.19	0.15
	III	0.14	0.15	0.09	0.09
	IV	0.15	0.14	0.08	0.11
MAE (u_y)	I	0.07	0.11	0.07	0.07
	II	0.05	0.05	0.08	0.06
	III	0.04	0.07	0.06	0.04
	IV	0.06	0.10	0.04	0.06
[b] MAE (u)		0.85	1.03	0.80	0.77

[a] MAE (u_x) and MAE (u_y) are computed by $\frac{1}{N}\sum_{i=1}^{N}\left|(u_e)_i-(u_n)_i\right|$, where u_e signifies the experimental data of u_x or u_y, and u_n represents the numerical data of u_x or u_y, and N denotes the total number of data in each cross-section. [b] MAE (u) is defined as $\sum\left\{\frac{1}{N}\sum_{i=1}^{N}\left|(u_e)_i-(u_n)_i\right|\right\}$, namely the sum of MAE (u_x) and MAE (u_y) for all four representative cross-sections.

compare the results of the present study to three different turbulent models (*i.e.* the constant eddy viscosity model, the Smagorinsky LES model and the *k*-ε model) and the experimental data in the literature. Furthermore, Table 2 presents the mean absolute error (MAE) between the experimental data and the numerical data for each cross-section. In Table 2, MAE (u_x) and MAE (u_y) are computed by $\frac{1}{N}\sum_{i=1}^{N}\left|(u_e)_i-(u_n)_i\right|$, where u_e signifies the experimental data of u_x or u_y, and u_n represents the numerical data of u_x or u_y, and N denotes the total number of data in each cross-section. Sum of MAE is defined as MAE $(u)=\sum\left\{\frac{1}{N}\sum_{i=1}^{N}\left|(u_e)_i-(u_n)_i\right|\right\}$, and is calculated as the sum of MAE (u_x) and MAE (u_y) for all four representative cross-sections. The medium mesh almost results in the same accuracy as the fine mesh for the present K-Omega-SST model, which proves that the medium mesh is suitable enough under this condition. Table 2 illustrates that the K-Omega-SST model combined with the medium mesh leads to the smallest sum of MAE (MAE (u) = 0.77), which is slightly superior to the *k*-ε model (0.80) and the constant eddy viscosity model (0.85). The Smagorinsky LES model has the largest sum of MAE (MAE (u) = 1.03), which can be ascribed to the fact that the 2D depth-averaged shallow water equations are employed in Bombač et al. (2014, 2015), while the present study employs the 3D numerical model. In the remaining cases of the present study, the medium grid size and the K-Omega-SST turbulence model are adopted, as displayed in Table 1.

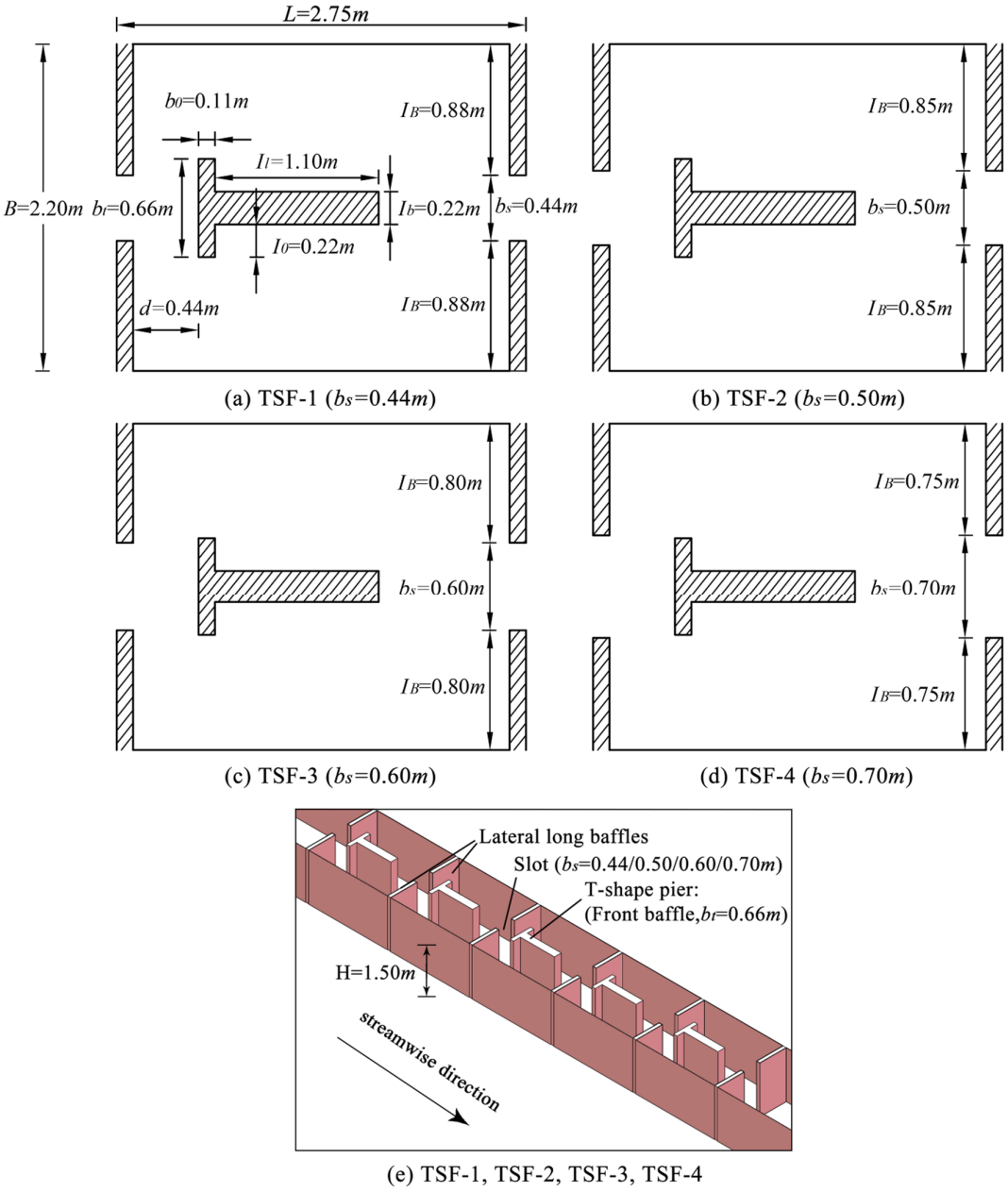

Fig. 5. The concrete sizes and 3D topologies of TSF-1, TSF-2, TSF-3 and TSF-4.

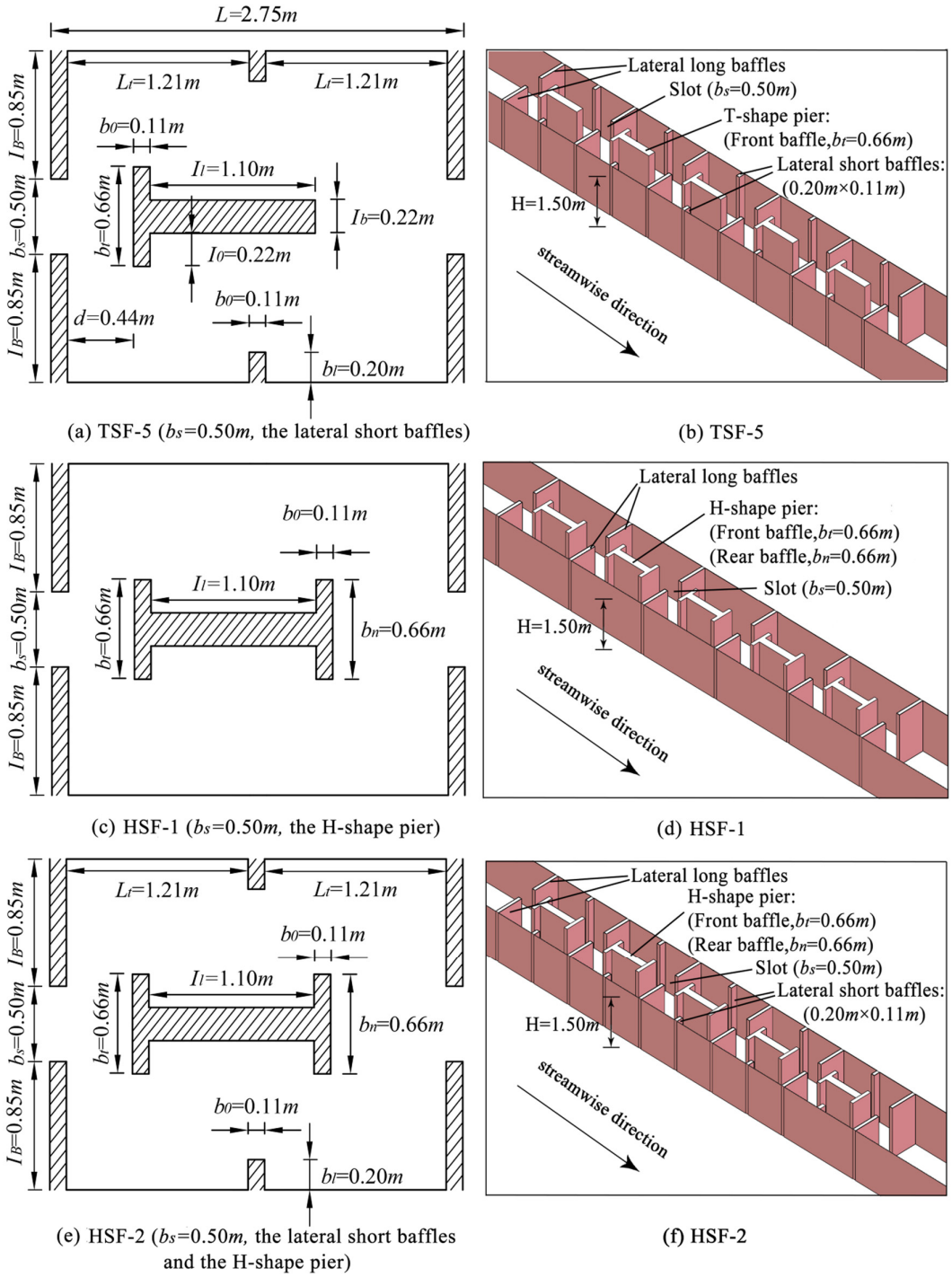

Fig. 6. The concrete sizes and 3D topologies of TSF-5, HSF-1 and HSF-2.

Research scope

This study is dedicated to proposing a novel H-shape fishway during the process of optimizing the original T-shape fishway (*i.e.* TSF-1) designed by Mao et al. (2012, 2019). The equal-proportional scaling has been carried out on the *X-Y* plane, with the purpose of ensuring that TSF-1 has the same width as VSF. Firstly, four tests are performed to ascertain the influence of various vertical-slot widths on the flow characteristics, namely TSF-1 (b_s = 0.44 m), TSF-2 (b_s = 0.50 m), TSF-3 (b_s = 0.60 m) and TSF-4 (b_s = 0.70 m), as shown in Fig. 5. Secondly, based on the optimal vertical-slot width (*i.e.* b_s = 0.50 m, being deduced from the discussions in the next chapter), other three research cases are further put forward, including the T-shape fishway with two lateral short baffles (*i.e.* TSF-5) and the H-shape fishway with or without two lateral short baffles (*i.e.* HSF-1 and HSF-2), as shown in Fig. 6. All the aforementioned seven cases have the characteristic parameters consistent with the validation test, such as the flow discharge (Q = 600 L/s), the bed slope (S_0 = 1.67%), the baffle height (H = 1.50 m) and the pool width (B = 2.2 m), to allow comparison. In addition, four discharges (*i.e.* Q = 400 L/s, 600 L/s, 800 L/s and

1000 L/s) have been simulated in order to exhibit the generalizability of the superiority of HSF-2 over VSF and TSF-1. To provide uniform flow condition at the inlet plane, a 100m long inlet reach is necessary during the simulation of different TSF and HSF schemes at Q = 400 L/s, 600 L/s and 800 L/s, and the corresponding water depth at the outlet plane is set as $\overline{h}_{out}$ = 0.68 m, 0.88 m and 1.078 m, respectively. However, when it comes to Q = 1000 L/s, $\overline{h}_{out}$ should be fixed as 1.30 m according to Bombač et al. (2015), and a 150 m long inlet reach is required for the application of the uniform flow condition at the inlet plane, and seven pools are necessary to provide the flow within the middle pool is not influenced by the inlet and outlet boundary conditions. Although a 6.0 m long inlet reach can be adopted in physical model test and 2D depth-averaged numerical simulation (Bombač et al., 2014; 2015), considering the fact that both the detailed velocity distribution and the water depth should be prescribed at the inlet plane when performing 3D Navier-Stokes numerical simulation, a much longer inlet reach (50 m, 100 m or 150 m) needs to be employed in the present study, because the velocity data and the water depth are not available within the 6.0 m long inlet reach in the literature. Consequently, the computational expense is apparently increased (about 0.25 million grid cells in Bombač et al. (2015), but about 3.5 million grid cells in the present study).

RESULTS AND DISCUSSION

Flow pattern

Fig. 7 presents the 2D time-averaged streamlines and velocity magnitude contours on a typical X-Y plane (*i.e.* the Z = 0.5h plane parallel to the bed) at Q = 600 L/s. The mean time-averaged water-depth of the whole middle pool, h, is listed in detail in Table 3 for different cases. Fig. 7(a) reveals that the

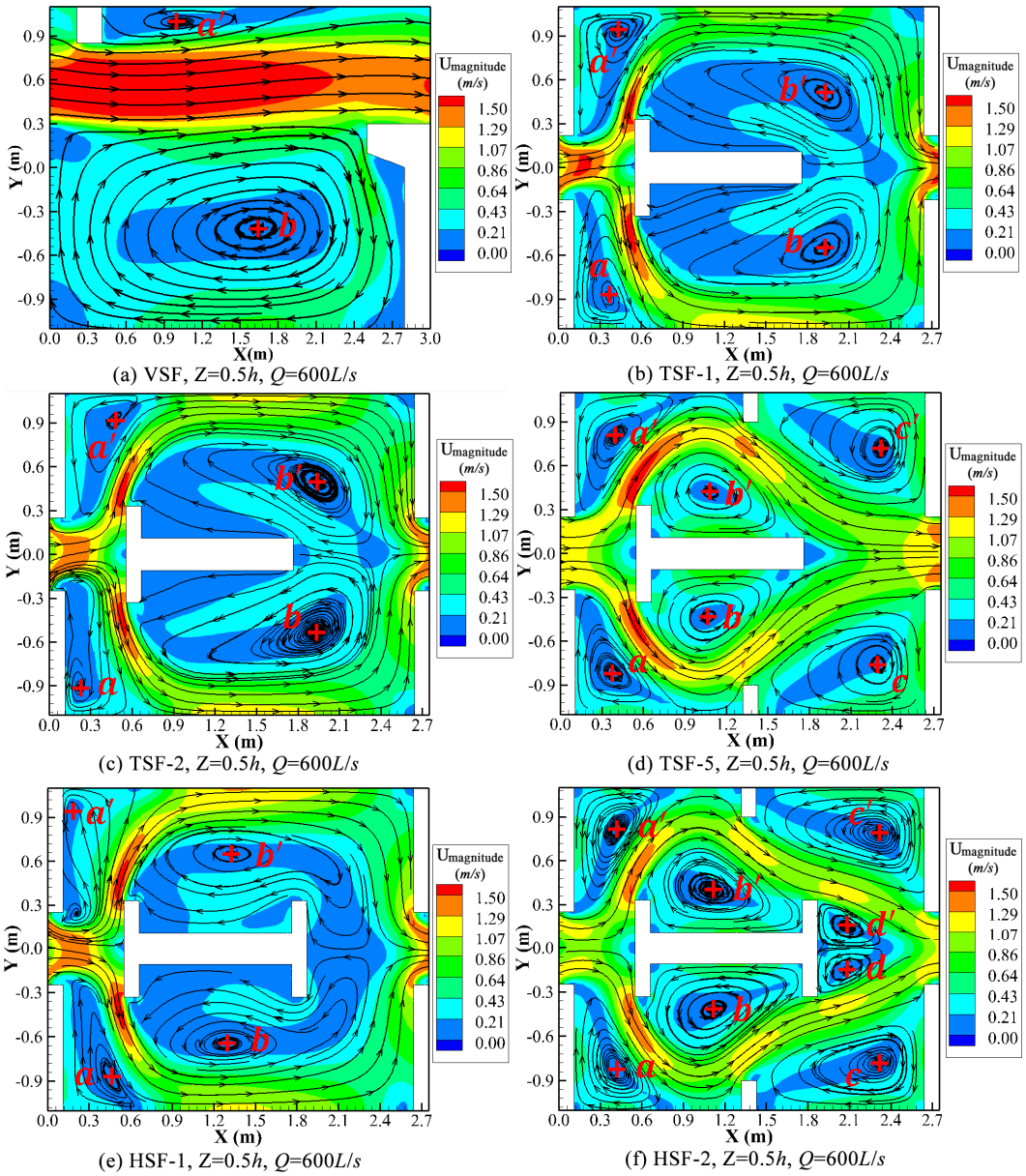

(a) VSF, Z=0.5h, Q=600L/s (b) TSF-1, Z=0.5h, Q=600L/s

(c) TSF-2, Z=0.5h, Q=600L/s (d) TSF-5, Z=0.5h, Q=600L/s

(e) HSF-1, Z=0.5h, Q=600L/s (f) HSF-2, Z=0.5h, Q=600L/s

Fig. 7. The 2D time-averaged streamlines and velocity magnitude contours in the Z = 0.5h plane within the middle pool for six representative cases (*i.e.* VSF, TSF-1, TSF-2, TSF-5, HSF-1 and HSF-2) at Q = 600 L/s, where h represents the corresponding mean time-averaged water-depth of the middle pool.

Table 3. The time-averaged water-depth, velocity-magnitude and turbulent kinetic energy within the middle pool for various cases at a discharge of Q = 600 L/s.

Variables	VSF	TSF-1	TSF-2	TSF-3	TSF-4	TSF-5	HSF-1	HSF-2
[a] h (m)	0.72	1.36	1.30	1.22	1.16	1.06	1.29	1.22
[b] $\mathrm{Max}\{U_{magnitude}\}$ (m/s)	2.07	1.71	1.66	1.75	1.74	1.73	1.70	1.48
[c] $\overline{U_{magnitude}}$ (m/s)	0.65	0.48	0.48	0.51	0.53	0.58	0.48	0.51
[d] k_{max} (m^2/s^2)	0.20	0.18	0.17	0.23	0.21	0.15	0.21	0.14
[e] $\overline{k}$ (m^2/s^2)	0.050	0.050	0.051	0.052	0.052	0.045	0.051	0.044
[f] $U_{magnitude} \le$ 0.30 m/s	35%	42%	44%	42%	39%	25%	51%	43%
$U_{magnitude} \le$ 0.43 m/s	51%	56%	56%	54%	53%	44%	61%	60%
$U_{magnitude} \le$ 0.54 m/s	61%	65%	64%	61%	59%	55%	69%	68%
$U_{magnitude} \le$ 0.66 m/s	68%	73%	72%	69%	66%	64%	76%	75%
$U_{magnitude} \le$ 0.78 m/s	71%	80%	78%	75%	73%	72%	82%	81%
$U_{magnitude} \le$ 0.81 m/s	71%	82%	79%	77%	74%	74%	83%	82%
$U_{magnitude} \le$ 1.00 m/s	75%	91%	89%	86%	83%	85%	92%	92%
$k \le 0.05$ m^2/s^2	63%	59%	56%	54%	54%	58%	59%	62%
$k \le 0.10$ m^2/s^2	83%	94%	93%	93%	94%	98%	94%	99%

[a] h is the mean time-averaged water-depth within the middle pool; [b] $\mathrm{Max}\{U_{magnitude}\}$ represents the maximum time-averaged velocity magnitude within the middle pool; [c] $\overline{U_{magnitude}}$ is the mean time-averaged velocity magnitude within the middle pool; [d] k_{max} indicates the maximum time-averaged turbulent kinetic energy within the middle pool; [e] $\overline{k}$ indicates the mean time-averaged turbulent kinetic energy within the middle pool; [f] $U_{magnitude} \le$ denotes the volume percentages of the time-averaged velocity magnitude less than some critical values within the middle pool.

flow field within the VSF pool is composed of a high-speed main-flow region and two low-speed recirculation regions. Concretely, the main flow directly runs through the adjacent slots without any noticeable deflection and diffusion, one large-scale clockwise vortex *b* can be observed between two neighboring long baffles, and another small counterclockwise vortex *a'* can be identified behind the short baffle.

The only difference among TSF-1, TSF-2, TSF-3 and TSF-4 is the variation of the vertical-slot width, and therefore they exhibit a similar flow pattern. Taking TSF-1 and TSF-2 as an example, as indicated by Fig. 7(b, c), the flow enters into the pool through the vertical-slot and is soon divided into two symmetrically-distributed branches due to the effect of the T-shape pier. The two symmetric branches firstly impinge on the side walls of the pool, next move towards the downstream along the side walls, then collide with the next-pool's two lateral long baffles, subsequently shift towards the central axis within the scope of X = 2.3 m~2.6 m, and finally converge with each other to form the mainstream in front of the next vertical-slot. One pair of recirculation regions (*i.e. a-a'*) are formed behind the two lateral long baffles, and another pair of relatively larger recirculation regions (*i.e. b-b'*) can be detected between the T-shape pier and the mainstream. In fact, Fig. 7(e) manifests that the flow topology of HSF-1 is overall similar to that of various TSF cases, except for the difference concerning the size and shape of two recirculation regions (*i.e. a-a'* and *b-b'*).

For the T-shape fishway with two lateral short baffles (*i.e.* TSF-5), Fig. 7(d) shows that the flow topology between the vertical-slot and the front baffle shares the same properties as various TSF schemes, such as the separation of the mainstream and the formation of *a-a'*. However, in TSF-5, the two symmetric branches will deflect at approximately $X \approx 1.1$ m, and ultimately converge at about $X \approx 2.0$ m slightly behind the trailing end of the T-shape pier. Further, when compared with TSF-1~TSF-4, the size of the vortices *b-b'* is much smaller in TSF-5, and a new pair of vortices (*i.e. c-c'*) can be observed in the downstream of the lateral short baffle. Fig. 7(f) illustrates that the H-shape fishway with two lateral short baffles (*i.e.* HSF-2) possesses the flow pattern that is nearly identical to TSF-5 for the first half of the pool. Nevertheless, when it comes to the flow topology within the second half of the pool, the difference between HSF-2 and TSF-5 becomes significant. Specifically, four pairs of recirculation regions (*i.e. a-a'*, *b-b'*, *c-c'* and *d-d'*) can be identified within the pool of HSF-2.

The recirculation region usually has a relatively lower velocity, and is believed to be beneficial to fish to take a short rest before passing through the high velocity zone (Bombač et al., 2017; Fuentes-Pérez et al., 2016; Yagci, 2010). With respect to the size of the recirculation region, it is not true to say that the bigger the better. Santos et al. (2012) and Tarrade et al. (2008) declared that a too large recirculation region has a tendency to disorient the fishes, which probably stay within the recirculation area for too long. In conclusion, regarding the distribution of the recirculation regions, HSF-2 is superior to the other seven fishway designs, in terms of both the relatively uniformly moderate sizes and the relatively evenly distributed locations of its four pairs of recirculation regions, which avoid the disorientation of the fishes and can provide more rest areas.

Water-depth

Table 3 quantitatively gives the mean time-averaged water-depth within the whole middle pool for various cases. Obviously, the h value of VSF, being equal to 0.72 m, is minimum among all the cases. For TSF-1~TSF-4, with the increase of the vertical-slot width, the h value decreases from h = 1.36 m (in TSF-1) to h = 1.16 m (in TSF-4), because the extended vertical-slot width means a higher discharge capacity for the fishway. In view of the fact that h = 1.06 m in TSF-5 is smaller than h = 1.30 m in TSF-2, and h = 1.22 m in HSF-2 is lower than h = 1.29 m in HSF-1, it can be concluded that the installation of the two lateral short baffles results in the reduction of the h value, although the existence of the two lateral short baffles actually promote the energy consumption of the flow within the pool.

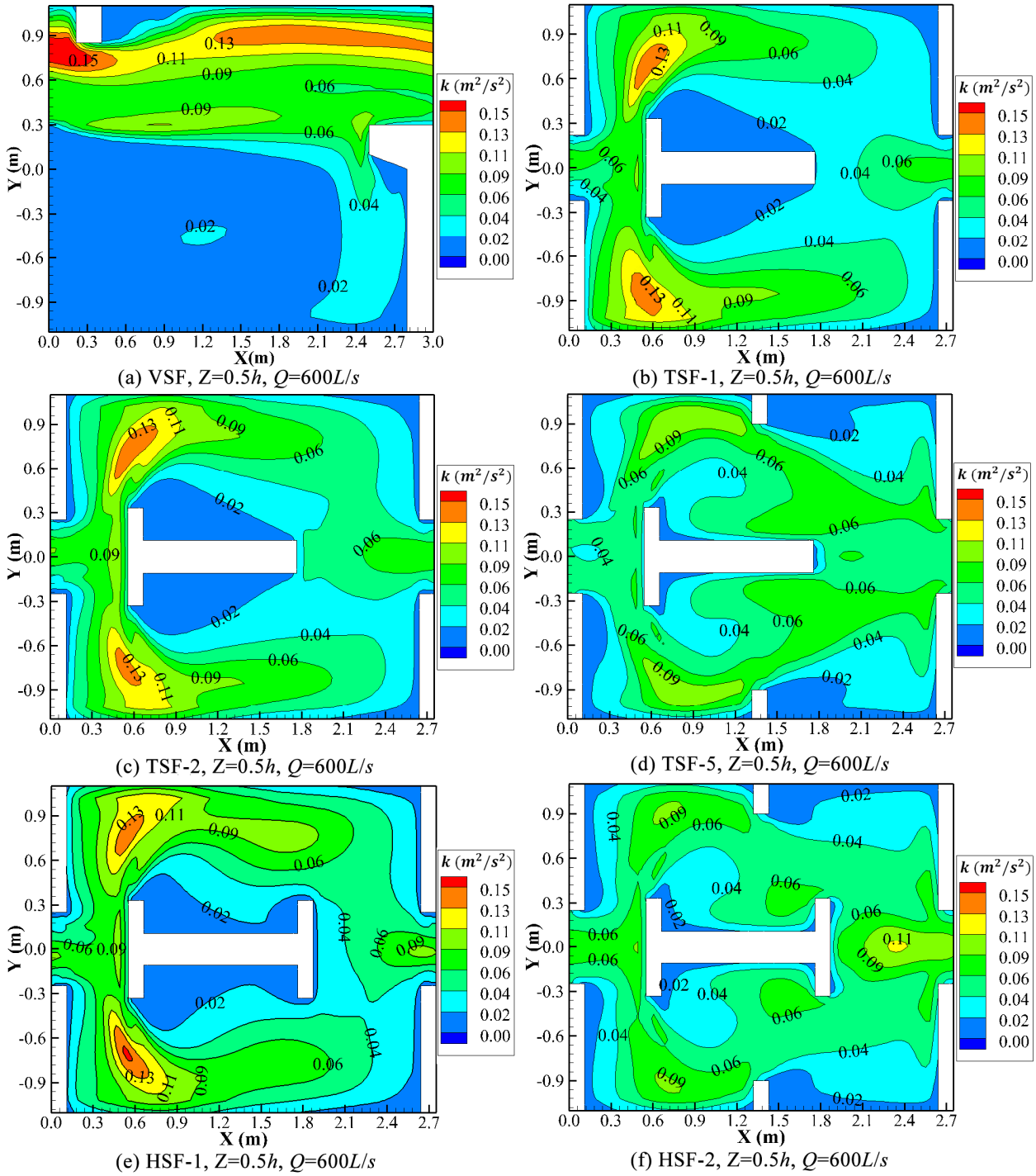

Fig. 8. The 2D contours of the time-averaged turbulent kinetic energy in the $Z = 0.5h$ plane within the middle pool for six representative cases (*i.e.* VSF, TSF-1, TSF-2, TSF-5, HSF-1 and HSF-2) at $Q = 600L/s$, where h represents the corresponding mean time-averaged water-depth of the middle pool.

Velocity field

One of the most important hydraulic parameters influencing the overall effectiveness of the fishway is the velocity magnitude (Fuentes-Pérez et al., 2016). Both the maximum velocity and the mean velocity of the fishway should be as small as possible in order to ensure that fishes are capable of passing through the fishway with high efficiency (Quaresma et al., 2018). For a fixed water-depth or a prescribed discharge, the volume percentages of the velocity lower than the critical swimming speeds of target fishes should be as large as possible.

Concerning the maximum time-averaged velocity magnitude within the middle pool Max$\{U_{magnitude}\}$, Table 3 manifests that HSF-2 has the lowest value (1.48 m/s), being much smaller than the other cases considered. Among the four TSF cases with different vertical-slot widths, Max$\{U_{magnitude}\}$ obtains the minimum value 1.66 m/s in TSF-2 (*i.e.* $b_s = 0.50$ m). This is the reason why the vertical-slot width of TSF-5, HSF-1 and HSF-2

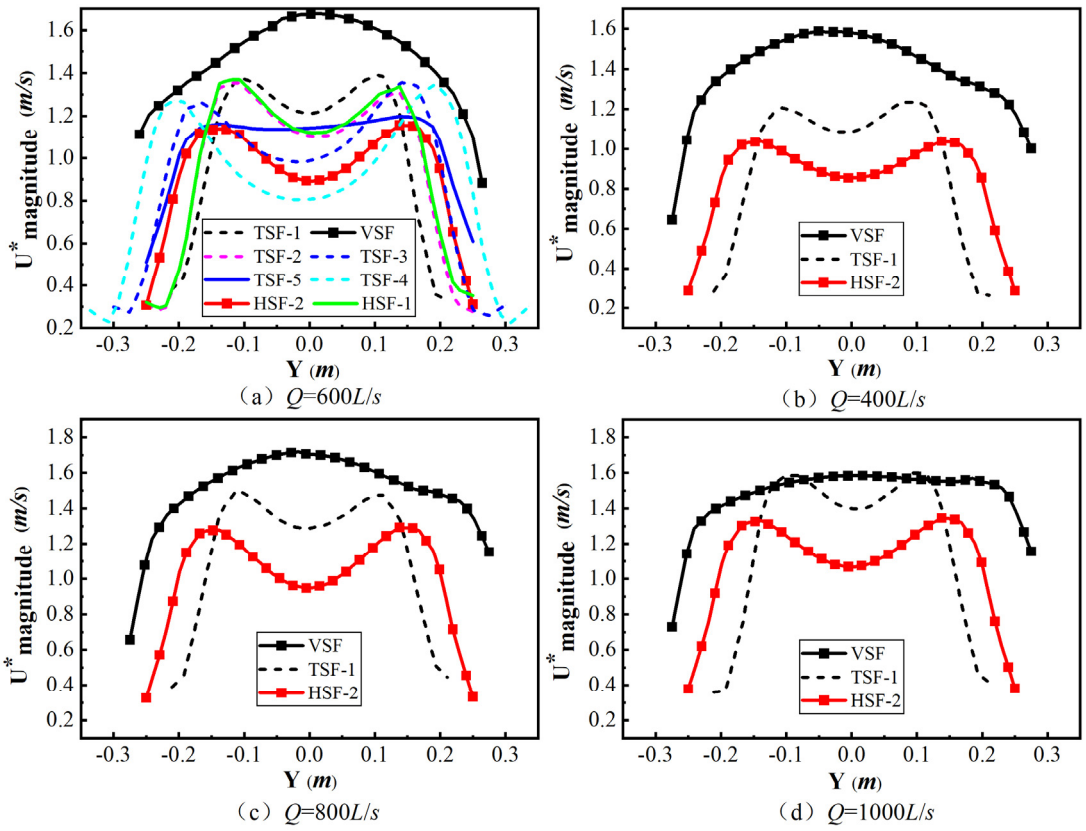

Fig. 9. The depth-mean time-averaged velocity magnitude along the vertical-slot section (*i.e.* $U^*_{magnitude}$) at four discharges (*i.e.* Q = 400 L/s, 600 L/s, 800 L/s and 1000 L/s).

is designed with $b_s = 0.50m$, as shown in Fig. 6. Besides, Fig. 7 reveals that the time-averaged velocity magnitude has relatively larger values in several regions, such as the vertical-slot area, the two sides of the front baffle, and the neighbouring domain of the two lateral short baffles.

With respect to the mean time-averaged velocity magnitude within the middle pool (*i.e.* $\overline{U_{magnitude}}$), Table 3 exhibits that TSF-1, TSF-2 and HSF-1 acquire the smallest value (*i.e.* 0.48 m/s), while TSF-3 and HSF-2 obtain the second lowest value (*i.e.* 0.51 m/s). Marriner et al. (2016) and Quaranta et al. (2019) stated that fish can have a better resting environment when the volume of $U_{magnitude} \leq 0.30$ m/s accounts for about 30%~50% of the entire pool. Obviously, except for the HSF-1 case, where the corresponding value is 51% and thus only slightly out of range, all the other seven research cases do fall within the scope of 30%~50% for $U_{magnitude} \leq 0.30$ m/s. When it comes to the volume percentages of $U_{magnitude} \leq 0.43$ m/s, 0.54 m/s, 0.66 m/s, 0.78 m/s, 0.81 m/s and 1.00 m/s, which are defined as the critical swimming speeds of several fish species given in Quaresma et al. (2018), the superiority of HSF-1 and HSF-2 over the remaining six fishway designs is noticeable, as displayed in Table 3.

The vertical-slot is one of the most crucial regions during the design of the fishway, and the velocity distribution at the vertical-slot section plays a decisive role when evaluating whether fishes can swim upstream successively. Fig. 9(a) makes a comparison of the depth-mean time-averaged velocity magnitude at the vertical-slot section (*i.e.* $U^*_{magnitude}$) at Q = 600 L/s for various cases. For the convenience of comparison, the vertical-slot centre has been translated up to 0.55 m along the Y direction for VSF in order to overlap with that of the other cases. It can be concluded that the maximum value of $U^*_{magnitude}$ for HSF-2 is the smallest among all the cases, and, simultaneously, even with regard to each point of the vertical-slot section, HSF-2 provides relatively low values of $U^*_{magnitude}$.

Turbulent kinetic energy

Turbulent kinetic energy (TKE or k) is another important hydraulic variable when evaluating the effectiveness of the fishway. Considering the fact that high TKE values will pose a negative effect on fish passage, a large area with a low TKE value (usually TKE < 0.05 m^2/s^2) must be guaranteed (Marriner et al., 2016; Quaranta et al., 2017), and the value of 0.10 m^2/s^2 is generally regarded as the maximum acceptable limit for the turbulent kinetic energy within the fishway (Quaranta et al., 2019).

Table 3 provides both the mean time-averaged turbulent kinetic energy $\overline{k}$ and the maximum time-averaged turbulent kinetic energy k_{max} within the middle pool at Q = 600 L/s for all the cases. It is evident that HSF-2 has the value of $\overline{k}$ = 0.044 m^2/s^2 and k_{max} = 0.14 m^2/s^2, respectively, which holds an advantage over the remaining seven cases. Furthermore, in terms of the volume percentages of $k \leq 0.05$ m^2/s^2 and $k \leq 0.10$ m^2/s^2, HSF-2 has a percentage of 62% (being the second largest among all the cases) and 99% (being the largest among all the cases), respectively. In addition, Fig. 8 exhibits the two dimensional contours of the time-averaged TKE in the $Z = 0.5h$ plane of the middle pool at Q = 600 L/s for six representative cases

(*i.e.* VSF, TSF-1, TSF-2, TSF-5, HSF-1 and HSF-2). As expected, HSF-2 and TSF-5 lead to relatively much smaller values of k, being consistent with $\overline{k}$ = 0.044 m^2/s^2 and k_{max} = 0.14 m^2/s^2 for HSF-2 (being the smallest among all the cases) and $\overline{k}$ = 0.045 m^2/s^2 and k_{max} = 0.15 m^2/s^2 for TSF-5 (being the second smallest among all the cases) in Table 3.

Different operating conditions

Besides Q = 600 L/s, other three discharge conditions (*i.e.* Q = 400 L/s, 800 L/s and 1000 L/s) have also been simulated for the purpose of demonstrating the generalizability of the superiority of HSF-2 over VSF and TSF-1. Table 4 proves that, in terms of Max$\{U_{magnitude}\}$, k_{max}, the volume percentage of $k \leq$ 0.10 m^2/s^2, and the volume percentages of $U_{magnitude}$ less than some critical values, HSF-2 does have a better performance than VSF and TSF-1 for all the four operating conditions. As far as $\overline{U_{magnitude}}$ is concerned, HSF-2 is still smaller than VSF, but is slightly larger than TSF-1 for all the four discharges. When it comes to $\overline{k}$ and the volume percentage of $k \leq$ 0.05 m^2/s^2, HSF-2 always outperforms TSF-1, however, only for Q = 400 L/s and 600 L/s, HSF-2 is better than VSF. Fig. 9 manifests that, with respect to the depth-mean time-averaged velocity magnitude at the vertical-slot section (*i.e.* $U^*_{magnitude}$), case HSF-2 is significantly superior to VSF and TSF-1 for all the four discharges.

Fig. 10(a) and Fig. 10(b) display the normalized locations and the normalized values of the maximum depth-mean time-averaged velocity magnitude, respectively, in different Y-Z planes within the middle pool at various discharges. At Q = 400 L/s, the similar distribution characteristics can be

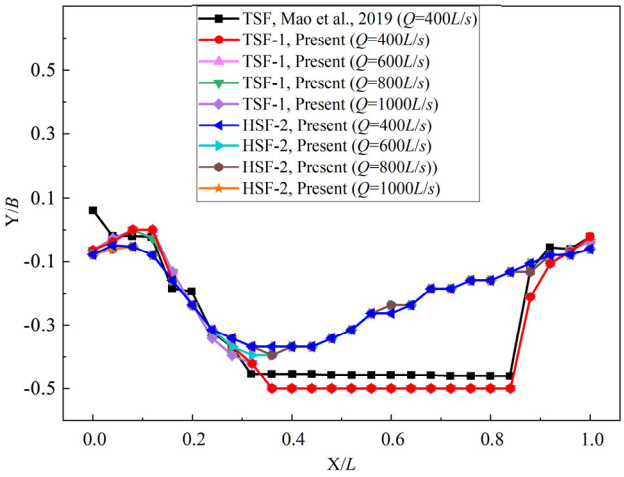

（a）Locations of the maximum depth-mean time-averaged velocity magnitude points in different Y-Z planes

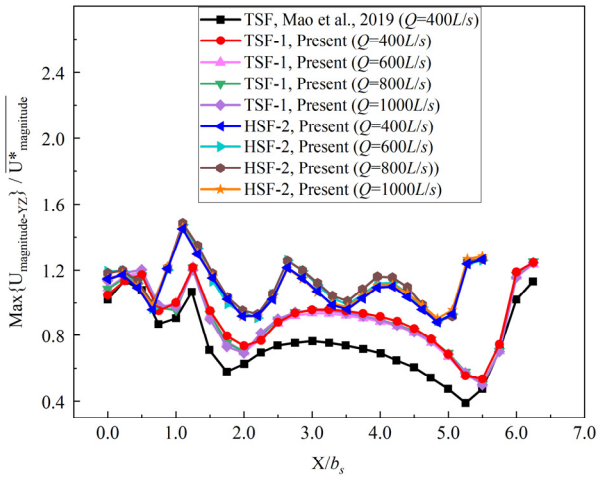

（b）The normalized maximum depth-mean time-averaged velocity magnitude values in different Y-Z planes

Fig. 10. The normalized locations and the normalized values of the maximum depth-mean time-averaged velocity magnitude in different Y-Z planes within the middle pool at various discharges.

Table 4. The time-averaged water-depth, velocity-magnitude and turbulent kinetic energy within the middle pool for various cases at four discharges (*i.e.* Q = 400 L/s, 600 L/s, 800 L/s and 1000 L/s).

Cases	Q = 400 L/s			Q = 600 L/s			Q = 800 L/s			Q = 1000 L/s		
	VSF	TSF-1	HSF-2	VSF	TSF-1	HSF-2	VSF	TSF-1	HSF-2	VSF	TSF-1	HSF-2
h (m)	0.49	1.02	0.91	0.72	1.36	1.22	0.92	1.67	1.50	1.15	1.96	1.76
Max$\{U_{magnitude}\}$ (m/s)	1.93	1.51	1.35	2.07	1.71	1.48	2.18	1.85	1.60	2.03	2.00	1.68
$\overline{U_{magnitude}}$ (m/s)	0.63	0.42	0.46	0.65	0.48	0.51	0.68	0.52	0.56	0.67	0.54	0.58
k_{max} (m^2/s^2)	0.15	0.13	0.10	0.20	0.18	0.14	0.20	0.19	0.17	0.21	0.24	0.18
$\overline{k}$ (m^2/s^2)	0.037	0.038	0.035	0.050	0.050	0.044	0.049	0.058	0.054	0.049	0.068	0.061
$U_{magnitude} \leq$ 0.30 m/s	36%	50%	50%	35%	42%	43%	31%	40%	38%	31%	39%	37%
$U_{magnitude} \leq$ 0.43 m/s	51%	61%	65%	51%	56%	60%	44%	54%	55%	44%	53%	55%
$U_{magnitude} \leq$ 0.54 m/s	61%	70%	72%	61%	65%	68%	54%	62%	64%	54%	60%	64%
$U_{magnitude} \leq$ 0.66 m/s	67%	77%	78%	68%	73%	75%	62%	70%	72%	62%	68%	70%
$U_{magnitude} \leq$ 0.78 m/s	71%	84%	86%	71%	80%	81%	68%	76%	77%	67%	74%	76%
$U_{magnitude} \leq$ 0.81 m/s	72%	85%	88%	71%	82%	82%	70%	78%	78%	70%	76%	77%
$U_{magnitude} \leq$ 1.00 m/s	75%	94%	97%	75%	91%	92%	74%	86%	88%	74%	84%	85%
$k \leq$ 0.05 m^2/s^2	69%	74%	81%	63%	59%	62%	62%	47%	51%	59%	35%	43%
$k \leq$ 0.10 m^2/s^2	92%	99%	100%	83%	94%	99%	85%	89%	96%	89%	82%	92%

h represents the corresponding mean time-averaged water-depth of the middle pool

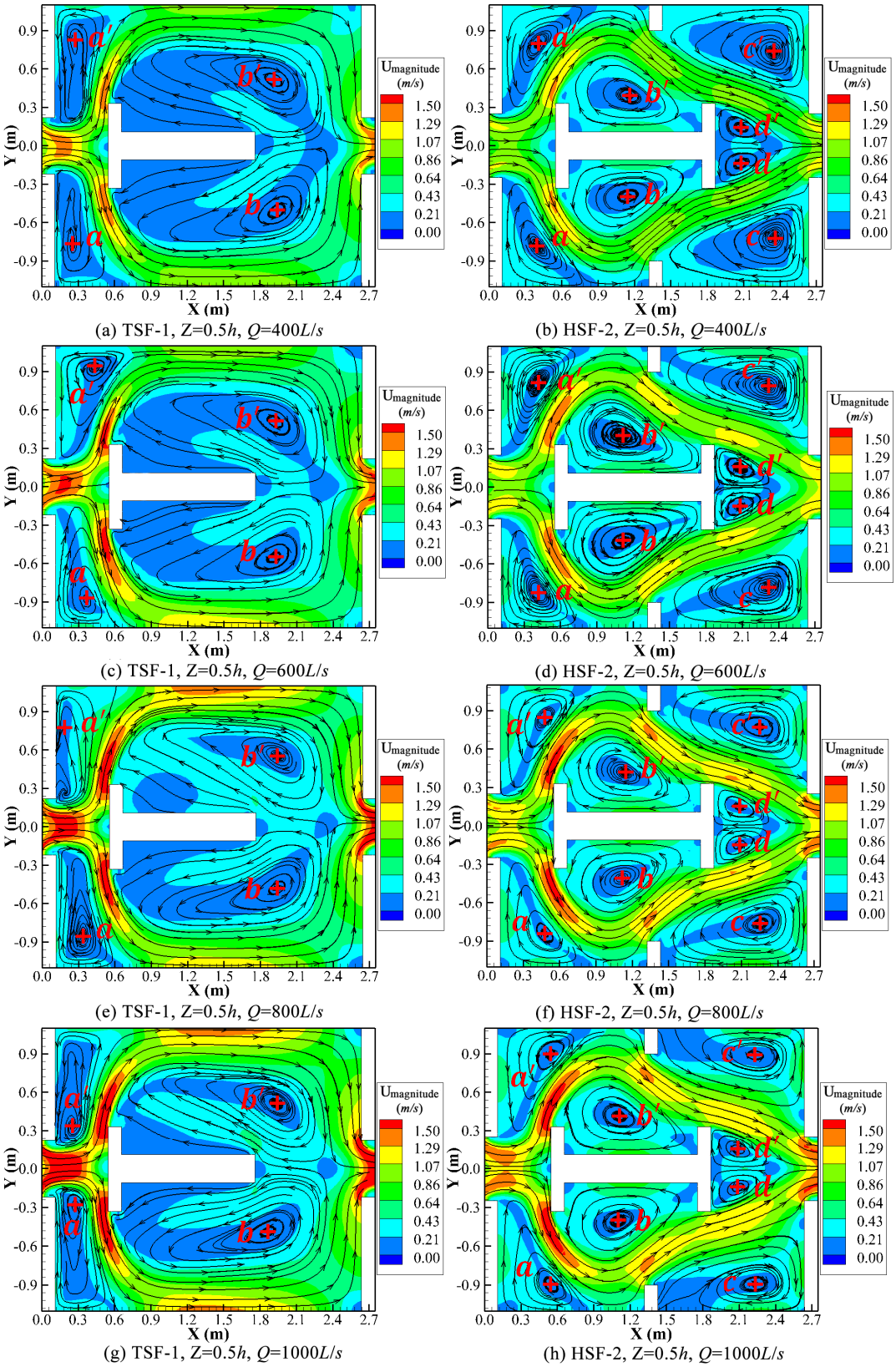

(a) TSF-1, Z=0.5*h*, *Q*=400*L*/*s*
(b) HSF-2, Z=0.5*h*, *Q*=400*L*/*s*
(c) TSF-1, Z=0.5*h*, *Q*=600*L*/*s*
(d) HSF-2, Z=0.5*h*, *Q*=600*L*/*s*
(e) TSF-1, Z=0.5*h*, *Q*=800*L*/*s*
(f) HSF-2, Z=0.5*h*, *Q*=800*L*/*s*
(g) TSF-1, Z=0.5*h*, *Q*=1000*L*/*s*
(h) HSF-2, Z=0.5*h*, *Q*=1000*L*/*s*

Fig. 11. The 2D time-averaged streamlines and velocity magnitude contours in the $Z = 0.5h$ plane for TSF-1 and HSF-2 at four flow discharges (*i.e.* Q = 400 L/s, 600 L/s, 800 L/s and 1000 L/s).

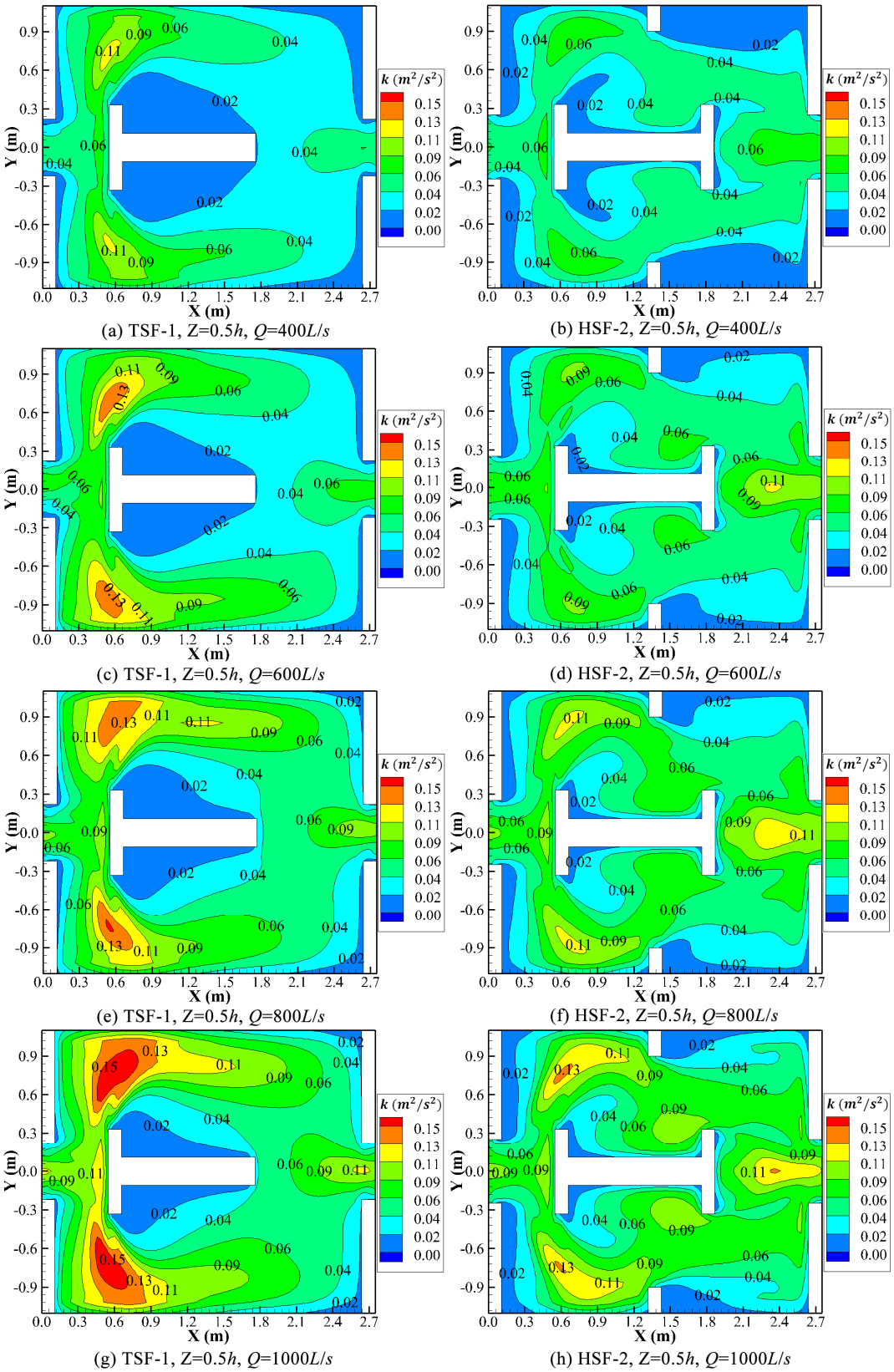

(a) TSF-1, Z=0.5*h*, *Q*=400*L*/*s*

(b) HSF-2, Z=0.5*h*, *Q*=400*L*/*s*

(c) TSF-1, Z=0.5*h*, *Q*=600*L*/*s*

(d) HSF-2, Z=0.5*h*, *Q*=600*L*/*s*

(e) TSF-1, Z=0.5*h*, *Q*=800*L*/*s*

(f) HSF-2, Z=0.5*h*, *Q*=800*L*/*s*

(g) TSF-1, Z=0.5*h*, *Q*=1000*L*/*s*

(h) HSF-2, Z=0.5*h*, *Q*=1000*L*/*s*

Fig. 12. The 2D contours of the time-averaged turbulent kinetic energy in the $Z = 0.5h$ plane for TSF-1 and HSF-2 at four flow discharges (*i.e.* Q = 400 L/s, 600 L/s, 800 L/s and 1000 L/s).

observed and only small discrepancy exists between the present TSF-1 and the TSF case proposed by Mao et al. (2019). Besides, whether for TSF-1 or for HSF-2, both the normalized locations and the normalized values of the maximum depth-mean time-averaged velocity magnitude in different Y-Z planes almost remain unchanged when changing the discharge. Fig. 11 and Fig. 12 demonstrate the 2D time-averaged flow pattern and the 2D contours of k in the $Z = 0.5h$ plane for TSF-1 and HSF-2. Similar distribution characteristics can be observed in each case for all the four discharges, but both the time-averaged velocity magnitude and the time-averaged turbulent kinetic energy continuously increase with the increase of the discharge. It should be emphasized that, even for different X-Y planes (*e.g.*, the $Z = 0.1h$ plane near the bed, the $Z = 0.5h$ plane at the middle of the water-depth and the $Z = 0.9h$ plane near the water surface), similar conclusions can be drawn from the velocity field and the TKE field, and therefore only the 2D contours in the $Z = 0.5h$ plane is presented in Fig. 7, Fig. 8, Fig. 11 and Fig. 12 for conciseness of presentation.

CONCLUSIONS

Flow characteristics of eight fishways (*i.e.* VSF, TSF-1~TSF-5, HSF-1 and HSF-2) have been analyzed in terms of the time-averaged flow pattern, water depth, velocity field and turbulent kinetic energy. The main findings include the following:

(1). Regarding the time-averaged flow structure, HSF-2 is superior to the other seven fishway designs, in view of both the relatively uniformly moderate sizes and the relatively evenly distributed locations of its four pairs of recirculation regions, which avoiding the disorientation of the fishes and can provide more rest areas.

(2). With respect to the time-averaged velocity distribution, HSF-2 has an overall advantage over the other seven cases in terms of $\mathrm{Max}\{U_{magnitude}\}$, $\overline{U_{magnitude}}$, $U^*_{magnitude}$, and the volume percentages of $U_{magnitude}$ less than some critical values.

(3). Concerning the time-averaged turbulent kinetic energy, HSF-2 also has the best performance, owing to the smallest value of $\overline{k} = 0.044$ m^2/s^2 and $k_{max} = 0.14$ m^2/s^2, the largest percentage of $k \le 0.10$ m^2/s^2 (99%), and the second largest percentage of $k \le 0.05$ m^2/s^2 (62%).

(4). Even for all the four operating conditions (*i.e.* $Q = 400$ L/s, 600 L/s, 800 L/s and 1000 L/s), the generalizability of the superiority of the recommended HSF-2 over VSF and TSF-1 can be clearly demonstrated in terms of $\mathrm{Max}\{U_{magnitude}\}$, $\overline{U_{magnitude}}$, $U^*_{magnitude}$, k_{max}, $\overline{k}$, $k \le 0.05$ m^2/s^2, $k \le 0.10$ m^2/s^2, and the volume percentages of $U_{magnitude}$ less than some critical values.

Acknowledgements. The authors wish to acknowledge the financial support provided by the National Natural Science Foundation of China (Grant No. 51922065 and 51909024), and the Hubei International Science and Technology Cooperation Base of Fish Passage (Grant No. HIBF2020004).

REFERENCES

An, R.D., Li, J., Yi, W.M., Mao, X., 2019. Hydraulics and swimming behavior of schizothorax prenanti in vertical slot fishways. J. Hydrodyn., 31, 1, 169–176.

Bombač, M., Novak, G., Rodič, P., Četina, M., 2014. Numerical and physical model study of a vertical slot fishway. J. Hydrol. Hydromech., 62, 2, 150–159.

Bombač, M., Novak, G., Mlačnik, J., Četina, M., 2015. Extensive field measurements of flow in vertical slot fishway as data for validation of numerical simulations. Ecol. Eng., 84, 476–484.

Bombač, M., Četina, M., Novak, G., 2017. Study on flow characteristics in vertical slot fishways regarding slot layout optimization. Ecol. Eng. ,107, 126–136.

Ead, S.A., Katopodis, C., Sikora, G.J., Rajaratnam, N., 2004. Flow regimes and structure in pool and weir fishways. J. Environ. Eng. Sci., 3, 5, 379–390.

Fuentes-Pérez, J.F., Sanz-Ronda, F.J., Martínez de Azagra Paredes, A., García-Vega, A., 2014. Modeling water-depth distribution in vertical-slot fishways under uniform and non-uniform scenarios. J. Hydraul. Eng., 140, 10, 06014016.

Fuentes-Pérez, J.F., Sanz-Ronda, F.J., de Azagra, A.M., García-Vega, A., 2016. Non-uniform hydraulic behavior of pool-weir fishways: a tool to optimize its design and performance. Ecol. Eng., 86, 5–12.

Fuentes-Pérez, J.F., Tuhtan, J.A., Eckert, M., Romão, F., Ferreira, M.T., Kruusmaa, M., Branco, P., 2019. Hydraulics of vertical-slot fishways: Nonuniform profiles. J. Hydraul. Eng., 145, 2, 06018020.

Katopodis, C., Rajaratnam, N., Wu, S., Tovell, D., 1997. Denil fishways of varying geometry. J. Hydraul. Eng., 123, 7, 624–631.

Katopodis, C., Williams, J.G., 2012. The development of fish passage research in a historical context. Ecol. Eng., 48, 8–18.

Mao, X., Fu, J.J., Tuo, Y.C., An, R.D., Li, J., 2012. Influence of structure on hydraulic characteristics of T shape fishway. J Hydrodyn., 24, 5, 684–691.

Mao, X., Zhang, J., Tang, K., Zhao, W., 2019. Designs for T shape fishways. Stavební obzor - Civil Engineering Journal, 28, 2, 270–280.

Marriner, B.A., Baki, A.B., Zhu, D.Z., Cooke, S.J., Katopodis, C., 2016. The hydraulics of a vertical slot fishway: a case study on the multi-species Vianney-Legendre fishway in Quebec, Canada. Ecol. Eng., 90, 190–202.

Menter, F.R., Kuntz, M., Langtry, R., 2003. Ten years of industrial experience with the SST turbulence model. Turbul. Model. Heat. Mass. Tran., 4, 1, 625–632.

Puertas, J., Cea, L., Bermúdez, M., Pena, L., Rodríguez, Á., Rabunal, J.R., Balairón, L., Lara, Á., Aramburu, E., 2012. Computer application for the analysis and design of vertical slot fishways in accordance with the requirements of the target species. Ecol. Eng., 48, 51–60.

Quaranta, E., Katopodis, C., Revelli, R., Comoglio, C., 2017. Turbulent flow field comparison and related suitability for fish passage of a standard and a simplified low gradient vertical slot fishway. River Res. Appl., 33, 8, 1295–1305.

Quaresma, A.L., Romão, F., Branco, P., Ferreira, M.T., Pinheiro, A.N., 2018. Multi slot versus single slot pool-type fishways: a modelling approach to compare hydrodynamics. Ecol. Eng., 122, 197–206.

Quaranta, E., Katopodis, C., Comoglio, C., 2019. Effects of bed slope on the flow field of vertical slot fishways. River Res. Appl., 35, 6, 656–668.

Rajaratnam, N., Katopodis, C., 1984. Hydraulics of Denil fishways. J. Hydraul. Eng., 110, 9, 1219–1233.

Rajaratnam, N., Katopodis, C., Mainali, A., 1989. Pool-orifice and pool-orifice-weir fishways. Can. J. Civ. Eng., 16, 5, 774–777.

Rajaratnam, N., Katopodis, C., Solanki, S., 1992. New designs for vertical slot fishways. Can. J. Civ. Eng., 19, 3, 402–414.

Rodríguez, T.T., Agudo, J.P., Mosquera, L.P., González, E.P., 2006. Evaluating vertical slot fishway designs in terms of fish swimming capabilities. Ecol. Eng., 27, 1, 37–48.

Santos, J.M., Silva, A., Katopodis, C., Pinheiro, P., Pinheiro, A., Bochechas, J., Ferreira, M.T., 2012. Ecohydraulics of pool-type fishways: getting past the barriers. Ecol. Eng., 48, 38–50.

Tarrade, L., Texier, A., David, L., Larinier, M., 2008. Topologies and measurements of turbulent flow in vertical slot fishways. Hydrobiologia, 609, 1, 177–188.

Yagci, O., 2010. Hydraulic aspects of pool-weir fishways as ecologically friendly water structure. Ecol. Eng., 36, 1, 36–46.

Zhang, D., Jiang, C., Liang, D., Chen, Z., Yang, Y., Shi, Y., 2014. A refined volume-of-fluid algorithm for capturing sharp fluid interfaces on arbitrary meshes. J. Comput. Phys., 274, 709–736.

Zhang, D., Jiang, C., Liang, D., Cheng, L., 2015. A review on TVD schemes and a refined flux-limiter for steady-state calculations. J. Comput. Phys., 302, 114–154.

Zhang, D., Cheng, L., An, H., Draper, S., 2021. Flow around a surface-mounted finite circular cylinder completely submerged within the bottom boundary layer. Eur. J. Mech. B Fluids., 86, 169–197.

NOMENCLATURE

B: pool width [m]
b_s: slot width [m]
b_0: width of the baffle for TSF and HSF [m]
b_t: length of the front baffle for the T-shape pier and the H-shape pier [m]
b_n: length of the rear baffle for the H-shape pier [m]
b_l: length of the lateral short baffle for TSF-5 and HSF-2 [m]
d: distance between the front baffle and the lateral long baffle for TSF and HSF [m]
h: mean time-averaged water-depth within the middle pool [m]
H: height of all the baffles [m]
$\overline{h}_{in}$: uniform-flow water depth at the inlet plane [m]
$\overline{h}_{out}$: water depth prescribed at the outlet plane [m]
I_l: length of the T-shape pier and the H-shape pier [m]
I_b: thickness of the trailing end for the T-shape pier [m]
I_B: length of the lateral long baffle for TSF and HSF [m]
k: time-averaged turbulent kinetic energy [m^2/s^2]
$\overline{k}$: mean time-averaged turbulent kinetic energy within the middle pool [m^2/s^2]
k_{max}: maximum time-averaged turbulent kinetic energy within the middle pool [m^2/s^2]
L: length of the pool [m]
L_t: distance between the lateral long baffle and the lateral short baffle [m]
MAE (u_x), MAE (u_y): mean absolute error between the experimental data of u_x (or u_y) and the numerical data of u_x (or u_y) for each cross-section [m/s]
MAE (u): sum of MAE (u_x) and MAE (u_y) for all four representative cross-sections [m/s]
n: the Manning coefficient [–]
$\overline{p}$: time-averaged pressure [Pa]
Q: flow discharge [m^3/s]
R: hydraulic radius [m]
S_0: bed slope [–]
u_x: depth-mean time-averaged streamwise velocity [m/s]
u_y: depth-mean time-averaged spanwise velocity [m/s]
$\overline{u}$: time-averaged velocity [m/s]
$\overline{u}_{in}$: uniform-flow velocity at the inlet plane [m/s]
$U_{magnitude}$: time-averaged velocity magnitude [m/s]
$\mathrm{Max}\{U_{magnitude}\}$: maximum time-averaged velocity magnitude within the middle pool [m/s]
$\mathrm{Max}\{U_{magnitude-YZ}\}$: maximum depth-mean time-averaged velocity magnitude in different Y-Z planes within the middle pool [m/s].
$\overline{U_{magnitude}}$: mean time-averaged velocity magnitude within the middle pool [m/s]
$U^*_{magnitude}$: depth-mean time-averaged velocity magnitude at the vertical-slot section [m/s]
$\overline{U^*_{magnitude}}$: depth-mean time-averaged velocity magnitude of the whole vertical-slot region [m/s]
X: streamwise coordinate [m]
Y: transverse coordinate [m]
Z: vertical coordinate [m]
ρ: density of the fluid [kg/m^3]
α_q : volume fraction of the water [–]
ω : specific dissipation rate [s^{-1}]
ν_t : turbulent viscosity [m^2/s]
Δx , Δy , Δz : cell size in streamwise, transverse and vertical directions, respectively [m]

Received 9 May 2022
Accepted 12 September 2022

J. Hydrol. Hydromech., 71, 2023, 1, 80–90
https://doi.org/10.2478/johh-2022-0041

sciendo Journal of Hydrology and Hydromechanics Institute of Hydrology SAS

Effect of water surface slope and friction slope on the value of the estimated Manning's roughness coefficient in gravel-bed streams

Monika Zwolenik*, Bogusław Michalec

University of Agriculture in Kraków, Department of Water Engineering and Geotechnics, Al. A. Mickiewicza 24/28 Kraków, Poland.
*Corresponding author. E-mail: monika.zwolenik88@interia.pl

Abstract: The aim of the study was to assess the possibility of using the empirical formulas to determine the roughness coefficient in gravel-bed streams, the bed slopes of which range from 0.006 to 0.047. Another aim was to determine the impact of taking into account the conditions of non-uniform flow on the application of these formulas and to develop the correlation relationships between the roughness coefficient and water surface slope and also between the roughness coefficient and friction slope in order to estimate the roughness coefficient n in gravel-bed streams.

The studies were conducted in eight measuring sections of streams located in the Kraków-Częstochowa Upland, southern Poland. The roughness coefficient n_0 for these sections was calculated from the transformed Bernoulli equation based on the results of surveys and hydrometric measurements. The values of n_0 were compared with the calculation results obtained from fourteen empirical formulas presenting the roughness coefficient as a function of slope.

The Lacey, Riggs, Bray and Sauer formulas were found to provide an approximate estimate of the n value, while the best roughness coefficient estimation results were obtained using the Riggs formula. It was also found that taking into account the non-uniform flow and using the friction slope in the formulas instead of the bed slope or water surface slope did not improve the estimated values of the roughness coefficient using the tested formulas. It was shown that the lack of differences in the RMSE and MAE error values calculated for the developed correlation equations between the roughness coefficient and the friction slope or with the water surface slope also indicate no influence of the assumed friction slope or water surface slope on the value of the estimated roughness coefficient.

Keywords: Roughness coefficient; Bed slope; Uniform flow; Non-uniform flow.

1 INTRODUCTION

Accurate estimation of the Manning's coefficient of roughness n is crucial in determining the water flow rate in open channels. If the estimated roughness is too low, this can result in an overestimated flow in the calculations, an underestimation of the flood flow surface levels and vice versa (Ladson et al., 2002). The roughness coefficient n was introduced by Manning into the Chézy equation:

$$n = (R^{2/3} S_f^{1/2}) / V \quad (1)$$

where R is a hydraulic radius, S_f is the friction slope, and V is the mean flow velocity.

The Manning equation is most often used to estimate the hydraulic parameters of water flow in open channels and applied in computational models (Bjerklie et al., 2005; Strupczewski and Szymkiewicz 1996; Zhu et al., 2020). The main limitation of the Manning equation is the assumption of a constant value of the friction coefficient regardless of the depth and velocity of water flow (Bellos et al., 2018). On the other hand, Ferguson (2010) considers this method of determining the hydraulic parameters of water flow to be non-optimal. In the engineering approach, the Manning equation calculates the water flow velocity for a given bed slope and assumed value of roughness coefficient. When the flow is uniform then the friction slope S_f can be replaced by the bed slope S (Ferguson, 2007). This means the parallelism of the bed slope and water surface slope S_w. The roughness coefficient is taken from the tables for a given type of mineral material in the watercourse bed. The roughness coefficient can also be calculated for the determined friction factor f presented in the Darcy-Weisbach equation:

$$f = (8gRS_f) / V^2 \quad (2)$$

The Equations (1) and (2) show the relationship between the friction factor and the roughness coefficient in the form (Yen, 2002):

$$R^{1/6} / n = (8g / f)^{1/2} \quad (3)$$

However, in engineering practice it is not a commonly used procedure. This coefficient can also be estimated using empirical formulas in which it is presented as a function of the bed grain size, slope, hydraulic radius and other parameters. The basic formulas describing the relationship between the roughness coefficient and sediment grain size were developed on the basis of the equation proposed by Strickler in 1923 (Lane, 2014):

$$n = a\, d_{50}^{1/6} \quad (4)$$

The formula developed by Strickler allows to determine the roughness coefficient based on the grain median, i.e. d_{50}, and on the determined value of the coefficient a. The formulas developed by various authors, following the example of Strickler's (4), may also adopt a grain size diameter other than d_{50}. Raudkivi (1976) used d_{65}, while Keulegan (1938), Meyer-Peter and Mueller (1948) and Bray (1982) used d_{90}. The development of empirical formulas was based not only on the size, shape and distribution of the grains of the bed material, but also on the wetted perimeter. These types of formulas have been developed by, among others, Limerinos (1970), Griffiths (1981), Bray (1982), Phillips and Ingersoll (1997). In these formulas, the

ratio of hydraulic radius to a characteristic roughness element size, such as grain size or a bed-form characteristic, defined as the relative submergence, was intended to help quantify the variability of flow resistance due to different flow depth. The relationships between the roughness coefficient and the bed slope, water surface slope or friction slope were developed (Table 1) apart from the formulas for calculating the roughness coefficient value described above. In the equations (5) of Lacey (1946), (7) of Bray (1979), of Jarrett (1984) and of Sauer (1990), the values are given in imperial units of measurement.

Table 1. Roughness coefficient in the function of slope and others parameters.

No	Author / Authors	Equation	Description
(5)	Lacey (1946)	$n = 0.0928\ S^{1/6}$	Low gradient stream, sediment of gravel size or smaller
(6)	Riggs (1976)	$n = 0.21\ A^{-0.33} R^{0.667}\ S_w^{0.095}$	Uniform cross-sectional area, nearly full natural channel, Water-surface slopes:0.0003–0.018, hydraulic radius up to 19 ft.
(7)	Bray (1979)	$n = 0.104\ S_w^{0.177}$	Gravel-bed channel, $h/d_{90} > 5$ and water-surface slope: 0.00022 – 0.015.
(8)	Bray (1982)	$n = 1/80\ R^{0.067}\ S_w^{0.21}$	Inappropriate for high-gradient streams and narrow channels with dense streambank vegetation, high within-bank flow: $h/d_{90} > 3$
(9)	Brownlie (1983)	$n = 1.694(R/d_{50})^{0.1374}\ S^{0.1112}\ \delta^{0.1605}\ 0.034 d_{50}^{0.167}$	Sand bed: dune and ripple in bed - lower regime flow
(10)	Brownlie (1983)	$n = 1.0213(R/d_{50})^{0.0662}\ S^{0.0395}\ \delta^{0.1282}\ 0.034 d_{50}^{0.167}$	Sand bed: flat bed and antidune - upper regime flow
(11)	Jarrett (1984)	$n = 0.39\ S_f^{0.38}\ R^{-0.16}$	Stable bed and bank materials (gravels, cobbles and boulders) energy gradients from 0.002 to 0.039 and hydraulic radius from 0.5 to 7 ft.
(12)	Bruschin (1985)	$n = (d_{50}^{1/6}/12.38)\ ((R/d_{50})\ S_f)^{1/7.2}$	Sand bed, upper regime flow, bed slope less than 0.037
(13)	Gessler (1990)	$n = R^{1/3} / ((2.21 + 2.03 \log(0.0251/S_f))\ (8g)^{0.5})$	Armored canal beds at the discharge that formed the armor coat
(14)	Sauer (1990)	$n = 0.11\ S_w^{0.18}\ R^{0.08}$	Calibrated to data from Barnes (1967): bottom of fine sand, silt, sand, gravel, boulders. Water-surface slopes: 0.0003–0.018, hydraulic radius up to 19 ft.
(15)	Rickenmann (1994)	$n = 0.01786\ (S^{0.33}\ d_{90}^{0.45}) / (g^{0.44}\ Q^{0.11})$	Wide range of flow conditions, mountain streams and torrents, bed-slope range: 0.008–0.63
(16)	Dingman and Sharma (1997)	$n = 0.217\ A^{-0.173}\ R^{0.267}\ S_w^{0.156}$	Calibrated to data from Barnes (1967): bottom of fine sand, silt, sand, gravel, boulders, water-slope range: 0.0002–0.052
(17)	Rice et al. (1998)	$n = 0.029\ (d_{50}\ S)^{0.147}$	Channels with rock riprap laid on steep slopes, slope range: 0.025–0.22
(18)	Yochum et al. (2014)	$n = 0.18\ S_w^{0.79}$	Cascade and step-pool streams with beds dominated by gravel, cobbles, or boulders at low flow - water-surface slope: 0.019–0.17.

where: No. – number of equation, S – slope of bed, S_w – slope of water surface, S_f – friction slope or energy gradient, R – hydraulic radius, T – top width of stream, A – cross-sectional area of flow, h – mean depth, Q – water discharge, d_x – the grain diameter for which x% is finer, δ – the geometric standard deviation of the sediment mixture.

The use of Brownlie equations (1983) (Table 1) requires determination of the flow regime. If the slope is greater than 0.006, flow is always of upper regime. Otherwise, the transition is correlated with the grain Froude number (F_g) as follows (Fischenich and Little, 2007): if $F_g \leq F_g$', then lower regime flow is observed, and if $F_g > F_g$', then upper regime flow is observed, where F_g and F_g':

$$F_g = V / ((s-1) g d_{50})^{0.5} \quad (19)$$

$$F_g' = 1.74 / S^{1/3} \quad (20)$$

where: s is specific gravity of sediment particles, S is the bed slope, V is mean velocity, and d_{50} is the grain diameter for which 50% is finer. A parameter δ in formulas (9) and (10) in the table 1 - i.e. the geometric standard deviation of the sediment mixture, is determined from the formula:

$$\delta = 0.5((d_{84}/d_{50}) + (d_{50}/d_{16})) \quad (21)$$

In the calculations of the friction factor f, friction slope S_f should be assumed as the slope value (Ferguson, 2007; Machiels et al., 2009). In the case of significant non-uniformity of the flow in the calculations, the use of the water surface slope S_w or mean bed slope S may result in obtaining a systematic error (Jarrett,

1984; Hicks and Mason, 1991). The flow is generally assessed based on the formulas developed for the friction slope determined experimentally for uniform flow conditions. In simple empirical formulas, Jarrett (1984), Bruschin (1985) and Gessler (1990) introduced a friction slope, also called an energy gradient (Table 1). Under steady flow conditions, the effects of bottom friction are precisely balanced by gravitational forces. Thus, for a uniform flow, the friction slope is assumed to be equal to the channel bed slope (e.g. Brownlie (1983), Lacey (1946), Rickenmann (1994) and Rice et al. (1998) – Table 1). For hydraulic conditions corresponding to a uniform flow, some authors provide the water surface slope in the proposed formulas, e.g. Riggs (1976), Bray (1979 and 1982), Saurer (1990), Dingman and Sharma (1997) as well as Yochum et al. (2014) (Table 1). When using these formulas for flow conditions other than uniform, the bed slope or water surface slope should be replaced by the friction slope. Determining the friction slope poses no problem when data from measurements are available surveying measurements will be made.

In the case of a design channel with non-uniform flow and irregular cross-section, the calculation of the friction slope requires not only calculation of bed and water surface slopes, but also the calculation of the height of the velocity line from the formula $\alpha V2/2g$, it is necessary to adopt the roughness coefficient if the calculations are conducted using the Manning's equation, or to adopt the friction factor when the Darcy-Weisbach equation is used. These coefficients are therefore adopted in order to calculate the height of the velocity line in the calculation cross-sections of the designed reach to calculate the friction slope. And yet, the friction slope itself was intended to be used for the estimation of these coefficients. The solution of this task requires iterative calculations, which is in contradiction with the practical and efficient estimation of the roughness coefficient, or the friction factor values as a function of the friction slope. The aim of this study was 1) to assess the possibility of using the empirical formulas presented to determine the roughness coefficient in streams with gravel bottoms, whose bed slopes range from 0.006 to 0.047, 2) to assess the impact of taking into account the conditions of non-uniform flow on using these formulas, 3) to develop the correlation dependencies between the roughness coefficient and water surface slope or friction slope for the estimation of the n values in gravel-bed streams. The obtained results may prove helpful in the assessment of hydraulic conditions of water flow in streams with similar morphological features. As a result of these studies, it will be possible to indicate an empirical formula or formulas that will allow to estimate the roughness coefficient on the basis of the stream bed slope, water surface slope or friction slope.

2 MATERIAL AND METHODS

Field studies were carried out on the reaches of the Będkówka, Racławka, Bolechówka and Wierzchówka streams selected for the experiment. These streams are tributaries of the Rudawa river, which is a tributary of the Vistula river. The catchments of these streams are located in the Olkusz Upland, which is a mesoregion being a part of the Kraków-Częstochowa Upland macroregion. They are located within the Kraków poviat, in the Lesser Poland voivodeship (Fig. 1). The basic parameters of the analyzed streams are presented in Table 2.

Measurement reaches with a length of 3 to 5 cross-section widths were selected for the tests. In every reach, the following cross-sections were determined: upper (initial) and lower (final), as well as three sections between the upper and lower section. The bottom ordinates were estimated in each of the eight cross-sections, in order to determine the bed slope as well as the water surface slope at a given flow. Hydrometric measurements were also conducted in the upper and lower section of each measurement reach. In these cross-sections, hydrometric risers were determined at intervals of 10 cm and hydrometric measurements were conducted in each riser at different heights above the bottom. Hydrometric measurements were conducted with a Valeport Model 801 induction flowmeter. Based on the results of hydrometric measurements, the water flow rate was calculated using the Harlacher method (Michalec and Zwolenik, 2020). Then, the hydraulic parameters for this reach were calculated according to the methodology provided by Nitsche et. al. (2012). A representative channel cross-section was interpolated from the vertical mean of multiple measured cross-sections. Using this reach-averaged cross-section, all hydraulic

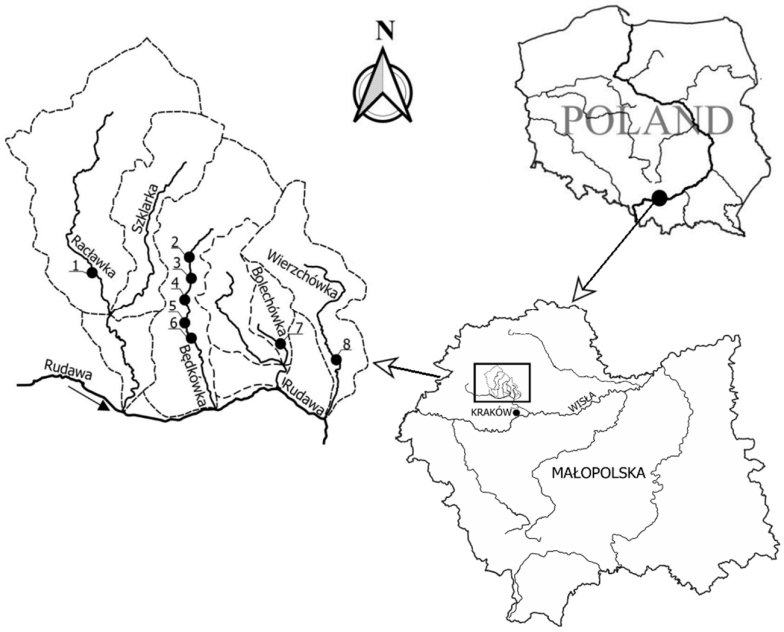

Fig. 1. Streams: Będkówka, Racławka, Bolechówka and Wierzchówka together with the location of measurement sections (from 1 to 8).

Table. 2. Basic parameters of the studied streams.

Stream	Lenght of stream (km)	Cachment area (km^2)	Mean bed slope of stream (–)	Mean bed slope of reach (–)
Racławka	16.52	39.78	0.009	0.006
Będkówka	12.00	24.90	0.018	0.006–0.023
Bolechówka	4.83	18.40	0.008	0.030
Wierzchówka	9.00	17.29	0.009	0.047

parameters were solved (i.e. mean flow depth h, hydraulic radius R and cross sectional area A) corresponding to reach-averaged discharge and reach-averaged velocity (Nitsche et al., 2012). Surveys and hydrometric measurements were conducted in three series on each of the eight reaches (Fig. 1). The results of each measurement series were obtained from the measurements conducted within 2 days under constant hydrological and meteorological conditions in the catchment area of the studied streams.

Based on the surveys and hydrometric measurements, the water flow rate Q, was calculated, followed by the calculation of the Manning's mean roughness coefficient n_0 by using the formula developed by Barnes (1967). This formula (22), derived from the Bernoulli equation, enables the calculation of the average Manning's roughness coefficient for sections of the watercourse with many cross-sections.

$$n_0 = \frac{1}{Q}\sqrt{\frac{(h_1 + h_{v1}) - (h_m + h_{vm}) - \sum_{i=2}^{m}(k_{i-1,i}\,\Delta h_{v_i\text{-}1,i})}{\sum_{i=2}^{m}\frac{L_{i-1,i}}{Z_{i-1}Z_i}}} \qquad (22)$$

where: h – water depth, h_v – velocity head, $k\Delta h_v$ – energy loss due to contraction of velocity or deceleration of velocity in contracting or expanding reaches, where k is a coefficient adopted as zero for contracting reaches and 0.5 for expanding reaches (Lee et al., 2017), $Z = AR^{2/3}$, where A is the cross-section area, R is the hydraulic radius and m is number of cross-sections.

The uncertainty of the mean rate flow Q, which is the arithmetic mean of the rate flow Q, calculated from the measurements in five sections, was determined on the basis of the standard deviation of the mean. Due to the small number of hydrometric measurements (n = 5), in order to avoid underestimating the specified uncertainty, the standard deviation of the mean was multiplied by the Student's t-test distribution coefficient ($t_{n,\alpha}$). This coefficient was adopted for the confidence level α = 95% and degrees of freedom (n – 1 = 4). The relative uncertainty (RU) was calculated as the quotient of the standard uncertainty, i.e. the standard deviation of the mean (SD) and the mean rate flow Q. The standard error (SE) was also calculated.

In order to determine the granulometric composition of the bed-material, sediment samples were taken from the bed of the streams between the upper and lower cross-sections. On the basis of the developed curves and particle size distribution, the characteristic diameters of the sediment were determined. Sieve analyzes were performed for three samples collected in each measuring reach. The mean percentage composition of the separated sediment fractions was determined. Fractions smaller than 1 mm were analyzed hydrometrically. On the basis of the developed curves and particle size distribution, the characteristic diameters of the sediment were determined. The standard deviation, i.e. the uncertainty of the arithmetic mean (Kolwalczyk et al., 2012), was calculated to describe the accuracy of determining the true value of the measured diameter d_{50}. The standard deviation of the mean (SD) was calculated for the d_{50} determined from the three specific grain size composition. Due to the small number of collected sediment samples (n = 3), in order to avoid underestimating the specified uncertainty, the standard deviation of the mean was multiplied by the Student's t-test distribution coefficient ($t_{n,\alpha}$). This coefficient was adopted for the confidence level α = 95% and degrees of freedom (n – 1 = 2). The relative uncertainty (RU) was calculated as the quotient of the standard uncertainty, i.e. the standard deviation of the mean (SD) and the mean d_{50}. The standard error (SE) was also calculated.

The hydraulic parameters calculated for the studied stream reaches allowed to calculate the roughness coefficient value from the Equation (22), which was compared with the n values calculated using the formulas presented in Table (1). In the first stage of calculations, the slope was used in these equations in accordance with the formulas themselves, using the bed slope, water surface slope or friction slope, respectively. The results of these calculations were compared with the values of n_0 from the measurements for each of the measurement reaches made in each measurement series. In the second stage of the calculations, due to the non-uniform flow, the friction slope was used in each formula (Table 1), regardless of the parameter given by its author, replacing the bed slope and water surface slope with friction slope, respectively. The results of all calculations were finally compared with each other in order to find the impact of changing the type of slope in the examined formulas on the results of the calculations compared to the actual values obtained from the measurements.

3 RESULTS

Hydrometric measurements in cross-sections were conducted at depths h ranging from 0.08 to 0.19 m in the first measurement series, from 0.10 to 0.21 m in the second measurement series and from 0.13 to 0.30 m in the third measurement series (Table 3). The bed slope and water surface slope were determined based on the measurements. The friction slope was calculated by taking into account the average flow velocity calculated from the measurements in the upper and lower cross-sections of the measurement reaches. The values of water surface slopes and friction slopes are presented in Table 3. This table also includes the roughness coefficient values calculated by the formula (22) for each of the measurement sections in a given measurement series.

The uncertainty of the mean rate flow Q of each reach, expressed by the standard deviation, is 0.0015–0.0039 for measurements series S1, 0.0014-0.0034 for measurements series S2, and 0.0024–0.0042 for measurements series S3. Taking into account the distribution coefficient ($t_{n,\alpha}$) of 2.7764, the corrected value of the standard deviation of the mean ($SDt_{n,\alpha}$) is 0.0043–0.0108 for measurements series S1, 0.0039–0.0095 for measurements series S2, and 0.0067–0.0117 for measurements series S3. Relative uncertainty (RU) and standard error (SE) for mean rate flow Q calculated in all reaches in measurement series are respectively: RU from 89.96 to 110.04 and SE from 0.0007 to 0.0017 for S1, RU from 92.44 to 107.56 and SE from 0.0006 to 0.0015 for S2 and RU from 94.30 to 105.70 and SE from 0.0011 to 0.0019 for S3.

Based on the specific grain size composition of the sediment collected from the bed (Table 4), the relative submergence h/d_{50} was calculated (Table 3) and the roughness criterion was determined according to Bathurst et al. (1981). The h/d_{50} values ranging from 2 to 7.5 indicate average roughness for nineteen measurement data and small roughness ($h/d_{50} > 7.5$) for five measurement data, i.e. on reaches IV and VI in measurement series S3, i.e. at the highest flows and on the reach VIII for all three measurement series. The uncertainty of the mean diameter d50, expressed by the standard deviation of the mean for each reach, is presented in Table 4. Taking into account the distribution coefficient ($t_{n,\alpha}$) of 4.303, the corrected value of the standard deviation of the mean ($SDt_{n,\alpha}$), relative uncertainty (RU) and standard error (SE) was calculated. The results are presented in Table 4.

3.1 Verification of empirical formulas

Table 3 presents the values of the roughness coefficients calculated using the formula (22). The values of these coefficients were compared with those calculated according to the formulas presented in Table 1. It was found that the roughness coefficients calculated by the formula (5) by Lacey (1946) are the most similar to those obtained as a result of the measurements – most of the points in the graph in Figure 2.a) are located on the proportionality line with a few cases of the value underestimation.

The Lacey's formula (5) was developed for low gradient streams. According to Yochum et al. (2012, 2014) the limit value is the dimensionless bed slope of 0.02–0.03, distinguishing

Table 3. Basic hydraulic parameters on the reach.

No.	h (m]	Q ($m^3 \cdot s^{-1}$)	R (m)	h/d_{50} (–)	S_w (–)	S_f (–)	n_0 ($m^{-1/3} \cdot s$)
Measurement series S1							
I	0.08	0.158	0.073	2.3	0.0171	0.0158	0.055
II	0.13	0.078	0.130	2.0	0.0205	0.0226	0.063
III	0.16	0.084	0.126	2.5	0.0142	0.0134	0.060
IV	0.11	0.087	0.105	4.9	0.0117	0.0086	0.054
V	0.08	0.099	0.081	2.1	0.0156	0.0157	0.061
VI	0.19	0.112	0.161	5.6	0.0082	0.0078	0.057
VII	0.11	0.051	0.088	2.6	0.0092	0.0077	0.056
VIII	0.15	0.115	0.140	7.0	0.0177	0.0197	0.062
Measurement series S2							
I	0.10	0.198	0.097	2.9	0.0080	0.0065	0.048
II	0.15	0.084	0.140	2.3	0.0141	0.0155	0.059
III	0.17	0.093	0.138	2.8	0.0103	0.0095	0.055
IV	0.14	0.105	0.136	6.4	0.0057	0.0083	0.052
V	0.12	0.115	0.114	2.9	0.0050	0.0053	0.051
VI	0.21	0.129	0.178	6.3	0.0059	0.0070	0.052
VII	0.12	0.059	0.103	2.8	0.0058	0.0031	0.054
VIII	0.17	0.168	0.157	8.0	0.0177	0.0194	0.060
Measurement series S3							
I	0.13	0.261	0.141	3.9	0.0022	0.0018	0.043
II	0.19	0.149	0.165	2.8	0.0196	0.0100	0.056
III	0.23	0.171	0.171	3.7	0.0103	0.0007	0.048
IV	0.19	0.209	0.186	8.8	0.0044	0.0021	0.047
V	0.18	0.228	0.169	4.4	0.0035	0.0038	0.046
VI	0.30	0.243	0.239	8.9	0.0047	0.0043	0.049
VII	0.24	0.144	0.204	5.8	0.0049	0.0025	0.051
VIII	0.21	0.336	0.199	10.1	0.0140	0.0190	0.055

where: No. – number of the reach, h – mean depth in the reach, Q – water flow rate, R – hydraulic radius, d_{50} – the grain size diameter for which 50% is finer, S_w – water-surface slope, S_f – friction slope, n_0 – resistance coefficient calculated from the measurement results.

Table 4. Characteristic diameters of bed sediment collected from the bed on the reach and uncertainty analysis for d_{50}.

No. of the reach	Characteristic diameters d_i (mm)												Uncertainty analysis parameters for d_{50}			
	d_5	d_{10}	d_{16}	d_{35}	d_{50}	d_{65}	d_{75}	d_{80}	d_{84}	d_{85}	d_{90}	d_{95}	DS	$SDt_{n,\alpha}$	RU (%)	SE
I	6.1	11	14	28	33	42	49	51	53	54	61	69	1.0	4.3	87.0 – 113.0	0.58
II	6.2	9.5	13	45	65	68	70	72	74	75	77	79	1.0	4.3	94.4 – 106.6	0.58
III	4.8	6.3	9	28	63	68	69	70	71	72	75	78	1.2	5.3	91.6 – 108.4	0.71
IV	3.3	5	6	13	22	33	47	53	62.5	63	67	74	0.6	2.5	88.7 – 111.3	0.33
V	5.5	10	17	20	40	51	63	68	71	72	78	81	0.7	3.0	92.5 – 107.5	0.40
VI	5	6.4	10	26	34	60	47	63	67	68	70.5	72	0.6	2.5	92.7 – 107.3	0.33
VII	2	4.5	6.2	23	41	60	66	69	70	70.5	74	79	0.6	2.5	93.9 – 106.1	0.33
VIII	4.3	5.1	6.4	12.5	21	34	50	59	65	66	70	72	0.6	2.5	88.2 – 111.8	0.33

where: DS – standard deviation, $SDt_{n,\alpha}$ – corrected value of the standard deviation of the mean, RU – relative uncertainty, SE – standard error.

between watercourses with low and high bed slopes. The bed slope of the examined reaches ranged from 0.005 to 0.047, and twelve of the twenty-four reaches had a bed slope smaller than 0.02, which is the lower limit of the Lacey range of slopes. For these reaches, roughness coefficients were obtained, the positions of which in Figure 2.a are at the greatest distance from the n_0 and n proportionality curve, where n_0 is the roughness calculated from the measurements, n – roughness estimated by the formulas from Table 1. This means that for the cross-sections located on the reaches with bed slope of <0.02 (low gradient streams) the worst results were obtained from the Lacey formula (5), which is dedicated to this range of slopes.

Much greater differentiation of n_0 values was obtained using the Riggs' formula (6) (1976) resulting in both underestimation and overestimation of the n value (Fig. 2.b). None of the hydraulic parameters affected the significant dispersion of the calculated roughness coefficient values. It can be assumed that the reason for significant discrepancies in the values of n determined by the Riggs' formula (6) and those obtained from the measurements, is the range of bed slopes. Riggs developed the formula (6) based on the measurement data of Barnes (1967), i.e. for dimensionless water surface slope of 0.0003–0.018, while in the studied streams the water surface slope was outside this range, i.e. it was from 0.0022 to 0.0205, which can be the reason for such significant discrepancies of the results.

The formulas: (7) of Bray (1979), (8) of Bray (1982) and (14) of Sauer (1990) allow for an approximate estimation of the roughness coefficient value, which is, however, somewhat overestimated (Fig 2.c and Fig 2.i). Slight discrepancies between the results of calculations of the roughness coefficient by the Bray's formula (7), compared to the one determined from the measurements may result from a slight exceedance of the maximum value of the water surface slope, for which this formula was developed. The upper limit of the dimensionless water surface slope range, according to Bray, is 0.015, while the measurements provided the values up to 0.0205. The reason for the discrepancy in the results may also be the range of the relative submergence h/d_{90} of the examined reaches. Bray developed the formula for h/d_{90} greater than 5, and the value of h/d_{90} for the examined cross-sections ranged from 1.05 to 4.27. Also the results of calculating the value of n using the formula (8) by Bray (1982) (Fig 2.d) are underestimated, but their position is close to line of perfect agreement. This formula is recommended by Bray (1982) for the channels, whose $h/d_{90} > 3$. Only five sections do not meet this condition. The Sauer's formula (14), like the Riggs' formula (6), was also developed on the basis of measurement data by Barnes (1967). In this case, despite the fact that the measured water surface slope is outside the range given by Sauer (1990), values of the roughness coefficient estimated using this formula indicate the possibility of its application in the case of the studied streams.

The values of n obtained from calculations by the formula (16) by Dingman and Sharma (1997) proved to be significantly overestimated (Fig. 2.j), which indicates that this formula should not be used to determine the roughness coefficient of the studied streams, despite the fact that the range of the water surface slopes corresponded to the range for which the formula (16) was developed. The roughness coefficients calculated by the formulas (9) and (10) of Brownlie (1983) (Fig. 2.e and Fig. 2.f), by the formula (12) of Bruschin (1985) (Fig. 2.g), by the formula (13) of Gessler (1990) (Fig. 2.h), as well as by the formula (17) of Rice et al. (1998) (Fig. 2.k) and by the formula (18) of Yochum et al. (2014) (Fig. 2.l) are also smaller than the one calculated from the measurements. Significant differences in the roughness coefficient values determined on the basis of measurements and according to empirical formulas were obtained using the formula (18) of Yochum et al. (2014) (Fig. 2.l). This formula was developed on the basis of measurement data at low flows, the water surface slope of which ranged from 0.019 to 0.17. The formula (18) of Yochum et al. (2014) was applied for low flows, where the water surface slope was smaller than the range for which this formula was developed, except for two reaches. Despite this, the calculation result also for these two cases is several times smaller than that obtained from the measurements.

Among the verified two Brownlie formulas, a smaller underestimation of the n value was obtained by using the formula (9) (Fig. 2.e) corresponding to the lower regime flow and bed slopes smaller than 0.006. On the other hand, the studied streams are characterized by an average bed slope greater than 0.006 (Table 2). Thus, by using the Brownlie's formula (10) for slopes greater than 0.006, the obtained calculation results should be closer to those obtained on the basis of the measurement results. However, this was not achieved as the results obtained using the formula (10) were worse (Fig 2.f) than those obtained by using the formula (9) (Fig. 2.e).

The results of roughness coefficient calculations by the formulas (11) of Jarrett (1984) and (15) of Rickenmann (1994) were not compared graphically with those calculated from the measurements. The roughness coefficient calculated by the Jarrett's formula (11) (1984) proved to be, on average, several times higher than that determined from the measurements. In some cases, it was even twenty or thirty times overstated. The formula (11) according to Jarrett (1984) is applicable for channels with energy gradients from 0.002 to 0.09 and for the tested reaches it ranges from 0.0007 to 0.0226, whereas for ten examined reaches the energy gradient was within the range given by Jarrett (1984). Also the range of the hydraulic radius calculated from the measurements does not correspond to the range given by Jarrett (1984). The hydraulic radius of the examined cross-sections ranged from 024 to 0.78 feet and only ten of these reaches were characterized with hydraulic radius greater than 0.5 feet. The roughness coefficient values obtained by using the formula (15) of Rickenmann (1994) were, on average, over eighty times smaller than those determined from the measurements. Despite the fact that only nine sections are characterized by a dimensionless bed slope smaller than that given by Rickenmann (1994), the value of which is 0.008 – 0.63, significantly underestimated values of the roughness coefficient were obtained for all sections.

Most of the verified formulas (Table 1) give an estimate of n depending on the bed slope or water surface slope S_w. Only the formulas (11) according to Jarrett, (12) according to Brunschin and (13) according to Gessler present the value of n in the function of friction slope S_f. During the measurements non-uniform flow was observed in the tested reaches of the streams, therefore the roughness coefficients were calculated for the friction slope using each of the formulas presented in Table 1. The values of the roughness coefficient calculated by the Lacey's formula (5) after the introduction of the friction slope (Fig. 3.a) proved to be underestimated compared to the ones obtained from the measurements and also more underestimated compared to the results of measurements with the bed slope S adopted in this formula (Fig. 2.a). The formula (6) by Riggs proved to be insensitive to the use of friction slope (Fig. 3.b) instead of the water surface slope (Fig. 2.b), because the scatter of the results of estimated values of n in relation to the proportionality line is similar regardless of whether S or S_f is used in this formula. The introduction of S_f into the Bray's formula (7) resulted in obtaining overestimated n values (Fig. 3.c) compared to the measurement results, also providing worse results, i.e. all of them were overestimated compared to the results of calculations with the water surface slope (Fig. 2.c). On the other hand, the change of S_f into

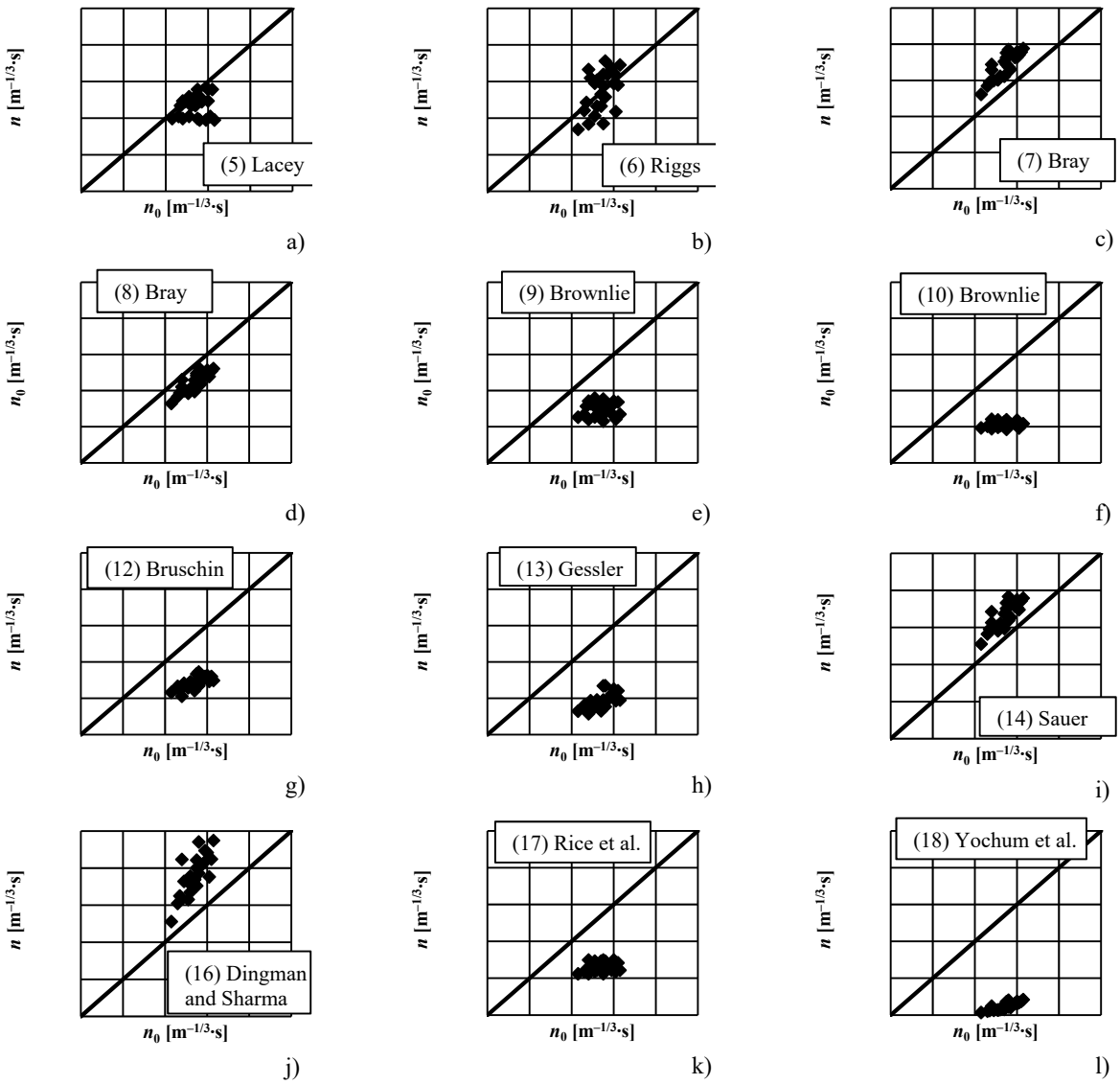

Fig. 2. Comparison of roughness coefficients calculated on the basis of the measurement results (n_0) and using empirical formulas (n) according to: a) (5) Lacey, b) (6) Riggs, c) (7) Bray, d) (8) Bray, e) (9) Brownlie, f) (10) Brownlie, g) (12) Bruschin, h) (13) Gessler, i) (14) Sauer, j) (16) Dingman and Sharma, k) (17) Rice et al., l) (18) Yochum et al. (2014).

S_w in the Bray's formula (8) (Fig. 2.d and Fig. 3.d), and in formulas (9) and (10) by Brownlie, does not cause a significant difference in the results, as can be seen when comparing Figures 2.e) and 3.e), and 2.d) and 3.d), respectively. The friction slope used in the Bray's formula (8) caused that some of the results became distant from the proportionality curve (Fig. 3.d). The use of S_f in the formula (9) by Brownlie causes the points to be moved away from the proportionality curve in Figure 3.e). This also applies to the formula (17) of Rice et al. (Figs. 2.k and 3.k). Using the formulas (14) of Sauer and (16) by Dingman and Sharmy with S_f, slightly better results were obtained (Fig. 3.i and 3.j) compared to the results of calculations using these formulas with S_w – points in Figures 2.i) and 2.j) are located closer to the proportionality curve. The change of S_f to S_w in the formula (18) by Yochum et al. (2014) causes such slight differences in the results that they are imperceptible and therefore they have not been presented in Figure 3. In these analyses, the results obtained from the formulas (11) of Jarrett and (15) of Rickenman also differed significantly from those obtained from the measurements.

3.2 An attempt to develop empirical formulas

The correlation relationships were developed for the measured water surface slope S_w and the calculated friction slope S_f, presented in Table 3, based on the example of the formula (5) proposed by Lacey (1946). These formulas have the form of:

$$n = 0.0837\ S_f^{0.0895} \tag{23}$$

$$n = 0.1038\ S_w^{0.1391} \tag{24}$$

Due to the small amount of data (N = 24), the developed formulas are an initial attempt to develop a relationship for streams with gravel bottom and bed slopes ranging from 0.0022 to 0.0205. The coefficient of determination r^2 for the developed equations amounts to 0.599 for the Equation (23) and 0.716 for the Equation (24). All parameters of independent variables are statistically significant at p = 0.05%.

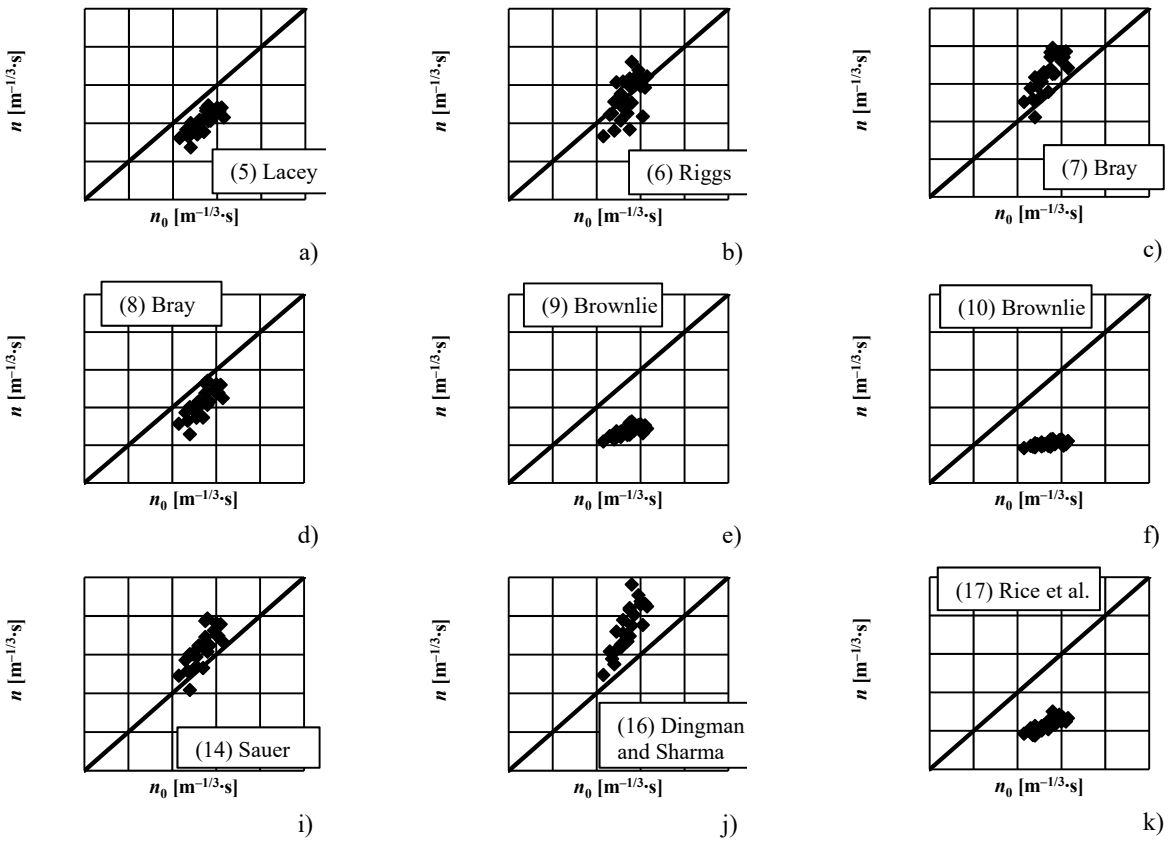

Fig. 3. Comparison of roughness coefficients calculated on the basis of the measurement results (n_0) and using empirical formulas (n), in which a friction slope was introduced in place of a slope, i.e. equations: a) (5) Lacey, b) (6) Riggs, c) (7) Bray, d) (8) Bray, e) (9) Brownlie, f) (10) Brownlie, i) (14) Sauer, j) (16) Dingman and Sharma, k) (17) Rice et al.

The predictive effectiveness of the developed models was statistically assessed using the following measures: root mean square error: RMSE = $(\Sigma(x_p - x_m)2/N)^{1/2}$ and mean absolute error: MAE = $\Sigma|x_p - x_m|/N$, where: x_p – value of predicted roughness coefficient or resistance coefficient, x_m – value of the measured roughness coefficient or resistance coefficient, N is the number of data.

The RMSE and MAE values for the model written in the form of Equation (23), in which the independent variable is the friction slope, are 0.0033 and 0.0029, respectively. For the Equation (24) with the water surface slope, the RMSE and MAE values are 0.0028 and 0.0024, respectively.

Control calculations were also performed to verify the influence of the applied slope in a given formula. Thus, the values of the roughness coefficient were calculated from the formula (23) by introducing the water surface slope calculated for the examined reaches instead of the friction slope. The predictive efficiency of this model for the independent variables S_w were determined by RMSE and MAE, the values of which are 0.0034 and 0.0029, respectively. The calculations with the formula (24) were also performed for the friction slope instead of for the water surface slope. The calculated RMSE and MAE values are 0.0041 and 0.0031 respectively.

4 DISCUSSION

The obtained results, verifying the application of the tested formulas (Table 1), indicate that the estimated values of the roughness coefficient for streams with gravel bottoms located in the Kraków-Częstochowa Upland can be obtained from the Lacey's formula (5), which shows the dependence of this coefficient on the bed slope. The *n* values calculated for the bed slopes of the examined streams, proved to be partially underestimated. Also Nguyen and Fenton (2004) found that the roughness coefficient values determined using the Lacey's formula are underestimated as compared to the values determined from the measurements, but in the case of those studies this observation concerned the entire range of measurements.

A parameter that is less determining while calculating the *n* value is the water surface slope, applied in the formulas (6) of Riggs, (7) and (8) of Bray and (14) of Sauer. On the basis of the obtained results, it was found that by using these formulas, it is possible to obtain the roughness coefficient values similar to the real ones. The formula (6) by Riggs gave both underestimated and overestimated *n* values. When using the Bray's formula (7), the *n* values were overestimated for the entire data range, similarly as in the case of the formula (14) of Sauer. On the other hand, the underestimated values of the roughness coefficient were obtained from the Bray's formula (8). According to Nguyen and Fenton (2004), the Bray's and Sauer's formulas underestimated the values of *n*.

Out of the fourteen verified formulas, only the formula (11) of Jarrett, (12) of Bruschin and (13) of Gessler were developed for the friction slope and only these formulas in their original form can be used in the conducted research due to the non-uniform flow occurring in the studied streams. However, the values of *n* calculated by the Jarrett's Equation (11) were over ten times overestimated, and the values obtained from the formulas (12) of

Bruschin and (13) of Gessler – were significantly underestimated (Fig. 2), which excluded their use. Machiels et al. (2011) state that in simple empirical formulas, which combine the channel roughness, flow variables and bed slope, the bed slope can be replaced with friction slope and thus determine the friction effect for the flow conditions other than uniform flow. Replacing the bed slope or water surface slope with friction slope in the assessment of applicability of the verified empirical formulas, did not improve the estimated n values. In the case of the Lacey's formula (5), worse results were obtained, i.e. the n values were more underestimated (Fig. 3.a). Using the formula (7) of Bray, in which the friction slope was used instead of the water surface slope, still results in obtaining overestimated n values (Fig. 3.c), while the formula (8) of Bray brings some of the results closer to the proportionality line. The roughness coefficients obtained from the Saurer's formula (16) with friction slope proved to be less overestimated (Fig. 3.i) than while using the water surface slope (Fig. 2.i). After applying the friction slope in the formula (6) of Riggs, some of the obtained results were less overestimated (Fig. 3.b) without causing significant changes in the arrangement of points in relation to the proportionality curve (Fig. 2.b). The results of the calculations with the other formulas using the friction slope appeared to be as unsatisfactory as of the calculations conducted for the bed slope or water surface slope.

The formulas (5) of Lacey, (6) of Riggs, (7) and (8) of Bray and (14) of Sauer, regardless of the water flow conditions, i.e. uniform or non-uniform flow, allow only an approximate estimate of the roughness coefficient in the studied streams. It is indicated by the calculated differences in the results Δ, as a percentage deviation of the estimated n value from the values obtained from the n_0 measurements. The values of Δ calculated for the slopes given in these formulas, i.e. without taking into account the non-uniform flow conditions, are from –38 to 3% for the formula (5) of Lacey, –33 to 39% for the formula (6) of Riggs, from 12 to 41% for the formula (7) of Bray, 27 to –4% for the formula (8) of Bray and from 10 to 43% for the formula (14) of Sauer (Fig. 2). When the friction slope was used in these formulas, the difference in the results (Fig. 3) is as follows: for the formula (5) of Lacey from –43 to –12%, (6) of Riggs: from –33 to 29%, (7) of Bray: from –41 to 12%, (8) of Bray: from –46 to –3% and (14) of Sauer: from –13 to 41%. For the remaining formulas, the obtained differences were significantly higher – the highest for the formula (6) of Riggs, amounting to 62%. The calculated differences in the results are significant and it can be concluded that there is no single equation that can consistently and accurately estimate the n values for all channels, as also demonstrated by Coon (1998). The differences in the obtained results are also caused by the fact that empirical formulas are developed for specific conditions that limit their application geographically, resulting from a specific research area or a deliberately selected research site in a channel with perfect characteristics (Coon, 1998). Another issue is the application of a given formula to the hydraulic conditions of the analyzed reach of a watercourse, taking into consideration the scope of conditions, for which the formula was developed. In many publications using empirical formulas, the Authors of these publications do not specify the scope of their application, or this description is not complete. A very extensive description of the formulas and their application is presented by Lang et al. (2004), however this description does not provide the range of slopes, relative submergence or hydraulic radius corresponding to the application of these formulas. Moreover, when applying some of the formulas, the authors of the studies do not pay attention to the source materials which provide statistical parameters of the formulas developed. An example is the formula (7) of Bray, for which the coefficient of determination is only 0.298, and yet it is widely used, e.g. in the studies by Coon (1998), Lang et al. (2004), Ferguson (2007), Ghani et al. (2007), López et al. (2007), Sefick et al. (2015), Zhu et al. (2020), Toufik and Mahmoud (2021), as well as in this study.

5 CONCLUSIONS

Out of the fourteen empirical formulas assessed, only the formulas (5) of Lacey, (6) of Riggs, (7) and (8) of Bray as well as (14) of Sauer allow for an approximate estimation of the roughness coefficient in the studied streams of the Kraków-Częstochowa Upland.

In the studied streams, the water flow was non-uniform and therefore the roughness coefficient was calculated using the tested formulas for the friction slope. Based on the obtained results of calculations for the estimated roughness coefficient values, it is not possible to clearly indicate the formula enabling the estimation of this coefficient. The Riggs equation (6) allows to obtain the roughness coefficient value that differs from the one obtained from the measurements by –33 to 29%. In the case of the remaining formulas, the differences in the results reached even 41% for the formula (7) of Bray and (14) of Sauer, and 43% for the formula (5) of Lacey and (8) of Bray.

Taking into account the occurring non-uniform flow and using the friction slope in the formulas instead of the bed slope did not improve the values of the roughness coefficient estimated using the examined formulas. The RMSE and MAE values calculated for the developed correlation Equations (23) and (24) showed that the adopted friction slope or water surface slope had no effect on the value of the estimated roughness coefficient. RMSE and MAE values for the formula (23), in which the friction slope was replaced by the water surface slope, amount to 0.0034 and 0.0029, respectively. These values do not differ from those obtained for this very equation, in which the friction slope was used according to its original form, because then the RMSE and MAE values are 0.0033 and 0.0029, respectively. When replacing the water surface slope with the friction slope in the Equation (24), the RMSE and MAE values for the estimated n value were 0.0041 and 0.0031, respectively. On the other hand, the values of RMSE and MAE for the calculations performed with the formula (24) with the water surface slope, i.e. in accordance with the provisions for this formula, are 0.0028 and 0.0024, respectively. In this case, after changing the type of slope in the formula, higher error values were obtained, i.e. by 46 and 29%, respectively. These values do not disqualify the change of slope in the formula (24), because the RMSE and MAE values mean that the actual values of the roughness coefficient obtained with this equation will deviate from the predicted ones by the absolute n values equal to only 0.41–0.31%. The obtained results allow to state that there are no significant differences in the obtained results, meaning that not taking into account the water flow conditions, i.e. uniform or non-uniform flow, does not affect the correct determination of the resistance impact acting in the examined streams. The roughness coefficient in streams with gravel beds, the morphological characteristics of which are similar to those presented in this paper, can be calculated using the Equations (23) and (24).

REFERENCES

Barnes, H.H., 1967. Roughness characteristics of natural channels. Water-Supply Paper 1849. U.S. Geological Survey.

Bathurst, J.C., Li, R.M., Simons, D.B., 1981. Resistance equation for large-scale roughness. J. Hydraul. Div. ASCE, 107,

12, 1593–1613. https://doi.org/10.1061/JYCEAJ.0005780
Bellos, V., Nalbantis, I., Tsakiris, G., 2018. Friction modeling of flood flow simulations. Journal of Hydraulic Engineering, 144, 12. DOI: 10.1061/(ASCE)HY.1943-7900.0001540
Bjerklie, D.M., Dingman, S.L., Bolster, C.H., 2005. Comparison of constitutive flow resistance equations based on the Manning and Chezy equations applied to natural rivers. Water Resour. Res., 41, 11, W11502. DOI: 10.1029/2004WR003776
Bray, D.I., 1982. Flow resistance in gravel-bed rivers. In: Hey, R.D., Bathurst, J.C., Thorne, C.R. (Eds.): Gravel-Bed Rivers. John Wiley and Sons, Chichester, UK, pp. 109–137.
Bray, D.I., 1979. Estimating average velocity in gravel-bed rivers. J. Hydraul. Div. ASCE, 105, 9, 1103–1122.
Brownlie, W.R., 1983. Flow depth in sand-bed channels. Journal of Hydraulic Engineering, 109, 7, 959–991.
Bruschin, J., 1985. Discussion of "Brownlie (1983): Flow depth in sand-bed channels". Journal of Hydraulic Engineering, 111, 736–739.
Coon, W.F., 1998. Estimates of Roughness Coefficients for Natural Stream Channels with Vegetated Banks. Report, US Geological Survey Water-Supply, Paper No 2441.
Dingman, S.L., Sharma, K.P., 1997. Statistical development and validation of discharge equations for natural channels. Journal of Hydrology, 199, 13–35.
Ferguson, R., 2007. Flow resistance equations for gravel- and boulder-bed streams. Water Resour. Res., 43, W05427. https://doi.org/10.1029/2006WR005422
Ferguson, R., 2010. Time to abandon the Manning equation? Earth Surf. Process. Landf., 35, 1873–1876. https://doi.org/10.1002/esp.2091
Fischenich, C., Little, C., 2007. Sediment sampling and analysis for stream restoration projects. U.S. Army Engineer Research and Development Center, Technical Note – Ecosystem Management and Restoration Research Program. http://hdl.handle.net/11681/3972
Gessler, J., 1990. Friction factor of armoured river beds. Journal of Hydraulic Engineering, 116, 531–543.
Ghani, A.A.B, Zakaria, N.R., Kiat, Ch.Ch., Ariffin, J., Hasan, Z.A., Ghaffar, A.B.A., 2007. Revised equations for Manning's coefficient for sand-bed rivers. International Journal of River Basin Management, 5, 4, 329–346. DOI: 10.1080/15715124.2007.9635331
Griffiths, G.A., 1981. Flow resistance in coarse gravel bed rivers. J. Hydraul. Div. ASCE, 107, 7, 899–918.
Hicks, D.M., Mason, P.D., 1991. Roughness Characteristics of New Zealand Rivers. DSIR Water Resources Survey, Wellington, 329 p.
Jarrett, R.D., 1984. Hydraulics of high-gradient rivers. J. Hydraul. Eng., 110, 11, 1519–1539.
Keulegan, G.H., 1938. Laws of turbulent flow in open channels. Journal of the National Bureau of Standards, Research Paper 1151, 21, 707–741.
Kowalczyk, A., Szlachta, A., Hanus, R., 2012. Standard uncertainty determination of the mean for correlated data using conditional averaging. Metrology and Measurement Systems, Rzeszów, Poland, 787–796.
Lacey, G., 1946. A general theory of flow in alluvium. Journal of the Institution of Civil Engineers, Paper No 5518, 27, 1, 16–47.
Ladson, A., Anderson, B., Rutherfurd, I., van de Meene, S., 2002. An Australian handbook of stream roughness coefficients: How hydrographers can help. In: Proceeding of 11th Australian Hydrographic conference, Sydney, 3–6 July, 2002.
Lane, S.N., 2014. Acting, predicting and intervening in a socio-hydrological world. Hydrol. Earth Syst. Sci., 18, 927–952.
Lang, S., Ladson, T., Anderson, B., 2004. A review of empirical equations for estimating stream roughness and their application to four streams in Victoria. Australasian Journal of Water Resources, 8, 1, 69–82, DOI: 10.1080/13241583.2004.11465245
Lee, K., Firoozfar, A.R., Muste, M., 2017. Technical Note: Monitoring of unsteady open channel flows using the continuous slope-area method. Hydrol. Earth Syst. Sci., 21, 1863–1874. https://doi.org/10.5194/hess-21-1863-2017
Limerinos, J.T., 1970. Determination of the Manning coefficient from measured bed roughness in natural channels. U.S. Geological Survey Journal of Research, 4, 3, 285–291.
López, R., Barragán, J., Colomer, M.A., 2007. Flow resistance equations without explicit estimation of the resistance coefficient for coarse-grained rivers. J. Hydrol., 338, 1–2, 113–121. http://dx.doi.org/10.1016/j.jhydrol.2007.02.027.
Machiels, O., Erpicum, S., Archambeau, P., Dewals, B., Pirotton, M., 2011. Theoretical and numerical analysis of the influence of the bottom friction formulation in free surface flow modelling. Water SA, 37, 2, 221–228.
Machiels, O., Erpicum, S., Archambeau, P., Dewals, B. and Pirotton, M., 2009. Bottom friction formulations for free surface flow modeling. In: 8th NCTAM Congress, Belgium. http://hdl.handle.net/2268/28208
Meyer-Peter, E., Muller, R., 1948. Formulas for Bed-load Transport. In: Proc. Third Meeting of IAHR, Stockholm, Sweden, pp. 39–64.
Michalec, B., Zwolenik, M., 2020. Preliminary verification of empirical formulas to define the roughness coefficient. Acta Sci. Pol. Formatio Circumiectus, 19, 4, 21–32. https://doi.org/10.15576/ASP.FC/2020.19.4.21
Nitsche, M., Rickenmann, D., Kirchner, J.W., Turowski, J.M., Badoux, A., 2012. Macroroughness and variations in reach-averaged flow resistance in steep mountain streams. Water Resour. Res., 48, W12518. DOI: 10.1029/2012WR012091.
Nguyen, H.T., Fenton, J.D., 2004. Using two-point velocity measurements to estimate roughness in streams. In: Rutherfurd, I.D., Wiszniewski, I., Askey-Doran, M., Glazik, R. (Eds.): Proc. 4th Austral. Stream Management Conf., Launceston, Tasmania, 19-22 Oct 2004. Dept. of Primary Industries, Water and Environment, Hobart, pp. 445–450.
Phillips, J.V., Ingersoll, T.L., 1997. Comparison of verified roughness coefficients for gravel-bed streams in central Arizona with other areas of the western United States. In: Floodplain Management in a Multi-Faceted World. In: Proceedings of the 21st Annual Conference of the Association of State Floodplain Managers; Little Rock, Arkansas, April 27-May 2 1997. Natural Hazards Research Centre, University of Colorado, pp. 158–158.
Raudkivi, A.J., 1976. Loose Boundary Hydraulics. Pergamon Press.
Rice, C.E., Kadavy, K.C., Robinson, K.M., 1998. Roughness of loose rock riprap on steep slopes. J. Hydraul. Eng., 124, 2, 179–185.
Rickenmann, D., 1994. An alternative equation for the mean velocity in gravel-bed rivers and mountain torrents. In: Cotroneo, G.V., Rumer, R.R. (Eds.): Proceedings of the Conference Hydraulic Engineering '94, vol. 1. ASCE, New York.
Riggs, H C., 1976. A simplified slope-area method for estimating flood discharges in natural channels. U.S. Geological Survey Journal of Research, 4, 3, 285–291.
Sauer, V.B., 1990. US Geological Survey, Written communication to W.F. Coon. Estimation of roughness coefficients for natural stream channels with vegetated banks, 1998. US Geological.
Sefick, S.A., Kalin, L., Kosnicki, E., Schneid, B.P., Jarrell, M.S., Anderson, C.J., Paller, M.H., and Feminella, J.W., 2015. Empirical estimation of stream discharge using channel geometry

in low-gradient, sand-bed streams of the Southeastern Plains. Journal of the American Water Resources Association (JAWRA), 1–12. DOI: 10.1111/jawr.12278

Strupczewski, W.G., Szymkiewicz, R., 1996. Analysis of paradoxes arising from the Chezy formula with constant roughness: I. Depth-discharge curve. Hydrological Sciences Journal, 41, 5, 659–673.

Toufik, H., Mahmoud, H., 2021. Friction coefficient equation in a gravel bed under bedload regime using the dimensional analysis. KSCE Journal of Civil Engineering, 25, 4252–4260 https://doi.org/10.1007/s12205-021-1576-6

Yen, B.C., 2002. Open channel flow resistance. Journal of Hydraulic Engineering, 128, 1, 20–39. http://dx.doi.org/10.1061/(ASCE)0733-9429(2002)128:1(20)

Yochum, S.E., Bledsoe, B.P., David, G.C.L., Wohl, E., 2012. Velocity prediction in high-gradient channels. Journal of Hydrology, 424–425, 84–98.

Yochum, S.E., Comiti, F., Wohl, E., David, G.C.L., Mao, L., 2014. Photographic Guidance for Selecting Flow Resistance Coefficients in High-Gradient Channels. Gen. Tech. Rep. RMRS-GTR-323. Fort Collins, CO: U.S. Department of Agriculture, Forest Service, Rocky Mountain Research Station. 91 p.

Zhu, X., Liu, B., Liu, Y., 2020. New method for estimating roughness coefficient for debris flows. Water, 12, 9, 2341. https://doi.org/10.3390/w12092341

Received 30 July 2022
Accepted 13 December 2022

J. Hydrol. Hydromech., 71, 2023, 1, 91–99
https://doi.org/10.2478/johh-2022-0038

sciendo Journal of Hydrology and Hydromechanics Institute of Hydrology SAS

Soil management and seasonality impact on soil properties and soil erosion in steep vineyards of north-western Croatia

Ivan Dugan[1], Igor Bogunovic[1*], Paulo Pereira[2]

[1] Faculty of Agriculture, University of Zagreb, Svetosimunska 25, 10000 Zagreb, Croatia. E-mail: idugan@agr.hr (Ivan Dugan)
[2] Environmental Management Laboratory, Mykolas Romeris University, LT-08303 Vilnius, Lithuania. E-mail: paulo@mruni.eu
[*] Corresponding author. E-mail: ibogunovic@agr.hr

Abstract: In order to mitigate vineyard degradation, we study different soil management to obtain the most suitable practices. To study the effects of water erosion on vineyards, a rainfall experiment (58 mm h^{-1} for 30 min) was applied on Anthrosols in humid conditions to assess the impact of treatment (Tilled, Straw and Grass) and season (Spring and Summer). Higher bulk density (BD) and soil water content (SWC) were on the Straw treatment in the Spring period. Also, the Tilled and Grass treatment noticed higher mean weight diameter (MWD) and water-stable aggregates (WSA). In the Summer, BD, SWC and MWD were significantly higher on the Grass treatment. Higher values of time to ponding (TP) and time to runoff (TR) in Spring were recorded on the Grass treatment, Runoff was higher on the Straw treatment. Higher sediment concentration (SC) and soil loss (SL) were noticed during the Tilled treatment. In the Summer period, TP was higher on the Straw treatment, while TR and Runoff were higher on the Straw, SC and SL on the Tilled treatment. This study confirms the positive effects of grass cover and straw mulching as a sustainable agricultural practice in sloped vineyards of north-western Croatia.

Keywords: Land degradation; Trafficking; Tillage; Overland flow; Nutrient loss.

1 INTRODUCTION

The rising global population is threatening food security and environmental degradation. Land degradation, especially soil erosion, is a major concern nowadays due to intensive land use and non–sustainable agriculture practices, which increase soil and nutrient losses and decrease soil fertility and crop yield (Bogunovic et al., 2020; Gholami et al., 2013). These kinds of threats are not acceptable due to larger food production requirements. The leading cause of soil erosion has been attributed to agricultural activities because anthropogenic influences are changing soil properties and processes, which have a major impact on soils (Telak et al., 2020). Soil erosion processes are influenced by soil properties and land management, such as tillage, canopy cover management, herbicide use, and higher soil compaction (García-Ruiz, 2010; Telak et al., 2020). Tillage is recognised as a great accelerator of soil erosion. Its intensity and the type of machinery that is used affect soil properties such as bulk density (BD), aggregate stability, soil porosity and organic matter (Curaqueo et al., 2010). All these properties affect soil structure disturbed by tillage interventions making the soil highly erodible during rainstorms. Heavy rainstorms are becoming frequent due to climate changes; thus, different soil management needs to be considered to reduce the impact of these events. These events can be mitigated by the use of reduced tillage (Ebabu et al., 2022), by leaving the surface grass-covered (Duan et al., 2022), or by mulching the soil surface (Biddoccu et al., 2017; Gao et al., 2022). Vineyards have been recognised as vulnerable agricultural areas highly exposed to high erosion rates due to frequent tillage and trafficking (Biddoccu et al., 2017; Bogunovic et al., 2020; Novara et al., 2011; Prosdocimi et al., 2016; Rodrigo-Comino et al., 2018). Several authors (Biddoccu et al., 2017; Bogunovic et al., 2020; Novara et al., 2011; Prosdocimi et al., 2016; Rodrigo-Comino et al., 2018) claim that soil erosion rates in vineyards are diverse due to the different land management, climate conditions, parent material, and soil properties. Also, soil erosion affects nutrient losses (Mishra et al., 2022), which are important for plant growth. Because of these facts, the temporary or permanent surface cover has been recognised as a nature-based solution for mitigating land degradation in permanent plantations, such as orchards and vineyards (Baiamonte et al., 2019; Morvan et al., 2014; Panagos et al., 2015). There are different types of surface cover, such as straw (Gholami et al., 2013), pomace (Parras-Alcántara et al., 2016), stones (Abu-Zreig et al., 2011), geotextiles (Kertész et al., 2007), wooden chips (Smets et al., 2008), pruning residues (Rodriguez-Lizana et al., 2008) and bark strands (Fernández and Vega, 2014) as good examples of mulching practices. They are instant solutions and need constant application due to their possibility to incorporate into the soil (Li et al., 2020; Zhang et al., 2021).

In 2020, the area under vineyards in Croatia covered 21450 ha, which is 11 magnitude orders less than maise production, which is Croatia's most represented crop (FAOSTAT, 2021). However, vineyard economic importance for producers is high. Some grape producers practice grass cover, but most bare soil using herbicides or intensive tillage. To assess potential erodibility and determine the sustainable and less sustainable practices throughout the year and to get closer to the real estimation, a rainfall simulator provides a cheap and fast possibility to measure such erosion events. However, using a rainfall simulator has limitations; thus, it is necessary to conduct time series of simulation experiments throughout several seasons to get results as similar as possible to the true state of the degraded area. Therefore, this study aimed to 1) assess the impact of soil management on soil erosion rates in vineyards in two different seasons, 2) determine the best soil conservation management, and 3) relate the soil properties and hydrological response.

The hypothesis is that treatments with grass cover will ensure sustainable soil properties and fewer soil losses, thereby lower nutrient losses in a steep vineyard in north-western Croatia.

2 MATERIALS AND METHODS

2.1 Study area

The study site was carried out in the northwest part of Croatia, near Zagreb, at Jazbina Experimental Station (45° 51′ S 16° 0′ E, 258 m a.s.l.) (Figure 1). According to climate classification, it is described as temperate continental. The type of soil is developed on Pleistocene loam and Pliocene clay substrata and is classified as Anthrosols created from Stagnosol (IUSS WRB, 2015). The soil texture is silty clay loam. Detailed soil information is presented in Table 1. The vineyard was raised in 1995 on an average slope of 11.3 °. The average row length is 92 m with southwest exposition. The mean annual temperature of 2020 was 12.6 °C, where January is the coldest (1.1 °C), and June is the warmest (22.9 °C). The annual precipitation was 950.4 mm, ranging from a minimum of 8.7 mm in January to a maximum of 159.6 mm in June (Figure 2).

Table 1. Soil properties in the studied vineyard.

Depth (mm)	0–600
Horizons	Ap
Soil colour	10YR 4/3
Organic matter (g kg^{-1})	5.34
pH in H_20 (w w^{-1} 1:5)	6.67
EC (µs cm^{-1})	54
CEC ($cmol_{(+)}kg^{-1}$)	18.3
P_2O_5 (g kg^{-1})	36.8
K_2O (g kg^{-1})	180
Clay (g kg^{-1})	320
Fine silt (g kg^{-1})	350
Coarse silt (g kg^{-1})	270
Fine sand (g kg^{-1})	20
Coarse sand (g kg^{-1})	40
Texture classification	Silty clay loam

2.2 Experimental design

Three types of treatment were studied: tilled vineyard (Till) - tillage was conducted two times per year (April and June) with a tractor, and use of rotary harrow, grass-covered vineyard (GC) – naturally grass species cover soil, and straw mulched vineyard (Straw) – this treatment was mulched using wheat straw, as it was the most acceptable, cheap and easy to acquire. All treatments were conducted in one vineyard with the same slope and exposition in which bare soil by using tillage and grass cover are alternated every second row. Before rainfall simulation experiments, the Straw treatment was established after tillage was performed season before the application dose (2.5 t ha^{-1}), and new doses was applied prior to rainfall simulation experiments. This dosage was used because it is enough to conserve the soil surface and cover it approximately 30–50% (Birkás et al., 2008). Tractor trafficking was usual, covering the needs for tillage management, grass mowing and pesticide application. From the beginning of the year to the end of our rainfall experiment in June, the tractor made 6 passes. For each treatment, 10 rainfall simulations were

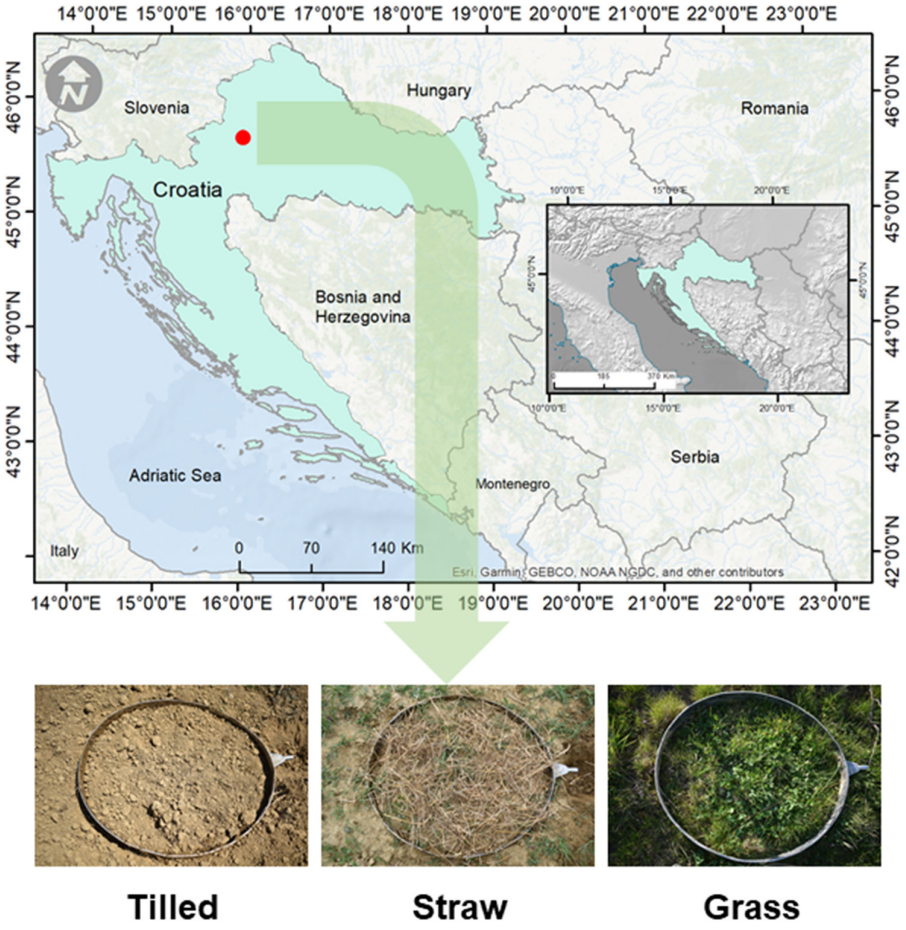

Fig. 1. Study site and treatments.

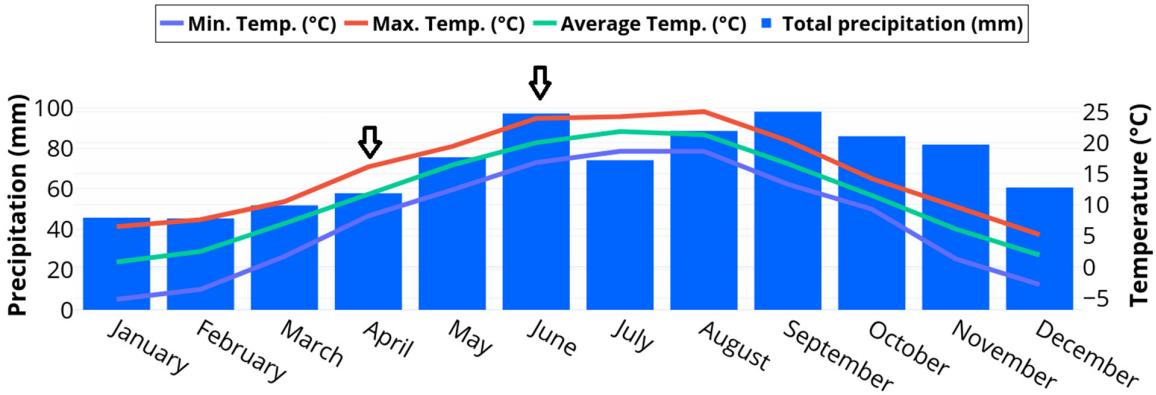

Fig. 2. Monthly mean precipitation and temperature (2020). Arrows indicate months when the measurement were performed.

carried out per season. The rainfall simulation experiments were conducted twice in 2020 (April and June). In total, 60 rainfall simulation experiments were conducted (2 seasons x 3 treatments x 10 repetitions). A rainfall simulator (UGT Rainmaker, Müncheberg, Germany) was used for the study purpose for half an hour at an intensity of 58 mm h^{-1} (Bogunovic et al., 2020). Plots were lined with a metal ring (1 m in diameter, area of 0.785 m^2) with the faucet, through which complete runoff from one simulation experiment will be collected. All plots were installed in the vineyard's middle of the inter-rows position. The runoff inside the metal ring with the faucet was collected into a plastic canister connected to collect overland flow, and subsequently weighed and filtered to measure sediment concentration and losses.

Before every simulation started, in close vicinity of plots, soil core samples of 100 cm^{-3} (53 mm in diameter) were taken from 0–10 cm depth for determining bulk density (BD), soil water content (SWC) and water holding capacity (WHC). At the same time, additional undisturbed soil samples were collected from 0–10 cm depth and stored in rectangular boxes to assess mean weight diameter (MWD) and water stable aggregates (WSA). Also, before every simulation, a digital level meter - Bosch GLM 80 + R60 Professional (Gerlingen, Germany) was used to determine the slope inside every metal ring. During each simulation, time to ponding (TP) and time to runoff (TR) were measured with a chronometer (CASIO HS-6-1EF chronometer (Tokyo, Japan).

2.3 Laboratory analysis

Sediment yield was determined after air-drying at room temperature for two weeks and the weighting of the filter paper. The mass of the sediment loss (SL) was given from the mass of overland flow to get the runoff (Bogunovic et al., 2020). Sediment concentration (SC) was calculated by dividing the sediment mass by the overland flow mass. Bulk density, WHC and SWC were determined using soil cores samples. The weighing was carried out before and after capillary wetting (natural suction) and drying at 105 °C for 48 h, after which they were calculated according to the gravimetric method:

$$BD = dry\ sample / soil\ volume, \quad (1)$$

$$WHC = ((capillary\ wetted\ sample - dry\ sample) / soil\ volume) * 100, \quad (2)$$

$$SWC = ((sample\ with\ field\ water\ content - dry\ sample) / soil\ volume) * 100. \quad (3)$$

All undisturbed samples were prepared by hand, avoiding the possibility of breaking down the formed aggregates following Dıaz-Zorita et al. (2002). Samples were air-dried for one week in the laboratory at room temperature and dry-sieved in a sieve shaker for 30 seconds (Le Bissonnais, 1996) to obtain particular aggregate size fractions (<0.25, 0.25–0.5, 0.5–1.0, 1.0–2.0, 2.0–4.0, 0.4–0.5, and 0.5–0.8 mm) and calculate MWD using the following formula for calculation after weighting each aggregate size:

$$MWD = \sum_{i=1}^{n} xi * wi \quad (4)$$

where *xi* is the mean diameter of any particular size range of aggregates separated by sieving, and *wi* is the weight of aggregates in that size range as a fraction of the total dry weight of soil used. Eijkelkamp's wet sieving method derived from Kemper and Rosenau (1986) was used to determine WSA with Eijkelkamp's wet sieving apparatus on all previously dry sieved samples in the particle size range of 1.0–2.0 mm. The percentage of WSA was obtained with the equation:

$$WSA = \frac{Wds}{Wds + Wdw} * 100 \quad (5)$$

where: WSA is the percentage of stable water aggregates, *Wds* is the weight of aggregates dispersed in dispersing solution (g), and *Wdw* is the weight of aggregate dispersed in distilled water (g).

2.4 Statistical analysis

Data normality was tested with the Shapiro – Wilk test. Data normality was considered at a $p > 0.05$. Some variables followed the Gaussian distribution, but SLOPE, TR and SL did not follow the distribution, so those data were normalised with natural logarithm and square-root (SQRT) transformations to achieve data normality. A two–way ANOVA was performed to analyse the impact of land use and season on soil properties and overland flow, where significant differences were observed at a $p < 0.05$. Tukey's LSD post hoc test was performed. Principal component analysis (PCA) was performed on the SQRT transformed data (since it was the closest to normality), based on the correlation matrix to identify the associations between variables. All the data analyses were carried out using Statistica 12.0 for MS Windows. Figures were carried out with Plotly (https://chart-studio.plotly.com). All the data in the tables and graphs are presented in their original state.

3 RESULTS

3.1 Soil properties

The impacts of treatment and season on soil properties were analysed with two-way ANOVA and are shown in Table 2. Treatment, season and treatment x season had no significant impact on SLOPE. Bulk density, SWC, WHC, and WSA significantly differed for treatment, season and treatment x season (Table 2). As mentioned before, SLOPE had no significant differences in treatment and season. At the same time, BD showed significantly higher values in the Spring on the Grass treatment, while the Tilled and Straw treatment did not differ. Table 3 shows that in the Summer period, higher values were noticed on the Grass treatment compared to the Tilled and Straw one, but there was a slight increase in the Tilled treatment compared to the seasons. SWC in the Spring was significantly higher on the Straw treatment. This pattern was not observed in the Summer, so higher SWC was on the Grass treatment compared to the Tilled and Straw treatment. Water holding capacity was lower on the Straw treatment when compared to the Tilled and Grass treatment, but in the Summer, that pattern changed, and higher values were noticed on the Straw treatment (Table 3). Table 3 indicates that different values occurred between treatments, so in Spring, values of WSA were significantly lower on the Straw treatment compared to the Grass. In contrast, the WSA values on the Tilled treatment did not significantly differ from the Grass or Straw treatment. In the Summer, those values were significantly lower on the Tilled treatment than Straw, while the Grass treatment did not differ from the Straw or Tilled treatment, as shown in Table 3.

Table 2. Two-way ANOVA results for soil properties.

Variable	Factors	F	p
SLOPE	Land use	0.43	ns
	Season	0.02	ns
	Land use x Season	1.26	ns
BD	Land use	23.49	***
	Season	8.26	**
	Land use x Season	15.23	***
SWC	Land use	14.93	***
	Season	13.39	***
	Land use x Season	58.04	***
WHC	Land use	4.89	*
	Season	30.73	***
	Land use x Season	36.57	***
MWD	Land use	6.65	**
	Season	18.44	***
	Land use x Season	15.35	***
WSA	Land use	7.87	**
	Season	23.27	***
	Land use x Season	19.11	***

Significant differences were observed at $p < 0.05$*, $p < 0.01$** and $p < 0.001$***. No significant (ns) at a $p < 0.05$. Abbreviations: Bulk density (BD); soil water content (SWC); water holding capacity (WHC); mean weight diameter (MWD); water stable aggregates (WSA); time to ponding (TP); time to runoff (TR); sediment concentration (SC); sediment loss (SL).

Table 3. *Post-hoc* results for soil properties.

Season	Treatment	SLOPE (°)	BD (g cm^{-3})	SWC (%)	WHC (%)	MWD (mm)	WSA (%)
Spring (April)	Tilled	14.00 Aa	1.27 Ba	21.28 Ba	44.86 ABa	2.87 Ba	46.97 ABa
	Straw	13.90 Aa	1.40 Aa	30.13 Aa	38.01 Bb	2.65 Bb	42.10 Bb
	Grass	13.60 Aa	1.26 Bb	20.00 Bb	45.69 Aa	3.04 Aa	48.42 Aa
Summer (June)	Tilled	14.00 Aa	1.21 Ba	16.77 Ba	38.28 Bb	2.78 Ba	44.37 Ba
	Straw	13.90 Aa	1.42 ABa	17.34 Aba	41.88 Aa	2.52 Ba	55.23 Aa
	Grass	13.60 Aa	1.49 Aa	28.76 Aa	38.56 Bb	3.21 Aa	52.95 ABa

Different letters after mean values in the columns represent significant differences at $p < 0.05$. Different capital letters show statistical differences between treatments, and different lowercase letters show statistical differences between seasons. Bulk density (BD); soil water content (SWC); water holding capacity (WHC); mean weight diameter (MWD); water stable aggregates (WSA); time to ponding (TP); time to runoff (TR); sediment concentration (SC); sediment loss (SL).

3.2 Overland flow properties

Table 4 shows the impacts of treatment, season and treatment x season on the hydrological response. Treatment and seasonality had significant impacts on all soil properties. Treatment x season also has a significant impact on the overland flow properties. As for the TP, lower values in the Spring were recorded on the Tilled and Straw treatment, compared to the Grass treatment, while in Summer, significantly higher values were recorded on the Straw treatment. As for TP between seasons, on the Tilled and Grass treatment, higher values were in Spring, while on the Straw treatment, those values were lower (Table 5). In the Spring, RT was significantly higher on the Straw treatment compared to the Tilled and Grass one, while in the Summer, those values were significantly lower on the Tilled and Straw treatment. When comparing seasons, Spring were significantly higher values of RT compared to Summer (Table 5). Table 5 shows that Runoff was significantly higher on the Grass treatment than Tilled and Straw one, while in Summer, those values were significantly higher on the Tilled treatments. As for the seasons, lower values on every treatment were recorded in the Spring. Sediment concentration was significantly lower on the Straw and Grass treatments compared to the Tilled one in both seasons. However, in the Spring, the Tilled treatment had higher values than in Summer, while the Straw and Grass treatment had higher values in the Summer period. In the Spring, significantly higher on the Tilled treatment, compared to the SL was Straw and Grass one, while in Summer, those losses significantly increased compared to the Spring period, especially on the Straw treatment, which was significantly different from the Tilled and Grass treatment (Table 5).

3.2 Multivariate analysis

Four major factors were revealed with the PCA analysis, which explained 83.05 %. Factor 1 explained 39.83%, Factor 2, 23.57%, Factor 3, 11.01%, and Factor 4 explained 8.63% of all variances. The WHC, TR, and TP were highly associated, while those variables are negatively related to Runoff, SWC and BD. Mean weight diameter and WSA are highly associated but are negatively associated with SL and SC (Figure 3A). The differences are marked between treatments and are presented in Figures 3A and B.

4 DISCUSSION

Results showed in this study indicated that treatments with cover (Straw and Grass) impacted soil physical properties and overland flow. As presented in the results, there were no significant differences in SLOPE between treatments and seasons, which ensured the uniformity of this research. Bulk density in both seasons was lower on the Tilled treatment due to periodic tillage operations, which loosened the topsoil layer (Lampurlanés and Cantero-Martínez, 2003). Tillage break formatted

Table 4. Two-way ANOVA results for overland flow.

Variable	Factors	F	p
TP	Land use	71.82	***
	Season	125.11	***
	Land use x Season	135.91	***
TR	Land use	53.57	***
	Season	117.06	***
	Land use x Season	74.26	***
Runoff	Land use	15.05	***
	Season	44.66	***
	Land use x Season	67.10	***
SC	Land use	28.89	***
	Season	5.12	*
	Land use x Season	3.21	*
SL	Land use	6.98	**
	Season	6.47	*
	Land use x Season	7.21	**

Significant differences were observed at $p < 0.05$*, $p < 0.01$** and $p < 0.001$***. No significant (ns) differences at a $p < 0.05$. Time to ponding (PT); time to runoff (TR); sediment concentration (SC); sediment loss (SL).

Table 5. *Post-hoc* results for overland flow.

Season	Treatment	TP (s)	TR (s)	Runoff (m^3 ha^{-1})	SC (g kg^{-1})	SL (kg ha^{-1})
Spring	Tilled	522.00 Ba	1140.00 Ba	16.18 Bb	27.95 Aa	444.35 Ab
	Straw	180.00 Cb	1522.00 ABa	98.43 Aa	8.33 Ba	44.81 Cb
	Grass	1050.00 Aa	1564.00 Aa	4.61 Cb	7.00 Ba	93.78 Bb
Summer	Tilled	216.00 Bb	372.00 Cb	74.48 ABa	18.02 Aa	1271.93 Aa
	Straw	420.00 Aa	456.00 Bb	52.23 Bb	1.92 Ba	370.33 Ba
	Grass	258.00 Bb	522.00 Ab	91.51 Aa	9.42 Ba	818.14 Ba

Different letters represent significant differences at $p < 0.05$. Different capital letters show statistical differences between treatments. Different small letters show statistical differences between seasons. Time to ponding (PT); time to runoff (TR); sediment concentration (SC); sediment loss (SL).

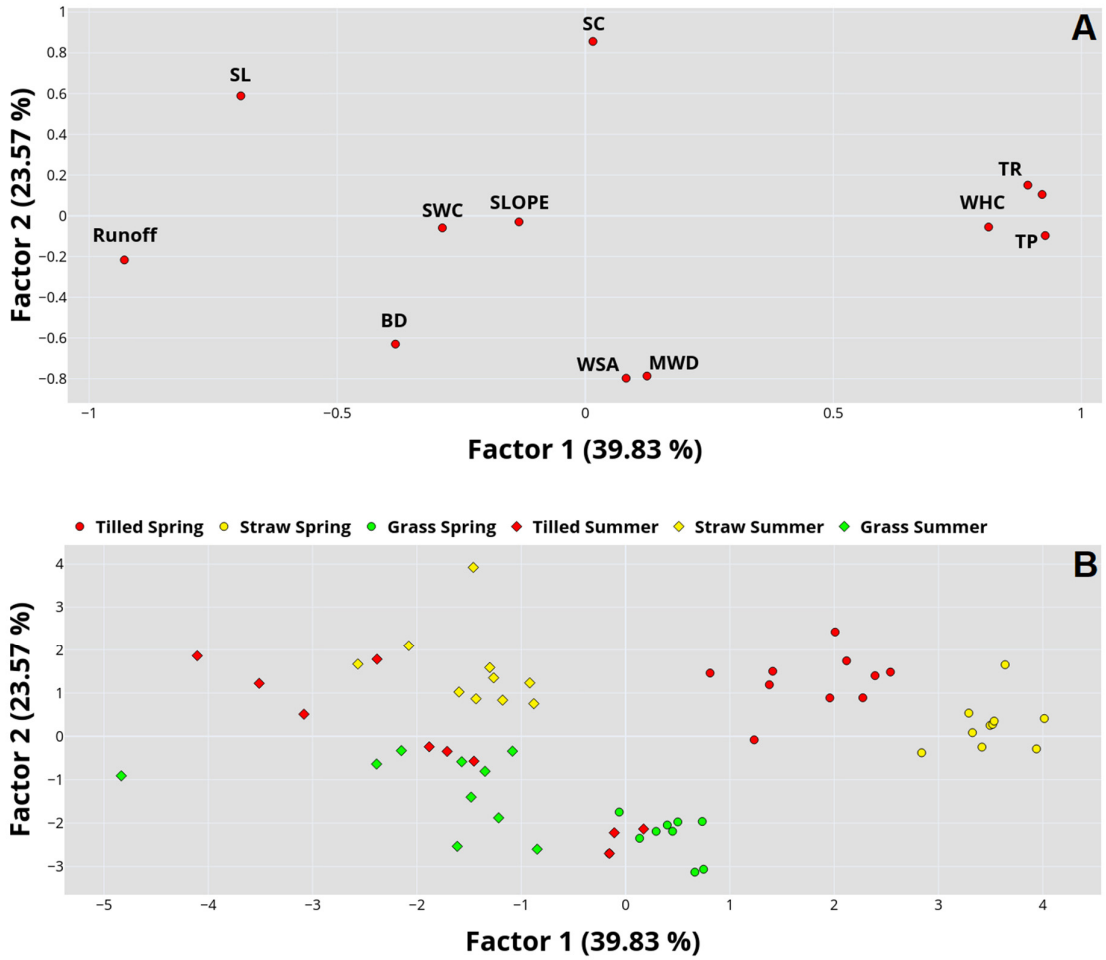

Fig. 3. Relation between Factors 1 and 2 A) variables, B) cases. Bulk density (BD); soil water content (SWC); water holding capacity (WHC); mean weight diameter (MWD); water stable aggregates (WSA); time to ponding (TP); time to runoff (TR); sediment concentration (SC); sediment loss (SL).

aggregates and ruined air-to-water ratio in soil (Mielke and Wilhelm, 1998). The BD on the Grass treatment in Summer was higher than in Spring. This can be attributed to more frequent tractor trafficking (Håkansson and Lipiec, 2000) between the two investigated seasons because of grass mowing and frequent pesticide application. Also, BD was high on Straw treatment every season compared to Tilled treatment. This can be explained by the fact that the tillage was performed a few weeks before the experiment started, and since then, the straw was applied, the soil compacted, and the tractor trafficking continued. Also, there was not enough time for straw to decompose and improve soil properties (Wang et al., 2011). Soil water content in Spring was higher on the Straw treatment due to straw cover, which has soil conservation ability (Ji and Unger, 2001). While on the Tilled treatment due to tillage operations, SWC was lower because of the moisture exhibited (Alvarez and Steinbach, 2009). On the Grass treatment, lower SWC can be explained by evapotranspiration of growing plants (Rahmati et al., 2020). In the Summer, SWC got lower on the Tilled and Straw treatment due to higher temperatures in that period which caused evaporation (Hupet and Vanclooster, 2005). However, on the Grass treatment, there was an increase because of the grass cover, which preserved water in this period and had better holding capacity (Ferrero et al., 2002). Also, grass cover is well known for having a better air-to-water ratio and higher organic matter, which is a binding agent of the soil structure (Annabi et al., 2007). While in Summer, there was a decrease in WHC on the Tilled and Grass treatment, there was an increase in the Straw treatment due to straw mixing with the soil (Gholami et al., 2013), thus ensuring better water capacity. Mean weight diameter was higher in both seasons of the Grass treatment because grass cover improves organic matter in the soil, which is in a role in forming soil aggregates (Belmonte et al., 2018; Chaplot and Cooper, 2015). At the same time, tillage on the Tilled treatment reduced soil structure, while the straw has incorporated into the soil, but not enough to mineralise and thus not able for topsoil layer to form larger aggregates (Jha et al., 2012). In Table 3. differences were noted for WSA on every treatment. In Spring, those values were higher on the Grass treatment, which can be explained by the fact mentioned earlier: higher organic matter concentrations increase aggregate stability. This phenomenon can also be seen in the Summer, when there is an increase of WSA on the Grass and on the Straw treatment.

In the overland flow observed in Table 5, the results revealed that treatment and season had a strong impact on the hydrological response. Thus this explains why TP and TR were delayed on the Straw and Grass treatments. Groundcovers are well known to intercept raindrops and decrease the raindrop energy impact on the

soil surface, thus slowing down the generation of ponds and runoff (Keesstra et al., 2019; Yang et al., 2021). Runoff was significantly higher on the Grass treatment than on the Tilled and Straw treatment in the Spring due to higher BD, which ensured faster water rising in the soil, thus making it more susceptible to runoff (Telak et al., 2021). In the Summer, the Tilled and Grass treatments recorded increased runoff, so the Straw treatment had significantly lower values than the Tilled and Grass treatment. Those changes are natural due to crust formation on the Tilled treatment (Abu-Awwad and Shatanawi, 1997) and high BD on both treatments. The sediment concentration in Spring on the Tilled treatment was significantly higher than on the Grass and Straw treatment. Grass and straw cover have intercepted raindrops and mitigated raindrop energy, destroying the soil surface (Qi et al., 2018). In the Summer, significantly higher SC was also noticed on the Tilled treatment due to raindrop impact, thus making finer particles more prone to erosion. Finally, SL in the Spring was significantly higher on the Tilled treatment due to smaller soil particles in that treatment, making them easily transferable (Nebeokike et al., 2020). While in Summer, there was an increase of SL in all the treatments, especially at the Tilled treatment. The grass and straw cover reduced SL by covering the soil surface all the time.

The PCA results show that different land use impacted soil properties and overland flow between seasons. Factor 1 negatively correlates SWC and WHC, while SWC had a highly positive correlation with Runoff, as higher SWC will lead to faster soil saturation and increased runoff (Warrick, 2003). The TP and TR were highly positively correlated but negatively correlated with Runoff because vegetation cover on the mulched treatments will intercept raindrops and, that way, postpone soil particle transfer (Gholami et al., 2013). Factor 2 showed that BD was positively correlated with MWD because higher soil compaction leads to a decrease of pores in soil and thus ruining soil structure (Chaudhari et al., 2013). Also, WSA was negatively correlated with SC since water-stable aggregates are bonded, which can detach when the erosion event occurs. Water-stable aggregates and SL were also negatively correlated due to higher organic matter in the soil, which positively affected binding soil aggregates, thus making aggregates more stable to erosion (Barthes and Rosse, 2002; Vermang et al., 2009). Usual vineyard management in Croatia is relatively uniform. In the drier Mediterranean part, it contains frequent tillage and herbicide use, thus making the soil surface vulnerable and susceptible to soil erosion. In Continental Croatia the use of grass cover is more frequent, but usually periodically. One year, one row is tilled due to easier fertiliser input, and every second row is in grass cover (Bogunovic et al., 2017). Current results of this work support the need for wider spread of the conservation practices in studied area. Current practices of grass cover in every second inter-row in the vineyard could be maintained if the vine producers adopt mulching as a practice after tillage interventions. Bare soil in the vineyard in studied area should be prohibited. Otherwise, the soil loss will be non-sustainable which will degrade the land and consequently lead to abandoning (van Leeuwen et al., 2019).

5 CONCLUSION

Results of this study in vineyards revealed that Spring and Summer and soil management treatments significantly impacted soil properties and overland flow. Mulch application increased BD and SWC in the Spring period. Also, seasons and treatment have led to different hydrological responses and erosion rates. Straw mulched treatment postponed TP and TR, as well as Grass treatment. Tilled treatment had increased SC and SL in the Spring, while those values were higher on the Straw treatment in the Summer period. The results show that Grass treatment is a sustainable agricultural practice in vineyards on sloped terrain. In contrast, the straw application has shown as a good substitute for grass-covered treatments in terms of soil erosion and soil properties. Mulch application management needs consistent application due to straw decomposition into the soil, a possible limitation factor for grape producers. This should be investigated in future works.

Acknowledgements. This research was funded by CROATIAN SCIENCE FOUNDATION through the project "Soil erosion and degradation in Croatia" (UIP-2017-05-7834) (SEDCRO). The authors are grateful to Dr. Leon Josip Telak for help during laboratory and field work.

REFERENCES

Abu-Awwad, A.M., Shatanawi, M.R., 1997. Water harvesting and infiltration in arid areas affected by surface crust: examples from Jordan. J. Arid Environ., 37, 3, 443–452.

Abu-Zreig, M.M., Tamimi, A., Alazba, A.A., 2011. Soil erosion control and moisture conservation of arid lands with stone cover. Arid Land Res. Manag., 25, 3, 294–307.

Alvarez, R., Steinbach, H.S., 2009. A review of the effects of tillage systems on some soil physical properties, water content, nitrate availability and crops yield in the Argentine Pampas. Soil Till. Res., 104, 1, 1–15.

Annabi, M., Houot, S., Francou, C., Poitrenaud, M., Bissonnais, Y.L., 2007. Soil aggregate stability improvement with urban composts of different maturities. Soil Sci. Soc. Am. J., 71, 2, 413–423.

Baiamonte, G., Minacapilli, M., Novara, A., Gristina, L., 2019. Time scale effects and interactions of rainfall erosivity and cover management factors on vineyard soil loss erosion in the semi-arid area of southern Sicily. Water, 11, 5, 978.

Barthes, B., Roose, E., 2002. Aggregate stability as an indicator of soil susceptibility to runoff and erosion; validation at several levels. Catena, 47, 2, 133–149.

Belmonte, S.A., Luisella, C.E.L.I., Stahel, R.J., Bonifacio, E., Novello, V., Zanini, E., Steenwerth, K.L., 2018. Effect of long-term soil management on the mutual interaction among soil organic matter, microbial activity and aggregate stability in a vineyard. Pedosphere, 28, 2, 288–298.

Biddoccu, M., Ferraris, S., Pitacco, A., Cavallo, E., 2017. Temporal variability of soil management effects on soil hydrological properties, runoff and erosion at the field scale in a hillslope vineyard, North-West Italy. Soil Till. Res., 165, 46–58.

Birkás, M., Szemők, A., Antos, G., Neményi, M., 2008. Environmentally-sound adaptable tillage. Akadémiai Kiadó, Godollo, Hungary.

Bogunovic, I., Bilandzija, D., Andabaka, Z., Stupic, D., Comino, J.R., Cacic, M., Brezinscak, L., Maletic, E., Pereira, P., 2017. Soil compaction under different management practices in a Croatian vineyard. Arab. J. Geosci., 10, 15, 1–9.

Bogunovic, I., Telak, L.J., Pereira, P., 2020. Experimental comparison of runoff generation and initial soil erosion between vineyards and croplands of eastern Croatia: A case study. Air, Soil Water Res., 13, 1178622120928323.

Chaplot, V., Cooper, M., 2015. Soil aggregate stability to predict organic carbon outputs from soils. Geoderma, 243, 205–213.

Chaudhari, P.R., Ahire, D.V., Ahire, V.D., Chkravarty, M., Maity, S., 2013. Soil bulk density as related to soil texture, organic matter content and available total nutrients of Coimbatore soil. IJSR, 3, 2, 1–8.

Curaqueo, G., Acevedo, E., Cornejo, P., Seguel, A., Rubio, R., Borie, F., 2010. Tillage effect on soil organic matter, mycorrhizal hyphae and aggregates in a mediterranean agroecosystem. Revista de la ciencia del suelo y nutrición vegetal, 10, 1, 12–21.

Dıaz-Zorita, M., Perfect, E., Grove, J.H., 2002. Disruptive methods for assessing soil structure. Soil Till. Res., 64, 1–2, 3–22.

Duan, J., Liu, Y.J., Wang, L.Y., Yang, J., Tang, C.J., Zheng, H.J., 2022. Importance of grass stolons in mitigating runoff and sediment yield under simulated rainstorms. Catena, 213, 106132.

Ebabu, K., Tsunekawa, A., Haregeweyn, N., Tsubo, M., Adgo, E., Fenta, A.A., Meshesha, D.T., Berihun, M.L., Sultan, D., Vanmaercke, M., Panagos, P., 2022. Global analysis of cover management and support practice factors that control soil erosion and conservation. Int. Soil Water Conserv. Res., 10, 2, 161–176.

Fernández, C., Vega, J.A., 2014. Efficacy of bark strands and straw mulching after wildfire in NW Spain: Effects on erosion control and vegetation recovery. Ecol., 63, 50–57.

Ferrero, A., Lisa, L., Parena, S., Sudiro, L., 2002. Runoff and soil erosion from tilled and controlled grass-covered vineyards in a hillside catchment. Technical Documents in Hydrology, 67, 105–111.

FOASTAT, 2021. FAO Statistics. Food and Agriculture Organization of United Nations.

Gao, Z., Xu, Q., Si, Q., Zhang, S., Fu, Z., Chen, H., 2022. Effects of different straw mulch rates on the runoff and sediment yield of young citrus orchards with lime soil and red soil under simulated rainfall conditions in southwest China. Water, 14, 7, 1119.

García-Ruiz, J.M., 2010. The effects of land uses on soil erosion in Spain: A review. Catena, 81, 1, 1–11.

Gholami, L., Sadeghi, S.H., Homaee, M., 2013. Straw mulching effect on splash erosion, runoff, and sediment yield from eroded plots. Soil Sci. Soc. Am. J., 77, 1, 268–278.

Håkansson, I., Lipiec, J., 2000. A review of the usefulness of relative bulk density values in studies of soil structure and compaction. Soil Till. Res., 53, 2, 71–85.

Hupet, F., Vanclooster, M., 2005. Micro-variability of hydrological processes at the maise row scale: implications for soil water content measurements and evapotranspiration estimates. J. Hydrol., 303, 1–4, 247–270.

IUSS WRB, 2015. World Reference Base for Soil Resources 2014, Update 2015: International Soil Classification System for Naming Soils and Creating Legends for Soil Maps. World Soil Resources Reports No. 106. FAO, Rome, Italy, pp. 150–200.

Jha, P., Garg, N., Lakaria, B.L., Biswas, A.K., Rao, A.S., 2012. Soil and residue carbon mineralisation as affected by soil aggregate size. Soil Till. Res., 121, 57–62.

Ji, S., Unger, P.W., 2001. Soil water accumulation under different precipitation, potential evaporation, and straw mulch conditions. Soil Sci. Soc. Am. J., 65, 2, 442–448.

Keesstra, S.D., Rodrigo-Comino, J., Novara, A., Giménez-Morera, A., Pulido, M., Di Prima, S., Cerdà, A., 2019. Straw mulch as a sustainable solution to decrease runoff and erosion in glyphosate-treated clementine plantations in Eastern Spain. An assessment using rainfall simulation experiments. Catena, 174, 95–103.

Kemper, W.D., Rosenau, R.C., 1986. Aggregate stability and size distribution. In: Klute, A. (Ed.): Methods of Soil Analysis. American Society of Agronomy, Inc., Soil Sci. Soc. Am., Inc., Madison, Wisconsin, pp. 425–442.

Kertész, A., Toth, A., Szalai, Z., Jakab, G., Kozma, K., Booth, C.A., Fullen, M.A.M., Davies, K., 2007. Geotextile as a tool against soil erosion in vineyards and orchards. WIT Transactions on Ecology and the Environment, Vol. 102, 9 p.

Lampurlanés, J., Cantero-Martínez, C., 2003. Soil bulk density and penetration resistance under different tillage and crop management systems and their relationship with barley root growth. Agronomy, 95, 3, 526–536.

Le Bissonnais, Y.L., 1996. Aggregate stability and assessment of soil crustability and erodibility: I. Theory and methodology. Eur. J. Soil Sci., 47, 4, 425–437.

Li, Y., Chen, H., Feng, H., Wu, W., Zou, Y., Chau, H.W., Siddique, K.H., 2020. Influence of straw incorporation on soil water utilisation and summer maise productivity: A five-year field study on the Loess Plateau of China. Agric. Water Manag., 233, 106106.

Mielke, L.N., Wilhelm, W.W., 1998. Comparisons of soil physical characteristics in long-term tillage winter wheat–fallow tillage experiments. Soil Till. Res., 49, 1–2, 29–35.

Mishra, P.K., Rai, A., Abdelrahman, K., Rai, S.C., Tiwari, A., 2022. Land degradation, overland flow, soil erosion, and nutrient loss in the eastern Himalayas, India. Land, 11, 2, 179.

Morvan, X., Naisse, C., Malam Issa, O., Desprats, J.F., Combaud, A., Cerdan, O., 2014. Effect of groundcover type on surface runoff and subsequent soil erosion in Champagne vineyards in France. Soil Use Manag, 30, 3, 372–381.

Nebeokike, U.C., Igwe, O., Egbueri, J.C., Ifediegwu, S.I., 2020. Erodibility characteristics and slope stability analysis of geological units prone to erosion in Udi area, southeast Nigeria. MESE, 6, 2, 1061–1074.

Novara, A., Gristina, L., Saladino, S.S., Santoro, A., Cerdà, A., 2011. Soil erosion assessment on tillage and alternative soil managements in a Sicilian vineyard. Soil Till. Res, 117, 140–147.

Panagos, P., Borrelli, P., Meusburger, K., Alewell, C., Lugato, E., Montanarella, L., 2015. Estimating the soil erosion cover-management factor at the European scale. Land Use Policy, 48, 38–50.

Parras-Alcántara, L., Lozano-García, B., Keesstra, S., Cerdà, A., Brevik, E. C., 2016. Long-term effects of soil management on ecosystem services and soil loss estimation in olive grove top soils. Sci. Total Environ., 571, 498–506.

Prosdocimi, M., Jordán, A., Tarolli, P., Keesstra, S., Novara, A., Cerdà, A., 2016. The immediate effectiveness of barley straw mulch in reducing soil erodibility and surface runoff generation in Mediterranean vineyards. Sci. Total Environ., 547, 323–330.

Qi, F., Zhang, R., Liu, X., Niu, Y., Zhang, H., Li, H., Li, J., Wang, B., Zhang, G., 2018. Soil particle size distribution characteristics of different land-use types in the Funiu mountainous region. Soil Till. Res., 184, 45–51.

Rahmati, M., Groh, J., Graf, A., Pütz, T., Vanderborght, J., Vereecken, H., 2020. On the impact of increasing drought on the relationship between soil water content and evapotranspiration of a grassland. Vadose Zone Journal, 19, 1, e20029.

Rodrigo-Comino, J., Keesstra, S., Cerdà, A., 2018. Soil erosion as an environmental concern in vineyards: the case study of Celler del Roure, Eastern Spain, by means of rainfall simulation experiments. Beverages, 4, 2, 31.

Rodríguez-Lizana, A., Espejo-Pérez, A.J., González-Fernández, P., Ordóñez-Fernández, R., 2008. Pruning residues as an alternative to traditional tillage to reduce erosion and pollutant dispersion in olive groves. Water Air Soil Pollut., 193, 1, 165–173.

Smets, T., Poesen, J., Knapen, A., 2008. Spatial scale effects on

the effectiveness of organic mulches in reducing soil erosion by water. Earth Sci. Rev., 89, 1–2, 1–12.

Telak, L.J., Pereira, P., Bogunovic, I., 2021. Management and seasonal impacts on vineyard soil properties and the hydrological response in continental Croatia. Catena, 202, 105267.

Telak, L.J., Pereira, P., Ferreira, C.S., Filipovic, V., Filipovic, L., Bogunovic, I., 2020. Short-term impact of tillage on soil and the hydrological response within a fig (*Ficus Carica*) orchard in Croatia. Water, 12, 11, 3295.

van Leeuwen, C.C., Cammeraat, E.L., de Vente, J., Boix-Fayos, C., 2019. The evolution of soil conservation policies targeting land abandonment and soil erosion in Spain: A review. Land Use Policy, 83, 174–186.

Vermang, J., Demeyer, V., Cornelis, W.M., Gabriels, D., 2009. Aggregate stability and erosion response to antecedent water content of a loess soil. Soil Sci. Soc. Am. J., 73, 3, 718–726.

Wang, Z., Wang, Z., Feng, H., 2011. Effects of pulverised and ammoniated straw on soil bulk density and soil water-holding characteristics. Transactions of the Chinese Society of Agricultural Engineering, 27, 11, 211–215.

Warrick, A.W., 2003. Soil Water Dynamics. Oxford University Press.

Yang, J., Liu, H., Lei, T., Rahma, A.E., Liu, C., Zhang, J., 2021. Effect of straw-incorporation into farming soil layer on surface runoff under simulated rainfall. Catena, 199, 105082.

Zhang, M., Zhao, G., Li, Y., Wang, Q., Dang, P., Qin, X. Zou, Y., Chen, Y., Siddique, K. H., 2021. Straw incorporation with ridge–furrow plastic film mulch alters soil fungal community and increases maise yield in a semiarid region of China. Appl. Soil Ecol., 167, 104038.

Received 4 November 2022
Accepted 2 December 2022

J. Hydrol. Hydromech., 71, 2023, 1, 100–110
https://doi.org/10.2478/johh-2022-0030

sciendo Journal of Hydrology and Hydromechanics Institute of Hydrology SAS

Proposal of a new method for drought analysis

Ognjen Bonacci[1], Duje Bonacci[2], Tanja Roje-Bonacci[1], Adrijana Vrsalović[1*]

[1] University of Split, Faculty of Civil Engineering, Architecture and Geodesy, 21000 Split, Matice hrvatske 15, Croatia.
E-mails: obonacci@gradst.hr (O.B.); bonacci@gradst.hr (T.R.-B.); avrsalovic@gradst.hr (A.V.)
[2] University of Zagreb, Faculty of Croatian Studies, 10000 Zagreb, Borongajska cesta 83d, Croatia. E-mail: dbonacci@hrstud.hr (D.B.)
[*] Corresponding author. E-mail: avrsalovic@gradst.hr

Abstract: Below-average precipitation and above-average air temperature are important factors in the occurrence and intensity of drought. In the context of global climate change, air temperature increase, as a key climatological parameter, has to be considered when calculating the drought index. We introduce a new method of drought analysis, relying on standardized values of precipitation and mean air temperatures for a certain period. The standardized value is calculated by subtracting the average value for each period from each measured value and dividing the obtained value by the standard deviation of the sample. Next, the New Drought Index (NDI) is calculated by subtracting the standardized temperature value from the standardized precipitation value. NDI values were determined for the monthly and annual precipitation time series and mean monthly and annual air temperatures measured at the stations Split-Marjan and Zagreb-Grič between 1948 and 2020. The NDI indicates that the risk of drought has intensified significantly in recent decades, which may be related to the effect of global warming.

Keywords: Drought; Air temperature; Precipitation; New Drought Index (NDI); Split-Marjan; Zagreb-Grič.

INTRODUCTION

Drought is a complex phenomenon (Van Loon, 2015; Wong et al., 2013; Yevjevich et al., 1983) that can potentially have catastrophic consequences at multiple levels, e.g., agriculture, water resources. The literature dealing with drought effects is considerable (Barker et al., 2016; Bonacci, 1993; Ferina et al., 2021; Hisdal, 2002; Li et al., 2021; Mishra and Singh, 2010; Morid et al., 2006; Palmer, 1965; Pandžić et al., 2020; Tadić et al., 2015; Van Lanen et al., 2013). In the context of climate change, the duration and intensity of drought are expected to be strongly influenced by increase in temperature (Dai, 2011). Using the Standard Weighted Average Precipitation Index, Zhao et al. (2020) pointed to the possibility that during the 21st century climate change will frequently lead to more sudden changes in droughts and floods.

The generally accepted definition of a drought relates to a deficit of water relative to the normal conditions prevailing in an area (Lloyd-Hughes, 2014). Panu and Sharma (2002) claim that droughts are perceived as extreme events in climate systems, whereas in reality, they need to be considered common occurrences. AghaKouchak et al. (2021) consider that the traditionally accepted definition of drought as a deficit of water-related variables and/or activities (e.g., precipitation, soil moisture, surface and groundwater reserves, irrigation water, etc.) caused by natural variability is incomplete because it does not consider local factors. In this paper, we consider that droughts must be defined and understood differently within the coupled human-water system. To meet this goal, it is necessary to consider the complex interrelated dynamics of natural phenomena and changes induced by human activities. A so-called anthropogenic drought should be understood as a phenomenon that combines several dimensions at different time scales. Drought is governed by a combination of natural water variability, climate change, human activities and decisions, as well as micro-climatic conditions that occur due to changes in land exploitation and water management. Anthropogenic drought in a broader context should be defined as the occurrence of drought caused or intensified by human activities.

Several concepts and methods are at hand for studying, identifying and quantifying drought. Since these approaches (hydrological, meteorological, agronomic, socio-political, etc.) treat droughts differently, they are prone to deliver contrasting results. The latter can potentially jeopardize the design and implementation of effective and timely drought mitigation actions strongly influenced by temperature increase (Dai, 2011).

Due to the complexity of the drought phenomenon, it is necessary to use objective and transparent approaches to define it. Several indices, which differ in their definition and the data needed to calculate them, are used in the literature to describe drought. Despite numerous efforts, no universal drought index has been established to date. Another term, also used in the literature, is the aridity index which represents the relationship between the mean annual potential evapotranspiration and precipitation that controls the mean annual inflows of surface and groundwater in an area (Neto et al., 2020).

The need to quantify the characteristics of drought has resulted in the development of numerous drought indices that assess this phenomenon in various ways. The characteristics of drought commonly defined are (1) duration (T); (2) strength or cumulative deficit (S); (3) deficit intensity (S/T). In addition, it is essential to define the beginning of the drought, while the end time is usually easier to determine since it mainly occurs when abundant precipitation occurs in the monitored area. Lloyd-Hughes (2014) considers it essential to include evidence of water supply, demand, and management in the monitored area to quantify and more accurately describe drought. The same author states that there are more than a hundred specialised drought indices in the related literature, which indicates the complexity of this phenomenon, but also the difficulty in defining generally acceptable and reliable indicators. The fact is that many of the parameters used in calculating drought indices are highly correlated, but they must be applied with caution when defining the concept of “drought” in the broader sense. In de-

termining a hydrological drought, the fact of a non-linear response of terrestrial processes to climatic stimuli should be considered (Van Lanen et al., 2013; Van Loon, 2015).

Although numerous studies related to the quantification of drought have been conducted so far (and are being carried out intensively even today), many doubts and uncertainties continue to prevail. The Standardized Precipitation Index (SPI) is considered as the most reliable drought index by multiple authors (Pandžić et al. 2020; Tadić et al. 2015; WMO, 2012). Based on the probability of precipitation occurring over a given period, it is developed as a spatially independent indicator of drought, considering the importance of weather intervals in analyses of water availability and use (Dragičnić et al., 2017). The fact that it exclusively uses precipitation data somewhat limits its ability to characterize the properties of various types of drought. Barker et al. (2016), using the Standardized Streamflow Index and the Standardized Precipitation Index, examined the relationships between hydrological and meteorological drought in the UK.

The Palmer Drought Index was developed for monitoring changes in soil water balance (Palmer, 1965). In the US, it is used as a standard to study meteorological drought. It depends on many factors (Pandžić et al., 2006), and it is based on the hydrological balance of precipitation water movement in the soil-plant-atmosphere system. In addition to precipitation and air temperature, data on the amount of moisture in the soil, evapotranspiration, and the rate of moisture filling in two surface soil layers bordering the atmosphere (upper up to 20 cm, and lower up to 80 cm), are required to define it. This method requires data that are rarely measured, so less reliable estimations are used. This index should determine long-term droughts lasting several months.

Given that drought is mainly caused by rainfall deficiencies and high evapotranspiration rates, Fassouli et al. (2021) have proposed a Factual Drought Index (FDI) as a composite tool, based on precipitation and potential evapotranspiration (PET).

Here, we propose a New Drought Index (NDI), relying on precipitation and air temperature data. The NDI leverages the fact that in the context of drought analysis, temperatures have an inversely proportional effect from precipitation. Higher-than-average precipitation and lower-than-average temperatures have a more favourable effect on drought mitigation and vice versa (Ljubenkov and Bonacci, 2011).

MATERIALS AND METHODS

Climatological data used

We use annual and monthly precipitation data along with mean monthly and mean annual air temperatures observed at the main meteorological stations of the State Hydrometeorological Institute (DHMZ) Zagreb-Grič (hereinafter Zagreb) and Split-Marjan (hereinafter Split) during a period of 73 years, from 1948 to 2020 (Data generously provided by DHMZ).

The distance between the meteorological stations Zagreb and Split is 259 km (Figure 1). At the meteorological station Zagreb, the climate is moderately warm and humid with warm summers (Šegota and Filipčić, 2003). According to the Köppen and Geiger (1936) climate classification, it belongs to the Cfb class. The station is at an elevation of 157 meters above sea level (m a.s.l.), and the geographical coordinates are 45° 48' 52" N and 15° 58' 19" E. The meteorological station Split has a Mediterranean climate with hot summers (Šegota and Filipčić, 2003). According to the Köppen and Geiger (1936) climate classification, it belongs to the Csa class. The station is at an elevation of 122 m above sea level, and the geographical coordinates are

Fig. 1. Map of the study area.

43° 30' 30"N and 16° 25' 35" E. Both stations are located in fast-growing cities, but since they are placed on the tops of hills, they are not exposed to strong urbanization (this is especially true for the Split station), and the impact of the urban heat island effect remains limited.

Statistical methods used

We used linear and nonlinear regression and correlation methods for the analyses of time series. For determining the statistical significance of differences between variances and mean values of successive subsets of precipitation, mean temperatures, and New Drought Indices, we used the nonparametric F-test and t-test (McGhee, 1985).

The Rescaled Adjusted Partial Sums (RAPS) method served to determine the sub-period with a statistically significant difference in average values over complete time series (1948–2020) of precipitation and temperature (Bonacci and Roje-Bonacci, 2020; Garbrecht and Fernandez, 1994). The statistical significance of the differences was determined using the F-test and the t-test. The equation for calculating RAPS is:

$$RAPS_k = \sum_{t=1}^{k} \frac{Y_t - Y_m}{S_y} \quad (1)$$

where Y_t, represents precipitation or mean temperature in a given time interval, t, Y_m, the average value of the entire analysed series, S_Y, the standard deviation, n, the number of data in a series, $k \in (1, 2\ldots, n)$, the counter of sums for the k analysed time unit in a series of the total, n.

The statistical significance of the linear trends of the series of annual and monthly precipitation, mean temperatures, and NDI, was determined using the Mann-Kendall (M-K) test (Hamed and Ramachandra, 1998; Kendall, 1975; Mann, 1945). At present, this test is considered the most reliable procedure for assessing the statistical significance of trends in the analysed time series. One of its essential advantages is that it does not require the analysed data to be adjusted to any distribution curve, i.e., the M-K test is nonparametric. Therefore, it is also most widely used in the time series analysis of climatological parameters, especially temperature and precipitation (Allen et al. 2015; Hori et al., 2017; Wang and Stephanson, 2018). We used the pyMannKendall, a python package, in this paper

(Shourov and Mahmud, 2019). Our null hypothesis was that there is no monotonic trend in the analysed time series. An alternative hypothesis was that the trend exists. In this paper, the probability value, $p<0.05$, was used as a criterion for accepting the alternative hypothesis (existence of a statistically significant linear trend).

New Drought Index (NDI)

In this paper, we introduce the New Drought Index (NDI), using precipitation and air temperature data. Both climatological parameters used to define NDI values play a key role for determining all drought characteristics such as duration, severity, intensity, as well as the beginning and end of the drought period. Potential and/or real evapotranspiration are a crucial parameter in many drought characteristics determination methods. The different methods, approaches and equations at hand give very different and, for engineering practice very often, unreliable results. Bonacci (2004) considers that evapotranspiration is the most unreliably assessed variable in the determining of the water balance, as well as of drought. Therefore, we opted in our study for using air temperature instead of real or potential evapotranspiration.

In the case of precipitation, the intensity of the abovementioned drought features is influenced by its deficit (deficit in relation to the average values of the analysis period in the monitored area), in the case of temperature, it is influenced by temperatures higher than the average of the analysis period. Ultimately, the use of temperature data for calculating the drought index is becoming more and more relevant due to global climate change and the related temperature increase.

Prior to their use in one index, both climate parameters need to be transformed into dimensionless quantities by the standardization process. We propose to determine the NDI via the following equation:

$$NDI_i = [(P_i - P_{av})/S_P] - [(T_i - T_{av})/S_T] \quad (2)$$

where:
P_i, precipitation in the year or month, i,
P_{av}, the average value of the analysed series of precipitation in the analysis period,
S_P, the standard deviation of the analysed series of precipitation in the analysis period,
T_i, the mean temperature in a year or month,
T_{av}, the average value of the analysed series of mean temperatures in the analysis period, and
S_T, the standard deviation of the analysed series of temperatures in the analysis period.

Since this paper analyses the series from 1948 to 2020, a total of 73 years or 876 months, the values of i span different data sets. When analysing annual values, $i \in (1, 2...,73)$, and when analysing monthly values from January 1948 to December 2020, $i \in (1, 2..., 876)$.

RESULTS AND DISCUSSION

Analysis of annual series of precipitation and temperatures

In the first row of Table 1, the values of average annual precipitation, P_{pr}, temperature, T_{pr}, and standard deviations, S, for Split and Zagreb in the period from 1948 to 2020 are listed. In the considered period, the average precipitation measured in Zagreb was 884.2 mm/year, 73.4 mm/year higher than in Split, which was 810.8 mm/year. The average annual temperature measured in Split was 16.36 ºC, 4.25 ºC higher than that of 12.11 ºC measured in Zagreb.

Figure 2 shows the series of annual precipitation for Split and Zagreb in the period 1948 to 2020. The figure also shows the linear regression directions, and the equations of the linear regressions, the values of the linear correlation coefficients, r, and the probability values of the M-K test, p. We noted no statistically significant trend in the series of annual precipitation at either station. Although the complete time series of precipitation at both stations do not show any trend within 73 years, subperiods have emerged with statistically significant different average values.

Using the RAPS method, graphically represented in Figure 3A, we found four sub-periods in Split (1948 to 1958; 1959 to 1982; 1983 to 1994; 1995 to 2020) and three sub-periods in Zagreb (1948 to 1958; 1959 to 1966; 1967 to 2020). Graphic representations of four subsets of Split and three subsets of Zagreb are shown in Figure 3B.

Although the annual precipitation measured at these two stations does not differ significantly, as confirmed by the high value of the linear correlation coefficient, $r = 0.581$, their behaviour during the observed 73 years is significantly different. The differences between consecutive average values of the subperiod were tested with the F-test and t-test. The probabilities, p, for consecutive subsets obtained with the t-test, are shown in Table 2.

Table 1. Values of the average annual and monthly precipitations, P_{av}, air temperatures. T_{av}. and standard deviation, S, measured at the two meteorological stations during the analysed period (Jan. 1948–Dec. 2020).

Period	SPLIT				ZAGREB			
	P_{av} (mm)	S (mm)	T_{av} (ºC)	S (ºC)	P_{av} (mm)	S (mm)	T_{av} (ºC)	S (ºC)
year	810.8	155.2	16.36	0.678	884.2	144.3	12.11	0.993
January	77.9	45.1	7.95	1.56	52.8	33.5	1.45	2.57
February	66.2	40.7	8.40	1.91	47.0	28.4	3.49	3.04
March	63.3	46.1	10.80	1.67	51.7	28.8	7.76	2.33
April	62.6	33.0	14.39	1.39	62.7	31.0	12.47	1.68
May	57.3	36.7	19.11	1.51	81.2	37.8	16.08	1.62
June	50.1	35.7	23.24	1.49	96.9	38.0	20.23	1.57
July	27.6	28.0	26.05	1.35	88.3	44.8	22.14	1.54
August	38.6	40.3	25.78	1.64	85.2	50.4	21.58	1.81
September	71.6	53.1	21.55	1.46	90.8	47.9	17.33	1.52
October	78.8	50.7	17.13	1.21	77.7	51.4	12.23	1.43
November	113.4	55.0	12.7	1.39	85.5	48.4	7.03	2.11
December	103.3	66.6	9.32	1.26	64.5	36.1	2.65	2.03

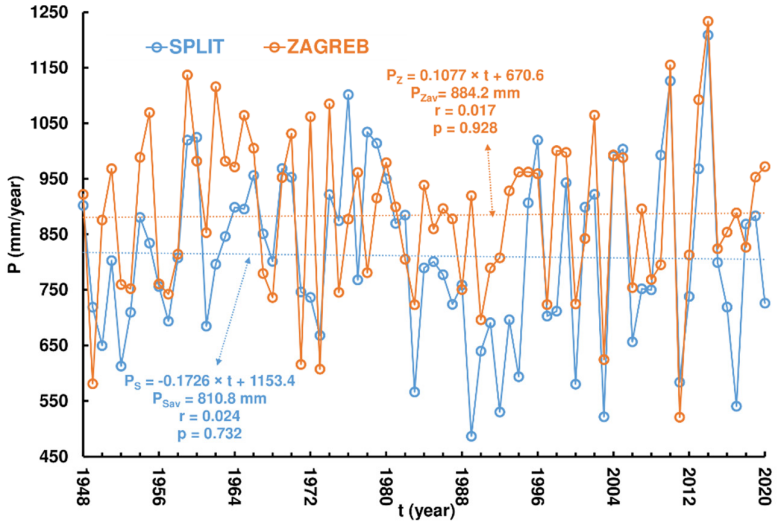

Fig. 2. Series of annual precipitation of Split and Zagreb in the period 1948 to 2020.

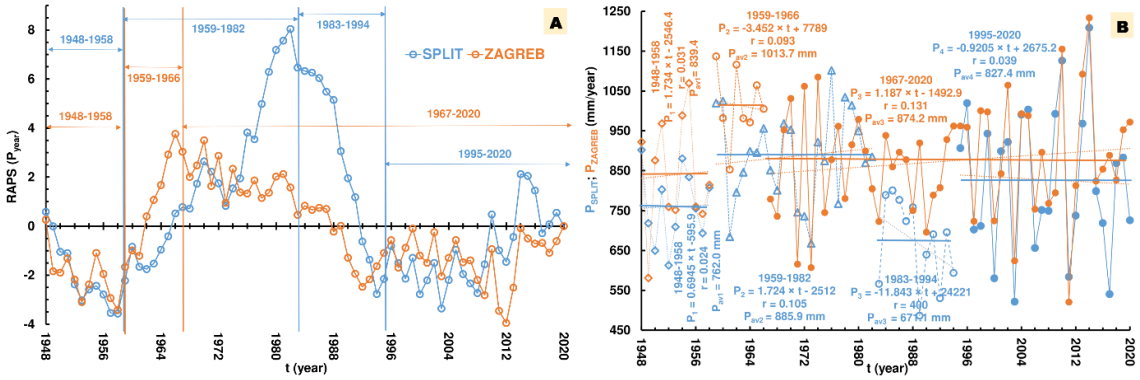

Fig. 3. Graphic representation of RAPS for the series of annual precipitation of Split and Zagreb in the period 1948 to 2020 (A) and representation of four subsets of precipitation in Split and three subsets of precipitation in Zagreb determined by RAPS method (B).

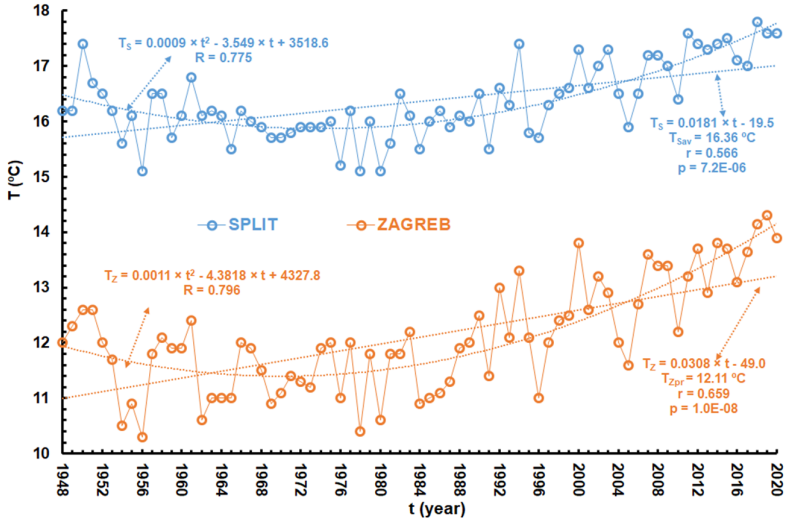

Fig. 4. Series of mean annual temperatures of Split and Zagreb in the period 1948 to 2020.

Figure 4 shows the mean annual temperatures series of Split and Zagreb in the period 1948 to 2020. The linear regression lines, the linear regression equations, the values of the linear correlation coefficients, *r*, and the probability values of M-K test, *p*, are provided in the figure, as well as the second-order curves and their equation and values of the nonlinear (parabolic) correlation index, *R*. At both stations, linear growth trends are statistically significant. However, it should be noted that the

Table 2. Matrix of the average annual precipitation, P_{av}, in the sub-periods defined by the RAPS method and the probability of the t-test, p, between consecutive sub-periods.

Station	Sub-period	P_{av} (mm)	p (t-test)
SPLIT	1948–1958	762.0	3.4E–03
	1959–1982	885.9	5.3E–06
	1983–1994	671.1	8.7E–03
	1995–2020	827.4	
ZAGREB	1948–1958	839.4	7.0E–03
	1959–1966	1013.7	9.7E–03
	1967–2020	874.2	

Table 3. Matrix of the average annual air temperature, T_{av}, in the sub-periods defined by the RAPS and the probability of the t-test, p, between consecutive sub-periods.

Station	Sub-period	T_{av} (°C)	p (t-test)
SPLIT	1948–1997	16.04	5.9E–12
	1998–2020	17.06	
ZAGREB	1948–1991	11.53	1.4E–12
	1992–2020	12.97	

second-order curves adjust much better to the analysed series and that the squares index values of the nonlinear correlation are significantly higher than those of the linear correlation coefficients. It is visually noticeable that the sharp rise in temperatures began in the last decades of the twentieth century. Similar time series temperature behaviour was observed throughout the Western Balkans (Bonacci, 2010; 2012), as well as in several other locations on the planet (Kim et al., 2015; Kothawale and Kumar, 2005; Levi, 2008; Li, 2010; Pandžić et al., 2020).

The graphical representation of RAPS mean annual temperatures (Figure 5A) shows that at the Split station the sudden rise in temperatures began in 1998, while at the Zagreb station it began six years earlier in 1992. Graphical representations of the two subsets of Split and Zagreb are shown in Figure 5B. It is important to notice that at both stations in recent years the M-K test indicates statistically significant (ongoing) growth trends. The probabilities, p, for consecutive subsets obtained with the t-test, are shown in Table 3. The value of the square linear correlation coefficient between the mean annual temperatures at the two observed stations is high and amounts to, $r = 0.906$.

Analysis of the monthly series of precipitation and temperatures

Table 1 lists the average monthly precipitation values, P_{pr}, temperature, T_{pr}, and standard deviations, S, for Split and Zagreb, between 1948 and 2020. To clearly highlight the differences in precipitation regimes at the two stations over twelve months, the average monthly values and their differences, $\Delta P_i = P_{i.SPLIT} - P_{iZAGREB}$, are shown in Figure 6A.

Although the annual precipitation amounts differ only by 10%, the differences in the precipitation regime during the year are significant and considerably affect the potential drought regimes in these two locations. In Split, heavy precipitation occurs in the cold period of the year. The maximum occurs in November and the minimum in July. In Zagreb, heavy precipitation occurs from May to November, with a maximum in June and a minimum in February. From November to March, the average monthly precipitation in Zagreb is lower than in Split, while from May to September, it is higher. In April and October, they are practically the same.

The regime of average values of mean monthly temperatures during the year at both stations is very similar. Figure 6B shows the average monthly values and their differences, $\Delta T_i = T_{i.SPLIT} - T_{iZAGREB}$. The maximum occurs in July and the minimum in January. The largest differences occur in December and amount to $\Delta T_{12} = 6.66$ °C, while the minimal occur in April when the difference is $\Delta T_4 = 1.93$ °C.

Table 4 lists the values of the linear correlation coefficients, r, and the results of the M-K test, p, for the series of monthly precipitation and mean monthly temperatures at both stations for the period 1948 to 2020. The results for series with a statistically insignificant downward trend ($p>0.05$) are marked in blue. The results for series with a statistically significant upward trend ($p<0.05$) are marked in bold red, while the results for series with a statistically insignificant increase trend ($p>0.05$) are marked in black characters. For the monthly precipitation series, we have found downward trends (marked in blue) and upward trends (marked in black) – nearly all of them being statistically insignificant. For mean monthly temperatures series, we identified a completely different pattern. All monthly series at both stations show an upward trend. In most months, especially during the summer period, these upward trends are also statistically significant.

Analysis of annual values of NDI

The bar chart shown in Figure 7A reveals the series of the New Drought Index, NDI_i, $i \in (1, 2...,73)$, defined on the basis of 73 annual values of precipitation and mean annual temperatures of Split and Zagreb for the period 1948 to 2020. The second-order curves, their equations, and indices of nonlinear correlation, R, are also given. The subperiods in which the F-test and t-test yield consecutive average NDI values with a

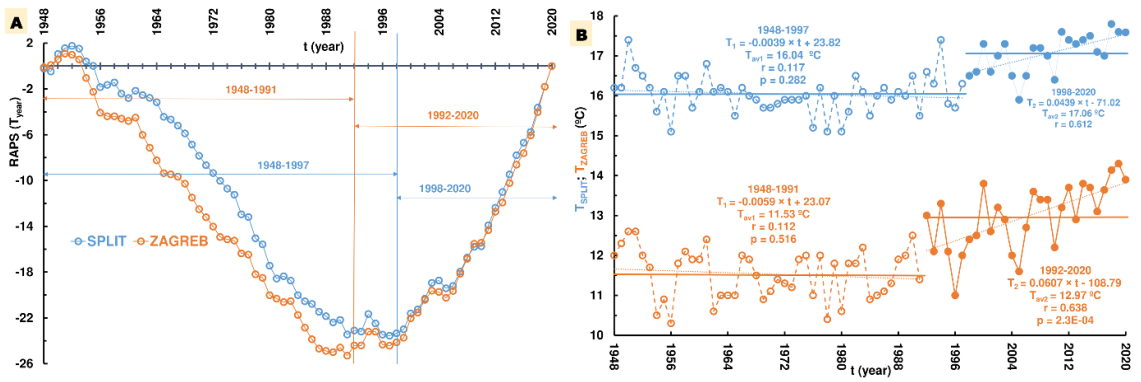

Fig. 5. Graphic representation of RAPS for the series of mean annual temperatures of Split and Zagreb in the period 1948 to 2020 (A) and representation of two subsets of mean annual temperatures of Split and Zagreb determined by RAPS method (B).

Table 4. Values of the coefficient of linear correlations, *r*, and the probability of the M-K test, *p*, for the monthly time series of precipitations and air temperatures, measured at the two analysed stations during the analysed period (1948-2020).

Month	Precipitation				Air temperature			
	SPLIT		ZAGREB		SPLIT		ZAGREB	
	r	*p*	*r*	*p*	*r*	*p*	*r*	*p*
January	0.085	0.363	0.161	0.105	0.130	0.282	**0.307**	**9.5E-03**
February	0.065	0.801	0.140	0.561	0.163	0.277	0.258	0.072
March	0.044	0.587	0.022	0.973	**0.284**	**0.029**	**0.360**	**4.9E-03**
April	0.027	0.753	0.085	0.440	**0.300**	**0.007**	**0.374**	**6.8E-04**
May	0.076	0.336	0.098	0.443	**0.256**	**0.017**	**0.342**	**1.7E-03**
June	0.071	0.179	0.107	0.353	**0.446**	**1.3E-04**	**0.498**	**1.7E-05**
July	0.042	0.238	0.091	0.644	**0.478**	**5.6E-05**	**0.534**	**9.2E-07**
August	0.083	0.127	0.003	0.932	**0.421**	**3.2E-04**	**0.490**	**1.9E-05**
September	0.072	0.376	0.259	0.114	0.062	0.658	0.118	0.548
October	0.050	0.775	0.201	0.096	0.191	0.117	**0.283**	**0.019**
November	0.017	0.797	0.033	0.992	**0.246**	**0.048**	**0.235**	**0.045**
December	0.095	0.338	0.011	0.890	0.066	0.472	**0.233**	**0.022**

blue numbers designate statistically insignificant decreasing trends
red bold numbers designate statistically significant increasing trends
red numbers designate statistically insignificant increasing trends

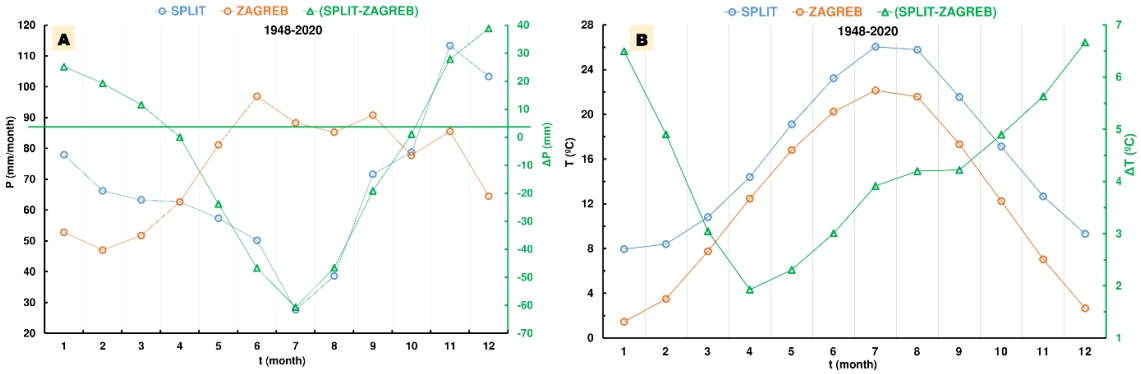

Fig. 6. (A) Average monthly values of precipitation at the observed stations during the period 1948 to 2020, and the differences between them, $\Delta P_i = P_{i.SPLIT} - P_{iZAGREB}$; (B) Average monthly values of temperatures at the observed stations during the period 1948 to 2020, and the differences between them, $\Delta T_i = T_{i.SPLIT} - T_{iZAGREB}$.

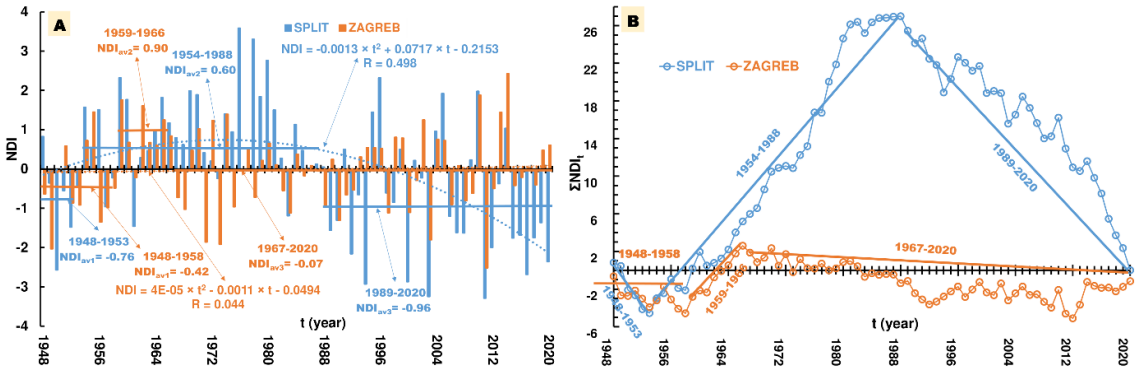

Fig. 7. Representation of the series (A) of the NDI_i, $i \in (1, 2 ..., 73)$, and the sums (B) of the New Drought Indices, ΣNDI_i, $i \in (1, 2 ..., 73)$, defined according to the annual values of precipitation and mean annual temperatures of Split and Zagreb in the period 1948 to 2020.

statistically significant difference is also shown. In Figure 7B, a graphical representation of the sum of ΣNDI_i, $i \in (1, 2..., 73)$ is used to determine the sub-period. Table 5 presents the matrix of average values of annual New Drought Indices, NDI_{av}, in the sub-periods depicted in Figure 7B and the results of the t-test, *p*, between successive sub-periods. When the year is considered a unit of analysis, it can be assumed that the occurrence of drought near Split began in 1988 and was intense. This finding is evident from the slope of the direction illustrated in Figure 7B for the sub-period 1989 to 2020. In the case of Zagreb, the NDI shows the occurrence of a milder drought in the period 1967 to 2020. Moreover, it seems that in the sub-period 2012 to 2020, the drought ceased, and a wet sub-period appeared. Note that this finding could not be corroborated by testing.

Table 5. Matrix of the average annual New Drought Index, NDI_{av}, in the sub-periods defined in Figure 7B and the probability of the t-test, p, between consecutive sub-periods.

Station	Sub-period	NDI_{av}	p (t-test)
SPLIT	1948–1953	–0.758	2.4E–03
	1954–1988	0.901	6.9E–05
	1989–2020	–0.844	
ZAGREB	1948–1958	–0.416	4.9E–03
	1959–1966	0.897	9.7E–03
	1967–2020	–0.070	

Table 6. Matrix of the average monthly New Drought Index, NDI_{av}, in the sub-periods defined in Figure 8 and the probability of the t-test, p, between consecutive sub-periods.

Station	Sub-period	NDI_{av}	p (t-test)
SPLIT	I 1948 – IX 1952	–0.424	9.3E–05
	X 1952 – VI 1987	0.385	1.1E–03
	VII 1987 – VII 1999	–0.073	8.5E–03
	VIII 1999 – XII 2020	–0.490	
ZAGREB	I 1948 – IX 1952	–0.366	5.0E–08
	X 1952 – VIII 1987	0.434	3.3E–04
	IX 1987 – II 1999	–0.076	6.4E–03
	III 1999 – XII 2020	–0.580	

Table 7. Values of the coefficient of linear correlations, r, and the probability of the M-K test, p, for every monthly time series of the New Drought Index, NDI_i, $i \in (1,2,3,\ldots, 73)$, measured at the two analysed stations during the analysis period (1948–2020).

Month		SPLIT	ZAGREB
January	r	0.159	**0.332**
	p	0.232	**0.003**
February	r	0.069	0.081
	p	0.764	0.577
March	r	0.153	0.217
	p	0.207	0.102
April	r	0.173	**0.288**
	p	0.136	**0.004**
May	r	0.103	**0.254**
	p	0.348	**0.044**
June	r	**0.310**	**0.374**
	p	**0.008**	**1.6E-04**
July	r	**0.320**	**0.374**
	p	**1.9E-04**	**0.002**
August	r	**0.285**	**0.288**
	p	**0.003**	**0.007**
September	r	0.006	0.084
	p	0.928	0.735
October	r	0.094	0.539
	p	0.449	0.943
November	r	0.192	0.195
	p	0.172	0.076
December	r	0.076	0.268
	p	0.438	0.079

blue numbers designate statistically insignificant decreasing trends
red bold numbers designate statistically significant increasing trends
red numbers designate statistically insignificant increasing trends

Analysis of NDI monthly values

To study the occurrence of drought and changes between dry and wet sub-periods and because of the seasonality of each climate regime, a month, as a relatively short unit of time is better suited for reliably characterizing the occurrence of drought. Figure 8 shows the sums of monthly NDI, ΣNDI_i, $i \in (1, 2..., 876)$, from January 1948 to December 2020. Similar behaviour of the time series sum is observed at both stations regardless of their difference in climatic characteristics. In both cases, we identified four sub-periods. Table 6 shows the average values of the annual New Drought Indices, NDI_{av}, in the sub-periods defined in Figure 7 and the t-test results, p, between successive sub-periods. The long-term decrease in the total value of NDIs at the Split station began in August 1999, while at the Zagreb station it started five months earlier, in March 1999. During the last period, there were occasional wet sub-periods, but the general trend indicates that drought prevails at both stations and will probably continue if air temperatures continue to rise, as expected due to global warming, and if precipitation remains the same.

Next, we investigated the behaviour of the NDI time series for each month during the period 1948 to 2020. Our analysis spans the monthly behaviour of the NDI during the monitored 73-year period.

Figure 9 shows the series of New Drought Indices, NDI_i, $i \in (1, 2..., 73)$, defined according to the monthly values of precipitation and average annual temperatures of Split and Zagreb in January for the period 1948 to 2020. In Figure 10, the sums of the New Drought Indices, ΣNDI_i, $i \in (1, 2..., 73)$, are shown for each month individually, in the period 1948 to 2020.

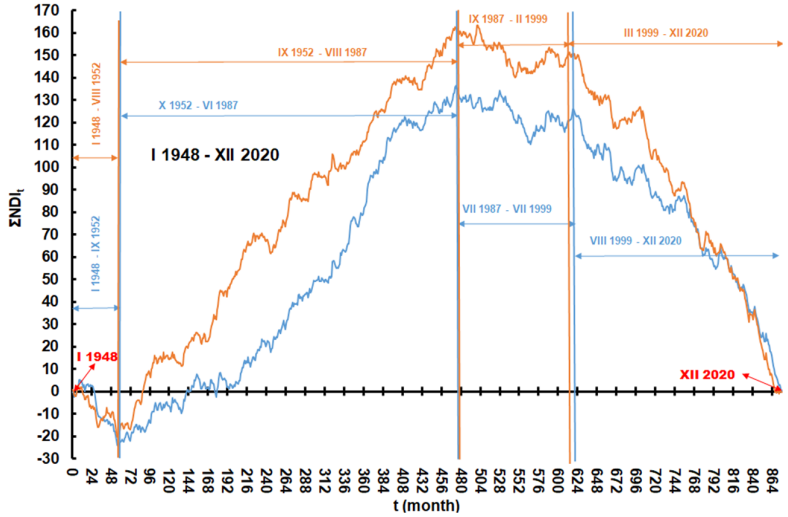

Fig. 8. Representation of the sums of the New Drought Indices, ΣNDI_i, $i \in (1, 2..., 876)$, according to the monthly values of precipitation and mean annual temperatures of Split and Zagreb in the period January 1948 to December 2020.

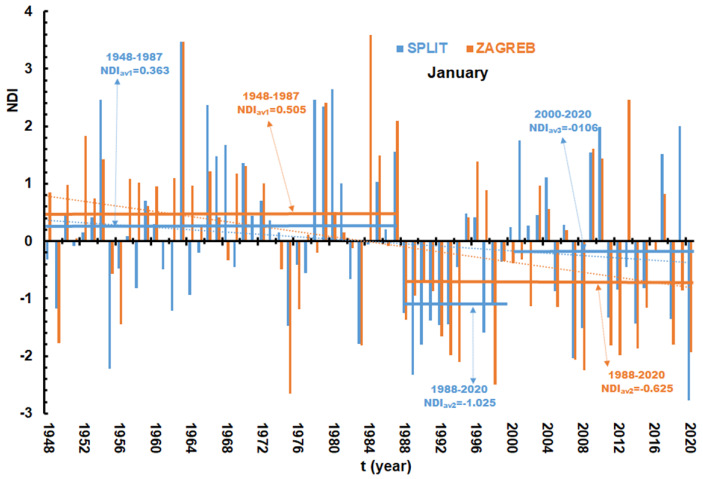

Fig. 9. Representation of the series of the New Drought Indices, NDI_i, $i \in (1, 2..., 73)$, defined according to the monthly values of precipitation and mean annual temperatures of Split and Zagreb in January in the period 1948 to 2020.

Table 8. Matrix of the average monthly New Drought Index, NDI_{av}, for Split and Zagreb station for each individual month, in the sub-periods defined in Figures 10, and the probability of the t-test, p, between consecutive sub-periods.

Station		**SPLIT**			**ZAGREB**	
Month	**Sub-period**	NIS_{av}	p **(t-test)**	**Sub-period**	NIS_{av}	p **(t-test)**
January	1948–1987 1988–1999 2000–2020	0.363 –1.025 –0.106	0.0012 0.049	1948–1987 1988–2020	0.505 –0.625	0.0004
February	1948–1980 1981–1988 1989–2002 2003–2020	–0.033 1.436 –0.937 0.151	0.008 0.0003 0.023	1948–1980 1981–1988 1989–2002 2003–2020	0.0038 1.317 –1.042 0.192	0.0148 0.0002 0.0268
March	1948–1988 1989–2020	0.385 –0.494	0.0164	1948–1988 1898–2020	0.405 –0.519	0.0111
April	1948–1955 1956–2005 2006–2020	–1.011 0.481 –1.065	0.007 0.0004	1948–1953 1954–2006 2007–2020	–1.035 0.523 –1.538	0.014 3.7E–06
May	1948–1999 2000–2009 2010–2020	0.227 –1.393 0.191	0.007 0.029	1948–1991 1992–2012 2013–2020	0.463 –1.047 0.205	0.009 0.043
June	1948–1995 1996–2020	0.483 –0.927	0.0004	1948–1995 1996–2020	0.560 –1.076	0.0004
July	1948–1952 1953–1986 1987–2020	–0.679 0.807 –0.707	0.027 4.5E–05	1948–1981 1982–2005 2006–2020	0.752 –0.170 –1.372	0.027 4.5E–05
August	1948–1962 1963–1984 1985–2006 2007–2020	–0.292 1.285 –0.128 –1.504	0.003 0.009 0.005	1948–1962 1963–1989 1990–2020	–0.185 0.921 –0.713	0.007 0.0002
September	1948–1966 1967–1978 1979–1995 1996–2003 2004–2020	–0.571 0.866 –0.675 1.639 –0.450	0.033 0.004 0.021 0.001	1948–2020	0.0003	
October	1948–1964 1965-1969 1970–1982 1983–1987 1988–1992 1993–2020	0.093 –1.256 0.899 –0.697 1.195 –0.338	0.013 0.035 0.014 0.002 0.034	1948–1964 1965–1969 1970–1994 1995-2020	0.003 -1.438 0.678 -0.378	0.015 0.006 0.019
November	1948–2010 2011–2020	0.180 –1.131	0.004	1948–1993 1994–2020	0.315 –0.535	0.0096
December	1948–1960 1961–2012 2013–2020	–0.491 0.249 –0.818	0.012 0.005	1948–1961 1962–1970 1971–1975 1976–1982 1983–1991 1992–2002 2003–2012 2013–2020	–0.066 1.491 –0.919 0.838 –0.770 0.539 –0.225 –1.314	0.007 0.001 0.009 0.003 0.0004 0.042 0.0005

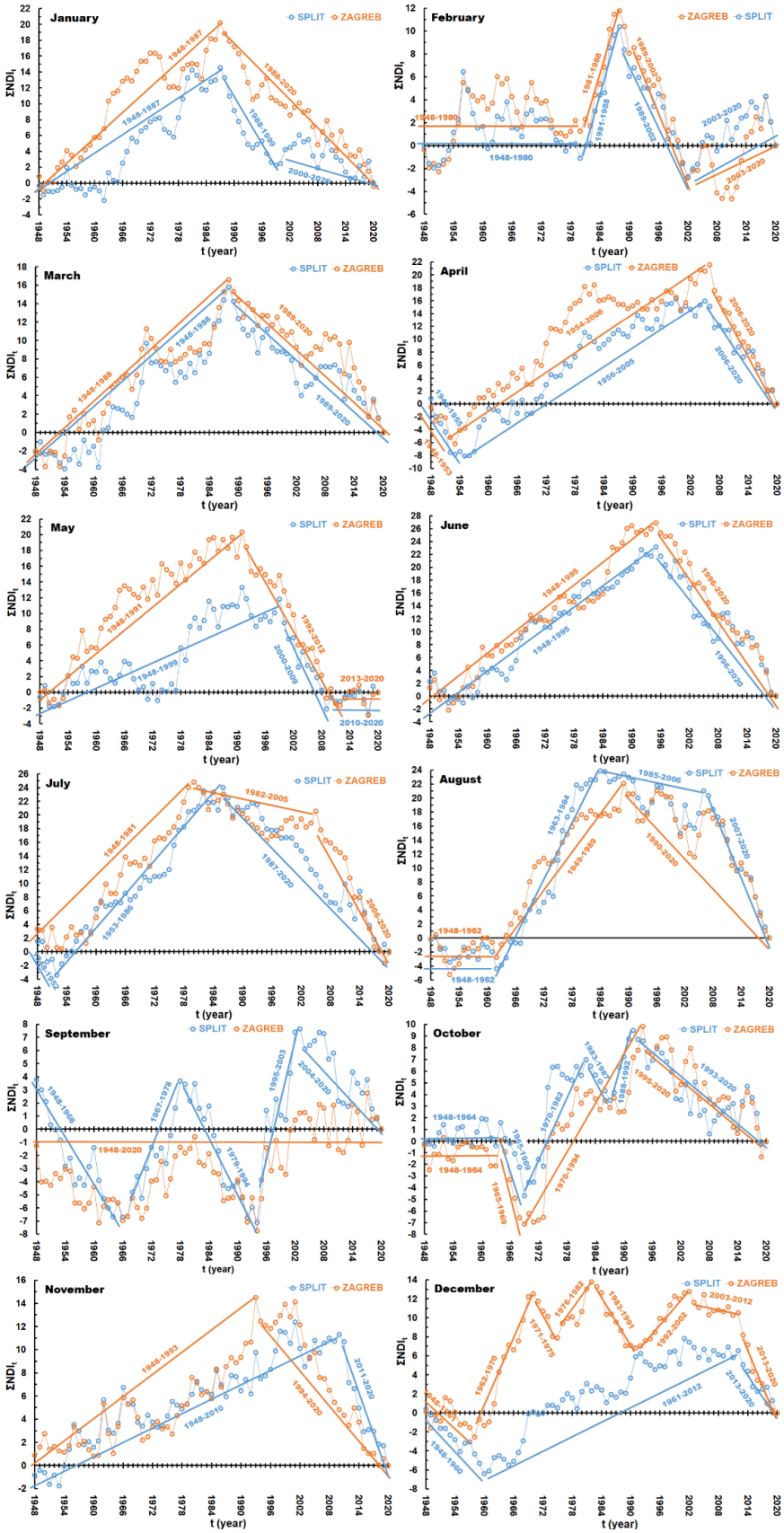

Fig. 10. Representation of the sums of the New Drought Indices, Σ*NDI$_i$*, *i* ∈(1, 2..., 73), defined according to the monthly values of precipitation and mean annual temperatures of Split and Zagreb in the 12 months in the period 1948 to 2020.

Table 7 lists the values of the linear correlation coefficients, r, and the results of the M-K test, p, for the series of individual monthly New Drought Indices, NDI_{av}, at both stations for the period 1948 to 2020. We found downward trends for all months, except September. Statistically significant downward trends are more frequent at the Zagreb station and occur for six months, in January and from April to August. At the Split station, statistically significant downward trends were determined only from June to August. The NDI indicates that drought is more pronounced during the warm period of the year.

Table 8 lists the average values of the monthly New Drought Indices, NDI_{av}, for each month in the sub-periods specified in Figure 10 and the t-test results, p, between successive sub-periods. From the data listed in Table 8, and the graphs in Figure 10, we found the NDI to behave differently during sub-periods within the overall observed 73-year period. Note that we also found evidence for cases of similar behaviours of monthly NDIs in both stations. Overall, they differ most in September, when at the Zagreb station, there is almost no statistically significant difference between wet and dry sub-periods, while at the Split station, as many as five such sub-periods do interchange.

CONCLUSIONS

We live in a time when the world is plagued by droughts, and it is almost certain that the situation will worsen in the near future. Numerous methods and a growing number of articles and books show that both science and daily practice are far from understanding and effectively combating this pervasive planetary disaster. Although many institutions and individuals are addressing the problem of drought, there is still a need and challenge to develop objective methods and efficient techniques to assess the intensity of droughts and predict their onset and end (Panu and Sharma, 2002). Drought monitoring and the development of drought early warning systems are fundamental for effectively fighting this increasing threat (AghaKouchak et al., 2021; Barker et al., 2016; Thompson, 2021).

Drought monitoring and early warning systems based on different drought indices could be crucial in mitigating and preventing their consequences. It is necessary to bring the results of drought research closer to practice, i.e., to end-users, to create the conditions for an effective fight against this increasingly dangerous threat. Although drought can generally be considered a natural phenomenon, there are several anthropogenic (e.g., excessive water demand, deforestation, land degradation, insufficient potable water supply, irrigation, etc.) and combined causes, at least some of which may be partly caused by global warming and climate change. The effect of global warming will continue to affect the intensification of drought in many areas in the near future. It needs to be noted that in each location, even in the vicinity of each other and with similar climatic properties, drought might lead to different consequences. For example, local water shortages may go unnoticed because water transfers from one location to another. Other shortages can be chronic in communities that always require more water than is available, even in wet periods (e.g., in case of water pollution). All the above and many other reasons not mentioned here call for a better conceptualization of the drought issue (Slette et al., 2019; Thompson, 2021).

In this context, the complementarity to existing indices and the main advantages of the proposed NDI are: (1) a readily availability of air temperatures and precipitations; (2) a large number of climatological stations, which monitor air temperature and precipitation all over the world; (3) long lasting time series of these two climatological parameters.

The purpose of this paper is to present to researchers, engineers, and practitioners a new, original, and practical approach based on the calculation of a simple drought index. The new and original NDI presented in this paper can serve as a new and meaningful drought metric and contribute to a better understanding and explanation of this phenomenon. The research presented in this paper is a contribution geared towards solving this complex contemporary issue and is part of the analysis of drought processes rather than a proposal for a new and reliable index.

Certainly, it is also necessary to continue the research efforts to overcome the existing dilemmas related to the identification and quantification of the phenomenon of drought. Our paper aims to make such contributions by combining two crucial parameters for drought formation: precipitation and temperature. We are confident that this method, when presented to relevant audiences, will be accepted by them as a tool of choice. Its value will be demonstrated in its application under different climatological and environmental circumstances. This is a process that will require the participation of many experts from around the world.

Funding. This research was supported through project KK.05.1.1.02.0024 "VODIME-Waters of Imotski region", a project financed by Croatian Government and the European Union through the European Structural Fund – within the call "Strengthening the applied research for climate change adaptation measures" KK.05.1.1.02.

This research is partially supported through project KK.01.1.1.02.0027, a project co-financed by the Croatian Government and the European Union through the European Regional Development Fund – the Competitiveness and Cohesion Operational Programme.

Acknowledgement. The data used in this study was provided courtesy of the Croatian Meteorological and Hydrological Service, for which we thank them.

Conflicts of Interest. The authors declare no conflict of interest.

REFERENCES

Allen, S.M., Gough, W.A., Mohsin, T., 2015. Changes in the frequency of extreme temperature records for Toronto, Ontario, Canada. Theoretical and Applied Climatology, 119, 3–4, 481–491. DOI: 10.1007/s00704-014-1131-1

AghaKouchak, A., Mirchi, A., Madani, K., Di Baldassarre, G., Nazemi, A., Alborzi, A., Anjileli, H., Azarderakhsh, M., Chiang, F., Hassanzadeh, E., Huning, L.S., Mallakpour, I., Martinez, A., Mazdiyasni, O., Moftakhari, H., Norouzi, H., Sedegh, M., Sadeqi, D., Van Loon A.F., Wanders, N., 2021. Anthropogenic drought: definition, challenges, and opportunities. Reviews of Geophysics, 58, 2, e2019RG000683. DOI: 10.1029/2019RG000683

Barker, L.J., Hannaford, J., Chiverton, A., Svensson, C., 2016. From meteorological to hydrological drought using standardised indicators. Hydrolgy and Earth System Sciences, 20 6, 2483–2505. DOI: 10.5194/hess-20-2483-2016

Bonacci, O., 1993. Hydrological identification of drought. Hydrological Processes, 7, 3, 249–262. DOI: 10.1002/hyp.3360070303

Bonacci, O., 2004. On the role of hydrology in water resources management. IAHS Publication 286, pp. 88–94.

Bonacci, O., 2010. Analiza nizova srednjih godišnjih temperatura zraka u Hrvatskoj. Građevinar, 62, 9, 781–791.

Bonacci, O., 2012. Increase of mean annual surface air temperature in the Western Balkans during last 30 years. Vodoprivreda, 44,

255–257, 75–89.
Bonacci, O., Roje-Bonacci, T., 2020. Primjena metode dan za danom (day to day) varijabilnosti temperature zraka na podatcima opaženim na opservatoriju Zagreb-Grič (1887-2018.). Hrvatske Vode, 28, 112, 125–134.
Dai, A., 2011. Drought under global warming: a review. Wiley Interdisciplinary Reviews, 2, 1, 45–65. DOI: 10.1002/wcc.81
Dragičić, J., Bezdan, A., Pejič, B., Mesaroš, M., Blagojević, B., 2017. Analiza pojave suše na području Severnog Banata. Annals of Agronomy, 41, 2, 77–84.
Fassouli, V.P., Karavitis, C.A., Tsesmelis, E., Alexandris, S., G., 2021. Factual Drought Index (FDI): a composite index based on precipitation and evapotranspiration. Hydrological Sciences Journal, 66, 11, 1638–1652. DOI: 10.1080/02626667.2021.1957477
Ferina, J., Vučetić, V., Bašić, T, Anić, M., 2021. Spatial distribution and long-term changes in water balance components in Croatia. Theoretical and Applied Climatology, 144, 3–4, 1311–1333. DOI: 10.1007/s00704-021-03593-1
Garbrecht, J., Fernandez, G.P., 1994. Visualization of trends and fluctuations in climatic records. Water Resources Bulletin, 30, 2, 297–306. DOI: 10.1111/j.1752-1688.1994.tb03292.x
Hamed, K.H., Ramachandra, R., 1998. A modified Mann-Kendal trend test for autocorrelated data. Journal of Hydrology, 204, 14, 182–196. DOI: 10.1016/S0022-1694(97)
Hisdal, H., 2002. Regional aspects of drought. Dissertation. Faculty of Mathematics and Natural Sciences, University of Oslo, Norge.
Hori, Y., Gough, W.A., Butler, K., Tsuji, L.J., 2017. Trends in the seasonal length and opening dates of a winter road in the western James Bay region, Ontario, Canada. Theoretical and Applied Climatology, 129, 3–4, 1309–1320. DOI: 10.1007/s00704-016-1855-1
Kendall, M.G., 1975. Rank Correlation Methods. 4th edition. Charles Griffin, London, UK.
Kim, Y.H., Kim, M.K., Lau, W.K.M., Kim, K.M., Cho, C.H., 2015. Possible mechaNDIm of abrupt jump in winter surface sir temperature in the late 1980s over the northern hemisphere. Journal of Geophysical Research Atmospheres, 120, 12, 474–485. DOI: 10.1002/2015JD023864
Köppen, W., Geiger, R., 1936. Handbuch der Klimatologie: Das geographische System der Klimate. Gebrüder Borntraeger Verlag, Berlin.
Kothawale, D.R., Kumar, K.R., 2005. On the recent changes in surface temperature trends over India. Geophysical Research Letter, 32, 18, L18714. DOI: 10.1029/2005GL023528
Levi, B.G., 2008. Trends in the hydrology of the western US bear the imprint of manmade change. Physics Today, 61, 4, 16–18. DOI: 10.1063/1.2911164
Li, G., 2010. Changes of the Yellow River water resources and countermeasures. Climate change and adaptation for water resources in Yellow river basin, China. IHP VII Technical Documents in Hydrology, UNESCO Office in Beijing, pp. 11–23.
Li, J., Wu, C., Xia, C.A., Yeh, P.J.F., Hu, B.X., Huang, G., 2021. Assessing the responses of hydrological drought to meteorological drought in the Huai River Basin, China. Theoretical and Applied Climatology, 144, 3–4, 1043–1057. DOI: 10.1007/s00704-021-03567-3
Lloyd-Hughes, B., 2014. The impracticality of a universal drought definition. Theoretical and Applied Climatology, 117, 3, 607–611. DOI: 10.1007/s00704-013-1025-7
Ljubenkov, I., Bonacci, O., 2011. Utvrđivanje i određivanje suše na otoku Korčuli. Hrvatske Vode, 19, 77, 181–194. (In Croatian.)
Mann, H.B., 1945. Non-parametric test of randomness against trend. Econometrica, 13, 3, 245–259. DOI: 10.2307/1907187
McGhee, J.W., 1985. Introductory Statistics. West Publishing Company, St Paul and New York.
Mishra, A.K., Singh, V.P., 2010. A review of drought concept. Journal of Hydrology, 391, 202–216, DOI: 10.1016/j.jhydrol.2010.07.012
Morid, S., Smakhtin, V., Moghaddasi, M., 2006. Comparison of seven meteorological indices for drought monitoring in Iran. International Journal of Climatology, 26, 7, 971–985. DOI: 10.1002/joc.1264
Neto, A.A.M., Roy, T., de Oliveira, P.T.S., Troch, P.A., 2020. An aridity index-based formulation of streamflow components. Water Resources Research, 56, e2020WR027123. DOI: 10.1029/2020WR027123
Palmer, W.C., 1965. Meteorological drought. Research Paper No. 45. US Department of Commerce Weather Bureau, Washington DC.
Pandžić, K., Šimunić. I., Tomić, F., Husnjak, S., Likso, T., Petošić, D., 2006. Comparison of three mathematical models for the estimation of 10-day drain discharge. Theoretical and Applied Climatology, 85, 1, 107–115. DOI: 10.1007/s00704-005-0165-9
Pandžić, K., Likso, T., Curić, O., Mesić, M., Pejić, I., Pasarić, Z., 2020. Drought indices for the Zagreb-Grič Observatory with an overview of drought damage in agriculture in Croatia. Theoretical and Applied Climatology, 142, 1–2, 555–567. DOI: 10.1007/s00704-020-03330-0
Panu, U.S., Sharma, T.C., 2002. Challenges in drought research: some perspectives and future directions. Hydrological Sciences Journal, 47, S19–S30. DOI: 10.1080/02626660209493019
Shourov, M.M.H., Mahmud, I., 2019. pyMannKendall: a python package for non-parametric Mann Kendall family of trend tests. Journal of Open-Source Software, 4, 9, 1556. DOI: 10.21105/joss.01556
Slette, I.J., Post, A.K., Awad, M., Even, T., Punzalan, A., Williams, S., Smith, M. D., Knapp, A.K., 2019. How ecologists define drought, and why we should do better. Global Change Ecology, 25, 10, 3193–3200. DOI: 10.1111/gcb.14747
Šegota, T., Filipčić, A., 2003. Köppenova podjela klima i hrvatsko nazivlje. Geoadria, 8, 1, 17–37.
Tadić, L., Dadić, T., Bosak, M., 2015. Usporedba različitih metoda za ocjenu suše na području kontinentalne Hrvatske. Građevinar, 67, 1, 11–22, DOI: 10.14256/JCE.1088.2014
Thompson, E., 2021. A better way to understand drought. Eos, 102. DOI: 10.1029/2021EO155289
Van Lanen, H.A.J., Wanders, N., Tallaksen, L.M., Van Loon, A.F., 2013. Hydrological drought across the world: impact of climate and physical catchment structure. Hydrology and Earth System Sciences, 17, 5, 1715–1732. DOI: 10.5194/hess-17-1715-2013
Van Loon, A.F., 2015. Hydrological drought explained. Wiley Interdisciplinary Reviews Water, 2, 25, 359–392. DOI: 10.1002/wat2.1085
Wang, H., Stephenson, S.R., 2018. Quantifying the impacts of climate change and land use/cover change on runoff in the lower Connecticut River Basin. Hydrological Processes, 32, 9, 1301–1312. DOI: 10.1002/hyp.11509
WMO, 2012. Standardized Precipitation Index User Guide. World Meteorological Organization WMO-No 1090, Geneva, Switzerland.
Wong, G., van Lanen, H.A.J., Torfs, P.J.J.F., 2013. Probabilistic analysis of hydrological drought characteristics using meteorological drought. Hydrological Sciences Journal, 58, 2, 253–270. DOI: 10.1080/02626667.2012.753147
Zhao, Y., Weng, Z., Chen, H., Yang, J., 2020. Analysis of the evolution of drought, flood, and drought-flood abrupt alternation events under climate change using the daily SWAP Index. Water, 12, 7, 1969. DOI: 10.3390/w12071969
Yevjevich, V., Da Cuncha, L., Vlachos, E.C., 1983. Coping with Droughts. Water Resources Publications. Littleton, Colorado, US.

Received 24 November 2021
Accepted 19 September 2022

J. Hydrol. Hydromech., 71, 2023, 1, 111–122
https://doi.org/10.2478/johh-2022-0037

sciendo Journal of Hydrology and Hydromechanics Institute of Hydrology SAS

Accuracy of radar-estimated precipitation in a mountain catchment in Slovakia

Patrik Sleziak[1*], Martin Jančo[1], Michal Danko[1], Ladislav Méri[2, 3], Ladislav Holko[1]

[1] Institute of Hydrology, Slovak Academy of Sciences, Dúbravská cesta 9, 841 04 Bratislava, Slovakia.
[2] Slovak Hydrometeorological Institute, Jeséniova 17, 833 15 Bratislava, Slovakia.
[3] Department of Astronomy, Physics of the Earth, and Meteorology, Comenius University in Bratislava, Mlynská dolina 842 48, Bratislava 4, Slovakia.
[*] Corresponding author. E-mail: sleziak@uh.savba.sk

Abstract: Accurate estimation of precipitation in mountain catchments is challenging due to its high spatial variability and lack of measured ground data. Weather radar can help to provide precipitation estimates in such conditions. This study investigates the differences between measured and radar-estimated daily precipitation in the mountain catchment of the Jalovecký Creek (area 22 km^2, 6 rain gauges at altitudes 815–1900 m a.s.l.) in years 2017–2020. Despite good correlations between measured and radar-based precipitation at individual sites (correlation coefficients 0.68–0.90), the radar-estimated precipitation was mostly substantially smaller than measured precipitation. The underestimation was smaller at lower altitude (on average by –4% to –17% at 815 m a.s.l.) than at higher altitudes (–35% to –59% at 1400–1900 m a.s.l.). Unlike measured data, the radar-estimated precipitation did not show the differences in precipitation amounts at lower and higher altitudes (altitudinal differences). The differences between the measured and radar-estimated precipitation were not related to synoptic weather situations. The obtained results can be useful in preparation of more accurate precipitation estimates for the small mountain catchments.

Keywords: Radar-estimated precipitation; Precipitation estimates; Daily precipitation; Synoptic weather situations.

INTRODUCTION

Hydrological cycle in the mountain environment has some specific features. The distribution of basic climatic elements (atmospheric precipitation and air temperature) and vegetation is significantly affected by large altitudinal differences. Windward and leeward effects during precipitation, movement of snow from the ridges to the feet of slopes and into the valleys and the influence of terrain configuration are typical phenomena found in mountains. Small mountain catchments in the highest mountains of Slovakia are often forested, their average elevation exceeds 1000 m a.s.l., the slopes are steep (e.g. the average slope of about 30° as in the catchments of the Tatra Mountains) and they have shallow soils (depth around 1 meter) and small riparian areas (Holko et al., 2011).

Precipitation is one of the basic elements of the water balance and the most important input in catchment hydrological modelling. It is measured by rain gauges at selected sites (points). Due to the extreme natural conditions (i.e. complex topography and highly elevated regions), mountain catchments are less populated and therefore sparsely covered by measurement networks. Precipitation stations are often situated in the lower parts of the catchments. This might pose a problem especially in small mountain catchments, because due to positive elevation gradients in precipitation, catchment areal precipitation can be underestimated. The radar-based precipitation products provide a potential source of useful data on precipitation in larger regions (Fairman et al., 2015). They could potentially be useful also in small mountain catchments. However, they are affected by various uncertainties. For instance, the radar signal over high elevated areas may be affected by beam blockages, vertical reflectivity profiles, fluctuation in atmospheric conditions, etc. (McKee and Binns, 2016; Villarini and Krajewski, 2010).

A number of studies illustrated the potential of the radar-based precipitation products for hydrological applications (e.g., Abon el al., 2016; Berne et al., 2005; Espinosa et al., 2015; Gilewski and Nawalany, 2018; Hazenberg et al., 2011). For example, Abon el al. (2016) tested the added value of radar-based rainfall estimates for streamflow simulations in the Marikina River Basin (the Philippines). They showed that for their study site, the radar-based product performed similarly as the measured rainfall data. Berne et al. (2005) tested the potential of weather radar in southern Ardennes, France. Their results showed biases of the radar estimates with respect to gauge estimates between +128% and −42% for six precipitation events. Espinosa et al. (2015) compared three Doppler radar datasets against rain gauge measurements for two storm events in a desert area of Southern California, USA. Their results pointed out that topographic interference with the radar outcomes can be a significant factor leading to major differences between the radar and rain gauge data. Germann et al. (2006) presented radar algorithm improvements for better radar precipitation estimates over Switzerland. They showed that modifications in the algorithms of the operational QPE (Quantitative Precipitation Estimate) product has resulted in reduction of bias/scatter. The improvement in scatter was mainly achieved by the meso-beta profile and the local bias correction. Fairman et al. (2015) showed that the radar precipitation product provided a useful depiction of the annual distribution of precipitation across the Great Britain and Ireland. Gilewski and Nawalany (2018) compared the performance of three different precipitation data sources (rain gauge, radar and satellite precipitation estimates) for event-based hydrologic modelling in a small mountainous catchment (the Upper Skawa catchment) in Poland. They concluded that radar and satellite precipitation estimates were suitable for the event-based modelling. Hazenberg et al. (2011) showed that for the hilly region of

the Belgian Ardennes, the radar product underestimated the amount of precipitation as compared to the rain gauges. Kreklow et al. (2020) evaluated two radar products (RADOLAN and RADKLIM) against the rain gauge data (annual/seasonal/hourly) for the territory of Germany. Both radar products tended to underestimate total precipitation amounts and high intensity rainfalls. Schleiss et al. (2020) tested the accuracy of six different radar products in four countries (Denmark, Finland, the Netherlands and Sweden) with the emphasis on quantification of discrepancies between the radar precipitation estimate and measured precipitation during heavy precipitation. They showed that although the overall agreement in heavy precipitation was good (correlation coefficient 0.7–0.9), all six radar products exhibited a clear pattern of underestimation compared with rain gauges. Hofstätter et al. (2018) evaluated the variability of heavy precipitation over central Europe with respect to cyclone track types. High frequency of strong cyclones was found to be the key factor in explaining the seasonality of heavy precipitation.

While some studies reported underestimation of measured precipitation (e.g., Goudenhoofdt and Delobbe, 2016; Hazenberg et al., 2011; Kreklow et al., 2020; Schleiss et al., 2020; Smith et al., 2012) other showed its overestimation (e.g., Fairman et al., 2015; Marra and Morin, 2015). Despite the existence of numerous studies, the results are difficult to compare due to different regions, physiographic conditions, differences in radar hardware, correction algorithms, etc. Comparative studies in other regions are therefore still needed. Hydrological Forecasting Service (HFS) of Slovak Hydrometeorological Institute recently drew attention to the problem of acceptable flood forecasting in mountains, related to the accuracy of precipitation estimates. They could not forecast recent big rainfall-runoff event (18 July 2018) in the mountainous Jalovecký Creek catchment with required accuracy (Hrušková and Hlaváčiková, 2022). A more detailed analysis showed that precipitation input data derived by the radar were significantly underestimated; the radar-based precipitation estimate was approximately 40 mm while measured precipitation was around 140 mm. Therefore, a more detailed analysis could be useful to improve the radar-based estimates.

This study evaluated a new radar product developed for the territory of Slovakia. Comparison of the differences between the radar-estimated and measured precipitation at different elevations in a small mountain catchment in northern Slovakia (the Jalovecký Creek catchment) was supplemented by the analysis of the differences during different synoptic weather situations. The objectives of the study are a) to evaluate the differences between measured precipitation and the newly developed radar-estimated daily precipitation product at different elevations, b) examine if the differences depend on the synoptic weather situation and c) quantify the differences for greater precipitation amounts that can cause flood situations.

MATERIALS AND METHODS

Study area and data

The study was conducted in the mountain catchment of the Jalovecký Creek located in the Western Tatra Mountains (Fig. 1). The catchment features high altitudinal differences (815 to 2178 m a.s.l.) in a small area (22.2 km^2). Hydrological research aimed at the improvement of knowledge on hydrological cycle of the highest part of the Western Carpathians is conducted there

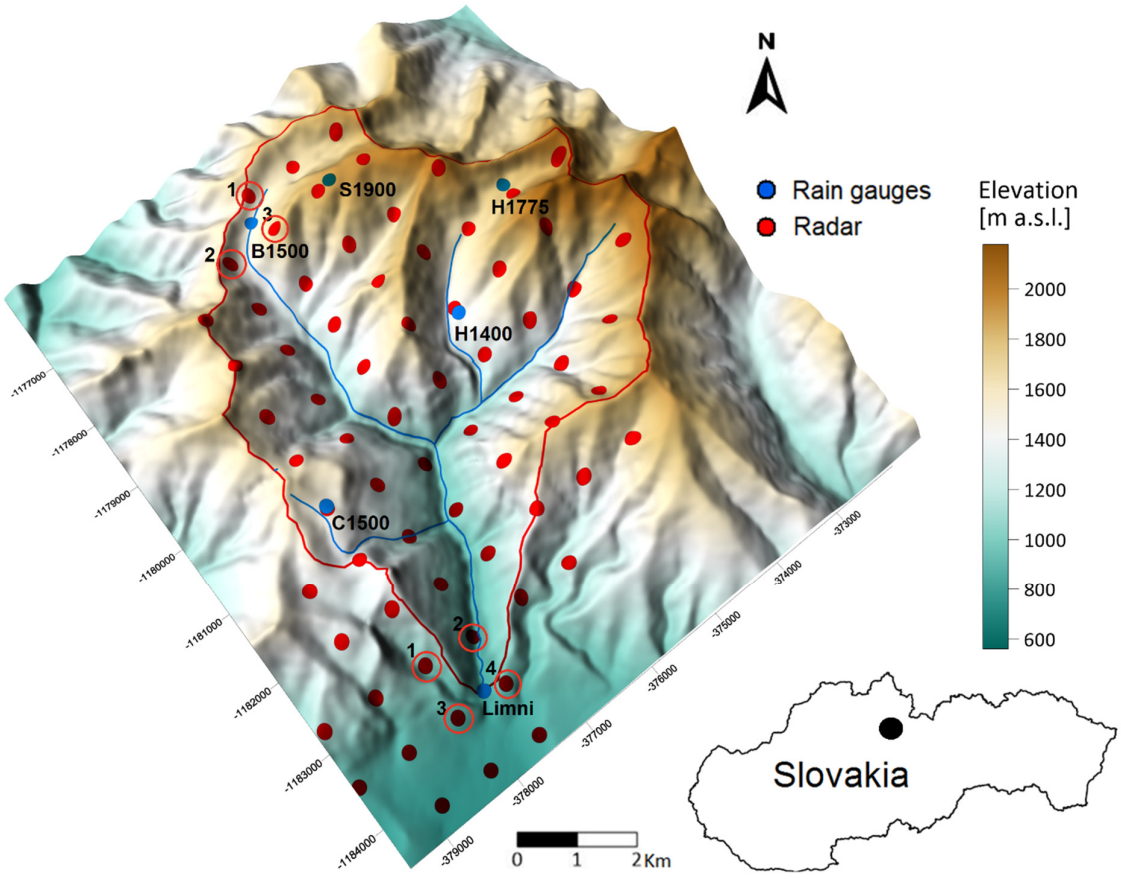

Fig. 1. Precipitation measurement network (the blue points) and the nodes of radar images (the red points); the circled points indicate nodes that were used for computation of averages for sites Limni and B1500.

since the end of the 1980s (e.g. Holko et al., 2021). Precipitation measurement network built in the catchment is denser than in other small mountain catchments of Slovakia and provides data for hydrological modelling (Danko et al., 2015a, b) or investigation of precipitation spatial and temporal variability (e.g. Holko et al., 2014).

The study is based on daily precipitation data measured at six sites in years 2017–2020. The sites were selected to cover different altitudes, ranging from 815 to 1900 m a.s.l. (Fig. 1). Precipitation stations C1500 (1500 m a.s.l.) and Limni (815 m a.s.l.) provided daily precipitation for the entire year measured by the weighing gauge TRwS 504. Tipping bucket rain gauges (Pronamic Pro) provided the spatially distributed precipitation data at other four sites H1400 (1400 m a.s.l.), B1500 (1500 m a.s.l.), H1775 (1775 m a.s.l.) and S1900 (1900 m a.s.l.) in summer months (June to September).

Radar-based precipitation estimates

The radar-based precipitation product used in our study was derived from the network of four C-band, dual-polarized Selex-Gematronik Meteor 735 CDP10 weather radars of the Slovak Hydrometeorological Institute and computed by the qRad and qPrec software packages developed at the Slovak Hydrometeorological Institute (Méri et al., 2021). The qRad software estimates the actual quality of the radar volume data by various quality indices and corrects some undesirable effects on the measurement (e.g., beam-blockage, ground-clutter, non-meteorological echoes). The qPrec package uses the probabilistic approach to estimate the rainfall intensity based on heterogeneous input data (rain gauges, radars, satellites). The nodes from a regular grid (spatial resolution of 1x1 km identical to the resolution of the qPrec product) covering the Jalovecký Creek catchment were used in the study. Separate calibration functions to convert reflectivity values to rainfall probability and rainfall rate are derived for each radar according to the latest rain-gauge measurements. The aim of the calibration functions is to reduce the systematic bias in the radar-based precipitation estimate taking into account also the seasonal changes. Only one calibration function per radar is computed and represents the average for the entire area covered by the given radar. This can lead to over – or under estimation in some sub-areas of the domain. The calibrated input data fields are combined according to their precision and actual quality (Méri et al., 2021). The main limiting factors of radar measurements in mountainous areas are the beam-blockage and ground clutter with its possible removal from the reflectivity values by the radar software. These effects can be depicted by the minimal detectable height map for the used network shown in Fig. 2. The yellow and greenish areas in the Figure represent radar beam near the ground level where precipitation estimation can be done more precisely. However, these areas are also more influenced by the ground clutter (high reflectivity values due to radar beams hitting the surface). The blue and purple areas in Fig. 2 indicate that radar beams are higher above the ground level due to the blockage of the lower beams. The reflectivity values detected in these areas represent a higher level of the atmosphere and are less correlated with the rainfall intensities on the ground.

The evaluation of radar-based precipitation estimates was based on the comparison with measured precipitation. Radar data from the nodes close to rain gauges C1500, S1900, H1775 and H1400 were directly used in the comparison. Averages of the radar-based precipitation estimates from four and three surrounding nodes were used for rain gauges Limni and B1500, respectively (Fig. 1). The agreement between the two precipitation datasets was examined by the bias expressed in per cents (Equation (1) below) and in millimeters (Equation (2)). Pearson correlation coefficients between measured and radar-based precipitation and visual examination were used as well.

$$\Delta P_{\%} = \left(\frac{P_{radar} - P_{measured}}{P_{measured}} \right) * 100 \quad (1)$$

$$\Delta P_{mm} = P_{radar} - P_{measured} \quad (2)$$

The differences between the radar-estimated and measured precipitation were evaluated also with account of the synoptic weather situations that occurred on particular days. The aim was to find out how are the differences related to particular synoptic situation. Synoptic weather situation for each day of the study period was obtained from the Slovak Hydrometeorological Institute (SHMI, 2021). At present, a common typing of synoptic weather situations is used in Slovakia and in the Czech Republic. The typing is based on the catalogue of Hess and Brezowsky (1997), Brádka et al. (1961) and Ballon et al. (1964). It contains 28 types (Table 1) characterized by the direction of the air masses flow or its typical short-term changes, regime of the pressure field, the way the front passes and the influx or alternation of air masses having certain origin (SHMI, 2021).

Table 1. Synoptic weather situations.

Synoptic situations	Abbreviation
trough over central Europe	B
travelling trough	Bp
cyclone over central Europe	C
upper cyclone	Cv
east cyclonic	Ec
north cyclonic	Nc
north-east cyclonic	NEc
north-west cyclonic	NWc
south-east cyclonic	SEc
south-west cyclonic of the 1st type	SWc1
south-west cyclonic of the 2nd type	SWc2
south-west cyclonic of the 3rd type	SWc3
west cyclonic	Wc
west cyclonic with southern pathway	Wcs
entry of the frontal zone	Vfz
anticyclone over central Europe	A
travelling anticyclone of the 1st type	Ap1
travelling anticyclone of the 2nd type	Ap2
travelling anticyclone of the 3rd type	Ap3
travelling anticyclone of the 4th type	Ap4
east anticyclonic	Ea
north-east anticyclonic	NEa
north-west anticyclonic	NWa
south anticyclonic	Sa
south-east anticyclonic	SEa
south-west anticyclonic	SWa
west anticyclonic	Wa
west anticyclonic of summer type	Wal

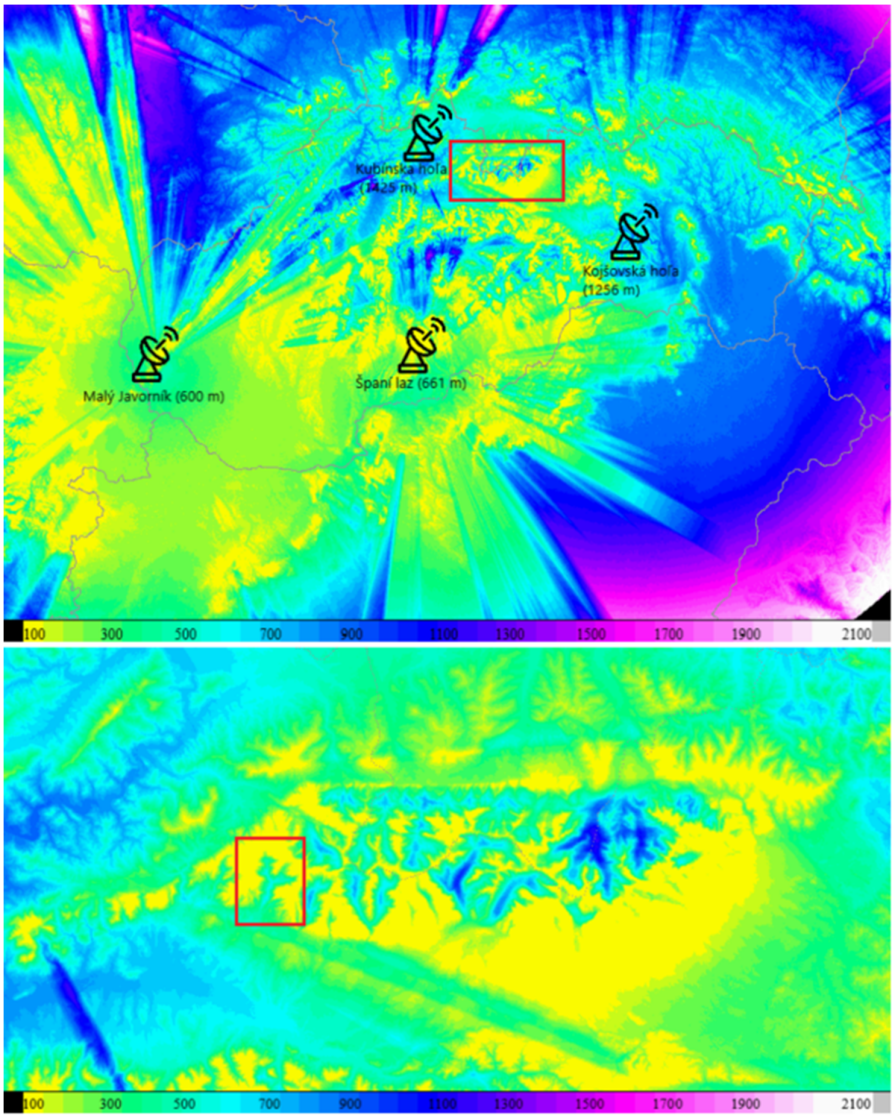

Fig. 2. Location of the radars used in this study, heights of the antennas above the sea level and minimal detectable height above the ground [m]; the red rectangle in the upper panel indicates the Tatra Mountains region that is shown in a greater detail in the lower panel; study area is indicated in the lower panel by the red triangle.

RESULTS

Characteristics of measured precipitation and catchment runoff

Precipitation occurred in the catchment quite often, i.e. in 48% to 60% of days in the study period (Table 2). Daily precipitation rarely exceeded 100 mm even at higher altitudes (1–2 times at different sites in the study period) and it was most frequently in the interval 0.1 mm to 5 mm (in 42% to 61% of days with precipitation). The difference in daily precipitation between the lower and higher altitudes becomes visible for greater precipitation amounts – while days with precipitation of up to 20 mm represented 95% of all days with precipitation at 820 m a.s.l. (site Limni), at higher altitudes they represented only 93% (less in the warm period of the year).

Precipitation occurred most frequently in days with synoptic weather situations B, Bp, NEc, NWc and Wc (12%, 11%, 9% and 9% of all days with precipitation at C1500, respectively). B and Bp are synoptic situations characterized by trough of the low air pressure above or passing through the Central Europe, respectively. NEc, NWc and Wc are cyclonal situations (north-eastern, north-western and western). In the warm part of the year (June to September), precipitation occurred most frequently during synoptic weather situations B, Bp, and NEc (16%, 18% and 14% of days with precipitation at C1500, respectively). The same synoptic weather situations were the most important also from the point of view of precipitation amounts (Fig. 3). The wettest one was the NEc that brought about 20% of annual precipitation (25%–29% of precipitation in period June to September).

The radar-based precipitation estimation is especially important for flood forecasting, i.e. for the high flows caused either by short, very intensive precipitation or long wet periods. Fig. 4 shows daily measured catchment (areal) precipitation and runoff in the warm period of years 2017 to 2020 and the relationship between the peakflow and daily precipitation

Table 2. Total number of days in the study period, number of days with precipitation and frequencies of days with daily precipitation in intervals 0.1–5.0 mm (1*), 5.01–10 mm (2*), 10.01–15.0 mm (3*) and 15.01–20 mm (4*). Values on the top/bottom characterize measured/radar-based precipitation, respectively.

Period	Site	Total number of days	Days with precipitation (0.1 mm and more) [%]	1* [%]	2* [%]	3* [%]	4* [%]	Σ 1*–4* [%]
January to December	**Limni**	1553	53	66	19	7	3	95
			52	66	19	9	2	96
	C1500	1553	66	62	17	9	5	93
			51	68	17	9	2	96
June to September	**Limni**	488	49	56	20	11	6	93
			50	58	21	11	3	93
	C1500	488	58	54	17	10	7	88
			51	57	19	13	5	94
	H1400	488	58	45	16	12	7	80
			51	58	19	11	4	92
	B1500	488	58	47	19	12	5	83
			52	59	18	10	6	93
	H1775	488	57	42	19	11	8	80
			53	58	21	10	3	92
	S1900	488	60	48	17	11	8	84
			53	58	19	10	6	93

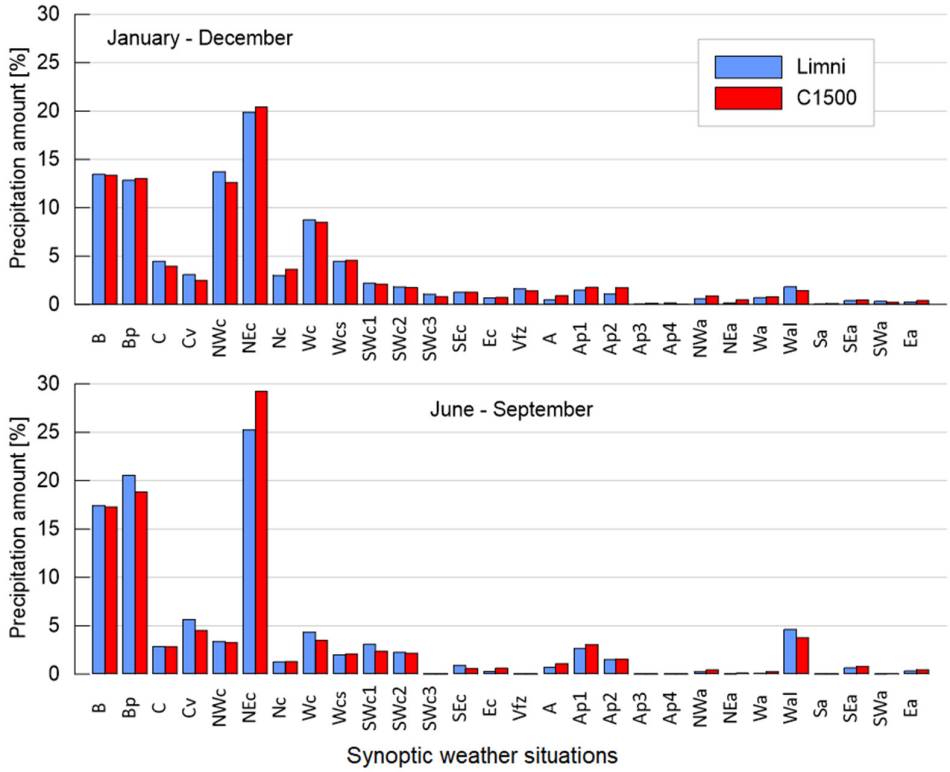

Fig. 3. Contribution of measured precipitation during different synoptic weather situations to total annual precipitation amount (January–December) and to total precipitation in the warm period of the year (June–September).

during selected events with high peakflow. Except for 2019, greater response of catchment runoff to precipitation occurred only 1–2 times in the warm periods of years 2017–2020. Although some events were caused by wet periods longer than one day, daily peakflow from the Jalovecký Creek catchment was well correlated with daily precipitation (coefficient of determination 0.89) that highlights the importance of correct estimation of the short-term high precipitation events. The cold period of the year (i. e. October to May) was excluded from the evaluation to avoid the uncertainties in the rainfall-runoff relations caused by the snow cover formation and melt.

Comparison of measured and radar-estimated precipitation

The differences between measured and radar-estimated precipitation summarized over longer periods (entire years, warm periods of the years) are given in Table 3. The radar-estimated precipitation was smaller than measured precipitation. The underestimation for the stations located in mountains and at higher altitudes (1400–1900 m a.s.l.) was substantially greater (between –35% and –59%) than for the station located at the lowest elevation (815 m a.s.l.) near catchment outlet (between –4% and –17%).

Table 3. Average bias values (in % – the value on the top, in mm – the value below it) at different elevations in the entire year (January–December) and in its warm period (June–September); the bias was calculated for precipitation totals over particular periods; minus signs (–) indicate that the radar-based precipitation underestimated the observed precipitation.

Period	Site	2017	2018	2019	2020
January to December	**Limni**	11 111	–7 –54	–7 –73	–23 –285
	C1500	–38 –644	–40 –519	–31 –436	–45 –747
June to September	**Limni**	–4 –25	–11 –52	–9 –35	–17 –113
	C1500	–35 –316	–39 –293	–35 –185	–37 –331
	H1400	–59 –761	–56 –590	–49 –338	–56 –661
	B1500	–46 –457	–43 –367	–40 –243	–51 –530
	H1775	–54 –673	–52 –544	–53 –407	–55 –669
	S1900	–50 –528	–52 –529	–53 –293	–55 –527

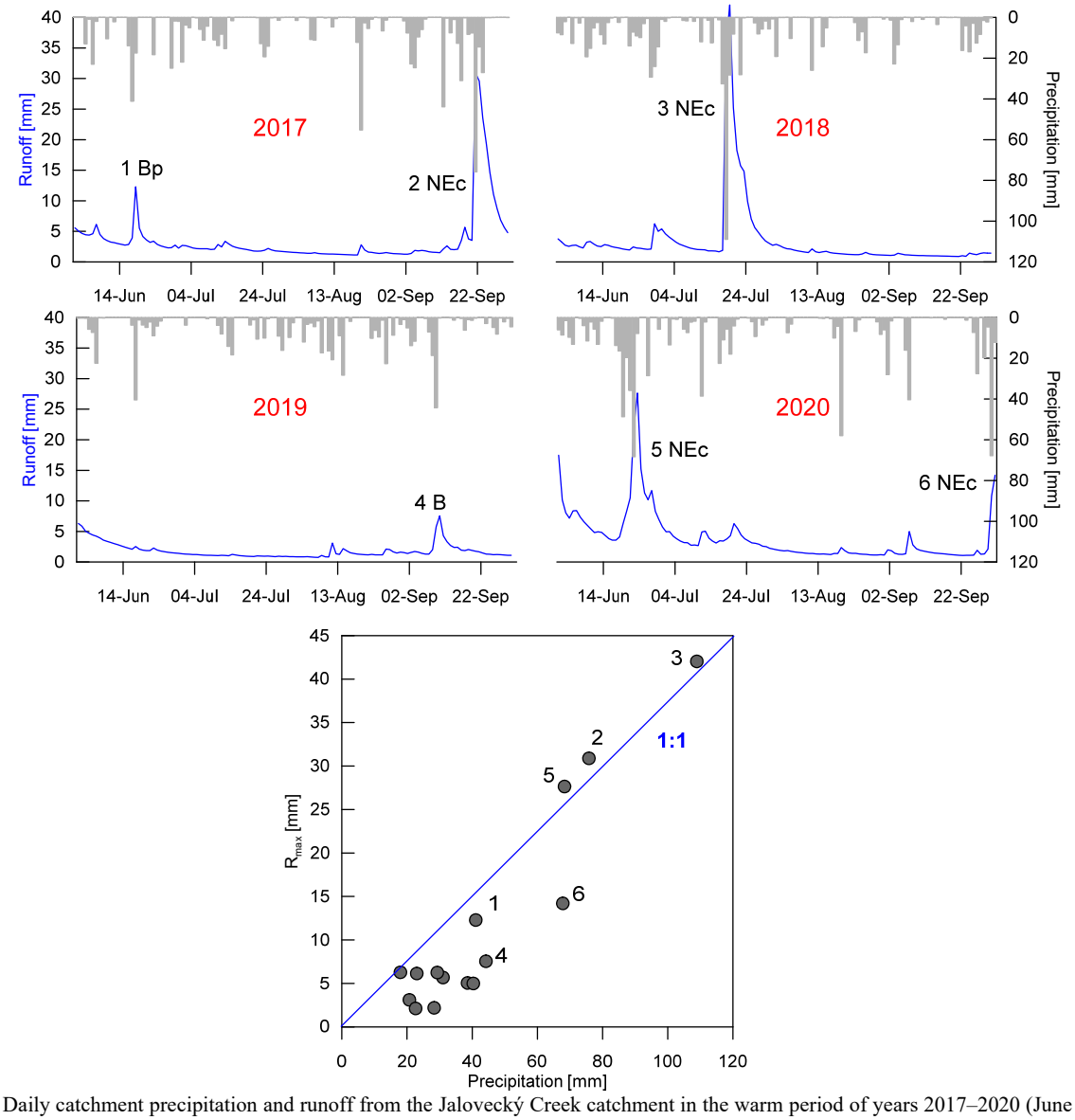

Fig. 4. Daily catchment precipitation and runoff from the Jalovecký Creek catchment in the warm period of years 2017–2020 (June to September) and the relationship between the event peakflow and daily precipitation on the same day or on the day preceding the peakflow; the numbers denote selected greatest runoff events in individual years and synoptic weather situations during which they occurred.

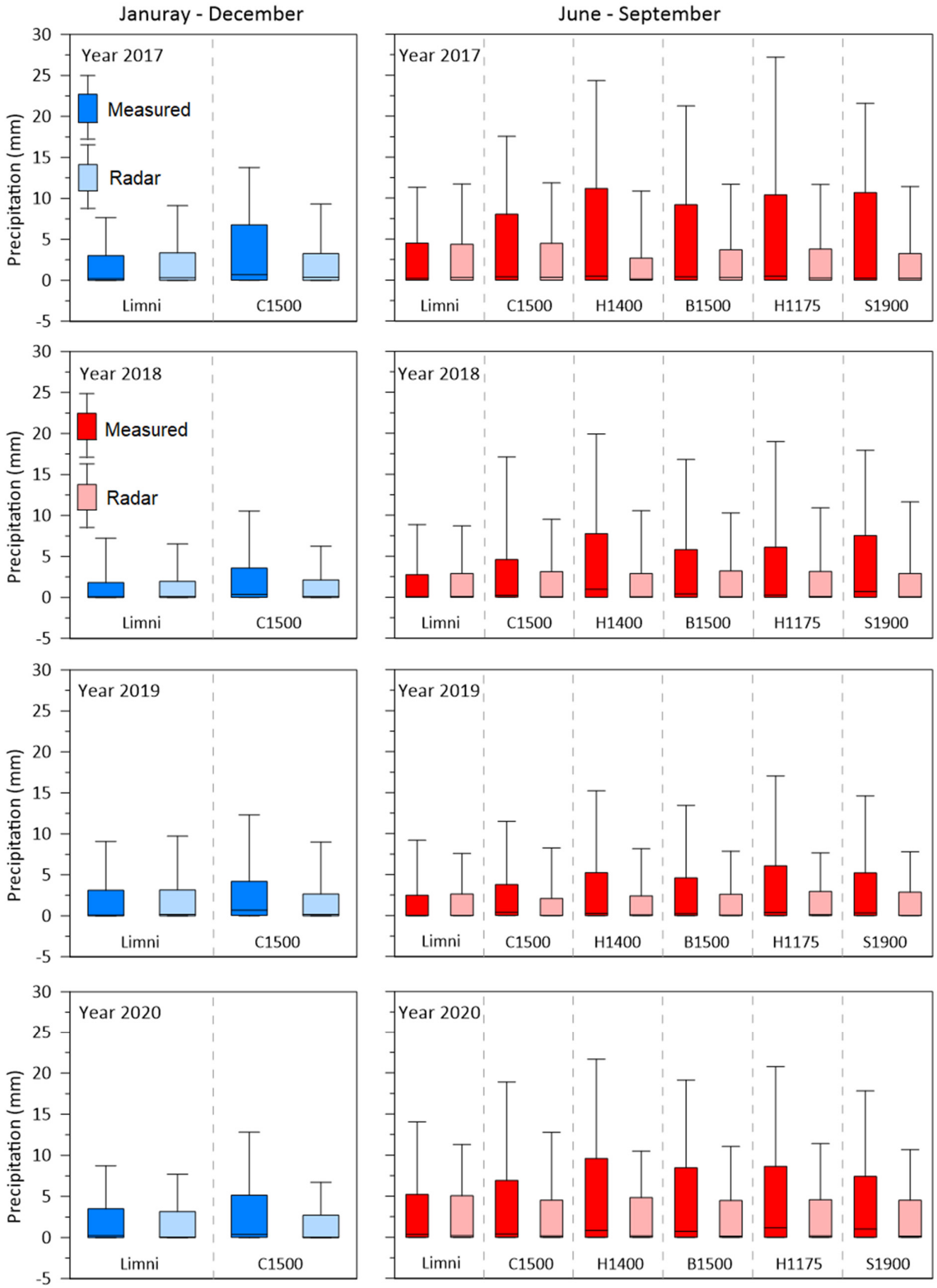

Fig. 5. Boxplots of measured and radar-estimated daily precipitation; the whiskers represent percentiles 10 and 90, the boxes are the upper and lower quartiles and the center line shows medians.

Fig. 5. indicates that except the lowest altitude (Limni), underestimation of the radar-based daily precipitation was systematic (smaller upper quartiles and maxima compared to measured data).

Systematic underestimation is confirmed by Fig. 6 showing daily scatterplots of measured against radar-based precipitation. The underestimation was especially significant for the high

measured precipitation amounts which are important for flood formation.

The Pearson correlation coefficients (Fig. 7) between measured and radar-estimated precipitation varied between 0.68 and 0.90. Except site H1400 they varied quite a lot between the years. The differences between the correlations calculated for the entire years and their warm periods were small, especially for the year of 2017 at site Limni.

Comparison of measured and radar-based daily precipitation during selected runoff events with the greatest peakflow in the warm periods of years 2017–2020 (Fig. 4) shown in Fig. 8 confirms substantial underestimation of the radar-based precipitation except for event 4 which had the smallest peakflow of all selected events. Fig. 8 also shows that while measured data mostly documented a big difference in precipitation amounts between the lowest-elevation and the higher-elevation stations, the radar-based data do not reveal such a pattern. This is also shown in Fig. 9 showing measured and radar-estimated summer precipitation totals (June to September) at different altitudes. The differences in precipitation amounts in different warm seasons are much less visible in the radar-based precipitation as well.

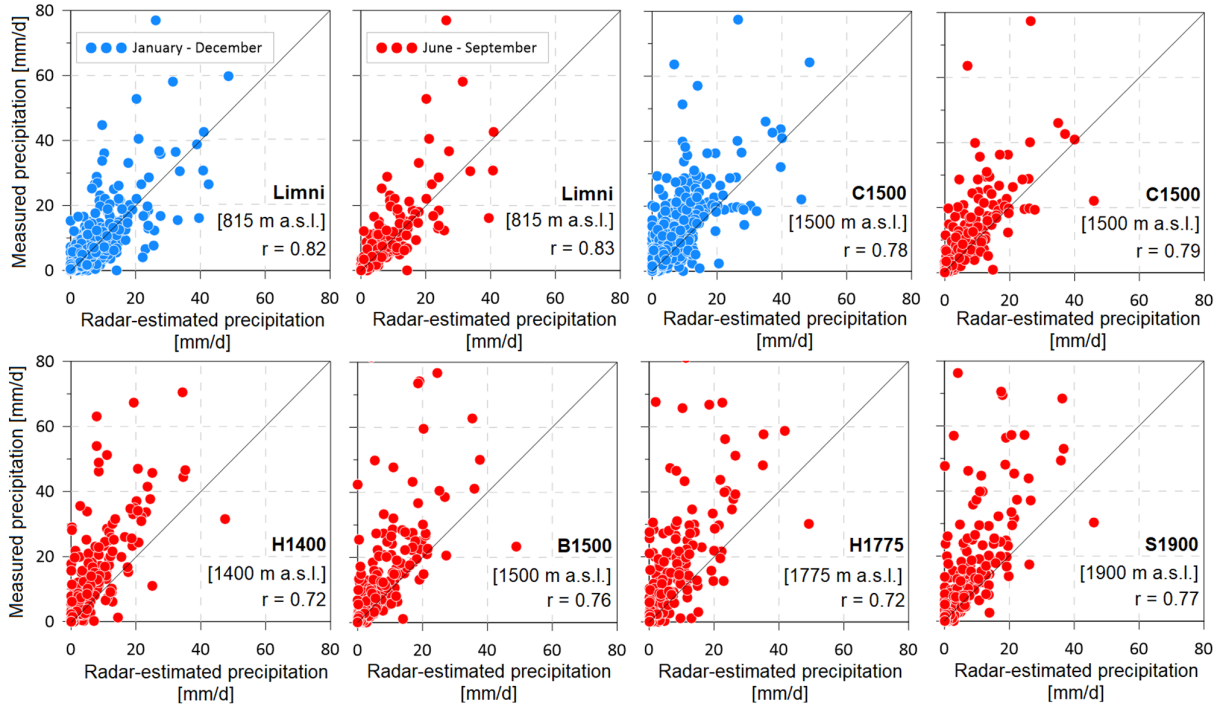

Fig. 6. Measured versus radar-estimated daily precipitation at different elevations in the entire year (January–December) and its warm period (June–September) in the study period 2017–2020; the diagonal represents the 1:1 line.

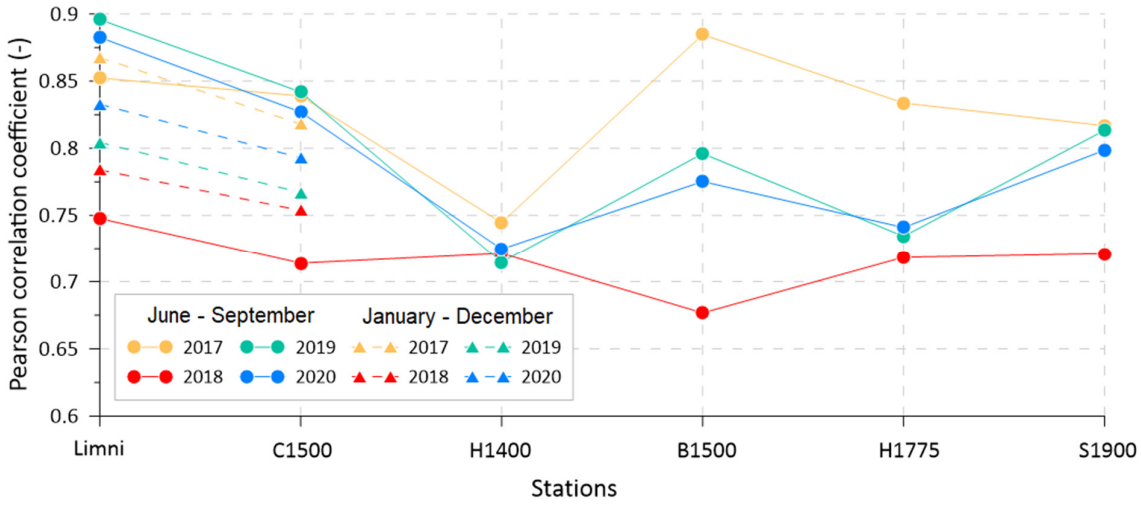

Fig. 7. Correlations between measured and radar-based precipitation at six stations in the entire years and in their warm periods.

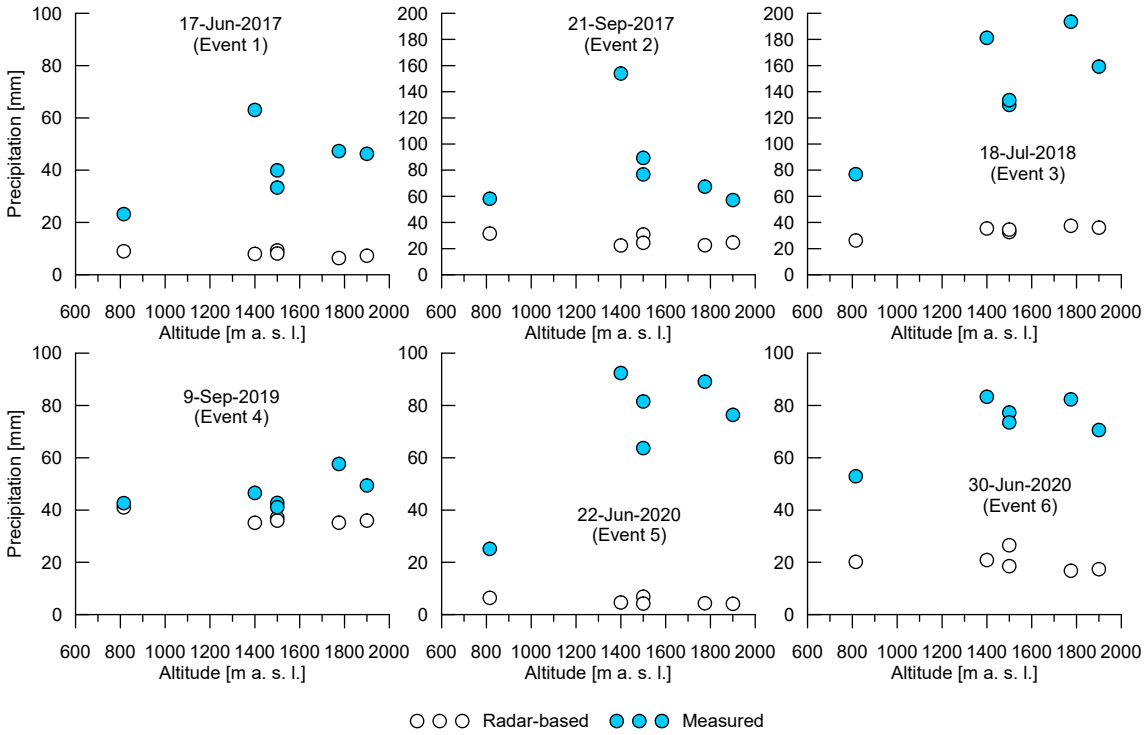

Fig. 8. Measured and radar-estimated daily precipitation at different altitudes for the selected greatest runoff events (the events are shown in Fig. 4).

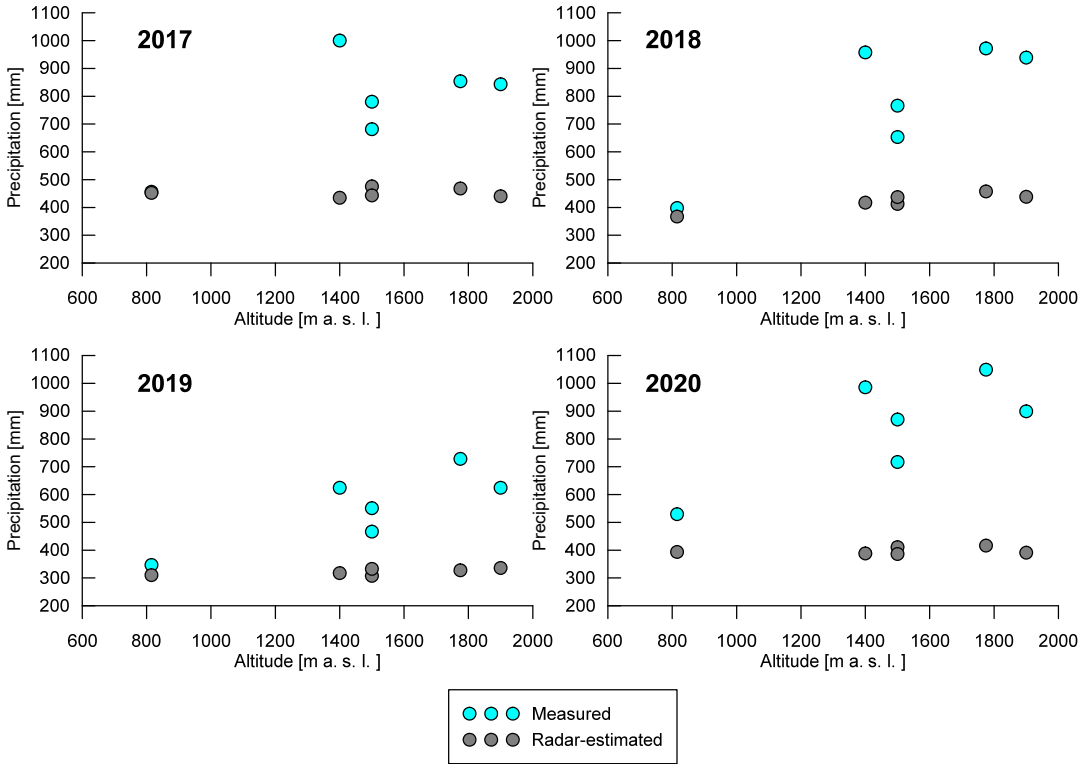

Fig. 9. Measured and radar-estimated total summer precipitation (June to September) at different altitudes; the two numbers are almost the same at the altitude of 800 m a.s.l. in summer 2017.

The bias of the radar-estimated precipitation did not show clear relationships with the synoptic weather situations (Figs. 10 and 11). It was often substantial for all weather situation, but the underestimation of the radar-based precipitation for synoptic weather situations NEc and NWc was greater than for B and Bp. The radar-based precipitation for the site Limni was mostly

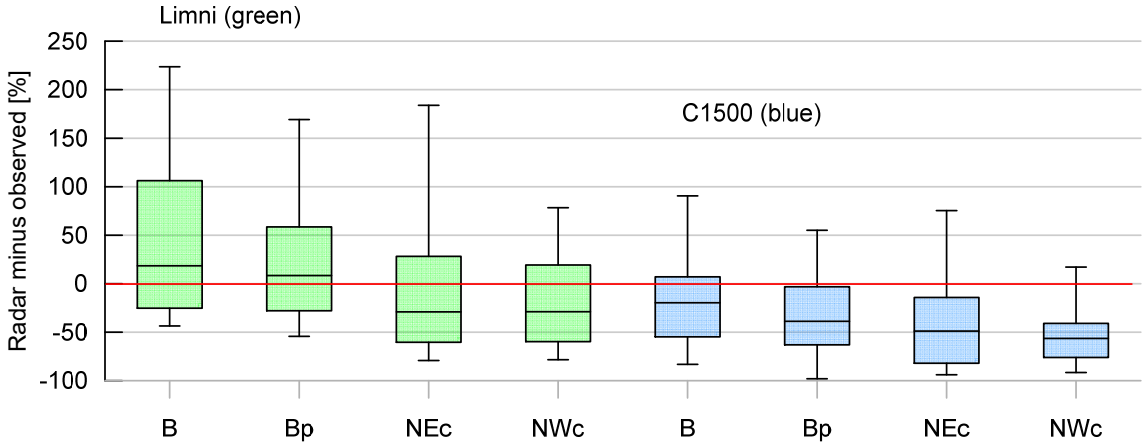

Fig. 10. Comparison of radar-estimated and measured daily precipitation for sites Limni and C1500 in the entire year (January–December) for the synoptic weather situations that were most frequently accompanied by precipitation; the whiskers represent percentiles 10 and 90, the boxes are the upper and lower quartiles and the center line shows medians; the number of values for individual boxplots varies between 86 and 113.

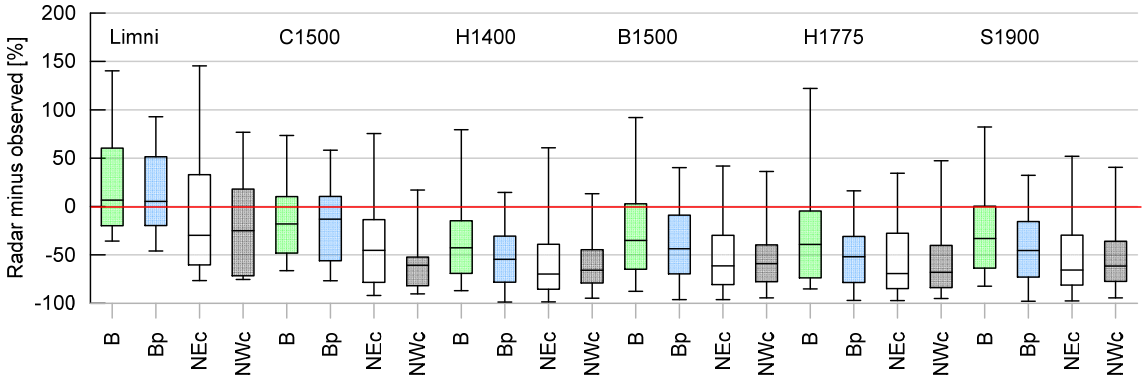

Fig. 11. Comparison of radar-estimated and measured daily precipitation for all stations for the warm period of the year (June–September) for synoptic weather situations that were most frequently accompanied by precipitation; the whiskers represent percentiles 10 and 90, the boxes are the upper and lower quartiles and the center line shows medians; the number of values for individual boxplots vary between 10 and 115.

greater than measured precipitation during synoptic weather situations B and Bp. For other situations and sites it was mostly lower than measured precipitation. Median bias between measured and radar-estimated precipitation during the NEc weather situation (i.e. the one bringing the highest precipitation amounts) in the warm period of the year (when the floods usually occur), were mostly greater than –50% (except for station Limni).

DISCUSSION

Our results show that the weather radar precipitation product mostly substantially underestimated measured precipitation in the studied mountain catchment. This conclusion is consistent with several studies evaluating the accuracy of various radar-based precipitation products (e.g., Goudenhoofdt and Delobbe, 2016; Hazenberg et al., 2011; Kreklow et al., 2020; Schleiss et al., 2020; Smith et al., 2012). The underestimation of measured precipitation was more significant for higher elevations. This may be related to radar coverage/signal that is limited due to terrain complexity and the shading problem. As it was pointed out by Berne et al. (2005), interception of the radar beam in mountainous areas by surrounding terrain is generally a major concern of the accuracy of radar-based precipitation products. Other sources of errors that affect the weather radar quality can be related to distance from the radar site, hardware, correction algorithms, etc. (e.g. McKee and Binns, 2016; Sokol et al., 2021). Underestimation of measured precipitation found in our study area is in general agreement with the results presented e.g. by Schleiss et al. (2020) or Kreklow et al. (2020).

High values of the correlation coefficients (the correlations explained 82% to 95% of variability) suggest that although the radar-based precipitation was underestimated compared to measured precipitation, the underestimation at individual sites was relatively stable.

Examination of the radar-based precipitation estimates for the six greatest runoff events in individual years (June to September) showed that the radar-estimated precipitation did not reproduce the observed altitudinal pattern of precipitation (much greater precipitation amounts at higher altitudes). Precipitation during five of the six events were significantly underestimated by the radar (except the event that occurred in September 2019). This may be caused by the fact that the calibration algorithm employs measured precipitation data for each radar from radius of about 240 km. This radius is probably often too high for the correct estimation of precipitation in mountains, because it covers large areas where precipitation is much smaller than in mountains.

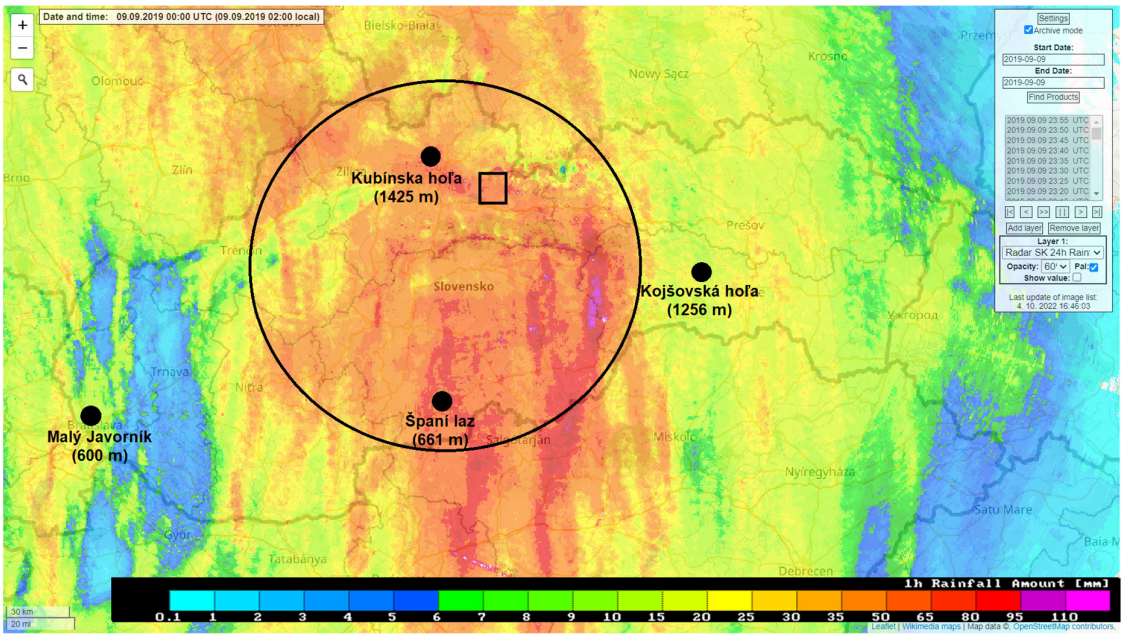

Fig. 12. 24-hour radar-estimated precipitation on 9, September 2019; the study area is indicated by a rectangle.

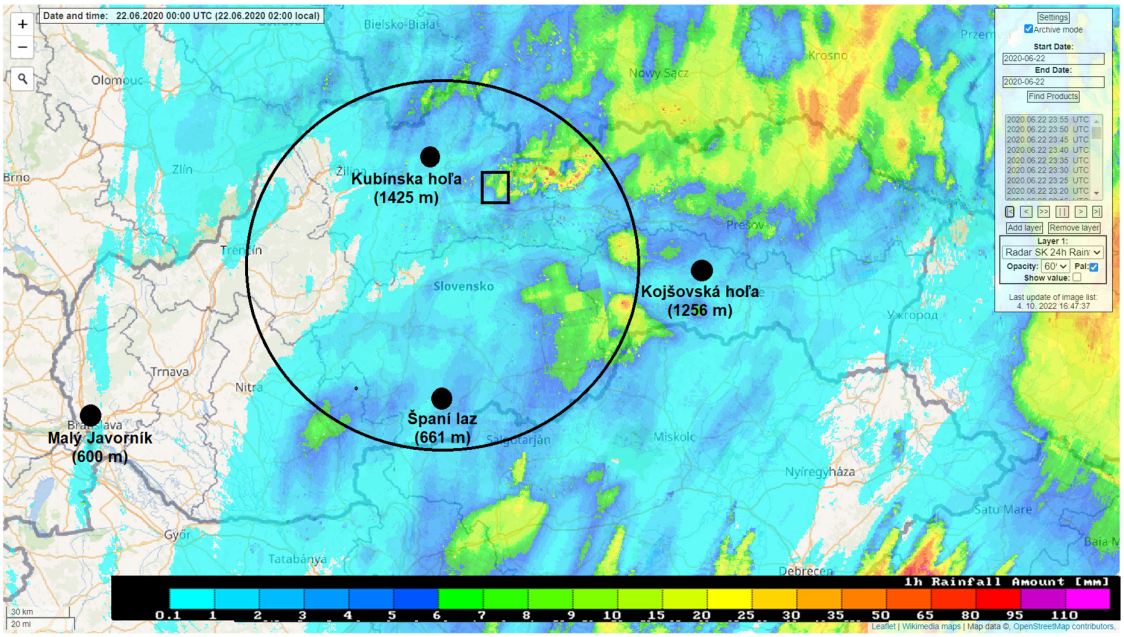

Fig. 13. 24-hour radar-estimated precipitation on 22, June 2020; the study area is indicated by a rectangle.

Thus, the radar-based precipitation estimates would be biased towards smaller precipitation amounts. This could be confirmed by Fig. 12 showing the situation around the radar at Kubínska hoľa that has the highest weight for precipitation estimates in the study area. It shows that on 9 September 2019, when the radar-based precipitation estimates were most similar to measured precipitation, a large territory surrounding the radar had high amounts of precipitation, i.e. the spatial differences in precipitation were less significant. Spatial differences in precipitation during other selected events (e.g. on 22 June 2020, Fig. 13), were greater, and thus the resulting calibration function also produced greater bias.

Similarly to precipitation during selected events, total summer radar-based precipitation failed to reproduce the elevation gradient found in measured data. It can thus be concluded that the radar-based precipitation could not provide correct input data for the event-based hydrological modelling in the studied mountain catchment (e.g. runoff forecasting, simulation of spatial distribution of soil moisture, runoff generation, etc.). This result does not agree with that of Gilewski and Nawalany (2018) who also studied a small mountainous catchment located on the northern part of the Carpathian Mountains. However, unlike our study catchment, the catchment of the Upper Skawa river is much larger (240.4 km^2) and had smaller mean altitude. Gilewski and Nawalany (2018) also used different precipitation product than the one that was used in our study.

Our study extends previous assessments by the analysis of the differences between the radar-estimated and measured precipitation taking into account synoptic weather situations. The

differences for trough situations B and Bp were smaller than for the cyclonal situations NEc and NWc (Fig. 11). However, it was not possible to conclude that the radar-estimated precipitation estimates are acceptably accurate for a particular synoptic weather situation or part of the year (summer versus the entire year).

CONCLUSIONS

We have compared the radar-estimated and measured precipitation in a small mountain catchment to assess the potential using the earlier for hydrological simulations. The results indicated major challenges in the radar-based precipitation estimation over complex topography. The weather radar consistently and significantly underestimated the measured precipitation and did not correctly reflect the differences in precipitation amounts at low and high altitudes.

The underestimation of measured precipitation was probably caused by local deviations from the average calibration curves per radar used by the qPrec software. More localized or altitude-based bias-correction of the radar precipitation estimates combined with installation of more rain gauges in mountains could help to solve the detected problems. Reduction of the effects caused by the topography by means of a gap-filling x-band radar can be considered as well. In the future, it would also be useful to fix the radar-estimated precipitation with a correction function that includes the altitude. Hourly precipitation estimates from the modified radar product that are more important for the correct flood forecasting can be tested in the future if the daily estimates will better compare to measured precipitation.

Acknowledgements. This study was supported by the grants from the Slovak Academy of Sciences (project VEGA No. 2/0065/19) and from the Slovak Research and Development Agency (project APVV No. 19-0340). Financial support by the Stefan Schwarz grant of the Slovak Academy of Sciences is also gratefully acknowledged.

REFERENCES

Abon, C.C., Kneis, D., Crisologo, I., Bronstert, A., David, C.P.C., Heistermann, M., 2016. Evaluating the potential of radar-based rainfall estimates for streamflow and flood simulations in the Philippines. Geomat. Nat. Hazards Risk, 7, 1390–1405.

Ballon, L., Forgáč, P., Molnár, F., 1964. Weather over the territory of Slovakia in typical weather situations. Hydrometeorologický ústav, Prague, 30 p. (In Slovak.)

Berne, A., ten Heggeler, M., Uijlenhoet, R., Delobbe, L., Dierickx, P. de Wit, M., 2005. A preliminary investigation of radar rainfall estimation in the Ardennes region and a first hydrological application for the Ourthe catchment. Nat. Hazards Earth Syst. Sci., 5, 267–274.

Brádka, J., Dřevikovský, A., Gregor., Z., Kolesár, J., 1961. Weather over the territory of Bohemia and Moravia in typical weather situations. Hydrometeorologický ústav, Prague, 31 p. (In Czech.)

Danko, M., Holko, L., Kostka, Z., Tachecí, P., 2015a. Simulation of snow water equivalent, snowmelt rate and runoff in mountain catchment during winter period. Acta Hydrologica Slovaca, 16, 1, 42–50. (In Slovak.)

Danko, M., Holko, L., Kostka, Z., Krajčí, P., Hlavčo, J., 2015b. Long-term simulation of snow water equivalent in mountain catchment using MIKE SHE / MIKE 11. Acta Hydrologica Slovaca, 16, 227–234. (In Slovak.)

Espinosa, B., Hromadka, T.V., Perez, R., 2015. Comparison of radar data versus rainfall data. MethodsX, 2, 423–431.

Fairman, J.G., Schultz, D.M., Kirshbaum, D.J., Gray, S.L., Barrett, A.I., 2015. A radar-based rainfall climatology of Great Britain and Ireland. Weather, 70, 153–158.

Germann, U., Galli, G., Boscacci, M., Bolliger, M., 2006. Radar precipitation measurement in a mountainous region. Q. J. Roy. Meteorol. Soc., 132, 1669–1692. DOI: 10.1256/qj.05.190

Gilewski, P., Nawalany, M., 2018. Inter-comparison of rain-gauge, radar, and satellite (IMERG GPM) precipitation estimates performance for rainfall-runoff modeling in a mountainous catchment in Poland. Water, 10, 1665.

Goudenhoofdt, E., Delobbe, L., 2016. Generation and verification of rainfall estimates from 10-yr volumetric weather radar measurements. J. Hydrometeor., 17, 1223–1242.

Hazenberg, P., Leijnse, H., Uijlenhoet, R., 2011. Radar rainfall estimation of stratiform winter precipitation in the Belgian Ardennes. Water Resour. Res., 47, 257.

Hess, P., Brezowsky, H., 1977. Katalog der Großwetterlagen Europas 1881-1976. 3rd Ed. Berichte des Deutschen Wetterdienstes, 113, 1–140. (In German.)

Hofstätter, M., Lexer, A., Homann, M., Blöschl, G., 2018. Large-scale heavy precipitation over central Europe and the role of atmospheric cyclone track types. Int. J. Climatol., 38, e497–e517. https:// doi.org/10.1002/joc.5386

Holko, L., Sleziak, P., Danko, M., Sleziak, P., 2021. Snowmelt characteristics in a pristine mountain catchment of the Jalovecký Creek, Slovakia, over the last three decades. Hydrol. Process., 35, e14128.

Holko, L., Hlavčo, J., Kostka, Z., 2014. Spatial distribution of precipitation in a mountain catchment. Acta Hydrologica Slovaca, 15, 102–109. (In Slovak.)

Holko, L., Kostka, Z., Danko, M., Liová, S., 2011. Hydrological Cycle in Mountain Environment. Životné prostredie, 45, 59–63.

Hrušková, K., Hlaváčiková, H., 2022. How to improve hydrological model forecast using precipitation data from small experimental basin. In: Book of Abstracts of the 18th Biennial Conference ERB 2022 Euromediterranean Network of Experimental and Representative Basins. Portoferraio, Elba Island, Italy, p. 37.

Kreklow, J., Tetzlaf, B., Burkhard, B., Kuhnt, G., 2020. Radar-based precipitation climatology in Germany – Developments, uncertainties and potentials. Atmosphere, 11, 217.

Marra, F., Morin, E., 2015. Use of radar QPE for the derivation of Intensity–Duration–Frequency curves in a range of climatic regimes. J. Hydrol., 531, 427–440.

McKee, J.L.; Binns, A.D., 2016. A review of gauge–radar merging methods for quantitative precipitation estimation in hydrology. Can. Water Resour. J., 41, 186–203.

Méri, L., Gaál, L., Bartok, J., Gažák, M., Gera, M., Jurašek, M., Kelemen, M., 2021. Improved radar composites and enhanced value of meteorological radar data using different quality indices. Sustainability, 13, 9, 5285.

Schleiss, M., Olsson, J., Berg, P., Niemi, T., Kokkonen, T., Thorndahl, S., Nielsen, R., Nielsen, J.E., Bozhinova, D., Pulkkinen, S., 2020. The accuracy of weather radar in heavy rain: A comparative study for Denmark, the Netherlands, Finland and Sweden. Hydrol. Earth Syst. Sci. Discuss., 1–42.

Slovak Hydrometeorological Institute (SHMI), 2021. Types of weather situations (http://www.shmu.sk/sk/?page=8) (In Slovak.)

Smith, J.A., Baeck, M.L., Villarini, G., Welty, C., Miller, A.J., Krajewski, W.F., 2012. Analyses of a long-term, high-resolution radar rainfall data set for the Baltimore metropolitan region. Water Resour. Res., 48, 616.

Sokol, Z., Szturc, J., Orellana-Alvear, J., Popová, J., Jurczyk, A., Célleri, R., 2021. The role of weather radar in rainfall estimation and its application in meteorological and hydrological modelling – A review. Remote Sens., 13, 351.

Villarini, G., Krajewski, W.F., 2010. Review of the different sources of uncertainty in single polarization radar-based estimates of rainfall. Surv. Geophys., 31, 107–129.

Received 5 August 2022
Accepted 27 October 2022